ON THE INFLUENCE OF PRECESSIONAL MILANKOVITCH CYCLES ON THE LATE CRETACEOUS CLIMATE SYSTEM: COMPARISON OF GCM-RESULTS, GEOCHEMICAL, AND SEDIMENTARY PROXIES FOR THE WESTERN INTERIOR SEAWAY OF NORTH AMERICA

Doctoral Thesis

Submitted in partial fulfillment of the requirements for the doctoral degree
at the Faculty of Mathematics and Natural Sciences of the
Christian-Albrechts-University
Kiel, Germany

by

Sascha Flögel

Kiel 2001

Abstract

A multidisciplinary study of upper Cenomanian-lower Turonian strata of the late Cretaceous Western Interior Seaway explored possible mechanisms for the formation of cyclic bedding sequences seen in the Western Interior Seaway. Numerical climate modeling was used to investigate the sensitivity of the climate to changes of one of the Earth's orbital parameters, the precession of the equinoxes.

Nine sections along a transect from southern Canada through northern Mexico were measured and analyzed, using geochemical (Total organic carbon, $CaCO_3$, and $\delta^{13}C_{org}$.) and sedimentological data. Assuming average sedimentation rates of 2.25 cm/ka, the stratigraphic sections show Milankovitch-like periodicities, but bedding couplets could not be seen in all of them. The northern sections (Alberta and Montana) do not show any lithological cyclicity. Bedding couplets form only in the central (New Mexico) and southern (Texas and Nuevo Leon) parts of the seaway. Lithological cyclicity with periodities of ~22 ka and ~27 ka (precession) is indicated for the central part. In the southern part, the sediment record indicates periodities close to 40 ka and 44 ka cycles (obliquity). Geochemical analysis has indicated periodities closely related to Milankovitch parameters. Sections in southern Canada show a cyclicity of 266-288 ka for the $\delta^{13}C_{org}$, total organic carbon and $CaCO_3$ parameters and a 122 ka variation of the $CaCO_3$ content. One of the New Mexican sections shows cyclic variation of the total organic carbon- and $CaCO_3$ content with periodicities of 16 ka and 22 ka. The Texan section shows a periodicity of the $CaCO_3$ parameter close to the 42 ka obliquity cycle, whereas the Mexican section does not show any geochemical cyclicity.

The resemblance between Milankovitch-type periodicities in the Earth's orbital elements and Late Cretaceous rhythmic bedding sequences at the Cenomanian/Turonian boundary in the Western Interior seaway strongly suggests an orbital influence on sedimentary regimes during non-glacial times.

A reference paleoclimatic model was simulated by a control run with a circular orbit, an obliquity of 23.5°, and 5 x present day CO_2.The control run predicts a global mean annual temperature of ~20.7°C, almost 6°C higher than the present mean annual temperature. The results of the control run suggest global atmospheric and oceanic circulation systems that were very different from today. Modeling results suggest that there were no effective subtropical and polar fronts in the ocean. The lack of these frontal systems implies that there were changes in the location and strength of the westerly winds, suggesting that there may have been seasonally two rather than three atmospheric cells per hemisphere at some times of the year. A two-cell/hemisphere circulation was generated by the model during hemispheric winters demonstrating that this is possible when the Earth has warm poles.

One complete precessional cycle was simulated with four orbital runs; 1) northern spring equinox at perihelion, 2) northern winter solstice at perihelion, 3) northern fall equinox at perihelion, and 4) northern summer solstice at perihelion. Although global mean annual changes are slight, there are major monthly variations of these parameters. Precessional Milankovitch cycles result in changes in the distribution of solar radiation at the top of the atmosphere resulting in significant seasonal variations in global temperature and precipitation, and in surface- and subsurface runoff over land. The cyclic organization of limestone/shale couplets seen in the sedimentological record of the central part of the Western Interior Seaway can be interpreted as reflecting climatic cycles. The most important mechanism for the formation of bedding couplets were changes induced by the precession of the equinoxes. The most important variable was surface runoff, which affected both the discharge of rivers and the amount of sediment transported into the Western Interior Seaway. Annual river discharge from western North America into the seaway was equivalent to a layer of fresh water ~0.3m thick. River discharge into the Arctic Ocean was even greater, equivalent to a layer more than 1m thick each year. These very large supplies of fresh water from land were adequate to maintain low salinity surface waters in the Arctic Ocean and the Western Interior Seaway. High surface runoff from the highlands bordering the Western Interior Seaway to the west occured during summer in three of the orbital configurations but low surface runoff when northern hemisphere winter is at perihelion. The precession signal seen in the sediment is interpreted as being produced by the elimination of high summer surface runoff when perihelion occurs during northern hemisphere winter.

In summary, the Cenomanian/Turonian Western Interior Seaway can be divided into three units controlled by different climatic, topographic and oceanographic factors:

1) A northern unit where bedding couplets did not develop. Sediments were deposited beneath low salinity (<24 ‰ ?), relatively cool waters, excluding of calcareous microplankton and calcareous benthic foraminifers. The variations of surface runoff to changes of the precessional parameter are slight, but the topographic and climatic conditions of northern western North America delivery of large amounts of terrigenous material to the seaway.

2) The central unit responded to changes of the precessional parameter with the formation of bedding couplets. It had more normal warm saline marine conditions and large-scale carbonate production from calcareous plankton. Due to the narrow and steep drainage basins to the west, changes of the surface runoff regime translated directly to varying sediment loads of rivers.

3) The southern unit was controlled by mechanisms similar to those influencing the central unit, but was open to the Gulf of Mexico. However, sensitivity to changes of the precession of the equinoxes was lower than for the central unit. The properties of the water masses resembled more those of an open ocean and sedimentation was probably controlled by changes in obliquity. Periodic carbonate dissolution produced by fluctuations of the depth of the lysocline may have been responsible for the formation of the rhythmic limestone and marl couplets.

1. Introduction

The goal of this investigation was to develop a paleoclimatic model for the Late Cretaceous Western Interior Seaway of North America (WIS) and to test it's sensitivity to changes of one of the Earth's orbital parameters, the precession of the equinoxes. Focussing on the Cenomanian/Turonian (C/T) boundary nine sections were sampled. These represent a North-South transect, extending from southern Canada through northern Mexico (Figure 1). Sedimentological, paleontological, and geochemical methods were used to test results of the paleoclimate simulations.

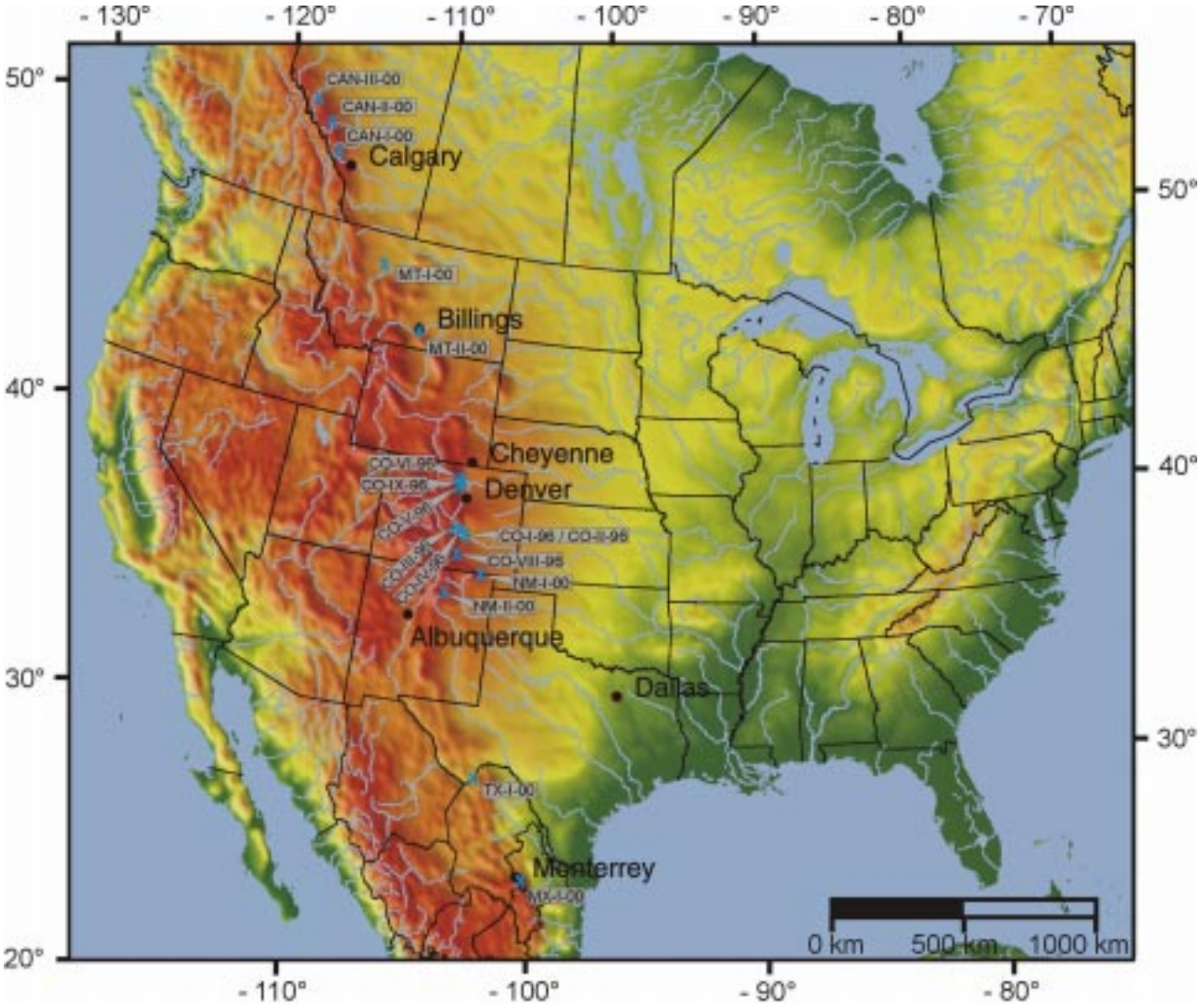

Figure 1: Present geographic position of the sampled locations (only locations labeled ...**-00** have been sampled during this study; locations labeled –96 were sampled in 1996).

1.1. Why the Cretaceous – Why the Cenomanian/Turonian boundary ?

Geological history shows that climatic “icehouse” states, like the one we have today, have alternated with times of a more even energy distribution (reduced temperature gradients from the equator to the poles), when the polar regions had no permanent ice cover and the mean temperature of polar oceanic water masses rose to temperatures as high as 15°C, the present global surface average. Sea levels were extremely high, both as a result of the lack of ice and of a decrease in volume of the ocean basins related to increased rates of sea-floor spreading and thermal uplift of the sea floor that accompanied massive volcanism (SCHLANGER et al., 1981; LARSON, 1991). Those times have been referred to as “greenhouse” states. During the Cretaceous the Earth’s climate reached an extreme greenhouse state, probably as a result of high pCO_2, estimated to be 3-12 times pre-industrial pCO_2 (BERNER, 1992, 1994; BERNER et al., 1983; BARRON and WASHINGTON, 1985; CERLING, 1991; BARRON et al., 1995). Average temperatures were higher than today (BARRON, 1983; BARRON et al., 1995; SPICER and CORNFIELD, 1992; SELLWOOD et al., 1994), as was the sea level (HAQ et al., 1987). Climatic models patterned on the present-day have failed to reproduce these conditions, suggesting that the greenhouse climate operated in a different mode. Knowledge of that mode is necessary for an understanding of the climate system as a whole.

The greenhouse state began in middle Cretaceous time, climaxed before the end of the period, and extended into the early Tertiary before giving way to the present icehouse.

For several reasons, the Cretaceous is *the* greenhouse episode to study. An understanding of global climate requires a global database. Due to seafloor spreading, the only records of pre-middle Jurassic oceans are scraps left in mountain belts. The Cretaceous is the oldest period for which accurate global reconstructions of ocean-continent distributions, based on magnetic lineations on the ocean floor, can be made.

Information on Cretaceous oceans is vastly better than for earlier periods, not only because much more material has been preserved but due to the rapid development and spread of calcareous plankton, which began in the Jurassic. These fossils provide a far better record of oceanic life than that available for earlier periods. In addition, Cretaceous plankton are directly comparable to today’s planktonic communities, making interpretations easier.

The high sea levels attained during the Late Cretaceous have left a particularly widespread and complete record of the shallower shelves, epicontinental seas like that of the Western Interior, and land areas. About 40% of the present land surface was flooded by seas with depths ranging up to several hundred meters.

Marine deposits of Cretaceous age show a very distinctive lithologic character. Among these are regular oscillations of hard and soft chalks, or pelagic limestones with marls and/or shales, with

periodicities between 20,000 and 400,000 years, thought to be driven by Earth orbital (Milankovitch) variations.

Another important feature of the middle Cretaceous (120-80 Ma) is the development of several globally widespread episodes of organic carbon burial in marine sequences (e. g. SCHLANGER and JENKYNS, 1976; ARTHUR and SCHLANGER, 1979; JENKYNS, 1980; ARTHUR et al., 1987; SCHLANGER et al., 1987; ARTHUR et al., 1990). The mid Cretaceous record is unusual because black shale deposition was not limited to local areas with special oceanic conditions (e. g., upwelling or small enclosed basins with restricted circulation) (HOFMANN et al., 1999). There were periods of widespread oxygen deficiency in oceanic mid- and deep-water masses that have been termed “Oceanic Anoxic Events (OAEs)”. The widespread occurrence of OAEs in time and space within the middle Cretaceous may imply fundamental changes in oceanic circulation and/or the rate and mode of delivery of organic matter to the deep sea. For example the distribution of oxygen-deficient conditions in the ocean and the fluxes of organic matter to the sea floor might have been different (SCHLANGER and JENKYNS, 1976; PEDERSEN and CALVERT, 1990). The stratigraphic occurrences of Cretaceous black-shales indicate that there were three major time envelopes of C_{org} deposition, late Barremian through Albian, late Cenomanian through early Turonian and Coniacian through Santonian (RYAN and CITA, 1977; JENKYNS, 1980). OAE II, the “Bonarelli ” event occurred at the Cenomanian/Turonian boundary. These OAE’s were periods of extreme sequestration of organic-carbon, reflecting conditions particularly favourable to petroleum source-rock formation. More than 29% of the world’s discovered original reserves of oil and gas have been generated by middle Cretaceous source rocks (KLEMME and ULMISHEK, 1991). Changes in the marine macro- and microfauna, sedimentary geochemistry and surface-water paleoproductivity through the last 500,000 years of the Cenomanian and first 300,000 years of the Turonian have been documented by GALE et al. (2000). Based on rates of faunal turnover, this period was identified as the third largest mass extinction in the post Paleozoic, exceeded in magnitude only by Cretaceous/Tertiary (K/T) and Norian/Rhaetian (late Triassic) events (RAUP & SEPKOWSKI, 1982). In the marine realm, 7% of families, 26 % of genera and 53% of species are estimated to have become extinct at the C/T boundary (SEPKOWKI, 1989; JABLONSKI, 1991; HARRIES, 1993).

The Western Interior Seaway of North America at the Cenomanian/Turonian boundary was chosen for this study because the sedimentological record of units of this age, the Agua Nueva Formation, the Ernst Member (Boquillas formation), the Bridge Creek Limestone Member (Greenhorn Formation), the Cone Member (Marias River Shale), and the Vimy Member (Blackstone Formation) provides a very good opportunity to study the Late Cretaceous greenhouse climate (Figure 8). The Western Interior is one of the most intensely studied and best understood epicontinental seas in the world. A high resolution stratigraphic record, based on sedimentological (e. g. marker beds),

paleontological, and geochemical data had already been established (KAUFFMAN, 1977, 1984, 1985; KAUFFMAN and CALDWELL, 1993; KAUFFMAN et al., 1991; SAGEMAN and ARTHUR, 1994; SAGEMAN et al., 1997, 1998). The stratigraphic record can serve as a firm base for reconstruction of the climatic and oceanographic conditions of the Late Cretaceous of the North American Interior.

2. Paleogeography, oceanographic, and geological setting

The history of the Western Interior Seaway is well documented in several compilations (PRATT et al., 1993: CALDWELL and KAUFFMAN, 1993; CAPUTO et al., 1994). Aspects of this history relevant to this study include the paleogeography, climatic system, oceanography, and the geological setting of the seaway during deposition of the Bridge Creek Interval in the central regions of the WIS and it's temporal equivalents in the northern and southern parts of the seaway.

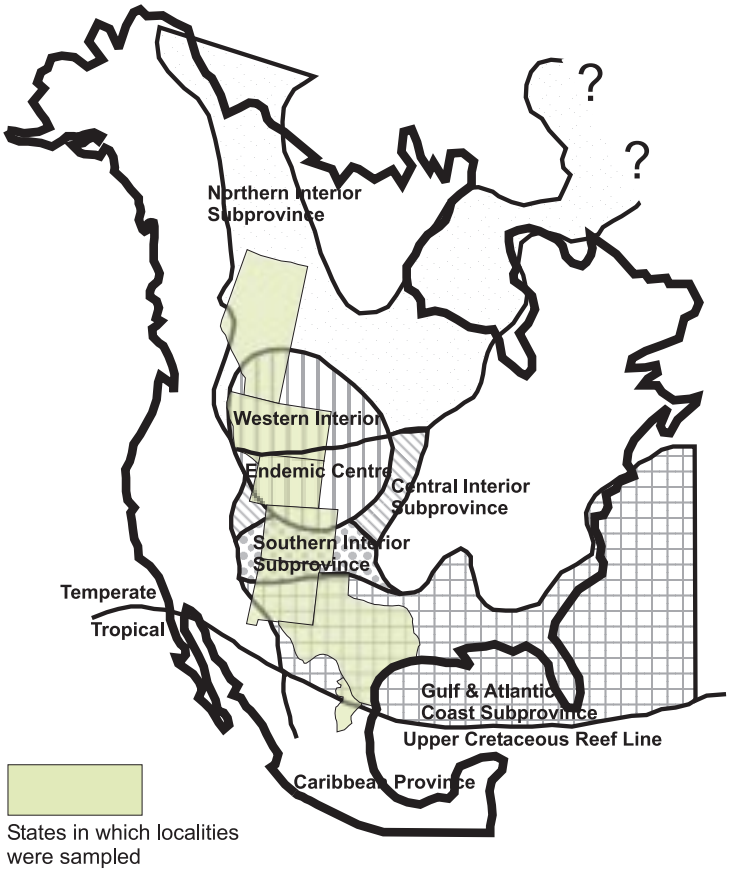

Figure 2: Map showing Northern, Central and Southern Interior paleobiogeographic subprovinces in the Cretaceous Western Interior Seaway of North America. Subprovinces (10-25 %) and provinces (25-50 %) are defined by molluscan endemism. The subprovinces also reflect endemic centres and have different regional biostratigraphic systems. After KAUFFMAN (1984).

Six third-order tectonoeustatic cycles of marine transgression and regression are recorded in Cretaceous strata of the Western Interior (KAUFFMAN, 1977, 1984, 1985; following the terminology of VAIL et al., 1977). The best developed and most extensive of these cycles is the early Cenomanian-middle Turonian Greenhorn cycle (WEST et al., 1998). During the Late Cenomanian and Early Turonian, a combination of foreland-basin subsidence and tectono-eustatic

sea level highstand resulted in maximum flooding of the Western Interior basin (JORDAN, 1981; KAUFFMAN, 1984). This was the highest sea level of the first-order Mesozoic-Cenozoic tectonoeustatic cycle (HANCOCK and KAUFFMAN, 1979; HAQ et al., 1987). It resulted in a meridional seaway that has no modern analog, extending across more than 50° of latitude and connecting the polar ocean of arctic Canada and Alaska to the subtropical-tropical western Tethys (Gulf of Mexico) (KAUFFMAN, 1977, 1984). Mixing of Tethyan and Polar waters undoubtedly occurred within the seaway (EICHER and WORSTELL, 1970; FRUSH and EICHER, 1975; KAUFFMAN, 1985; PRATT, 1985; EICHER and DINER, 1985; FISHER, 1991; FISCHER and HAY, 1999; HAY et al, 1993), yet the extent to which this mixing controlled the circulation remains unclear (KUMP and SLINGERLAND, 1999). There is evidence that warm water masses might have penetrated as far north as the prairie provinces of southern Canada. The rich fossil biotas blend along a broad paleobiogeographic ecotone near the middle of the meridional seaway (KAUFFMAN,1993). Exchange of oceanic and seaway waters may have been inhibited by the presence of sills at the northern and southern entrances (JELETSKY, 1970; SCOTT, 1977; KAUFFMAN, 1984, 1988; YOUNG, 1986). The east-west extension of the epicontinental seaway was between 1500 and 2000 km during highest eustatic sea level stand. A connection across Hudson Bay in northwestern Canada has also been proposed (WILLIAMS and STELCK, 1975; KAUFFMAN, 1977a; WHITE et al., 2000). Climatic interpretations from geological data suggest warm temperate to subtropical climates with humid to subhumid conditions for the central Western Interior region (KAUFFMAN, 1984; PRATT, 1984; UPCHURCH and WOLFE, 1993; LUDVIGSON et al., 1994; WITZKE and LUDVIGSON, 1994). The seaway received surface runoff from rivers that drained the Sevier orogenic belt on its western side and from the lowlands of the stable craton on its eastern side.

2.1. Tectonics

The WIS was the result of a phase of worldwide tectonic changes between Jurassic and Eocene times. It’s western side was an elongate, complex, eastward-migrating foreland basin that first developed during the Jurassic in response to uplift and eastward thrusting along the north-south trending Cordilleran Geanticline. The seaway extended across the asymmetric foreland onto the tectonically quiet stable craton. The north-south trending proto-Cordillera and foreland basin are expressions of Cretaceous global tectonic events: accelerated seafloor spreading; plate convergence and subduction; orogeny with associated plutonism and volcanism; and eustatic fluctuations of sea level, including the highest stand since the Paleozoic.
Major tectonic elements of the proto-Cordillera of the Rocky Mountains were a western subduction complex, a broad central calc-alkaline magmatic arc, and an eastern fold and thrust belt (Figure 3).

Major north-south trending tectonic elements developed in the Jurassic (PRICE et al., 1981; KAUFFMAN; 1985; MONGER, 1993; ARMSTRONG and WARD, 1993).

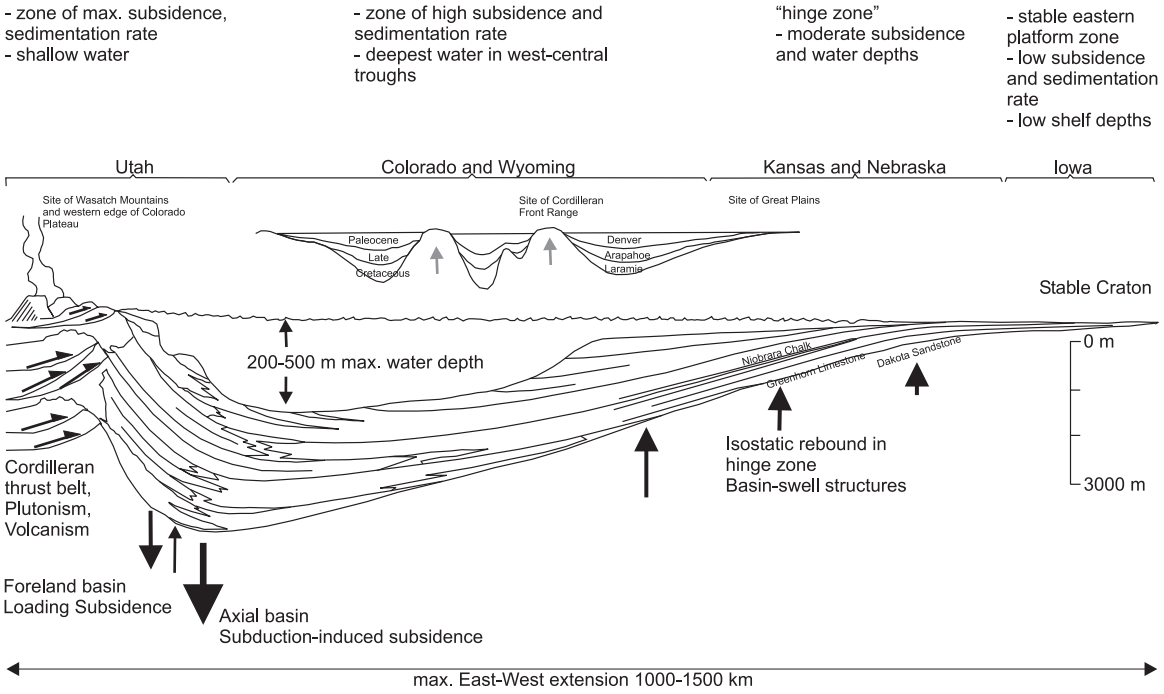

Figure 3: Generalized cross section of major tectonic zones of the Western Interior Seaway (after KAUFFMAN, 1984).

Accretion of terranes onto the western edge of North America started during the early Cretaceous. This led to renewed magmatic activity, dextral strike-slip fault movements, and growth of the fold and thrust belt which began to cannibalize older sediments. During the early Cretaceous the eastern Cordillera experienced thermal uplift of the eroded central geanticline which led to shedding of coarse-grained detritus across the developing foredeep of the basin. Further development of the foredeep associated with eastward thrusting and synorogenic sediment loading led to uplift of a forebulge, which trapped sediments in the foredeep. Early in the Late Cretaceous, marine sedimentation was limited to the Western Interior foreland basin, east of the Cordillera.

2.1.1. Tectonic zones of the basin

The seaway was composed of a series of longitudinal tectonic zones (Figure 3), which can be divided into five units (KAUFFMAN, 1977, 1984, 1985): The western foredeep had the highest sedimentation rates and underwent the greatest subsidence. Coarse-grained, synorogenic, terrigenous clastic sediments accumulated as coastal-plain to shallow-water marine facies (JORDAN, 1981). Further to the east, flanking the narrow foredeep, the forebulge was a set of arches along the length of the basin, approximately 150-200 km east of the eastern margin of the

Cordillera. The forebulge is not shown in Figure 4 because it was not developed in the central part of the U. S.; it was fully developed further north in Montana and Canada. The forebulge separated the coarse-grained, shallow-water sediments typical for the foredeep, from the finer-grained deeper water sediments typical of the eastern part of the basin. Further east lay the broad axial trough with fine-grained sedimentation and episodic, strong, rapid subsidence. Medium- to fine-grained terrigenous sediments with some interbedded pelagic carbonates accumulated. This trough is characterized by relatively deep waters, probably the deepest part (about 250 m) of the entire seaway. Nearly complete stratigraphic records are preserved in this trough. The axis of the trough was probably along the corridor from northeastern New Mexico to the Black Hills region of northeastern Wyoming and southwestern South Dakota (e. g. EICHER, 1969; KAUFFMAN, 1977; SAGEMAN and ARTHUR, 1994). The eastern part of the seaway was another broad tectonostratigraphic sector of the basin, bounded to the west by a fairly gentle slope rising eastward from the axial or west-median trough. Sedimentation rates were moderate to low and subsidence varied, being lower over the broad, gentle, eastern flank than over the narrower, steeper, western flank of the hinge. The eastern platform, which underlay one-third of the seaway, was tectonically stable. Subsidence was slow and episodic, leading to thin sequences of fine-grained terrigenous clastic and pelagic carbonate sediments. These were deposited under low-energy conditions on a broad, shallow, marine shelf with little tidal exchange. Coarse-grained, terrigenous clastic deposits were derived from the craton to the east but restricted to the near-shore portion of the platform (KAUFFMAN and CALDWELL, 1993).

2.2. A new paleogeographic reconstruction

Because accurate and high-resolution paleogeographic maps are critical for the simulation of paleoclimates (HAY, 1996; CROWLEY, 1998), a new Late Cretaceous paleogeography was constructed on a 2° x 2° grid. For this study a map for the Lower Turonian prepared by Alexander BALUKHOVSKY and Areg MIGDISOV (unpublished map, Vernadsky Institute of Geosciences, Moscow) was used to reconstruct the paleoshorelines. The original map (Figure: 4) is on a polyconic projection at a scale of 1:48,000,000.

Figure 4: Paleogeographic map for the Lower Turonian by BALUKHOVSKY & MIGDISOV (unpublished).

The paleogeography has been transferred onto a global plate tectonic reconstruction, which includes the 290 tectonic blocks and fragments of HAY et al. (1999) restored to their Turonian positions. Global topography is another important boundary condition for paleoclimate modeling. The topography affects the zonal mean circulation, storm track positons, precipitation patterns, and snowline (DeCONTO, 2000).

The paleogeographic map provides 3-dimensional data, because Balukhovsky and Migdisov distinguish three different topographic levels: low lands (0- 200 m of altitude), low mountains (200-500 m), medium high mountains (500-1000 m) and high mountains (1000-3000 m).

Like the shoreline data, paleoelevations were interpreted from the paleogeographic map and from information from KAUFFMAN, pers. comm.. Topographic data were superposed on the tectonic model and contoured with the paleoshorelines providing zero elevation. The elevations of the Late Cretaceous and Cenozoic Rocky Mountains and the Sevier Highlands are difficult to estimate from the geologic record, yet this variable plays an important role in the modeling of paleoclimates. Recent studies from DETTMAN and LOHMANN, 2001 have shown that the pattern of $\delta^{18}O$ of freshwater bivalves in the paleorivers of the Western Interior of North America was significantly affected by regional differences in altitude. The commonly held idea that there was low relief in the Western Interior during the Cretaceous (BLACKWELDER, 1915; EPIS and CHAPIN, 1975; BARRON, 1985) has been challenged by a number of studies (DECELLES et al., 1991; WOLFE et

al., 1998; MOLNAR and ENGLAND, 1990; KAUFFMAN, pers. comm.). The latter authors suggest paleoelevations of up to 3000 m.

The paleogeography used for the paleoclimatic simulations is shown in Figure 5.

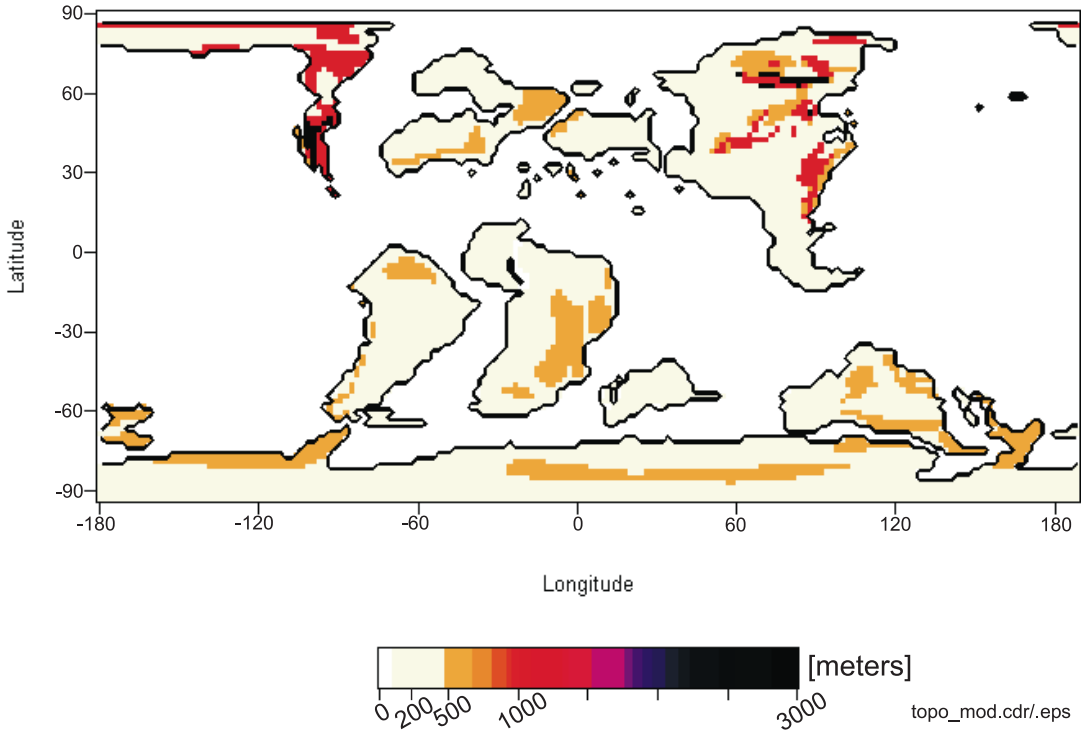

Figure 5: Lower Turonian paleogeography, providing the solid-earth boundary conditions for the modeling runs, including paleoshorelines and topography after BALUKHOVSKY & MIGDISOV (unpublished) superposed on the Late Cretaceous plate tectonic model of HAY et al. (1999).

If the present day positions of the sections sampled (Figure 1) are “rotated back” to their Late Cretaceous positions using the HAY et al. (1999) rotation files, the nine sections (from N to S) had the following paleolatitudes:

	Present day:	C/T boundary:
CAN-III-00	~52°	~61°N
CAN-II-00	~52°	~60°N
CAN-I-00	~51°	~59°N
MT-I-00	~47°	~55°N
MT-II-00	~45°	~52°N
NM-I-00	~36°	~42°N
NM-II-00	~35°	~42°N
TX-I-00	~29°	~36°N
MX-I-00	~25°	~31°N

3. Variation of the Earth's orbital parameters – Milankovitch cycles

3.1. History

Interpretations of past climates and climate change, based upon sedimentary and paleobiological observations, have a long and distinguished record in the geological literature (AGASSIZ, 1828; DARWIN, 1842). LYELL, for example, gave serious consideration to the climatic impact of changing continental distributions on the earth, and of the potential implications of Himalayan-scale mountains in polar positions for the climate of the planet as a whole (LYELL, 1840). LYELL was also very well aware of the potential for orbitally induced climate fluctuations like those resulting from changes in the eccentricity of the Earth's orbit.

Despite the complexity of the climate system, some major changes in the Earth's climate can be related directly to specific causes. Most notably, the alternate growth and melting of ice sheets in the northern hemisphere has been attributed to waxing and waning of the radiation received from the sun (insolation) as a result of changes in the Earth's orbital parameters (ADHÉMAR, 1842; CROLL, 1864, 1875; GILBERT, 1895; MILANKOVITCH, 1920; 1930; KÖPPEN and WEGENER, 1924; EMILIANI and GEISS, 1959; HAYS et al., 1976), amplified by positive feedback mechanisms (SALTZMAN et al., 1984; SATZMAN and MAASCH, 1988; BROECKER, 1995). Inspired by the "Révolutions de la Mer" of ADHÉMAR (1842), and employing the calculations of LAGRANGE (1772) for the maximum eccentricity of the Earth's orbit, CROLL proposed that the "eccentricity alone was great enough to account for every extreme of climatic change evidenced by geology" (IRONS, 1896). Those secular pertubations change the geographic distribution of incoming solar radiation at the top of the atmosphere periodically (MILANKOVITCH, 1941; BERGER et al., 1984; BERGER and TRICOT, 1986).

Basically, the astronomical theory assumes that the surface air temperature is directly related to the insolation available at the top of the Earth's atmosphere (transparent atmosphere) and that the climate is sensitive to the changes in the distribution of that insolation among latitudes and seasons (TRICOT and BERGER, 1986).

The values for orbital parameters beyond 20 million years can not be calculated accurately because the required information on celestial mechanics is not available. BERGER et al. (1992) found that the motion of the solar system, and especially the motion of the inner planets, is chaotic. Such chaotic motion has two consequences. First, it is impossible to compute the exact motions within the solar system. Second, the fundamental frequencies of the planetary system are not fixed quantities, but slowly vary with time. The main source of uncertainty in the computation of precession and obliquity of the Earth is found to arise from the changes of dynamical ellipsoidality

of the Earth which can occur during an ice age due to the formation of icecaps (LASKAR et al., 1993).

3.2. Insolation

The annual variations in insolation resulting from the tilt of the Earth's axis relative to the plane of the Earth's orbit around the sun produce the seasons, but the intensity of the seasonal insolation varies on timescales of 10^4-10^5 years because of variations in the Earth's orbital parameters (BERGER, 1977, 1981, 1984, 1987; IMBRIE & IMBRIE, 1980).
The major orbital variations affecting insolation are (Figure 6):

a.) the ellipticity (eccentricity) of the Earth's orbit, which changes the distance from the earth to the sun during the course of a year and varies on 100 ka timescale, with a longer cycle of variation at a 400 ka timescale;
b.) the tilt (obliquity) of the Earth's axis of rotation relative to the plane in which it orbits the sun, which varies between 21.8° to 24.4° (BRADLEY, 1985) on a 41 ka timescale (minor components at 29 and 54 ka).
c.) the precession of the elliptical orbit of the earth (the elliptical figure itself is rotating about one focus), which changes the time of the year when the planet is closest to the sun and has a period of approximately 105 ka.
d.) the precession of the Earth's axis of rotation (also known as lunisolar precession), which changes the season at which the earth is closest to the sun and has a period of 27 ka.
e.) the combined effect of precession of the elliptical orbit and the axis of rotation is to produce a period of 23 ka. Similarly, the cyclic changes in eccentricity and precession of the axis of rotation combine to produce an apparent period of 19 ka. The two periods, 23 and 19 ka blend together so that perihelion coincides with seasonal summer in each hemisphere approximately every 21.7 ka. This combined effect is termed the precession of the equinoxes.

These orbital motions are induced by the combined gravitational attraction of the moon, sun, and other planets. The precessional effects are opposite in each hemisphere, but the obliquity effects are not. This results in an asymmetry between the two hemispheres. The varying orbital motions produce only a negligible change in the total amount of insolation received by the earth during a year, but result in a seasonal redistribution. A low summer radiation total is compensated for by a high winter total, and vice versa (BERGER, 1980). The solar radiation in low and mid latitudes is most strongly affected by variations of precession of the equinoxes, whereas higher latitudes are mainly affected by variations in obliquity.

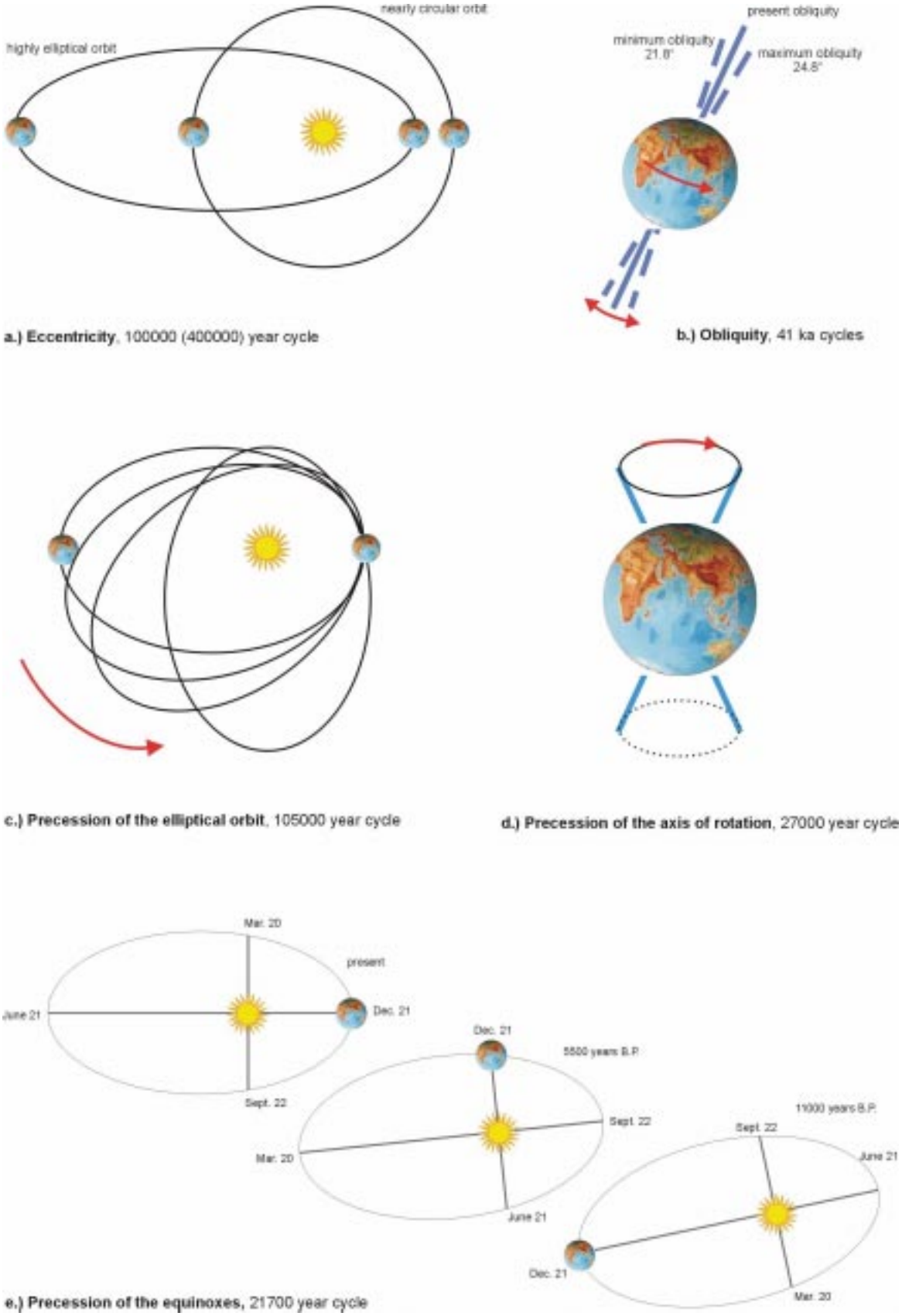

Figure 6: The major orbital variations affecting insolation (Milankovitch cycles). After BERGER, 1992; HAY et al., 1997.

3.2.1. Eccentricity

Changes in the eccentricity determine the amplitude of the effect of the precession of the equinoxes. It is also the only parameter which can change the amount of insolation received by the earth at perihelion (time when the earth is closest to the sun) and aphelion (time when the earth is farthest away from the sun) and the length of the seasons, through altering the mean distance from the Earth to the Sun (BERGER, 1977, BERGER and LOUTRE, 1994). The total energy is maximal for the most elliptical orbit and minimal for the circular orbit. The difference between the two extremes (e = 0.075 and e = 0) amounts to 0.25 %. If the orbit is circular (eccentricity e = 0.00), the insolation received during the year is equal at all times (this setup was used for the control run (93m6cold) of the paleoclimate simulations). Presently, the ellipticity is 0.0167 (the Earth is 5.1 million kilometers (~2%) closer to the Sun at perihelion than at aphelion) and the insolation received at perihelion is approximately 352 W/m^2, and at aphelion 329 W/m^2 , a difference of 6.68%. At the maximum eccentricity (0.075) during the past 5 million years, given by BERGER (1987b), the difference in insolation between perihelion and aphelion is 30%. When eccentricity reaches 0.05 the Earth receives 20% more energy at perihelion than at aphelion. The distribution of the energy received at perihelion and aphelion is modulated by the precession of the elliptical orbit and axis of rotation, so that the effects are concentrated alternately in one hemisphere and then the other.

The result is an oscillation of the intensity of seasonality between the northern and southern hemispheres, a displacement of the caloric equator into the hemisphere closest to the sun during its seasonal summer, and shifts of the low-latitude climate zones. The caloric equator connects places at sea level with the highest MAT's (Mean Annual Temperature); it is presently located in the Northern Hemisphere (NH).

3.2.2. Obliquity

Pertubations in obliquity tend to amplify the seasonal cycle in the high latitudes of both hemispheres simultaneously. The greater the tilt, the more intense are the seasonal differences in both hemispheres. Obliquity plays the same role in both hemispheres during the same local season. That means that the energy received at high latitudes gets redistributed, alternately concentrating and dispersing the insolation poleward of the polar circle. This results in alternate intensification and diminishing of the meridional minimum of summer insolation associated with the polar circle (HAY et al., 1997). Therefore, with greater obliquity summers get hotter and winters get colder (BROECKER & DENTON, 1990). It is often assumed that there is no annual change in the insolation received at the obliquity frequency. This is not quite the case. In polar regions, an increase in summer insolation cannot be balanced by a decrease in winter insolation because the insolation is already zero in the winter (polar night). Although obliquity controls the total amount of

energy received during a season, the length of the season is controlled by precession. The net annual change in insolation increases toward the poles and can reach maximum values of 17 W/m^2. This value is large enough to have significant climate effects (CROWLEY & NORTH, 1991). The effects of obliquity play a more important role in high latitudes than in the equatorial region but its power is always less than precession (BERGER, pers. comm.).

3.2.3. Precession

Taken together the two effects, precession of the elliptical orbit and the precession of the axis of rotation, result in the precession of the equinoxes (first recorded in 129 BC by HIPPARCHUS). This term is modulated by the eccentricity (precessional cycles wax and wane in strength with eccentricity) which splits the precession frequency. The periods of the modulated effect are 19 ka and 23 ka. These are the periods expected in the stratigraphic record, but extreme periods between 14 and 28 ka can occur (BERGER & TRICOT, 1986).The equinoxes (currently March 21 and September 22) and solstices (currently June 21 and December 21) slowly shift around the Earth's orbit, with a period of ~21700 years. The equinoxes are the two times in the year when the sun is above the equator and day and night are of equal duration. The precession of the axis of rotation is caused by the torque of the sun, moon, and the planets on the Earth's equatorial bulge which let the axis of rotation „wobble" like that of a spinning top. The net effect is that the North Pole describes a circle in space, with respect to the "fixed" stars (BEATTY, 1990; CROWLEY & NORTH, 1991). A significant effect not taken into account in climate simulations is that according to Kepler's 2nd Law, planets move more slowly at aphelion than they do at perihelion. As a result, Northern summer on Earth is presently 2 to 3 days longer than southern summer, which gives the Sun more time to warm the northern continents.
The precession of the equinoxes alters the Earth-Sun distance at any given time of the year and therefore causes latitudinal and seasonal redistribution of solar radiation at the top of the atmosphere. The precession determines whether the Earth is near or far from the sun during summer in a given hemisphere. In other words it determines whether the seasonality resulting from tilt changes is enhanced or weakened by the seasonality due to distance. The daily insolation is controlled by precession at all latitudes except during polar night, when the insolation goes to zero. The large changes in the seasonal insolation forcing do not appear in the global annual mean, because any increase in summer insolation is balanced by an equivalent decrease in winter insolation. The effect of precession is to produce warm winters and cool summers in one hemisphere while producing cold winters and hot summers in the other hemisphere. Although the obliquity effect is more important at high latitudes than at low latitudes, the long-term variations of the daily insolation are dominated by precession, except at the high latitudes of the winter hemisphere. The average value of insolation over a season (total amount divided by its length) is

mainly controlled by precession because obliquity varies only sligthly around a mean value. The surface temperature response to orbital insolation variations is a function of the land-sea distribution (SHORT et al., 1990). Over the open ocean, precession effects are generally small because the large heat capacity of water suppresses seasonal temperature changes. The higher heat capacity of the oceans was already mentioned by LYELL (1830-1832), when he said that the ocean tempered the climate, "moderating alike an excess of heat or cold". The lower heat capacity of land causes larger changes in the seasonal cycle of temperature. During the Cretaceous the greatest area of land is in the mid latitudes, where the thermal response to precessional forcing is greatest.

Over the last 100,000 years mid-latitude northern hemisphere insolation values at summer solstice have varied by about 8% around the mean (~40 W/m^2). For comparison, the radiative forcing from a doubling of CO_2 is about 4 W/m^2. However, CO_2 forcing is year-round and sensitivity to mean annual forcing is several times greater than sensitivity of the climate to seasonal forcing. Over longer time intervals, values at the summer solstice exceed 13% of the mean. Presently, perihelion occurs in northern winter (January 3) and aphelion during the northern summer. This makes the northern hemisphere winter warmer and the summer cooler than average. Thus 11,000 years ago the earth was at perihelion at the time of the summer solstice (June 21), which made the northern hemisphere summer hotter and the winter colder.

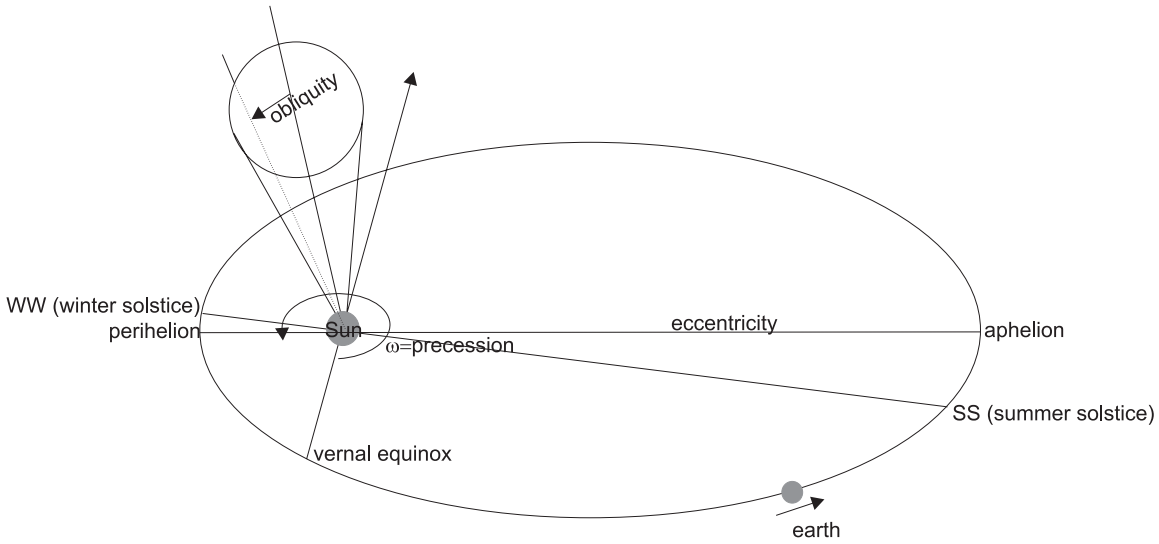

Figure 7:Elements of the Earth's orbit (After BERGER et al., 1993)

Climatic precession is expressed as: **precess. = eccentricity * sin ϖ** . Omega (ϖ) is the projection of the inclination of the axis of rotation on the ecliptic (the plane of the Earth's orbit), and therefore the longitude of the moving perihelion from the vernal equinox (Figure 7).

Omega (ϖ), called PRECU in GENESIS, is defined as the prograde angle from perihelion to the northern hemisphere vernal equinox.

3.3. Problems - Sources of Error

The fundamental challenge in determination of Milankovitch forcing from geological data stems from uncertainties in age-depth relationships. These result from time-scale uncertainties , sampling problems, interference by nonperiodic climatic or geologic factors, and nonlinearity in the sedimentary expression of periodic forcing (PARK and HERBERT, 1987).

The problem of time-series analysis during this project was the relatively poor age control of the sections. Even the best available time scale for the Upper Cretaceous (OBRADOVITCH, 1993) has an average error of +/- 0.6 Ma. This means that average sedimentation rates could have varied by as much as 1 cm/ka. Mean sedimentation rates, even if highly variable, are required to evaluate cyclicity. The second problem is that stratigraphic distance is usually taken to be a measure of time, but the Bridge Creek Interval is too short to have precise age-control for its duration. Estimates for the time represented by the Bridge Creek Interval range from 0.8 Ma (FISCHER, 1980) to 2.45 Ma (KAUFFMAN, 1977). Other uncertainties include the short-term variability of sedimentation rates and variability of the length of the Milankovitch cycles themselves. For example, the periodicity of the precessional parameter has a mean value of 21,700 years, but varies, with modes of 19,000 and 23,000, and extremes thought to range from 14,000 to 28,000 years. The variability in sedimentation rates within the bedding cycles is part of the complex cyclicity itself (FISCHER, 1993). It is not surprising that bedding couplets vary in thickness between 20 cm (see location NM-I-00 and NM-II-00) and 100 cm (see location TX-I-00 and MX-I-00) – a factor of five. The bedding couplets of the Bridge Creek Limestone and its equivalents are complex and do not consistently display the five couplets per meter that are characteristic of some other Cretaceous limestone/shale sequences (SCHWARZACHER and FISCHER, 1982). Because of the lack of information on the length of time it took to form these couplets, the determination which Milankovitch cycle(s) is (are) represented in the sedimentary record remains speculative. When working on Milankovitch-induced cyclicity in the WIS a problem arises because the cycles of precession and obliquity differ by a factor of two. This means one obliquity cycle could be misinterpreted as two precessional cycles. This study was initiated to test the sensitivity of the climate- and sedimentary-system to precessional forcing in order to investigate potential effects of one Milankovitch parameter. Therefore the specific question asked is: Could the precession of the equinoxes produce the bedding couplets? Continuous core material was not available. For proper spectral analysis at least seven complete 400 ka eccentricity cycles would be needed to calculate correct periodities of the other cycles. This would mean that sections of about 56 m would be needed (2cm/1 ka→8m/400 ka→8m x 7 cycles → 56 m). This was not possible at all locations. Therefore, this study can only be qualitative and not quantitative. Furthermore, only relatively widely spaced samples were taken from the sections.

4. Methods

4.1. High Resolution Event Stratigraphy (HIRES)

Modern geological analyses involving sedimentary rocks require a high resolution system of dating, integrating and correlating diverse stratigraphic, geochemical, and paleontological data. They must take into account the possibility that short-term phenomena (100 ka or less) exercise a strong control on sedimentation. Such phenomena may be extraterrestrial, tectonic, volcanic, oceanographic, climatic, sedimentologic, and/or biologic in origin. Most short-term phenomena are predictable and may be either autocyclic (locally regulated, with limited stratigraphic continuity) or allocyclic in nature (regionally to globally regulated, with extensive stratigraphic continuity) (BEERBOWER,1966). A stratigraphic system based on short-term phenomena would ideally be chronostratigraphic, involving the identification and regional tracing of “time lines” (isochronous surfaces or very thin event deposits). Such a system can be integrated with refined, independently derived biostratigraphic and geochronologic systems (KAUFFMAN, 1988).
As stratigraphic observation in the field and subsurface data have become more detailed and comprehensive, it has become apparent that widespread short-term to isochronous event deposits of millimeter to meter scale are far more common during the Cretaceous than during the recent geologic past. This may be due to the homogenous climatic conditions during the Cretaceous, which resulted in greater control of allocyclic processes on a global scale when compared to today’s highly variable, environmentally sensitive, glacially influenced, and autocyclically dominated sedimentary systems. This was especially true for shallow water systems like the Western Interior Seaway.
In fine-grained basinal facies like those of the Cretaceous Western Interior Seaway, short-term event deposits may dominate the stratigraphic record. Most of them reflect widespread allocyclic forcing mechanisms such as rapid regional tectonic movements, massive explosive volcanism, Milankovitch cycles, extraterrestrial impact, rapid shifts in ocean currents and stratification, giant and prolonged storm events, influence of short-term climatic cycles, and major climate pertubations. Many of these phenomena are regarded as “geologically instantaneous” in terms of their stratigraphic expression, i. e. they represent events lasting from a few hours to 100 ka. This means that they result in essentially isochronous or near-isochronous deposits (KAUFFMAN, 1988). It was necessary to develop field techniques and geochemical instrumentation which allowed analysis of data from stratigraphic sections sampled at the mm- to cm-range. This was the only way of comparing global events having the same origin in different basins worldwide.
KAUFFMAN gave the name “HIRES” to this new tool in geology. Its primary purpose is to provide

means of regional and interregional correlation based on such isochronous to near-isochronous surfaces/strata.
A surface or stratum can be regarded as a potential isochronous or short-term event deposit. If its extent can be demonstrated through correlation (standard or graphic techniques) to other sections. These event units fall into three basic categories:

1. *Physical event units* (PE) include i. e. volcanic ash and bentonite deposits, volcanic flows, storm beds, rapidly formed transgressive disconformity surfaces, and Milankovitch cycles.
2. *Chemical event units* (CE) are based on analysis of C_{carb}, C_{org}, $\delta^{13}C$ or other elements or isotopes. From these analyses emerges a chemostratigraphy, with regionally correlative short-term excursions, or “spikes” of unusual magnitude in the chemical data.
3. *Biological event units* (BE) are deposits representing ecological, evolutionary, or extinction events that are commonly discrete from biostratigraphic zones or zone boundaries.
4. *Composite event units* (CPE) combining physical, chemical, and/or biological events in their definition. A simple example would be a major ash fall (PE) that had a unique elemental compositon or chemical effect on sediments and/or water masses (CE), and that caused a mass mortality and then served as a unique sediment surface for colonization. (KAUFFMAN, 1988).

4.2. Sampling and description

In order to sample the sections, each section studied for HIRES analysis was trenched. The trenches were up to a meter wide and as deep as necessary to consistently encounter fresh rock. A 10-centimeter scale version of a Jacob´s staff with a sliding housing for a Brunton compass was used to define a 1-m flagged grid through the stratigraphic section. The flags served as calibration points for high-resolution stratigraphic description of smaller units. The stratigraphic section was then measured and described at the centimeter to 10-centimeter scale. The thickness of most bentonites was in this range. Individual stratigraphic units described and sampled during HIRES analysis were as small as a few millimeters, or, if sedimentation was monotonous and uninterrupted by events over a long interval, as thick as several meters. No differentiation in technique was made between the different sediment types. In addition to detailed lithologic description of major units, all potential event-stratigraphic units/surfaces were noted, sampled, and described in detail in each measured section.
The most important factor of the sampling strategy was to gain information about latitudinal changes of sedimentological and geochemical proxies associated with the Cenomanian/Turonian boundary
The sampling in the two southernmost locations (MX-I-00 / TX-I-00) was done in a slightly different manner because the dominance of limestones made it impossible to trench the section. The

limestones were sampled in their complete thickness. The orientation of the limestones was indicated by a label. This study focused on taking samples of each lithologic unit, instead at every 10 cm. However the description of the sections is at the centimeter level.

5. Sedimentology

Sedimentation in and around the Western Interior Basin during the later Mesozoic reflected dynamic interplay among five factors: (a) the interactive tectonic history of the Pacific margin of North America, the Cordilleran Geanticline, the western mobile fold and thrust belt, the complex foreland basin, and the stable craton; (b) global tectonoeustatic and, to a much lesser degree, climatoeustatic sea-level changes; these affected relative sea-level history, transgressive-regressive cyclicity, and sequence-stratigraphic response in the basin; (c) watermass dynamics within the epicontinental sea and their relationship to global oceanic changes reflected by the sediments, including stratification, oxygen levels, biological productivity, organic-carbon storage, and carbonate deposition; (d) long- and short-term thermal and climatic changes, especially those reflecting orbitally-forced Milankovitch climate cycles; and (e) the degree to which geologic, oceanographic, and climatic pertubations acting on the predominantly shallow epicontinental sea produced event stratification and short-term responses among environmentally sensitive marine and non-marine biotas (KAUFFMAN and CALDWELL, 1993).
Sedimentation in Western Interior Seaway was dominated by siliciclastic input from the uplifted fold and thrust belt to the west. There was little clastic sediment introduced from the east (KAUFFMAN, 1984). Deposition of the Bridge Creek Limestone and it’s corresponding sequences to the north and south began just prior to and spanned the peak sea level highstand event in the basin.

The lithology for all the measured sections is described in Figure 14 through Figure 22. Figure 10 gives a quick overview over the sampled sections and the “Photo Plates” in the “Appendix”.

5.1. Regional geologic setting - Lithostratigraphy

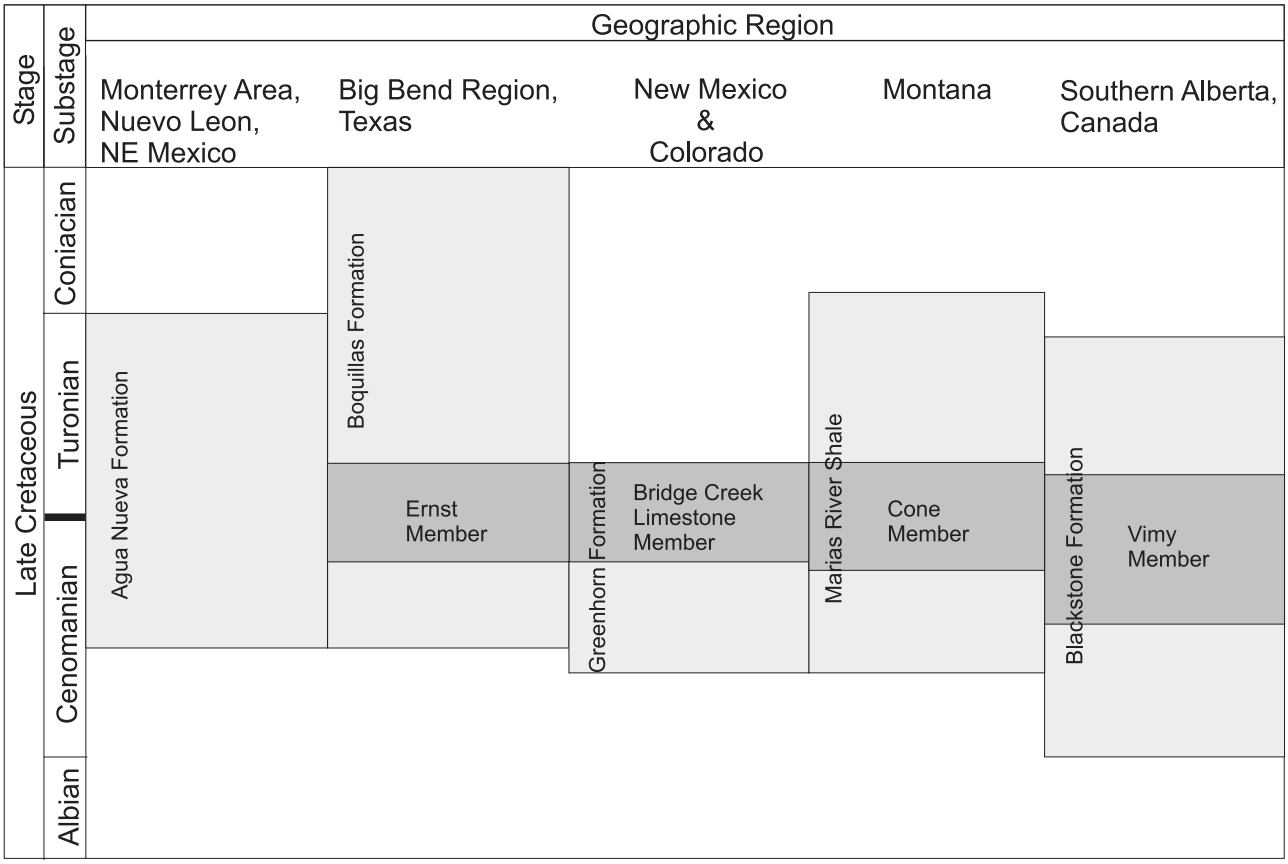

Figure 8: Lithostratigraphy of the Late Cretaceous for north-central Nuevo Leon (Mexico), southwestern Texas, New Mexico, Colorado, Montana, and southern Alberta (Canada).

The Cenomanian/Turonian boundary is characterized by several different geological units from Alberta to Mexico. The Bridge Creek Interval of the central part of the seaway and it's equivalents to the north and south were sampled during this study and are described below.

Blackstone formation - Vimy Member

The Vimy member of the Blackstone formation is exposed in the southern Alberta/Canada foothills region. The Blackstone formation is part of the late Cretaceous Colorado/Alberta Group, which consists predominantly of mudstone interspersed with relatively thin sandstone and conglomerate beds and deposited in the southwesternmost part of the Canadian foredeep. The Blackstone Formation is thought to record the initial transgression. The cycle began during the middle to late Cenomanian in southern Alberta and northeastern British Columbia, and reached its peak during the Turonian (STOTT, 1993). The calcareous, non-concretionary shale making up the Vimy Member of the Blackstone in Alberta and British Columbia is, in part, correlative with the widespread coccolithic Second White Speckled Shale which marks the peak transgression. It is the

northern correlative of part of the Greenhorn Formation of the United States (WILLIAMS and BURK, 1964; STELCK and WALL, 1954).

Marias River Shale - Cone Member

The calcareous Cone Member (equivalent to the Greenhorn Fm. of Colorado and New Mexico) is part of the Marias River Shale (upper unit of the Colorado group) on the Sweetgrass arch in northwestern Montana. The name Marias River Shale was given by COBBAN et al., 1959 to a 275-365 m thick sequence of dark gray Upper Cretaceous shale that lies between the Blackleaf and Telegraph Creek Formation. The Cone Member (also called Greenhorn Limestone of the Sweetgrass Arch) has been divided into four members. The Cone Member is defined as the calcareous beds between the non-calcareous Flowree Member, below, and the non-calcareous Ferdig Shale Member, above. At the location sampled for this study the total thickness is about 16 m (COBBAN et al., 1959), but the lower part is mostly covered by vegetation and small landslides. The Cone Member is a thin unit of latest Cenomanian and Turonian age. Most of the Cone Member is dark-gray highly calcareous shale. Other minor but easily recognized lithologic types include a persistent bed of large concretions of dark gray limestone at the base, and several thin, ledge-forming, shales. At the top fossiliferous shales are present. Several bentonite beds are also present.

Greenhorn Formation - Bridge Creek Limestone Member

The Bridge Creek Limestone Member was named by BASS (1926a) for a series of limestone beds at the top of the Greenhorn Limestone on Bridge Creek in Hamilton County, Kansas. It is part of the Greenhorn Formation and can be divided into three informal subdivisions (Lower, Middle, Upper) based on overall lithologic characteristics and slope forming section. The development and preservation of cyclic sedimentation during deposition of the Bridge Creek Member is largely the result of slow sedimentation rates of 0.5 to 1.0 cm/ka in the central Western Interior Seaway. Sedimentation rates characteristic of the fine-grained shelf and basinal facies range from 0.5-4.0 cm/ka before compaction (KAUFFMAN, 1988). Sedimentation rates of 1 to 2cm/ka are typical for modern calcareous pelagic deposits above the CCD (Carbonate Compensation Depth). Sedimentation of the Bridge Creek Limestone was characterized by oscillations between mud-rich and carbonate-rich facies that ultimately formed limestone/marlstone bedding couplets. These couplets are characterized by fluctuations in biofacies and organic carbon content, and interpreted by many (e. g. BARRON et al., 1985) to reflect changes in bottom-water oxygen content.
The outcrops are characterized by 10 to 40 cm thick micritic to chalky limestones or marlstones interbedded with 30 to 100 cm thick marly to chalky shale beds. The base is defined by a thick 20

to 50 cm limestone bed (PBC 1). PBC is an expression from KAUFFMAN, meaning Pueblo Bridge Creek. He introduced this terminology to describe the prominent marker beds in the Bridge Creek limestone Member.
The type section for the Cenomanian/Turonian Stage boundary is at Rock Canyon Anticline at Pueblo, Colorado and occurs in the Bridge Creek Limestone Member of the Greenhorn Formation.

Boquillas Formation – Ernst Member

The Boquillas Formation consists of almost one hundred meters of impure flaggy, chalky limestone beds interbedded with gray platy marls and calcareous shales. The Boquillas Formation contains ammonites, bivalves, ophiuroid and echinoid fragments, an abundance of foraminifera, and some ostracods, burrows and borings. Several genera of algae are present. It is underlain by the Buda Limestone and overlain by sediments of middle Turonian age, called the San Vicente Member of the Boquillas Formation. The Ernst Member is the lower part of the Boquillas Formation and about 150 meters thick. This limestone consists of strata from 1 to 10 cm thick and has a platy character. The common weathered color of both the limestone and the shales is light yellowish gray, but on fresh surfaces they appear bluish gray.

Agua Nueva Formation

The Agua Nueva Formation is characterized by rhythmic bedding consisting of thin- to medium- to thick-bedded clayey limestone and marl couplets with continuous parallel stratification and thin- to medium-bedded bentonite beds. Locally the limestone beds are rich in organic matter giving them a black coloration on fresh surfaces. This unit weathers to brownish, yellowish colors and forms synclinal valleys and slopes (LONGORIA, 1998).

5.2. Sedimentology of the sampled locations

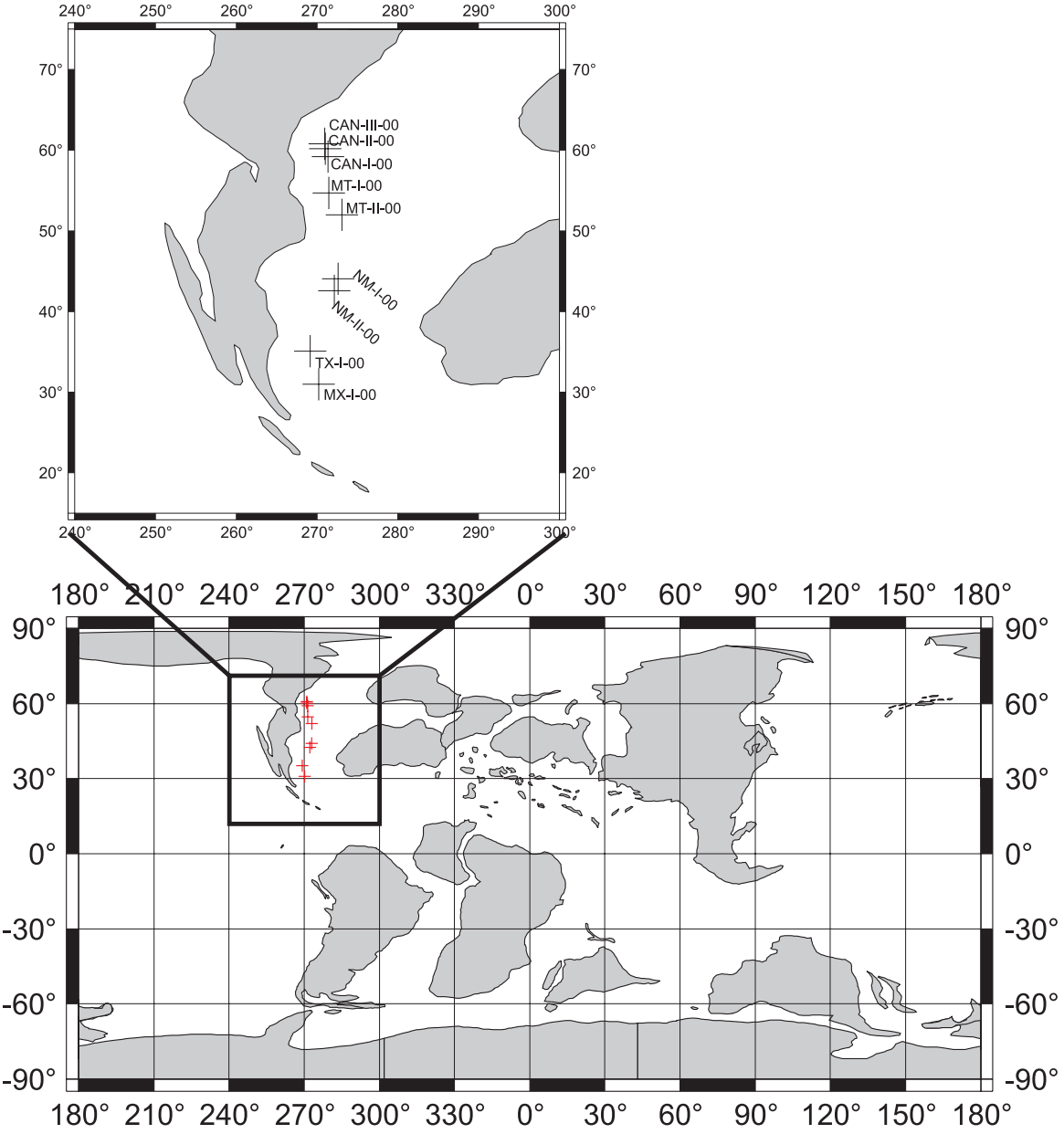

Figure 9: Paleogeographic position of the sampled locations.

During the field season 2000 (February/March and July/August) nine sections were sampled across the Cenomanian/Turonian stage boundary (Figure 1 and 9).

NOTE:

A composite figure of all sections is given in Figure 10.

The detailed lithology for all the measured sections is described in Figure 14 through Figure 22.

The key to lithology can be found in Figure 13.

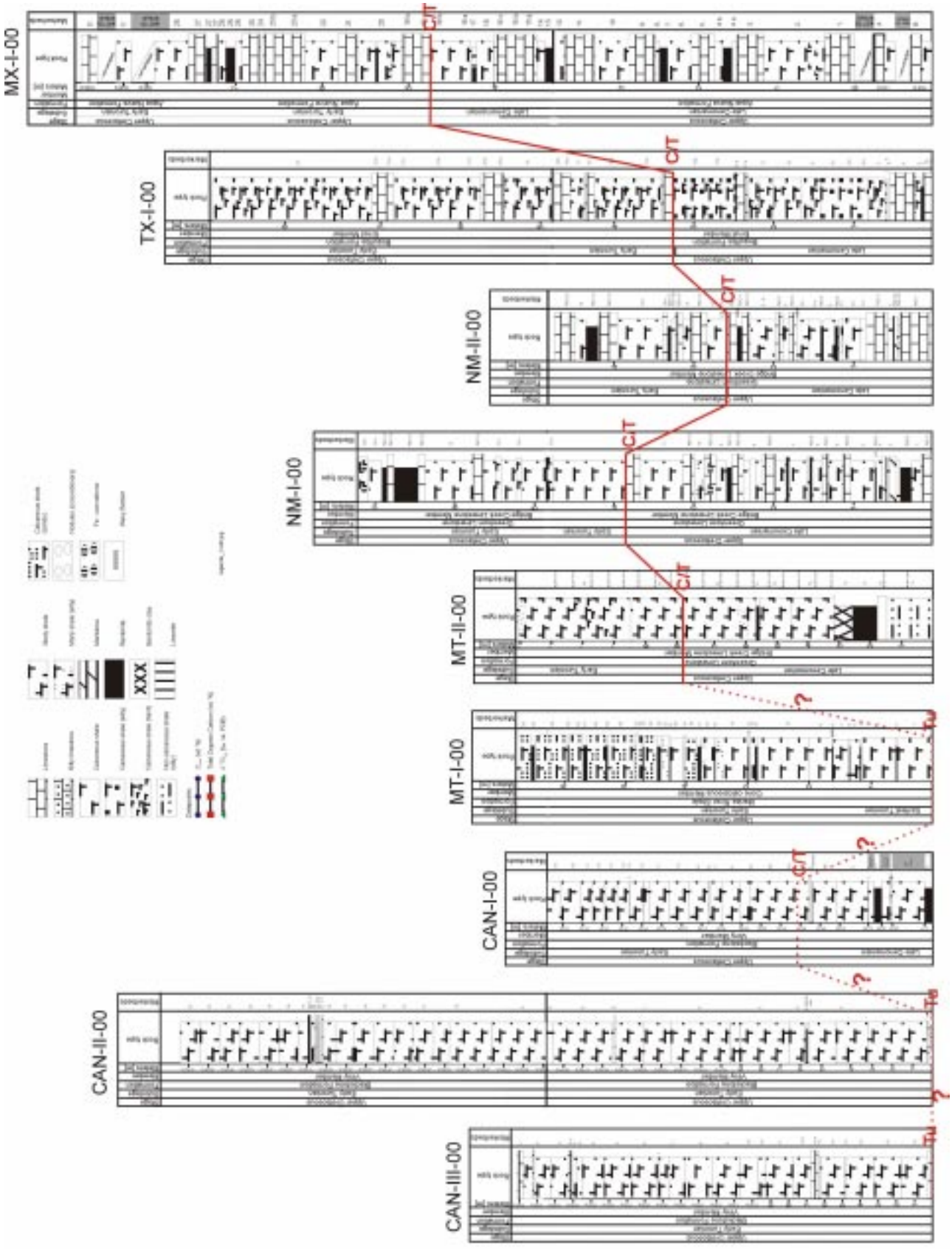

all_sections.cdr/.jpg

Figure 10: Lithology of all measured sections.

Thistle Creek, Alberta, Canada / CAN-III-00

The outcrop is located about 300 km northwest of Calgary in southern Alberta, Canada and 18 km south of the village of Cadomin, near the Cardinal River Road. From the Cardinal River Road (near Maskiki lake) it is a 6 km hike along a creek at the eastern boundary of Jasper National Park.
Location: 116º51´10´´ W / 52º47´45´´ N
The measured section at Thistle Creek, Alberta has a thickness of 23 m (see Figure 10). Because of the difficult access to this location I have extended the sample interval to 150 cm, but the description of the section remained in decimeter steps. The section is dominated by dark-gray to medium-gray marly shales with only one bed (bed 8) of calcareous shale, which has a wavy structure whereas the marly shales have a more platy structure. The shales weather to a light-gray color. The marly shales also show a lamination of dark- to light-gray beds in the mm-range. The limestones are micritic, like bed 12a, but also appear more layered like the limestones of beds -1, the limestone in bed 3 (fossiliferous), and bed 1, or as nodular beds like the one in bed 2. These nodules contain numerous fossils. They weather in a yellowish-brown, in parts orange-brown (rusty) color. The limestones occur dominantly in the upper part of the section, from bed 3 to 1 (see Photo plates 1 & 2 in the appendix). The strike and dip of the section is around 350/83 (bedding is overturned).

Big Horn River, Alberta, Canada / CAN-II-00

The Big Horn River section is about 210 km northwest of Calgary and 22 km WSW of Nordegg near the intersection of the Forestry Trunk Road (940) and State Highway 11. From State Highway 11 a dirtroad goes to the Crescent Falls campsite at the Big Horn River. It is a 8 km hike up the western edge of the Big Horn river.
Location: 116º18´00´´ W / 52º17´52´ N
The outcrop (see Photo: 3 & 4) has a thickness of about 100 m, but due to its remoteness of the only 37.50 m where measured and described (see Figure 10). The sampling was undertaken in 3 m steps below bed 10 (Figure 14), upward of bed 10 in 1 m steps, and between bed 17 and II.-11 in decimeter steps or with changing lithology. The description of the section always remained at the decimeter level.
The section is dominated by dark-gray to medium-gray marly shales, which weather light-gray. Most of the shales show a lamination of dark- light-gray beds in the mm-range. The shales break into pieces about 3 to 5 mm thick. The base is characterized by a concretionary micritic limestone bed. Besides this bed there is only one other marker bed in the lower part of the section, a 10 cm thick bentonite. Of special interest is a series of bedding couplets of shale and impure laminated

limestones between 30.00 and 31.00 m This part of the succession contains fossils (*Mytiloides hattini*), but only a few. The shales in this interval show very thin lamination. The strike and dip of the section is around 020/28 (the magnetic declination in Alberta is 20°).

Burnt Timber Creek, Alberta, Canada / CAN-I-00

This section is about 90 km northwest of Calgary and 8 km east of Forestry Trunk Road 940, north of the Ghost Rock wilderness area (16 km north of Black Rock Mountain). It is easily accessible by a dirt road (Hunter Valley Road). The section is next to a bridge crossing Burnt Timber Creek
Location: 115º 11´35´´ W / 51º 32´00´´ N
The outcrop exposes more than 150 m of section, but only 30 m of the section was sampled (see Figure 10) in 0.5 to 1.0 m steps (see Photo: 5). The lower 42.0 m were measured and described, but not sampled. The general strike and dip of the section is around 015/52.
The lower 42.50 m of the section is dominated by two thick bentonites (X and X-1) and very brittle medium- to dark-gray shales, which weather to a light- to medium-gray. The carbonate content of the shales is very low; there is only a very slow and poor reaction with 10 % HCl. Some of the shales are laminated on a sub-mm scale. The lamination consists of grayish to brownish beds. Other common features are bioturbation and burrows (bed 5.). Above the X-1 marker bed the shales contain numerous megafossils, such as ammonites and mollusks (*Mytiloides sp.*). Beds 2, 4 (ledge in the section, see Photo: 6), 5, 8 (silty, marly shale), and 9 are rich in fossil remains. There are no true limestone beds in the section, but one is a concretionary micritic limestone between the two thick bentonites.

Cone, Montana, USA / MT-I-00

Outcrop MT-I-00 is located about 35 km northwest of Great Falls in northwestern Montana and 6 km south of the little town of Power, Montana. It is on eastern side of the Muddy Creek, at the end of a small coulee.
Location: 108º 33´24´´ W / 47º 39´23´´ N
Quadrangle: Power, MT; N4737.5-W11137.5/7.5
Almost 7 m of the Cone Member were sampled at this locality (see Figure 10). The lower 6.5 m and the uppermost part of the 16 m thick Cone Member (see Photo: 7) were not exposed. Most of the section is dark-gray calcareous shale that weathers light bluish gray and yellowish white. The upper part of the section contains thin beds of argillaceous and micritic limestone that tend to form low ridges. Limestone concretions occur at several horizons. Several beds of bentonite are present. The lower part of the section is characterized by a dark-gray shale which weathers light blue and medium gray. Bed 16 consists of very hard and widely spaced limestone concretions that

are dark gray on fresh fracture but light bluish gray where weathered. The concretions are about 2 cm thick and 5 cm in diameter. Each is enclosed by a limonitic rind. Silty shale beds of the upper part of the member are thin and irregularly bedded (see Photo: 8). They are medium-gray where fresh and brownish-gray where weathered. These shale beds are hard and crop out as a series of small ledges in contrast to the slope formed by the softer shales of the lower part (LOPEZ, 1995). Limestones in the lower part of the measured section are argillaceous and shaly and softer than the “limestone/shale” beds higher in the outcrop (bed 22–36). No bedding couplets can be distinguished, but there is interbedding of bentonites and silty/sandy highly calcareous limestones/shales in the upper 3 m of the section.
The section contains many fossils, including ammonites (*Watinoceras sp.*) and mollusks (*Mytiloides mytiloides; Mytiloides sp.; Inoceramus sp.*), especially in beds 10, 14, 22, and 24.
The strike and dip of the section is around 026/06.

Billings Landfill, Montana, USA / MT-II-00

This location is situated 4 km south of Billings, MT. It is on the western side of the Billings landfill, south of the Yellowstone river.
Location: 111º 40´23´´ W / 45º 43´06´´ N
Quadrangle: Yegen, MT; N4537.5-W10830/7.5
A total of 13.0 m of this outcrop were trenched, measured, and described (see Photo: 9 and Figure 10). The lowermost part of this section is dominated by a dark-gray, slightly silty shale, which is non-calcareous. It weathers to pale yellowish brown and yellowish gray. The strike and dip of the section is around 127/05. Above this is a hard bench-forming silty shale (bed 2), with a thick bentonite (yellowish-greenish) and bentonitic (smectite) clay on top (see Photo: 10). Bed 2 contains numerous fossils. Above this, the section consists of a highly bioturbated marly shale, which is weakly calcareous (HCl test). Beginning with bed 6. the section becomes a more calcareous partly silty shale. The top of bed 9 is sandy. This section does not show any bedding couplets.
Fossiliferous beds are 4, 5, 6, and 8, including ammonites and mollusks (*Mytiloides sp., Watinoceras sp., Neocardioceras sp., Scaphites sp.*). Except for the thick bentonite and bentonitic clay, the sediments of this section are very homogenous.

Emery Gap, New Mexico, USA / NM-I-00

The Emery Gap section is about 20 km north of Folsom, New Mexico (45 km east of Raton, N. M.) and 10 km south of the Colorado border. It is located in a road cut on State Road 551
Location: 103° 52´20´´W / 36° 59´18´´N

Quadrangle: Emery Peak, New Mexico-Colorado; N3652,5-W10345/7.5
At this roadside locality a little more than 7.0 m of sediments were measured and sampled (see Figure 10). This locality shows very distinctive bedding couplets of micritic, very hard, dark-gray limestones and thinly foliated calcareous shales. In the lower part of the section limestones are “replaced” by hard, dark-gray marlstones which do not react with 10 % HCl. The section weathers light-gray. Two limestones contain Fe-concretions. These beds are also bioturbated and contain numerous fossil remains. Above bed 9, the section contains fossil-rich beds, especially upward of bed 12. Bentonites are present throughout the section and weather with a brownish-orange or yellowish color. Most of them are laminated and have a smectite-like appearance.
Distinctive elements of this section are the periodic bedding couplets (see Photo: 11). They have a mean periodicity of 40 cm for the lower 3.00 m of the section and a larger, but more irregular periodicity for the upper 4.00 m. The average thickness of the bedding couplets is ~60 cm.

Las Vegas, New Mexico, USA / NM-II-00

Another section with easy access is NM-II-00 which is 1km south of Las Vegas, N. M., next to Interstate Highway 25, just east of Exit 345.
Location: 105° 11´24´´W / 36° 14´50´´N
Quadrangle: Las Vegas, NM; 35105-E2-TF-024
The Las Vegas outcrop in northern New Mexico shows a sedimentation pattern similar (see Photo: 12 and Figure 10) to the Emery Gap section, described above. This is probably due to the “close” proximity, although they are 200 km apart. Only 4.50 m of sediments were measured, described, and sampled at this locality, because identification of the Cenomanian/Turonian (C/T) boundary interval is easy due to the presence of characteristic marker beds similar to those at the type section at Pueblo, Colorado. The section is dominated by an alternation of highly micritic dark-gray limestones and dark-gray marly- to calcareous shales. Numerous bentonites are present in the outcrop, as well as thin yellowish limonite bands. A thick limestone was identified as PBC1 (for marker bed 1 of the Pueblo Bridge Creek interval). It is one of the important marker beds for the Bridge Creek interval of the Greenhorn Formation. This section shows several sedimentary features, including a concretionary horizon with nodules (bed 2c) and wavy bases on the limestones (beds PBC6 and PBC 14). Another important sedimentological feature is the cyclical occurrence of limestone/shale couplets with an average thickness of 0.75 – 0.80 meters.

Hot Springs, Texas, USA / TX-I-00

The Hot Springs section is located in Big Bend National Park in southwestern Texas. The section is 40 to 50 m above the northern bank of the Rio Grande river, about ½ km northeast of Hot Springs.
Location: 102° 59´22´´W / 29° 11´20´´N
Quadrangle: Rio Grande Village, TX; 29102-B8-TF-024
8.50 m of section were measured at this locality (see Photo: 13 and Figure 10). Sampling started about 36.5 m above the contact of the Buda Limestone with the Boquillas Fm.. FRUSH and EICHER (1975) have placed the C/T boundary at this locality in this stratigraphic interval . The sediments strike and dip is 270/04. The section is characterized by thick (~1.00 m) bedding couplets, consisting of micritic limestones and very hard, calcareous shales.
The limestones have a very light brownish-grayish color where freshly exposed and weather orange-brown or sometimes reddish-brownish (see Photo: 14). They are very hard and break with sharp edges. Most of the limestones break easily, because they are already fractured.
The highly calcareous shales have a similar composition. They are very hard and break into more platy pieces. Their color ranges from a reddish light-brown to brownish-grayish. Some of the shale beds are silty and contain plenty of shell remains from various mollusks (e. g. bed 8.). Only one bentonite (bed 2), one limonite (bed 6) and one thin band of Fe-concretions in bed 11 occur. The shales become less silty in the upper part of the section. Another feature is the strong lamination or wavy structure of several shales, which is optically enhanced by different shadings of reddish and brownish colors.

La Boca Canyon, Nuevo Leon, Mexico / MX-I-00

The outcrop is located 15 km south of Monterrey in the state of Nuevo Leon in northeastern Mexico. Leaving road 85 between Monterrey and Linares to the east (just north of Santiago) leads to the Rodrigo Gomez Lake. At the eastern side of the lake is the La Boca Canyon Dam. The section is southwest of the dam, next to the road.
Location: 100°23´10´´W / 25° 40´00´´N
About 29 m of this roadside outcrop with a total thickness of about 300 m where measured and sampled (see Photo: 15 and Figure 10). The strike and dip of the section is around 250/40. The lower and upper 10 m where only sampled at 5 m intervals.
At La Boca Canyon (La Boca Canyon of Cerro de la Silla) section the Agua Nueva Formation consists of a homogenous alternation of thick-bedded micritic limestone beds (30-50 cm thick), with continuous parallel stratification and calcareous shales in beds varying in thickness from 30 to 50 cm. The outcrop weathers to light greyish to yellowish colors, enhancing the optical appearance of the limestone/shale couplets. These couplets have an average thickness of about 0,80 meters. The limestone samples show evidence of bioturbation. Another feature is the high abundance of

bentonites up to 10 cm thick (see Photo: 16). These occur mostly in-between the shales. Two shale beds, beds . and 20, contain Fe-concretions in their lower parts.
The section contains almost no macrofossils.

5.3. Comparison/Correlation of sedimentary results

At the northern-most of the three Canadian sections, Thistle Creek (CAN-III-00), marly shales dominate. Only a few limestones beds occur throughout the section and these show no distinctive cyclicity. 75 km further to the southeast, at the Big Horn River locality the sediments are much the same. 37 meters of marly shale are interrupted by a few continuos limestone beds. Only between 30 m and 31 m does cyclic sedimentation occur, in the form of very regular interbeds (6 couplets) of 5-10 cm thick limestones and 3-14 cm thick marly shales. Another 120 km to the southeast, the third Canadian location, Burnt Timber Creek, is also dominated by the sedimentation of marly shales. This monotonous sequence is only interrupted by the occurrence some bentonites and one concretionary limestone bed in the lower part of the section.
About 450 km to the southeast, location MT-I-00 (Cone) shows a different sedimentation pattern dominated by calcareous shales in the lower part and silty/sandy very hard calcareous shales towards the top. Bentonites appear cyclically every 30 to 100 cm. The next section is MT-II-00 (Landfill) near Billings, MT, which is located about 330 km SE of MT-I-00. There sedimentation is characterized by non-calcareous shales in the lower part, then marly shales and finally calcareous shales from about 4.50 m to the top.
About 1000 km further south, locality NM-I-00 (Emery Gap) is dominated by the well-known bedding couplets associated with the Cenomanian/Turonian boundary in the Western Interior Seaway (here: Bridge Creek Interval). The thickness of the bedding couplets averages ~60 cm with average thickness for the limestones of about 10-15 cm and 24-36 cm for the shales.
Sediments are similar at the second section in New Mexico, NM-II-00 (Las Vegas), located 180 km southwest of NM-I-00. There the average bedding couplet thickness is ~50 cm. Another important feature is the fact that limestones appear in pairs (PBC 1/PBC 3; PBC 6/PBC 7; PBC 15/PBC 16; PBC 18/PBC 20). These are separated not only by shales but also by bentonites or a combination of both. Average thickness for the limestones is ~18 cm and for the shales~24 cm.
750 km to the south the section measured in Big Bend National Park in Texas, TX-I-00 shows the typical bedding couplets, with an average thickness of ~1.0 m. The thickness of the limestones averages 20 cm and the shales 44 cm. The shales are highly calcareous.
The southernmost section (MX-I-00) was measured 200 km further SE in northern Mexico. Section MX-I-00 is very similar to section TX-I-00 with an average thickness of the couplets of 90 cm. Whereas the bedding couplets have almost identical thicknesses, the limestones are almost twice as thick (⌀ = 36 cm), and the shales are thinner, with an average thickness of ~30 cm. Highly calcareous shales occur throughout the section.

NOTE: The average thickness of the bedding couplets does not equal the thickness of the limestones and the shales.

5.4. Discussion - physical sediment record

Following the sections from the North to the South there is a clearly recognizable but gradual trend from outcrops dominated by the sedimentation of marly shales with no bedding couplets towards sections dominated by the sedimentation of massive micritic limestones and interbedded highly calcareous shales.
The bedding couplets of the Cenomanian/Turonian boundary, which are typical for the WIS do not occur in the Alberta or Montana sections, but they are well developed in the central and southern portions of the seaway.
Because power spectral analysis can not be conducted on outcrop samples mean sedimentation rates were used to evaluate which cycles dominate sedimentation. Assuming mean sedimentation rates of 1-2 cm/ka for the limestones and 2-4 cm/ka for the shales (KAUFFMAN, pers. comm.). These are typical for pelagic sedimentation rates above the CCD today, the sediments in section NM-I-00 indicate a cyclicity of ~27 ka, whereas location NM-II-00 would have a 22 ka cycle. Going further south, the duration of the cycles (thickness of the couplets) increases almost by a factor of two. This gives a mean cyclicity for section TX-I-00 of 44 ka and 40 ka for section MX-I-00.
The estimated length of the measured cycles suggests a very strong relation between the sedimentary system and changing orbital parameters, particularly the obliquity cycle, which has a quasi-periodicity of 41 ka, but minor components at 29 and 54 ka, and the precessional cycle, with it’s quasi-periodicity of 21.7 ka, major periods at 19 and 23 ka, and extreme periods between 14 and 28 ka).
Exact values for precession and obliquity in the Late Cretaceous are unknown, but BERGER et al. (1992) have calculated values of the main astronomical periods (precession and obliquity) for 100 Ma. Taking changes in the Earth’s spin due to tidal friction and in the planetary orbits due to the weakly chaotic nature of the orbits of the inner planets into account BERGER et al. (1992) have determined periods of 18.5 ka and 22.3 for precession and 38.8 ka and 50.2 for obliquity. If these periodicities would be considered, the same cycles as mentioned above could be recognized. However, if the sedimentation rate assumptions are correct the form of the modulations and repeat times would be similar.
Considering the mean duration of the cycles at the New Mexican sections, it appears that these are mainly controlled by changes of the precessional parameter. The mean periodicities of 22 ka (NM-II-00) and 27 ka (NM-I-00) coincide with the quasi-periodicity and one of the extreme periods known for the precessional parameter. The Texan (44 ka) and the Mexican (40 ka) outcrops seem to correspond to changes of the obliquity parameter (~41 ka).

6. Stratigraphy and Paleontology

Paleontological information from macrofossils, thin sections, and smear slides were used for stratigraphic age-control of the sections. From 150 taken about 120 thin sections and smear slides were made, especially where marker beds were not available as was the case for the sections in Texas and Mexico. The New Mexican sections were identified and correlated by event lithostratigraphy. The northern sections in Alberta and Montana were dated mainly by macrofossils. The thin sections and smear slides were kindly analyzed by Jose F. Longoria of the Florida International University in Miami, Florida, who made bio- and chronostratigraphic determinations.

Fossils found:
Samples and beds have the same nomenclature (see Figures 13 through 21).

CAN-III-00

Sample 16: *Mytiloides sp., Watinoceras devonense*
Sample 8: *Mytiloides. hattini*
Sample 5: *Vascoceras sp.*
Sample 4: *Mytiloides aff. hattini*
Sample 3: *Mytiloides labiatus*, *Mytiloides sp.*, *Mytiloides aff. hattini*
Sample 2: *Mytiloides labiatus*, *Mytiloides sp.*

According to biostratigraphic data, the section is completely of lower Turonian age.

CAN-II-00

Sample 6: *Mytiloides aff. hattini*
Sample 7: *Mytiloides hattini*
Sample 10: *Mytiloides sp.*
Sample II.-8: *Watinoceras devonense*, *Mytiloides sp.*, *Mytiloides labiatus*
Sample 18: *Mytiloides hattini*

The sampled interval is earliest to early Turonian.

CAN-I-00

Sample 2: *Sciponoceras gracile*, *Inoceramus pictus*
Sample 2b: *Inoceramus sp.*, *Neocardioceras sp.*
Sample 5a: *Watinoceras devonense*, Mytiloides sp., *Watinoceras sp.*
Sample 8: *Mytiloides sp.*, *Mytiloides aff. hattini*
Sample 9: *Watinoceras sp.*
Sample 10: *Mytiloides labiatus*
Sample 11: *Mytiloides sp.*, *Mytiloides labiatus*

Biostratigraphy of the section indicates that the C/T boundary was sampled. The boundary can not be located exactly, but it is between bed 2b and 5a.

MT-I-00

Sample 9a: *Mytiloides hattini* (late form).
Sample 10a:*Mytiloides mytiloides.*
Sample 10b: *Mytiloides sp..*
Sample 10c: *Watinoceras sp..*
Sample 14: *Mytiloides sp.*, *Mytiloides mytiloides.*
Sample 24: *Mytiloides sp.*, *Mytiloides arcuata*, *Mytiloides labiatus.*

The sampled interval is earliest to early Turonian. The C/T boundary is located just beneath bed 1.

MT-II-00

Sample BL96-24,3: *Neocardioceras sp.*, *Scapinoceras sp..*
Sample BL96-27,0: *Neocardioceras sp.*, *Scaphites sp.*, *Placentaceras sp..*
Sample BL96-28,0: *Neocardioceras sp..*
Sample BL96-30,5: *Neocardioceras sp..*
Sample BL96-31,0: *Watinoceras sp.*, *Mytiloides sp.* (first occurrence)..

The first appearance of *Watinoceras sp.* and *Mytiloides sp.* in bed BL96-31,0 puts the C/T boundary just below BL96-31,0.

NM-I-00

There is very good age control through lithostratigraphy (marker beds), but additional paleontological information was available, although only very few fossils could be found.
Sample 2a: *Inoceramus pictus. Inoceramus sp*
Sample 8: *Inoceramus sp.*, *Neocardioceras sp.*.
Sample 13:*Mytiloides hattini* (late form), *Mytiloides sp..*
Sample 14b: *Mytiloides kossmati, Mytiloides sp..*

The C/T boundary can be located at the top of PBC 14.

NM-II-00

There is very good age control through lithostratigraphy (marker beds), but additional paleontological information was also used.
Sample 2b: *Pycnodonte sp.* (juvenile).
Sample 4b: *Pycnodonte sp.* (juvenile), Gooseneck barnacle plates (Cirreped).
Sample 6.-8: Gooseneck barnacle plates (Cirreped), *Inoceramus sp..*
Sample 6.-8: *Inoceramus pictus*.
Sample 12: *Mytiloides hattini* (early form).
Sample 13: *Mytiloides kossmati*.
Sample 14b: *Pycnodonte sp.*, Inoceramid fragment.

The C/T boundary can be located at the top of PBC 14.

TX-I-00

Results from analysis of thin sections and smear slides:
Sample 1b: Abundant large globular hedbergellids (*Whiteinella archaeocretacea*; *Pseudoticinella* sp.), large single-keeled *Thalmanninella appenninica*.
Sample 3: Large globular hedbergellids (*Whiteinella archeocretacea, Pseudoticinella*), *Clavihedbergella simplex*.
Sample 10a: Abundant broken specimens of large globular hedbergellids.
Sample 16: Abundant calcified radiolarians; large globular hedbergellids (*Whiteinella sp.*), single-*keeled Thalmanninella sp.*.
Sample 18:Abundant radiolarians; few globular hedbergellids, double-keeled *Dicarinella sp..*
Sample 21a.: Large globular hedbergellids (*Whiteinella archaeocretacea*) mainly fragments and broken specimens. Large mollusk fragments.
Sample 22a.: Recrystalized, advanced neomorphism. Abundant radiolarians.

According to the microfossils sample 14 is already in the Turonian, so the C/T boundary in this section would be placed at the base of sample 14. Sample 1b which contains single-keeled Thalmanninella, is within the uppermost Cenomanian. So the interval between samples 1a and 14 corresponds to the so-called “large globigerina” biohorizon which is considered as the base of the Turonian. However, on the basis of double-keeled planktics as a phylogenetic novelty, the base of the Turonian is sample 14.

MX-I-00

Results from analysis of thin sections and smear slides:
Sample 4a: Contains globular hedbergellids, mostly broken chambers and calcified radiolarians.
Sample 11: Broken globular hedbergellids.
Sample 15a: Globular hedbergellids, and abundant calcified radiolarians.
Sample 15b: *Heterohelix sp.*, large globular hedbergellids, abundant calcified radiolarians.
Sample 15d: Broken globular foraminifera, hedbergellids, Heterohelix cf. moremani, calcified radiolarians.
Sample 16: *Heterohelix sp*; abundant large globular hedbergellids likely *Pseudoticinella sp.*; *Whiteinella archaeocretacea*.
Sample 18b: Very high abundance of broken globular hedbergellids, *Hedbergella brittonensis; Clavihedbergella simplex.*
Sample 19a: Abundant large globular hedbergellids (*Pseudoticinella sp.*), *Dicarniella sp.*.
Sample 19b: Abundant planktic fauna, large globular hedbergellids (*Pseudoticinella sp.*), *Thalmanninella, Dicarinella sp.*.
Sample 23: Recrystalized radiolarians.
Sample 26: Abundant planktics, large globular hedbergellids, *Thalmanninella sp.*.
Sample 28: Large globular hedbergellids.

From these findings sample 18b is defined as the base of the Turonian. The C/T boundary is marked by a biohorizon rich in large globular hedbergellids (*Pseudoticinella*).

7. Geochemistry

7.1. Lab techniques

From about 150 samples, 112 were analyzed for C_{carb}, C_{org}, and $\delta^{13}C_{org}$. Duplicate analyses were run for every sample, except for the $\delta^{13}C_{org}$ samples (duplicates every six samples). The two sets were then measured on two different days.

7.1.1. Carbonate (C_{carb}) and organic carbon (C_{org}/TOC)

The abundance of total carbon (TC) and organic carbon (C_{org} or TOC (Total Organic Carbon)) were obtained by combustion in a LECO^{TM} C/S-244 analyzer. For determination of C_{org} contents, 250 mg of powdered whole rock was reacted overnight at room temperature using 2N HCl (until complete decalcification), concentrated on a glass microfiber filter (Whatman GF/C), rinsed repeatedly with deionized water, dried overnight at 50-60°C, and combusted on the LECO analyzer. Concentrations of C_{carb} was determined by difference as follows: $C_{carb} = TC - C_{org}$. Results are given as weight percent (wt. %) of the whole rock.

7.1.2. $\delta^{13}C_{org}$

The samples were measured by the Isotopenlabor AWI (Albrecht-Wegener-Institute) Forschungsstelle in Potsdam/Germany.
For the determination of the isotopic composition of organic carbon $\delta^{13}C_{org}$, the whole-rock powder was decalcified overnight using 5N HCl, at room temperature. Every seventh sample was duplicated. After neutralization with deionized water the samples were dried overnight at 70°C. The remaining residue was placed together with copper oxide (CuO) in a baked quartz tube. The tube was sealed under vacuum and combusted overnight at 850°C. The CO_2 produced by the combustion was cryogenically distilled and filled into quartz tubes, which were then sealed. The CO_2 was analyzed in a Finnigan MAT 252 mass spectrometer. Results are reported as δ-values in standard per mill (‰) relative to the PDB standard. The PDB standard is derived from a belemnite (*Belemnitella americana*) from the Pee Dee Formation of Cretaceous rocks from South Carolina (CRAIG, 1957).
The standard used during the analysis was USGS-24 (Graphite) and has a value of –16.1 +/- 0.2‰, and relative to the PDB standard. The measurements could be reproduced with an uncertainty of +/- 0.2‰. Therefore the values where not corrected.

7.2. Background geochemical proxies

7.2.1. TOC

The TOC content of a sediment can be used as a proxy for surface paleoproductivity. However, It is dependant upon primary productivity in the overlying waters and on sediment accumulation rate (MÜLLER & SUESS, 1979; BERGER & HERUGA, 1992; MIDDELBURG et al., 1993; GALE et al., 2000). Higher productivity in the overlying water column results in a greater flux of organic matter to the sea bed, but there its preservation is heavily dependant upon sediment accumulation rates. Faster accumulation rates result in more TOC being preserved in the sediment. Consequently, TOC can stand as a proxy for relative primary productivity only if variation in sediment accumulation rates can be factored out. This is supported by results from wavelet analysis and spectral analysis from the C/T reference section in Pueblo, Colorado and a section in Youngstown, Alberta. No major fluctuations in the sedimentation rate and no hiatuses occured during OAE II (PROKOPH et al., 2001). The third factor controlling accumulation of organic carbon in marine sediments is closely connected to the accumulation rate. It is the preservation rate which is controlled by the oxygen content of bottom water, the extent of bioturbation, the composition of C_{org}, and the bulk sedimentation rate.

7.2.2. $CaCO_3$

There are four known mechanisms which could result in limestone rhythms. (a.) Periodic fluctuations of pelagic carbonate supply (Productivity cycles). Variation in surface water carbonate productivity leading to the formation of limestone-marl alternations has been proposed by many authors (COTILLON, 1985; EICHER and DINER, 1985; BOTTJER et al., 1986; PRATT and KING, 1986; TORNAGHI et al., 1989). Productivity changes are thought to be generally important for carbonate cycles which have an entirely pelagic carbonate fraction, and which do not show any signs of varying carbonate dissolution or terrigenous dilution. A pure productivity cycle is characterized by a fluctuating supply of pelagic carbonate during a steady contribution of clay. (b.) Periodic fluctuations of supply with terrigenous sediment (Dilution cycles). Periodic fluctuations in terrigenous dilution is thought to be a major process for calcareous depositional environments with a minor but oscillating terrigenous input, such as the outer shelf or epicontinental seas. Terrigenous input is through fluvial, eolian, or glacial processes, and thus is closely related to climatic changes influencing surface runoff and erosion on the continents (GARDNER, 1982; PRATT, 1984; BOTTJER, 1986; DEAN and GARDNER, 1986). In basins not far from land areas, the input of fluvial and eolian sediment in the silt and clay fraction can show considerable fluctuations in quantity and composition, depending on whether they are located in arid or humid climatic zones (SARNTHEIN, 1978; SIROCCO, 1989). (c.) Periodic dissolution of carbonate (Dissolution cycles). Dissolution of carbonate is most significant for sites situated within the

lysocline and the CCD, a zone which for the present oceans is 1 to 1.5 km thick (BERGER et al., 1982). Additional dissolution is observed for sites above the lysocline where the sediments are relatively rich in organic matter which can be decomposed and thus provide agressive CO_2 (EMERSON and BENDER, 1981; DIESTER-HAASS, 1991). Oceanic dissolution cycles are also thought to be common in the Upper Cretaceous deep sea carbonates, as the CCD was considerably shallower (3.5 to 5 km; SEIBOLD and BERGER, 1982). (d.) Calcareous redox cycles. Alternations composed of carbonate-rich beds and organic carbon-rich shales is a common bedding pattern in many black shale units and their facies transitions into marls and carbonates. Such alternations are found in environments that range from the epicontinental sea to the deep sea. Varve-type lamination within the black shale bed and burrowing in the limestones indicate fluctuating oxygenation of the bottom waters, i. e. redox cycles (Savrda et al., 1991).

7.2.3. $\delta^{13}C_{org}$

The C/T (Cenomanian/Turonian) event was one of the major perturbations of the Earth's carbon cycle, leading to a global positive carbon-isotope excursion registered in carbonate and organic matter. The extent of the carbon isotope excursion for carbonate is typically 2.5-3.0‰ and that for organic-carbon varies from 2.5-6.0‰. These excursions begin sharply in the uppermost *R. cushmani* planktonic foraminiferal zone and are essentially completed at the end of *the W. archeocretacea* zone (for detailed descriptions of biostratigraphy of the C/T boundary: see SCHLANGER et al., 1987; BRALOWER, 1988; KUHNT et al., 1990). The isotopic excursions in both carbonate and organic matter have been attributed to the widespread removal of isotopically light organic-carbon into black-shales during the C/T event, leading to enrichment in ^{13}C of the atmospheric and oceanic reservoirs of CO_2 (ARTHUR et al. 1987, 1988; SCHOLLE and ARTHUR, 1980). This event can be schematically divided into five different phases (Figure 11).

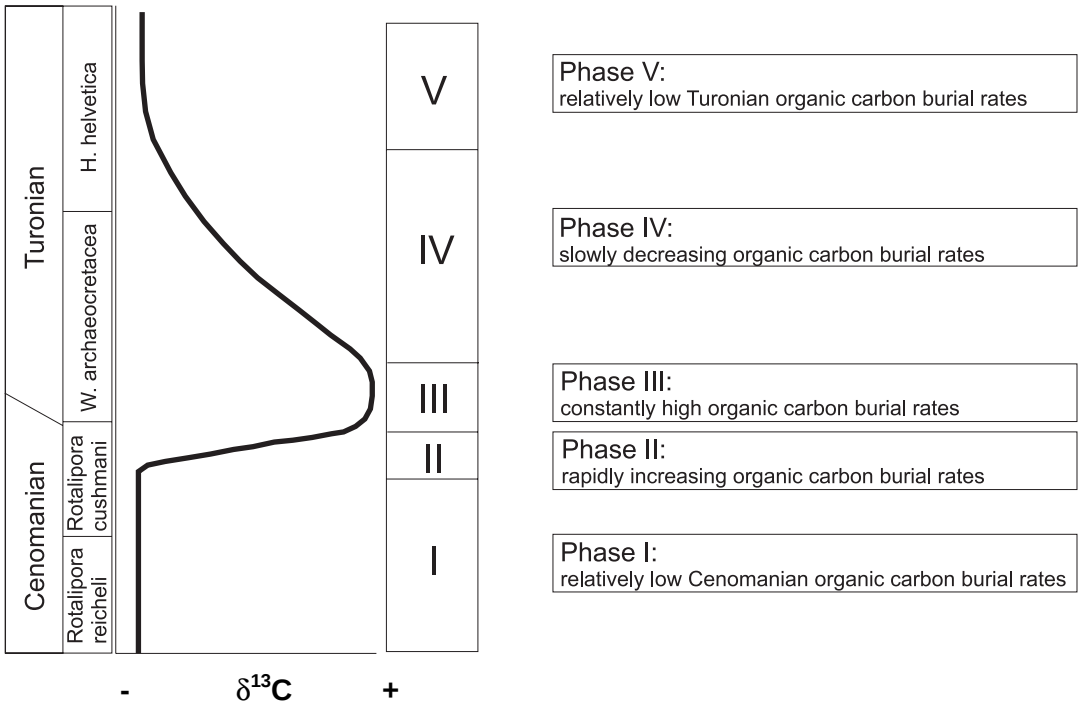

Figure 11: Schematic diagram showing the C/T carbon-isotope excursion of carbonate- and organic-carbon subdivided into five different phases of different organic-carbon burial rates. Planktonic foraminifera zones are indicated for reference (After http://kellia.nioz.nl/projects/ctnet/research.html).

Initial phase I of relatively low Cenomanian organic-carbon burial rates, phase II of rapidly increasing organic-carbon burial rates, phase III of constant, high organic-carbon burial rates, phase IV of slowly decreasing organic-carbon burial rates and final phase V of much reduced Turonian organic-carbon burial rates. The total duration of phase II-IV is estimated to be 300-600 ka, with phase II taking place in only 60 ka (KUYPERS et al., 1999a). These phases are recorded globally by the similar curves of $\delta^{13}C$ of carbonate and organic matter at various locations on different continents (GALE et al., 1993; JENKYNS et al., 1994; KUHNT et al., 1990) and in the South Atlantic, Pacific and Indian Oceans, the Tethys and the epicontinental Western Interior Seaway of the U.S.A. (e.g. SCHLANGER and JENKYNS, 1976; SUMMERHAYES, 1981; de GRANCIANSKY et al., 1984; HERBIN et al., 1986; SCHLANGER et al., 1987; KUHNT et al., 1990; KUHNT and WIEDMANN, 1995).

The stable carbon-isotopic composition of C_{org} often has been interpreted in terms of the source of the organic matter. The basis for interpreting the isotopic composition of C_{org} as a source signal is the fact that modern terrestrial vegetation generally is depleted in ^{13}C relative to modern marine plankton and therefore has values of $\delta^{13}C$ that are about 5-7 ‰ lighter (more negative, Figure 12) than those of marine plankton (DEINES, 1980; FRITZ and FONTES, 1989)

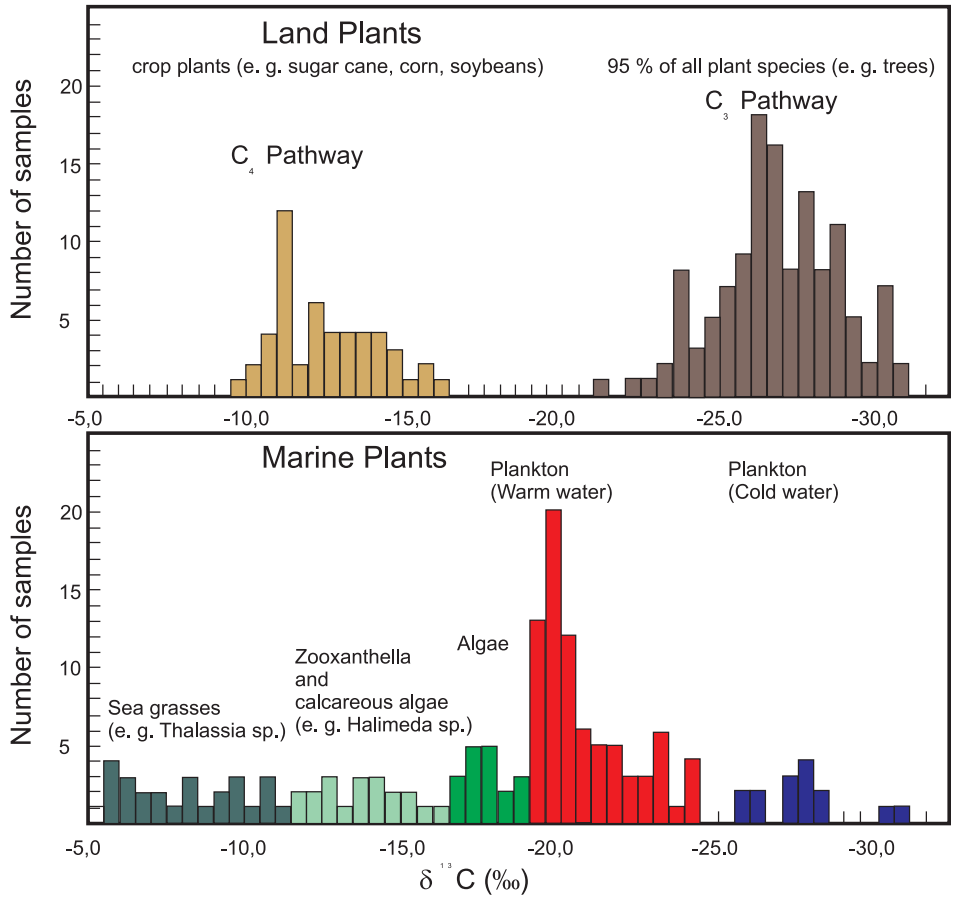

Figure 12: $\delta^{13}C$ values from terrestrial and marine plants, after FRITZ & FONTES (1989).

Most organic matter in modern marine sediments, judged by other geochemical criteria to be mainly marine, has a $\delta^{13}C$ value similar to that of marine plankton and particulate organic matter (about –22 ‰). This appears to be true of organic matter at least as far back as the early Miocene (ARTHUR et al., 1985a; DEAN et al., 1986) but the $\delta^{13}C$ of Cretaceous organic matter does not appear to follow the same behavior. On the basis of available data (DEAN et al., 1986), Cretaceous marine C_{org} is typically isotopically lighter than terrestrial C_{org} by 3 ‰ or more, with the exception of that in strata of Upper Cenomanian to Lower Turonian (ARTHUR et al., 1988) and Lower Albian (PRATT and KING, 1986) ages. This was demonstrated at DSDP Site 603 and 367, where the suspected terrestrial C_{org} has significantly heavier $\delta^{13}C_{org}$ values (-24 to –25 ‰) than relatively well-preserved marine C_{org} (-27 to –28 ‰).

Generally, there are four principal mechanisms which may account for large shifts in the isotopic composition of the C_{org}: (1.) Temperature-dependant isotopic fractionation by phytoplankton. (2.) Diagenetic alteration of the primary sedimented material. (3.) Mixing of C3- and C4-photosynthetic organic matter. (4.) Mixing of C3- photosynthetic terrigenous and marine organic matter. For this study the emphasis is not on what causes the isotopic excursion and shifts across the sections; instead the organic carbon isotopes are used here for stratigraphy and for recognition of periodicities.

7.3. Results of geochemical analyses

Introduction:

This chapter describes the results of the analysis of the three geochemical parameters ($CaCO_3$, TOC, $\delta^{13}C_{org}$) measured. A key to the lithologies and geochemical data is shown in Figure 13. Numeric values for all measured samples are listed in the Appendix; Data sheets/results of geochemical analyses.

The sampling intervals for the geochemical analyses were chosen to be larger than the usual intervals used for HIRES stratigraphy. The sampling interval depended primarily on changing lithologies. If a uniform sedimentation pattern as in the Canadian sections prevailed, large sampling intervals were chosen (1.5-3.0 m). If changes in the lithology occurred, each unit was sampled. For all other sections the sampling intervals varied between 0.1-0.3 m, depending on lithology changes. Previous works (PRATT, 1985; PRATT and THRELKHELD, 1993; SAGEMAN et al., 1997, 1998; FLOEGEL and RIPS, unpublished diploma thesis) on the WIS have shown that distinctive peaks are associated with certain beds. Using the strategy described above it was still possible to detect all peaks associated with particular beds.

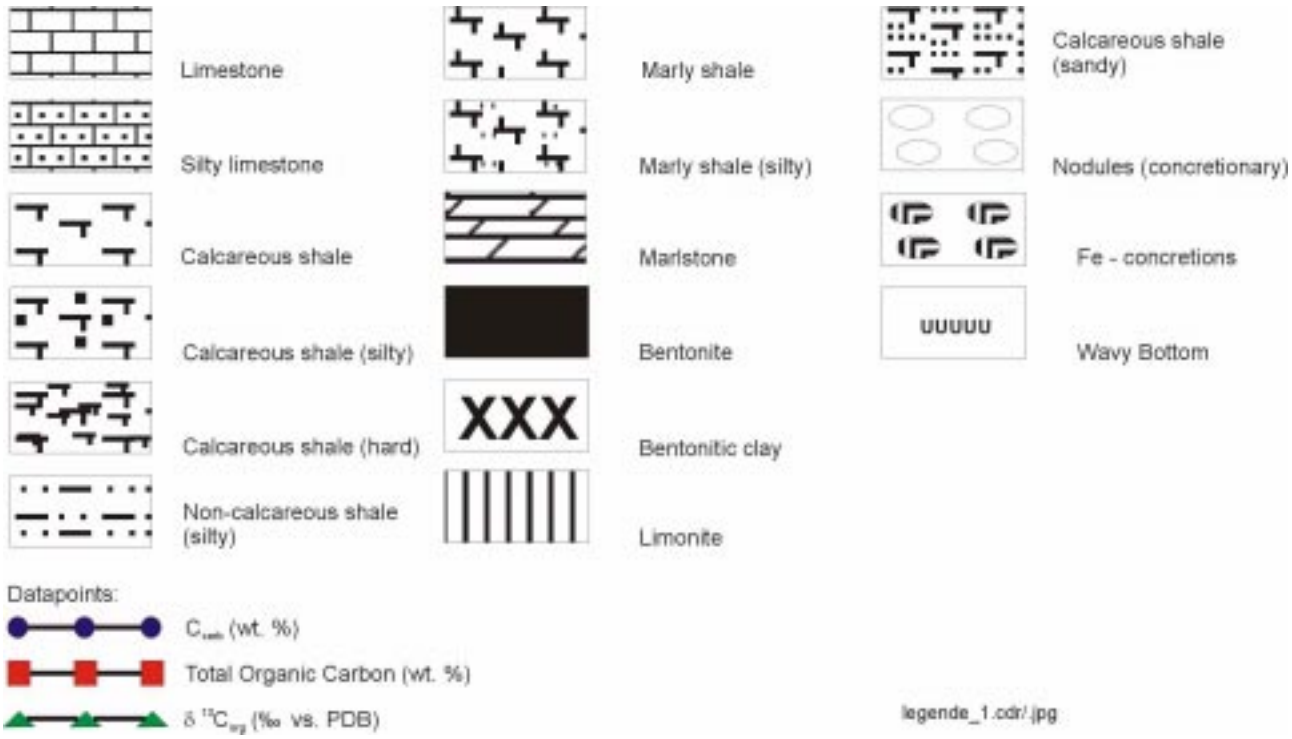

Figure 13: Key to lithologies and geochemical data.

Thistle Creek, Alberta, Canada / CAN-III-00

The carbonate and the organic carbon curves for this section show a very distinctive pattern which has highly regular cyclicity with a period of 6.50 meters. Those distinctive peaks occur in the limestone and calcareous shale beds. There is a strong negative correlation of carbonate and organic carbon content (Figure 14).

The average value of $CaCO_3$ is 56 wt. % for the limestones and 8 wt. % for the marly shales. The carbonate content in the shales has very uniform distribution. The same is true for the carbonate peaks in the limestone beds.

The TOC values show the opposite pattern to the $CaCO_3$ data, with their highest values in the shales, averaging 1.6 wt. % and their lowest values in the limestones and the calcareous shale bed 8. Here the values average 1.2 wt. % TOC.

Averages for the whole section are 20 wt. % for $CaCO_3$ and 1.4 wt. % for TOC.

The isotopic signature of the organic carbon ($\delta^{13}C_{org}$) of the Thistle Creek locality shows a pattern similar to the TOC and the $CaCO_3$ data. Every 6.50 m the $\delta^{13}C_{org}$ curve shows positive excursions with an amplitude of about 1.1 to 1.5 ‰.

The average for all measured samples is –25.9 ‰. Above of bed 12 there is general trend of values declining towards the top of the section.

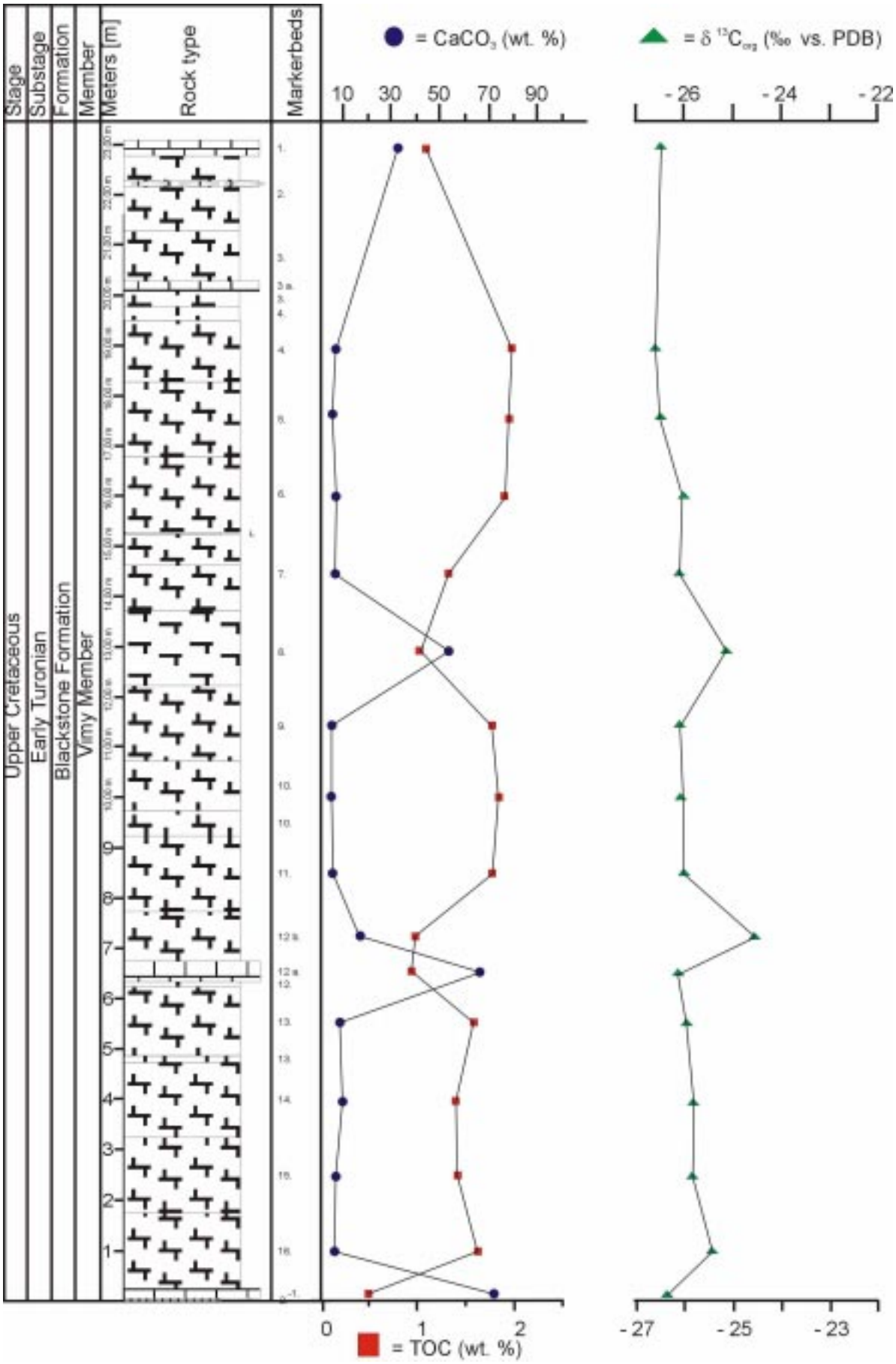

Figure 14: Section CAN-III-00 (Thistle Creek, Alberta, Canada).

Big Horn River, Alberta, Canada / CAN-II-00

The geochemical measurements of $CaCO_3$ and TOC (Figure 15) show a relatively uniform pattern in the lower 26.0 m of the section with two very distinctive peaks, in beds 1 and 8. Therefore the lower 26.0 m show $CaCO_3$ values for the shales of 9 wt. % (TOC = 1.6 wt. %) with extremes of 64 wt. % ($CaCO_3$) and 0.7 wt. % (TOC) in bed 1. Higher in the section the geochemical data vary with a higher amplitude and a shorter period.

The overall averages for $CaCO_3$ and TOC are 66 wt. % and 0.8 wt. % for the limestones and 13 and 1.5 wt. % for the shales.

The highest values for carbonate content are in limestone beds 1 and II.-1- through II.-11. TOC also remains fairly high through this interval, but the lowest TOC values occur in the beds having the highest carbonate content.

Averages for the whole section are 25 wt. % for $CaCO_3$ and 1.3 wt. % for TOC.

The $\delta^{13}C_{org}$ data shows a trend which can be divided into two parts. The lower 25 meters vary between –24.3 ‰ and –26.1 ‰ with no abrupt changes. The gradual nature of the changes might be due to the fact that the samples were taken at 3 meter intervals. Above 25 meters the isotope signal becomes more positive (-23.5 ‰ in bed 14; lightest value of this locality). Above bed 14, $\delta^{13}C_{org}$ shows a more variable pattern, including the lightest value in this section, -26.9 ‰ (bed 19). The same variability is noted in the TOC and the $CaCO_3$ values. Generally, $\delta^{13}C_{org}$ values become lighter upward through the section. The average of the whole section is –25.4 ‰.

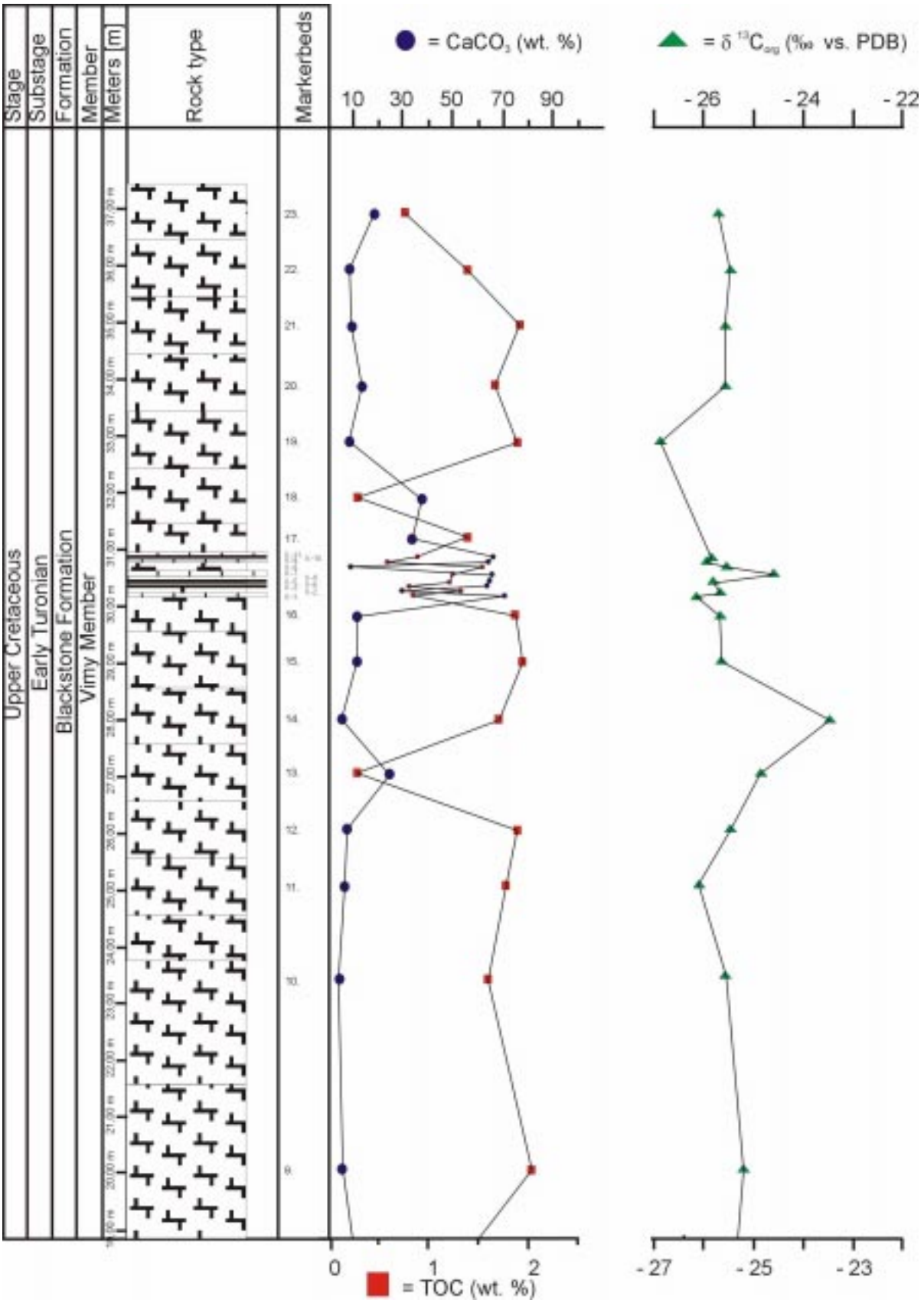

Section CAN-II-00; upper part (Big Horn River, Alberta, Canada).

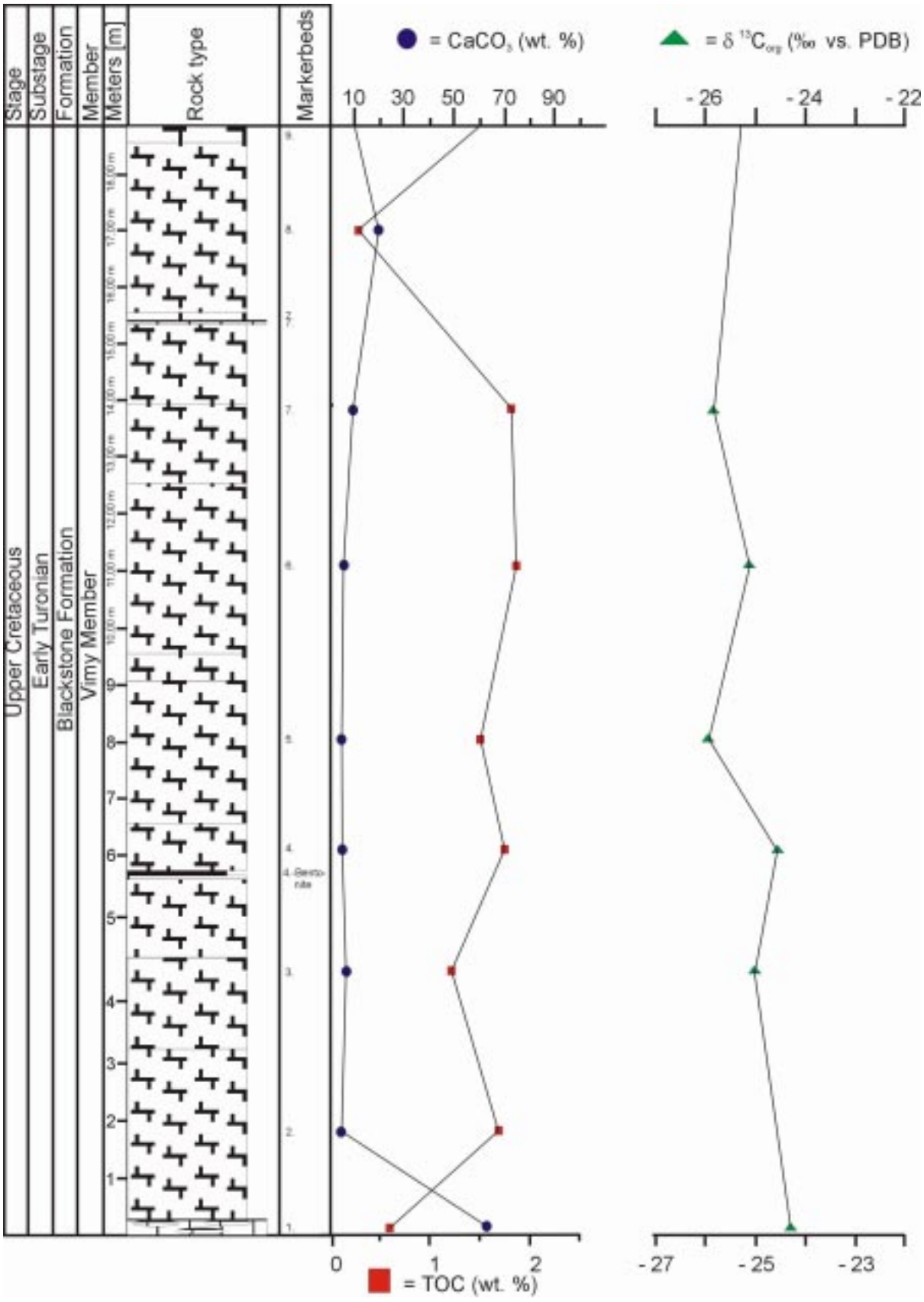

Figure 15: Section CAN-II-00; lower part (Big Horn River, Alberta, Canada).

Burnt Timber Creek, Alberta, Canada / CAN-I-00

The geochemistry of this section differs in many ways from the two other Canadian outcrops (Figure 16). The $CaCO_3$ content (avg. 22 wt. %) is the highest and the TOC-values (avg. 0.5 wt. %) are the lowest ones for all the shales of all three Canadian locations. Only one limestone bed is present in this section, below bed X-1. This section shows small amplitude variations with high periodicity; there are peaks in the carbonate curve about every 2.50 m. TOC values are also variable, but the periods are less regular.

The highest TOC value is in bed 10, 1.6 wt. %. Throughout most of the section TOC values are high, where carbonate values are low and vice versa, but there is no general trend toward higher or lower carbonate or organic carbon values.

The $\delta^{13}C_{org}$ data at this locality clearly show the positive isotopic excursion associated with the Cenomanian/Turonian boundary. A $\delta^{13}C_{org}$ value of –27.6 ‰ was measured in the lower part of bed 2a. Above this level $\delta^{13}C_{org}$ values rise until bed 8, with a positive maximum of –24.6 ‰. Higher in the section values decrease again (bed 19, -27.5 ‰). The carbon isotopic excursion takes place over more than 15 meters of section with a maximum amplitude in the isotopic signal of –3 ‰. On this “bulge” smaller cyclic variations of about of 1.7 ‰ occur. The average for the whole section is –26.1 ‰.

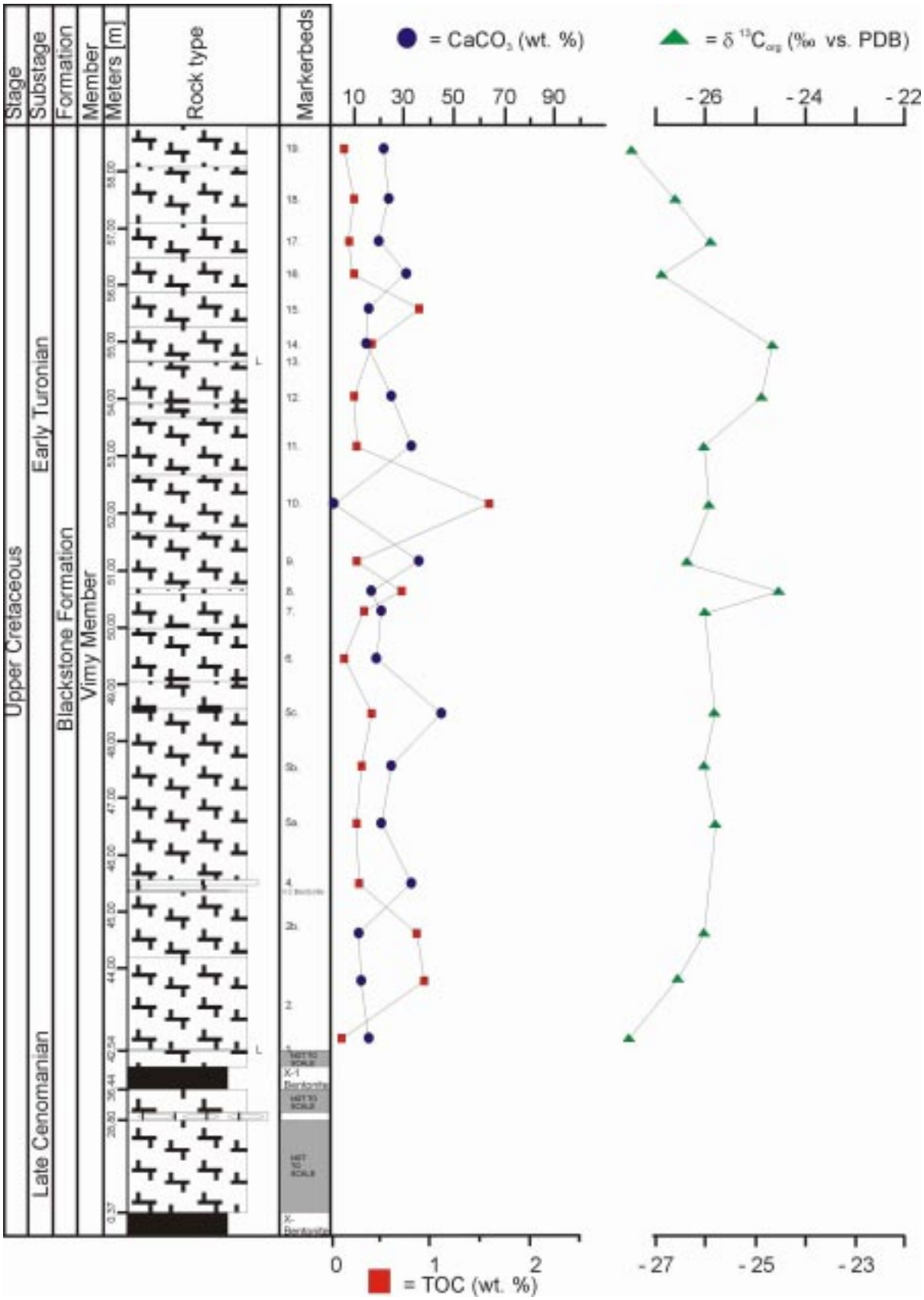

Figure 16: Section CAN-I-00 (Burnt Timber Creek, Alberta, Canada).

Cone, Montana, USA / MT-I-00

Locality MT-I-00 shows a highly irregular pattern of $CaCO_3$ and TOC contents. The average content of $CaCO_3$ is 33 wt. %, but the values range between 17 wt. % in the middle of bed 1 and 85 wt. % in bed 24 (Figure 17). The carbonate content shows a relatively even distribution in the lower ¾ of the section, with values of 22 wt. %. Carbonate content increases above the middle of bed 14.

The TOC shows a very wide range of values, too. The average for the measured section is 3.8 wt. % TOC, with extreme values of 0.5 wt. % in bed 24, which has the highest $CaCO_3$ content and 6.1 wt. % in the uppermost part of bed 14. Overall the TOC shows a trend, decreasing from the base to the top of the section, but with a cyclical distribution in the lower ¾ of the section and strongly decreasing values upward of bed 14. The highest values of TOC of any of the measured sections occur in this outcrop.

The $\delta^{13}C_{org}$ in this section has an average –26.1 ‰ (the same as at the Burnt Timber Creek section) with minima and maxima of –26.8 ‰ (bed 26) and –24.5 ‰ (bed 16b). There is no general trend towards lighter or heavier values across the section at this locality; instead the values shift around the average value of–26.1 ‰. The largest positive shifts occur in the lower portion of bed 9 (–24.8 ‰). and in the upper part of bed16 (–24.5 ‰); positive excursions with an amplitude of 2.2 ‰. The data appear to have a similar baseline value around –26.5 ‰, with positive periodic shifts.

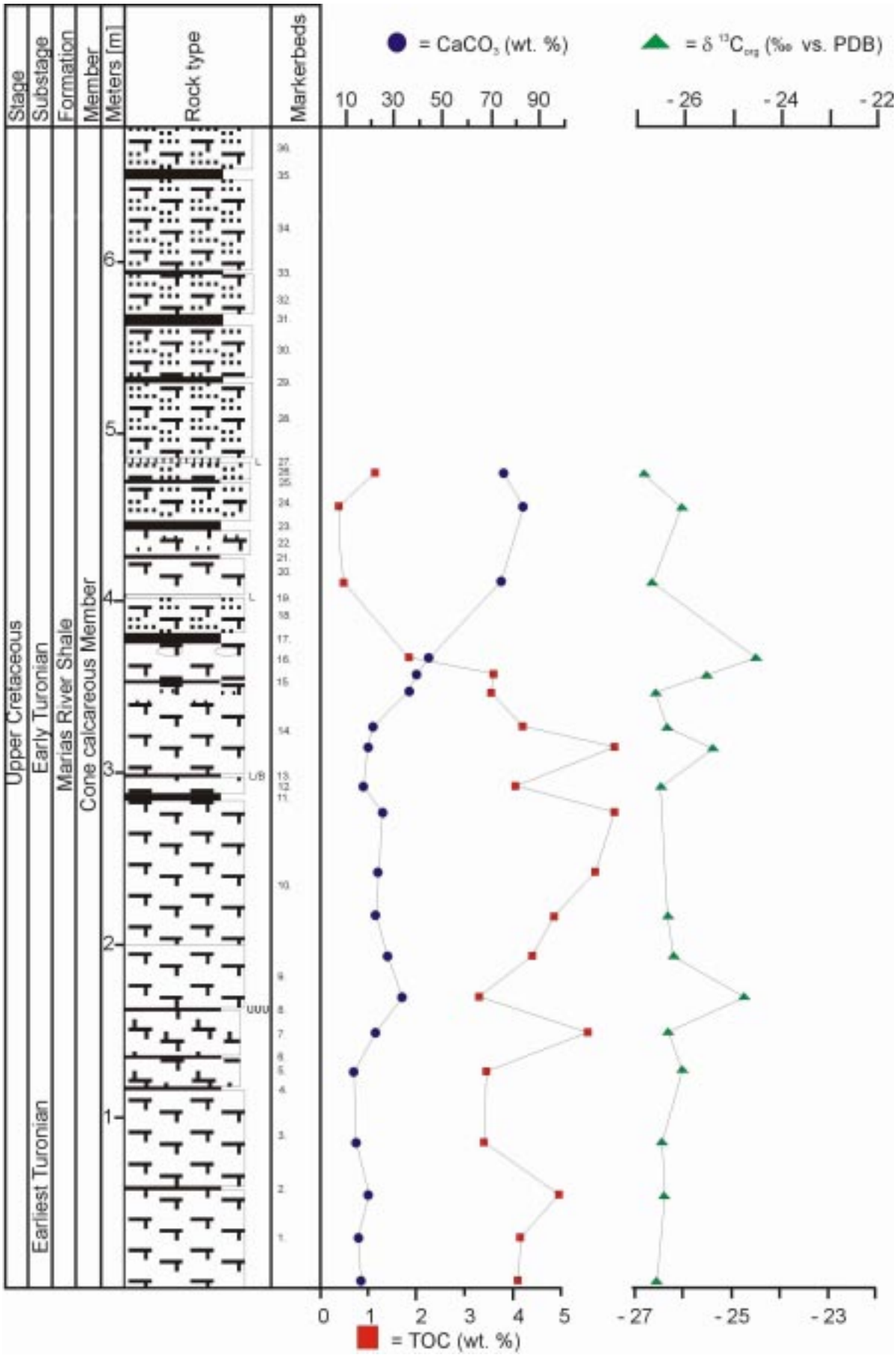

Figure 17: Section MT-I-00 (Cone, Montana, U.S.A.).

Landfill, Montana, USA / MT-II-00

Most of the samples examined from this locality were provided by R. M. Leckie (and co-workers) from the University of Massachusetts at Amherst, who measured and described the section in 1996.

The geochemical data of this locality show no significant variation throughout the section (Figure 18), neither for the $CaCO_3$, nor for the TOC data; this is not surprising since the sedimentation in this section is very homogeneous.

Unfortunately, the geochemical data measured for this section must be treated with caution, because the results suggest that weathering has changed the geochemical signature dramatically, especially the $CaCO_3$ content. Therefore the geochemical results are not interpreted in the subsequent chapters.

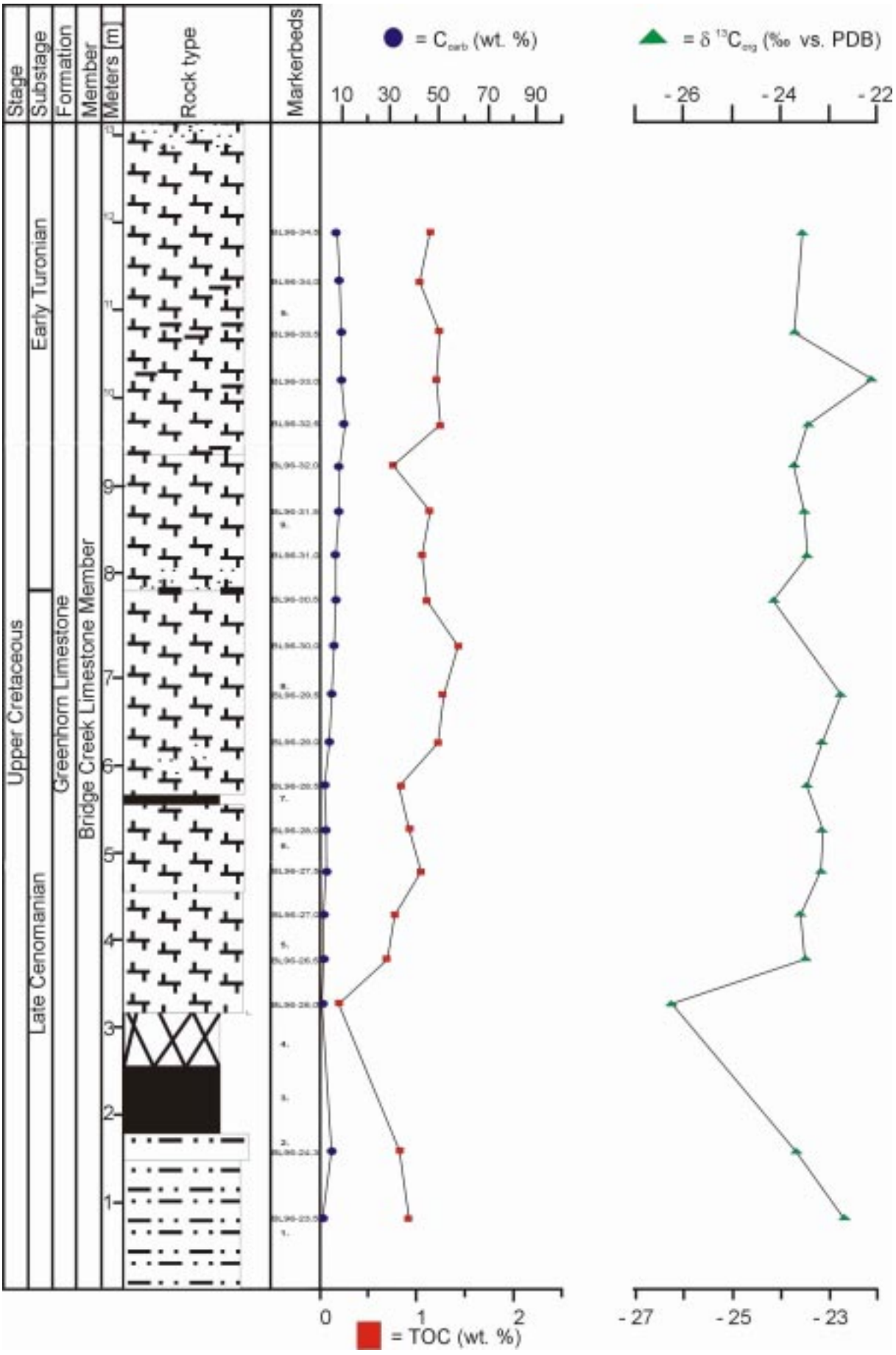

Figure 18: Section MT-II-00 (Landfill, Montana, U.S.A.).

Emery Gap, New Mexico, USA / NM-I-00

The geochemical analyses (Figure 19) show a uniform pattern throughout the section. The $CaCO_3$-content shifts around an average of 81 wt. %, with no large variation. The average for the TOC-value is 0.3 wt. % and shows only two peaks in the section, bed 2 and 9 (1.6 wt. % TOC).
The carbonate content for the limestones has a value of 85 wt. % and is about 8 wt. % higher than the carbonate content of the shales (77 wt. %).
The shales hand have a higher TOC-content, with an average of 0.5 wt. %, whereas the limestones only contain 0.2 wt. % TOC.
The largest variation of the geochemical curves occur the calcareous shale of bed 9.
Unfortunately only ten $\delta^{13}C_{org}$ measurements could be completed for this section due to problems during the analysis. These ten samples have an average of –25.5 ‰ with minima and maxima of –27.2 ‰ (bed 1.) and -24.1 (upper part of PBC 3). These few samples indicate a shift towards lighter values compared with the section to the north, Las Vegas, NM. The average isotopic value for the Las Vegas section is 2.4 ‰ heavier than the ones of this section. Except for the lower three data points which have large amplitude variation, the data show no significant variation or cyclicity.

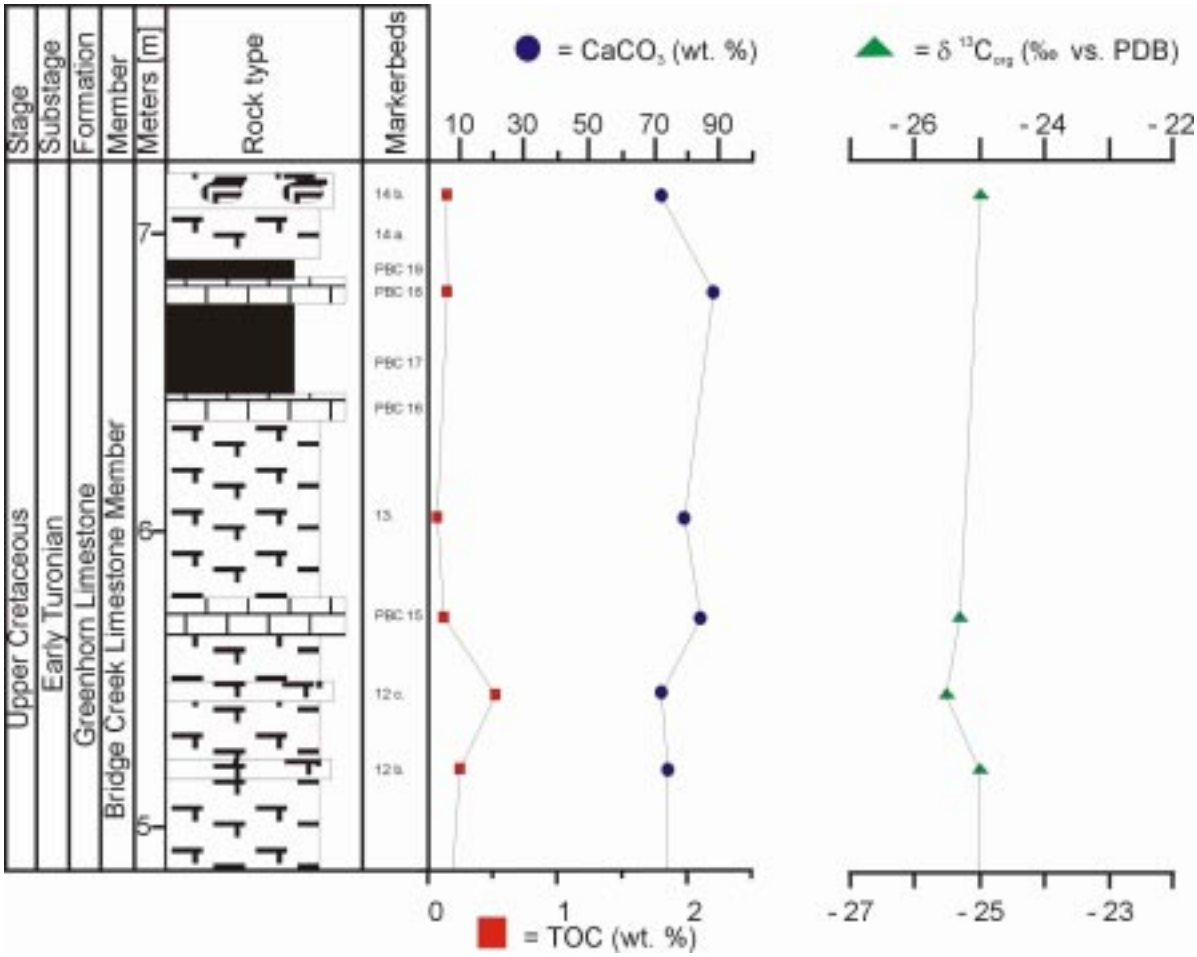

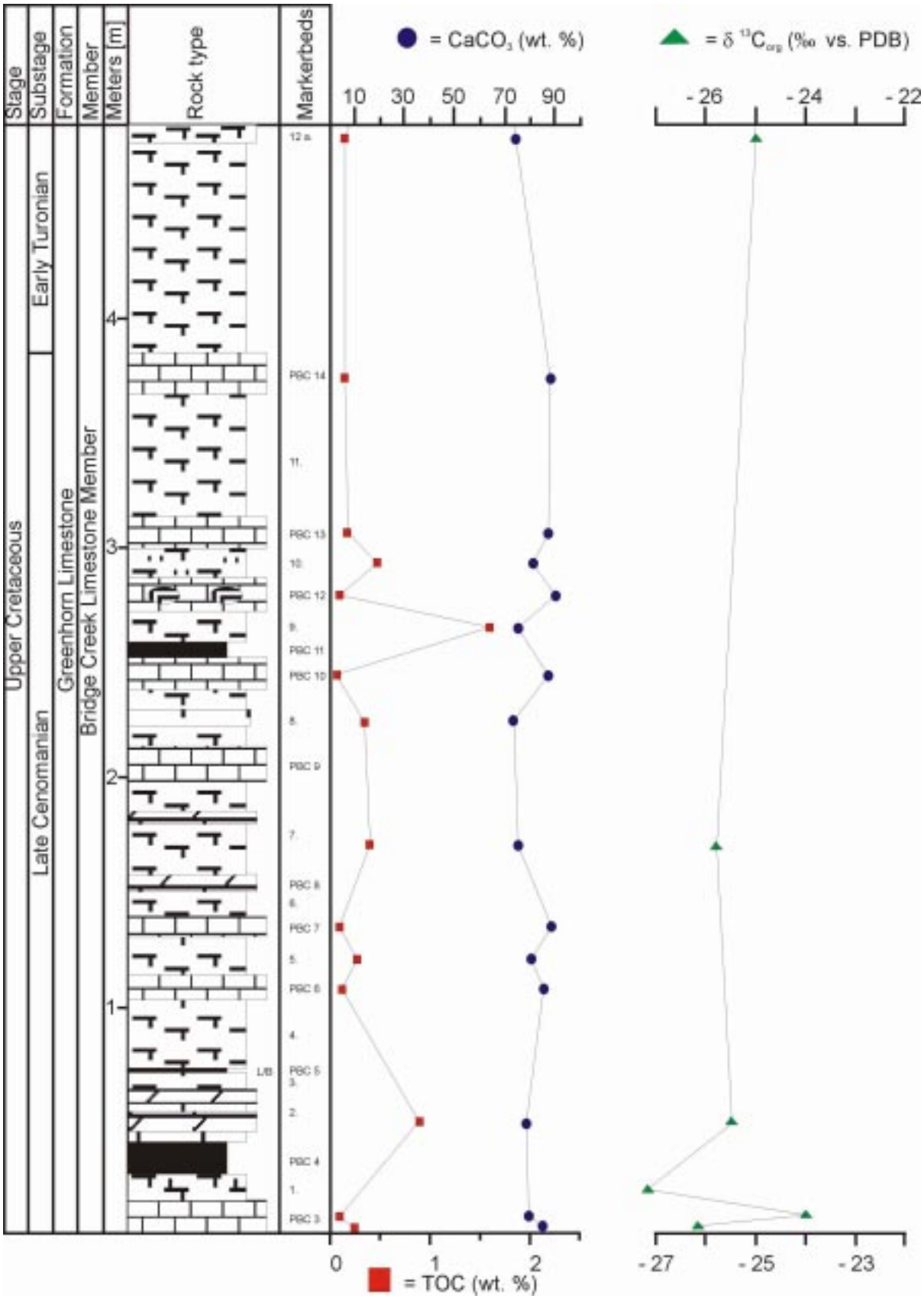

Figure 19: Section NM-I-00 (Emery Gap, New Mexico, U.S.A.).

Las Vegas, New Mexico, USA / NM-II-00

Sections NM-I-00 and NM-II-00 have a similar sedimentation pattern, but this not reflected in the geochemical data. The Las Vegas section is characterized by a highly variable geochemistry (Figure 20).

The lower 2.50 m show relatively stable $CaCO_3$- and TOC-contents, but above the Cenomanian/Turonian boundary, at the base of bed 12a (per convention from the type section at Pueblo, CO.) the data show large shifts, especially the TOC data.

Over the whole section the average $CaCO_3$-content is 70 wt. % (limestones = 79 wt. %; shales = 58 wt. %) and the TOC-value is 0. 5 wt. % (limestones = 0.2 wt. %; shales = 0.8 wt. %). The dynamic interval overlies bed 8. where the geochemical are more stable.

The $\delta^{13}C_{org}$ measurements for this section have a average value of –23.0 ‰. This is the heaviest value of all the sections measured during this study. The minimal and maximal values are –23.7 ‰ (PBC 20) and –22.1 ‰ (PBC 3). The data show the positive excursion associated with the C/T boundary, but the amplitude (~-1.6 ‰) of the signal is relatively small. Usually the carbon isotope excursion for organic-carbon varies between 2.6 and 6 ‰.

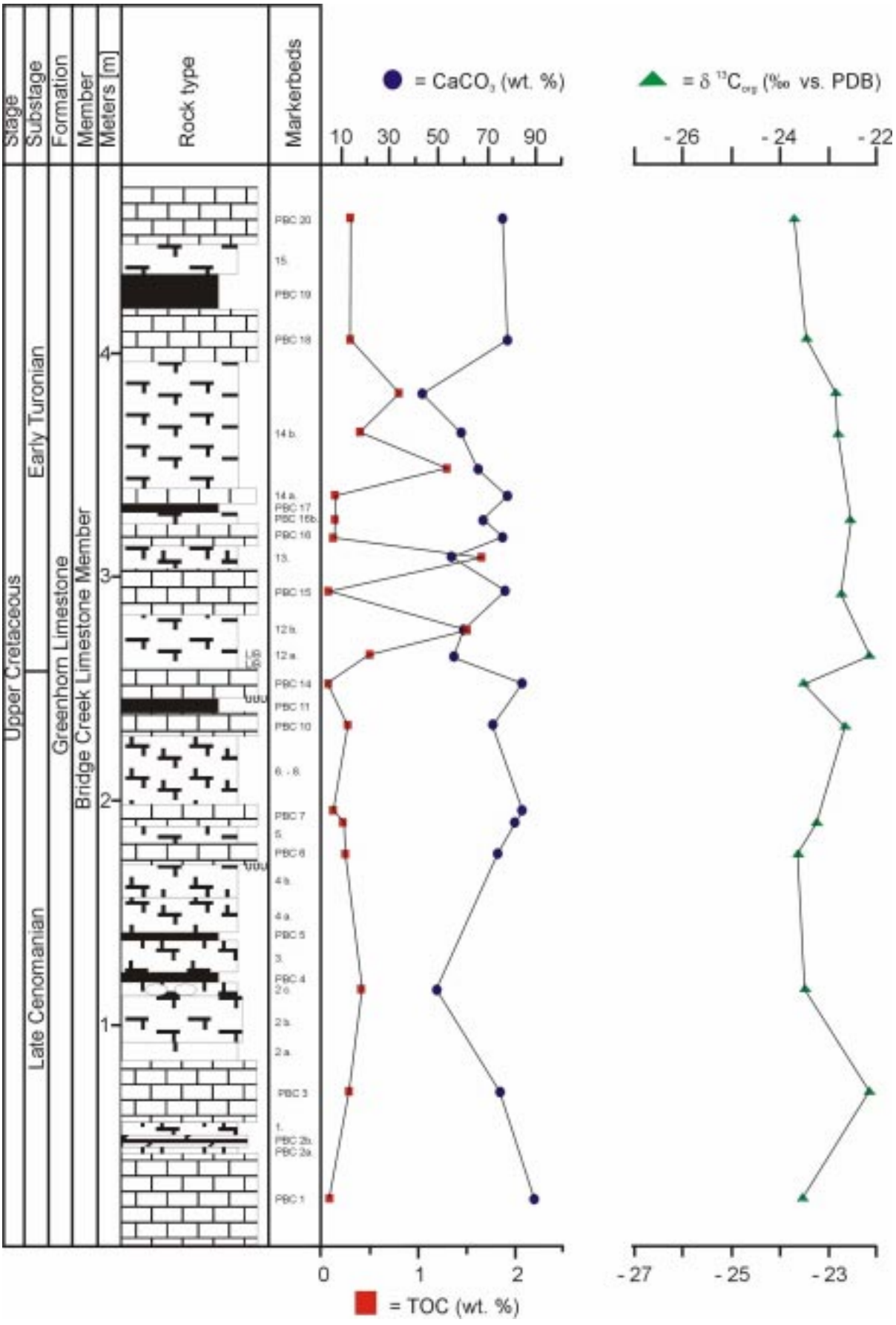

Figure 20: Section NM-II-00 (Las Vegas, New Mexico, U.S.A.).

Hot Springs, Texas, USA / TX-I-00

The geochemical fingerprint of the Hot Springs section in Big Bend National Park is slightly different from the other locations which were analyzed during this study, because one parameter (TOC) remains constant, whereas the other ($CaCO_3$) varies.
The TOC values show no significant variation in the lower 5.50 m of the section (Figure 21). Values are generally very low, around 0.1 wt. %, but there are higher values in the uppermost part of the section, going up to 0.7 wt. %. The average TOC-value is very low with a value of 0.1 wt. % (limestones = 0.1 wt. % and shale s= 0.1 wt. %). There is no correlation between the lithology and the TOC data.
The carbonate content of the limestones is higher than in the shales. The variation is relatively regular throughout the section with decreasing values in the upper part of the section.
Average carbonate value is 80 wt. % for the limestones and 67 wt. % for the shales. The average $CaCO_3$-value for the whole section is 73 wt. %.
The isotope data show a highly variable pattern with an average value of –27.1 ‰, which is the lightest value of all analyzed sections. At the same time the largest shifts can be seen here, for example the negative shift from bed 8 b to 8c (4.1 ‰). Minima and maxima for this section are –28.2 ‰ (bed 13a) and –24 ‰ (bed 8b). The isotopic data allow a division into two parts, from bed 1a to bed 8 c and from bed 8c to the top of the section (bed 22b). The lowermost part has relatively heavy values, but above 8c., values get very light and vary around –27.4 ‰. The upper 6 meters are characterized by cyclic variations with small amplitudes (positive excursions in 12b, 15b, 21c). The expected positive isotopic excursion can be seen at this locality, showing shape of the excursion, with sharply increasing values from bed 1 to 8 and the following decrease.

NOTE: Due to the exposure to a extremely arid and hot climate, comparative measurements for unweathered and slightly weathered rocks were conducted. These indicate that the error for the slightly weathered sediments is on the order of 3 to 6 % ($CaCO_3$) and up to a factor of four for the TOC content. The weathered sediments have lower values, for both TOC and $CaCO_3$. The $\delta^{13}C_{org}$ measurements show differences of about 15 % between unweathered and slightly weathered rocks.

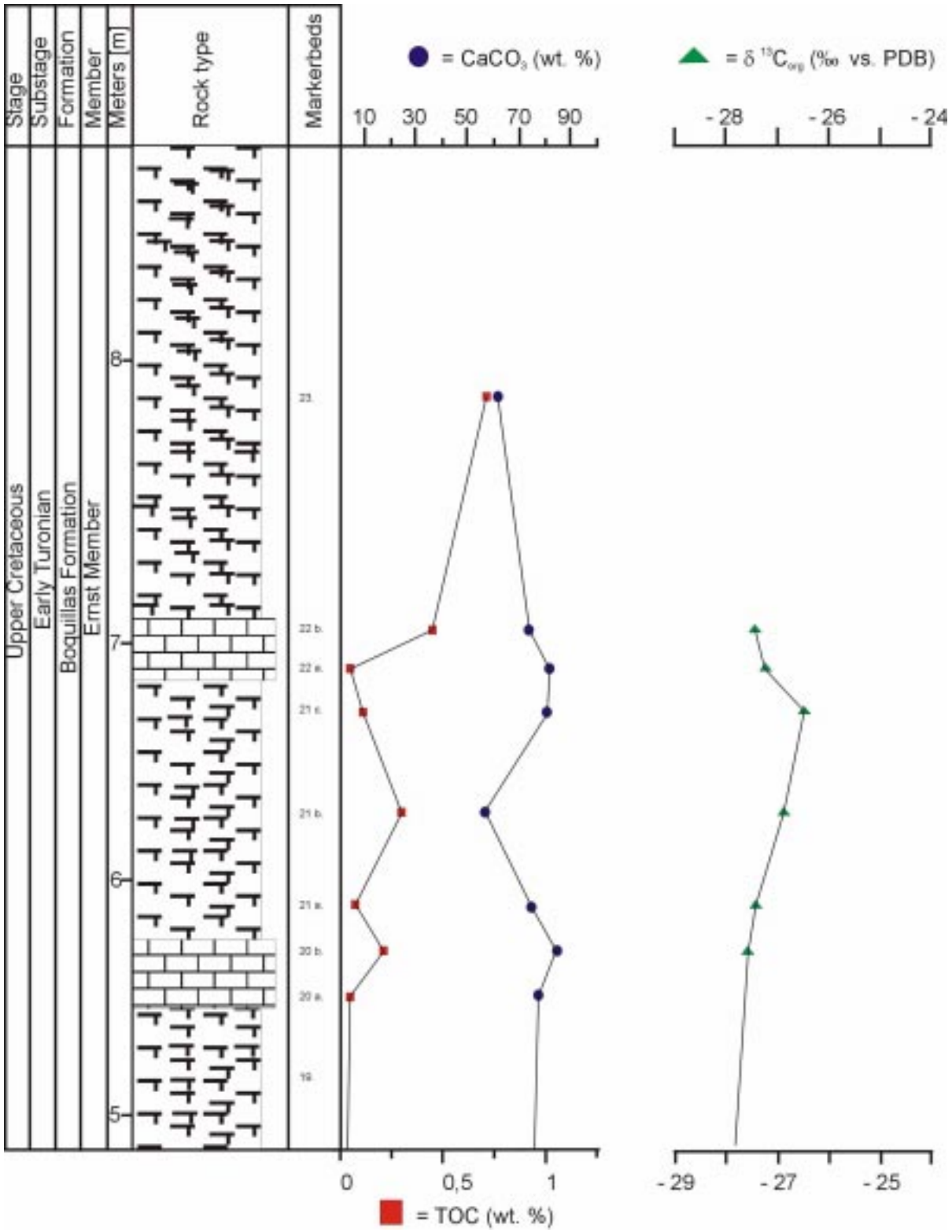

Section TX-I-00; upper part (Hot Springs, Texas, U. S. A.).

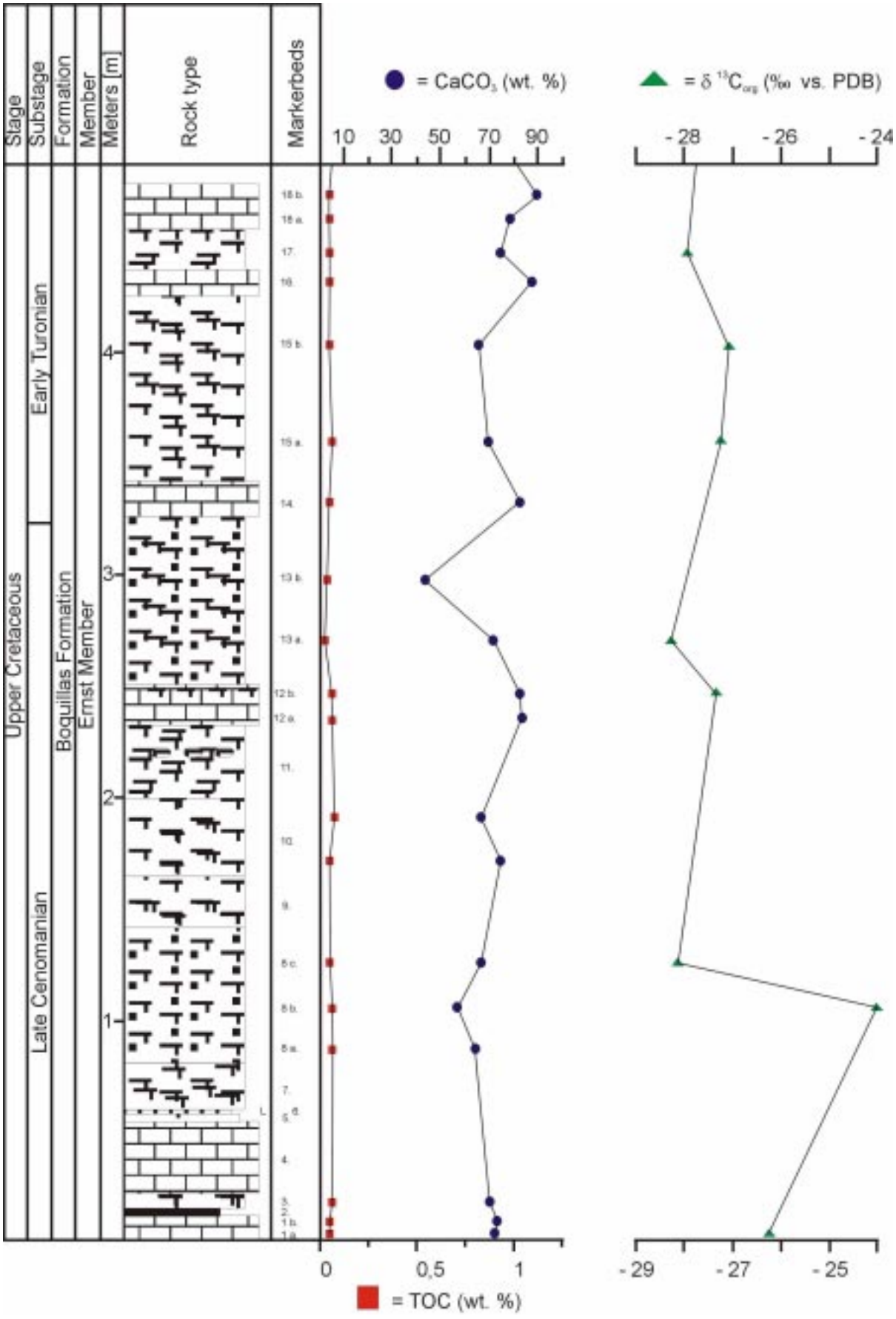

Figure 21: Section TX-I-00; lower part (Hot Springs, Texas, U. S. A.).

La Boca Canyon, Nuevo Leon, Mexico / MX-I-00

The La Boca Canyon section is characterized by high calcium carbonate contents for both limestone and shale. The average $CaCO_3$ of limestones is about 76 wt. %, whereas for the shales it is 72 wt. %. This gives an average $CaCO_3$ content of 74 wt. %.
The TOC values for this sections are very low and never exceed 0.6 wt. % in the limestones and 0.4 wt. % in the shales. The average value for the limestone is 0.2 wt. % and 0.1 wt. % for the shales. This gives an average TOC content of 0.2 wt. %.
Both curves (Figure 22) show a positive correlation throughout the section with small “peaks” in bed 15 and 23b. For the rest of the section the $CaCO_3$- and the TOC-content plot in a more or less straight line.
The $\delta^{13}C_{org}$ curve of this locality can be divided into two parts. A lower part (B to 12) and a upper part from bed 12 up to bed C. The lower part is characterized by a gradual increase towards heavier values from –26.1 ‰ to –24.8 ‰ (bed 10.). Above bed 10 the measured samples have more variable values with large negative shifts of up to 2 ‰. The average for the complete section is –25.3 ‰, with the lightest value being –26.9 ‰ and the heaviest value being –24.8 ‰.

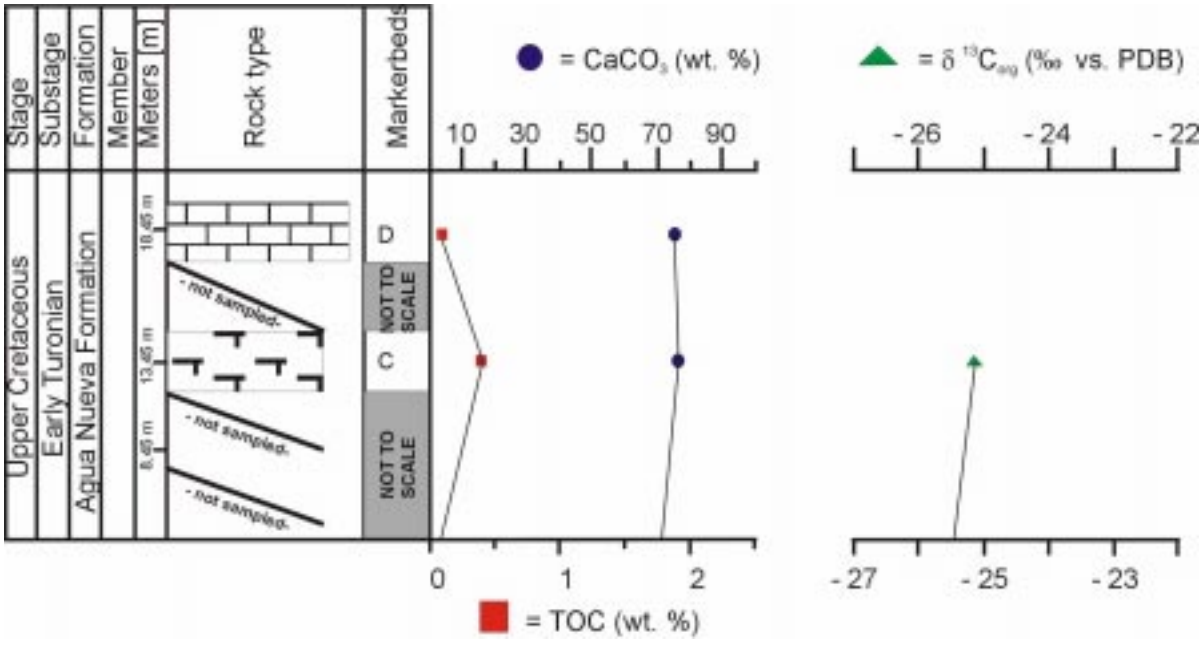

Section MX-I-00; upper part (La Boca Canyon, Nuevo Leon, Mexico).

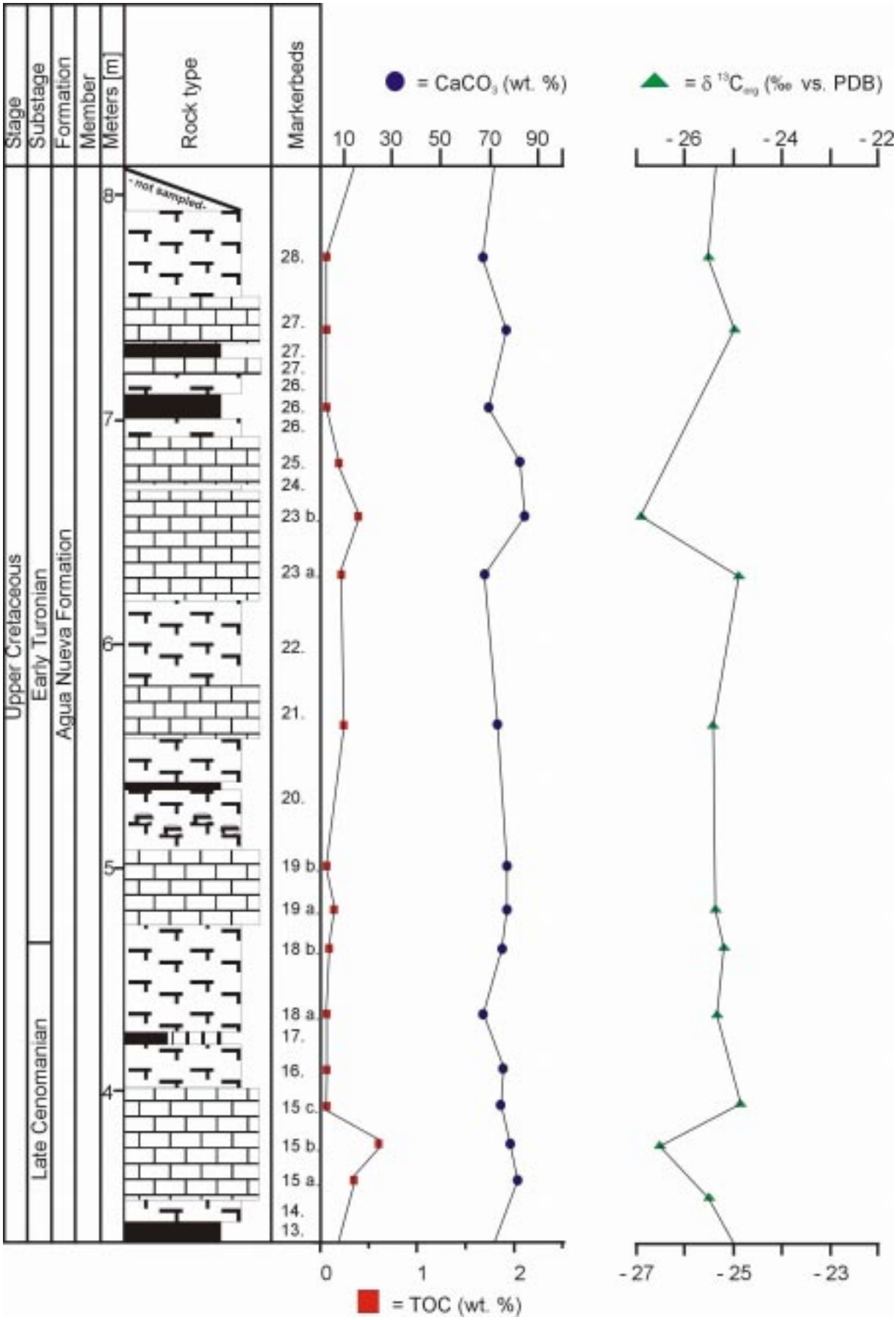

Section MX-I-00; middle part (La Boca Canyon, Nuevo Leon, Mexico).

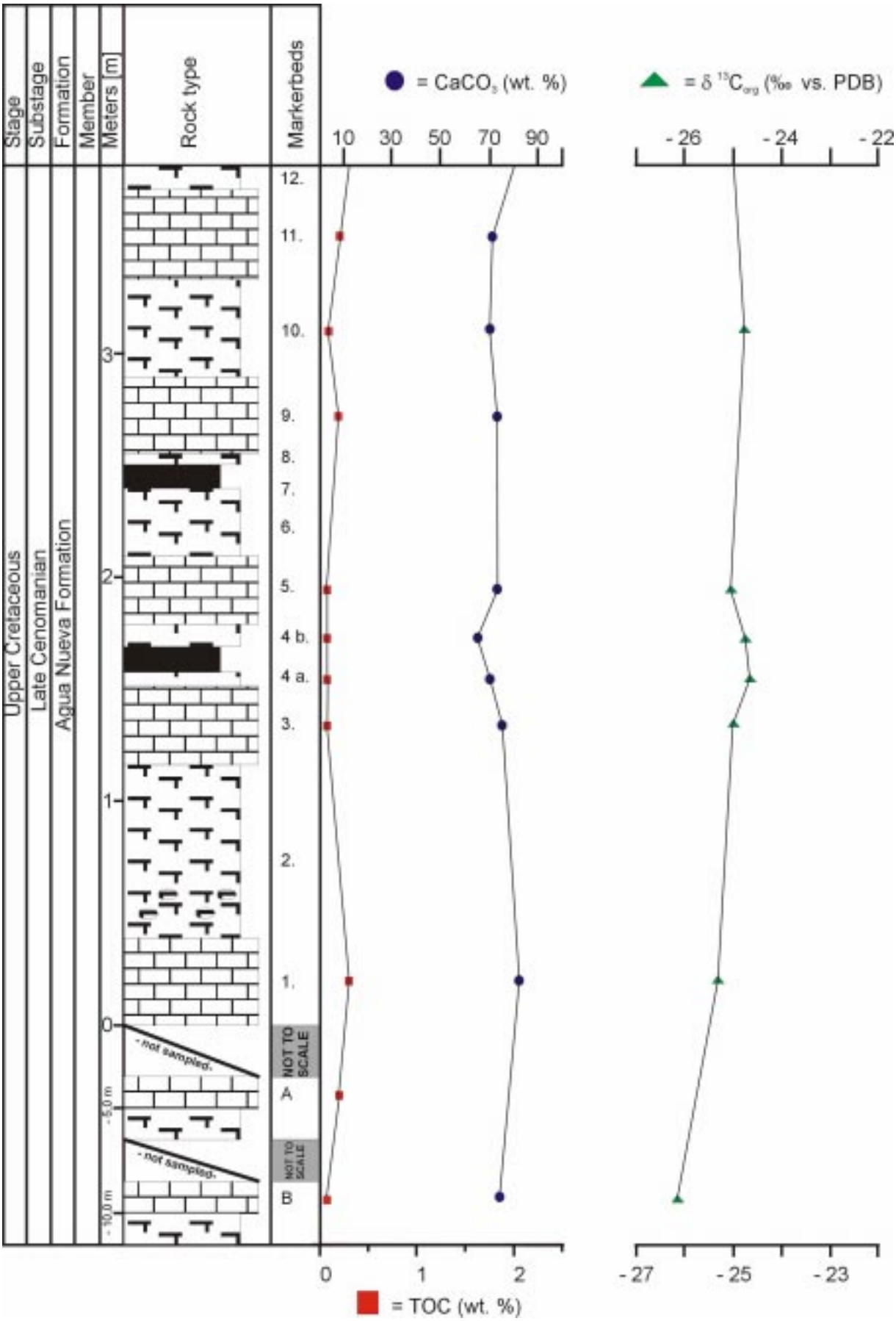

Figure 22: Section MX-I-00; lower part (La Boca Canyon, Nuevo Leon, Mexico).

7.4. Comparison/Correlation of the geochemical results

The following plots (Figure 23, 24, 25) show average data of all three measured geochemical parameters ($CaCO_3$, TOC, $\delta^{13}C_{org}$) which were analyzed for the sections. They have been plotted onto a N-S transect to determine whether latitudinal changes or trends occur.
The geochemical data for TOC and $CaCO_3$ show trends along the N-S transect (see Figure 23 and 24), but only three sections show definite cyclicity. The $\delta^{13}C_{org}$ data (Figure 25) do not show any general N-S trend.
There is a general decline from about 1.4 wt. % TOC at the northern-most location CAN-III-00 to values of ~0.1 wt. % TOC at the Mexican locality. A major exception is section MT-I-00, with a TOC content of ~3.8 wt. %. These high values, well-known for the Cone Member of the Marias River Shale and may explained by large scale watermass mixing and/or local factors. The Marias River Shale is considered to be a good potential source rock for oil (DYMAN, 1987), because of the relatively high hydrogen index values and above average organic carbon values (Clayton et al., 1983).
Distances (km) between the sections are shown below:

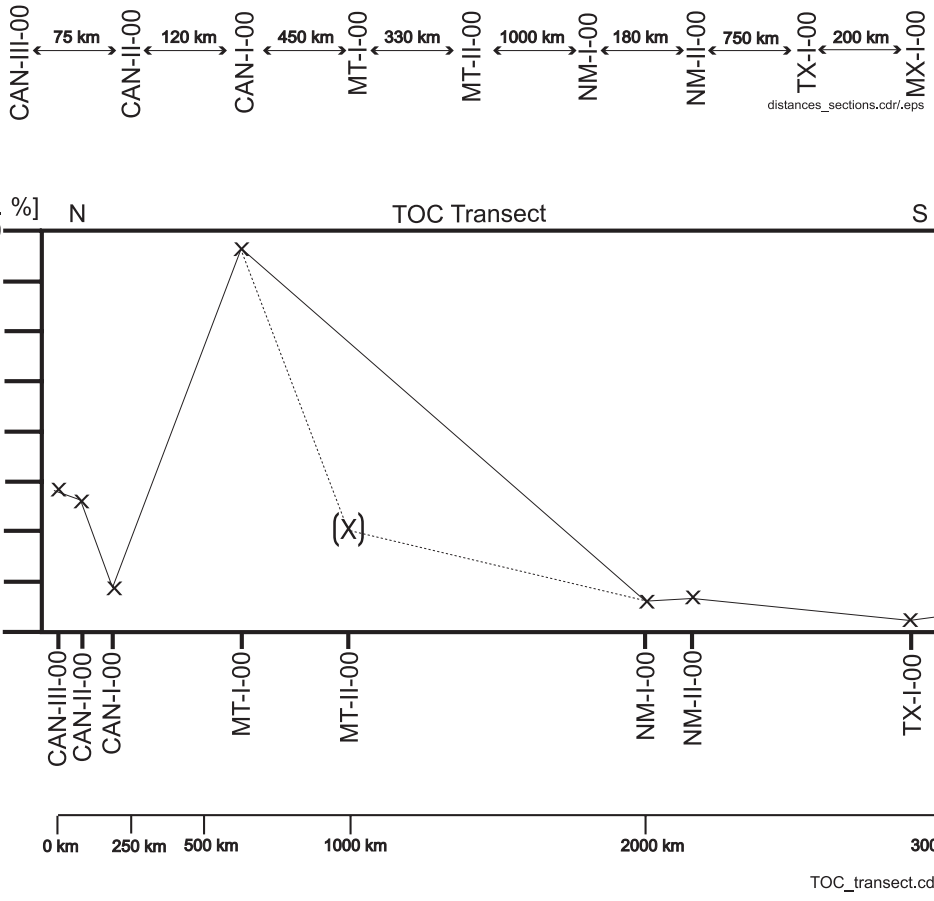

Figure 23: Average TOC data [wt. %] from north to south (to scale).

The $CaCO_3$ content (see Figure 24) rises from north to south, from 20 wt. % (CAN-III-00) to 74 wt. % (MX-I-00). Again there is a notable exception, the highest value is not at the southernmost location as might be expected, but at locality NM-I-00 (Emery Gap in NW-New Mexico).

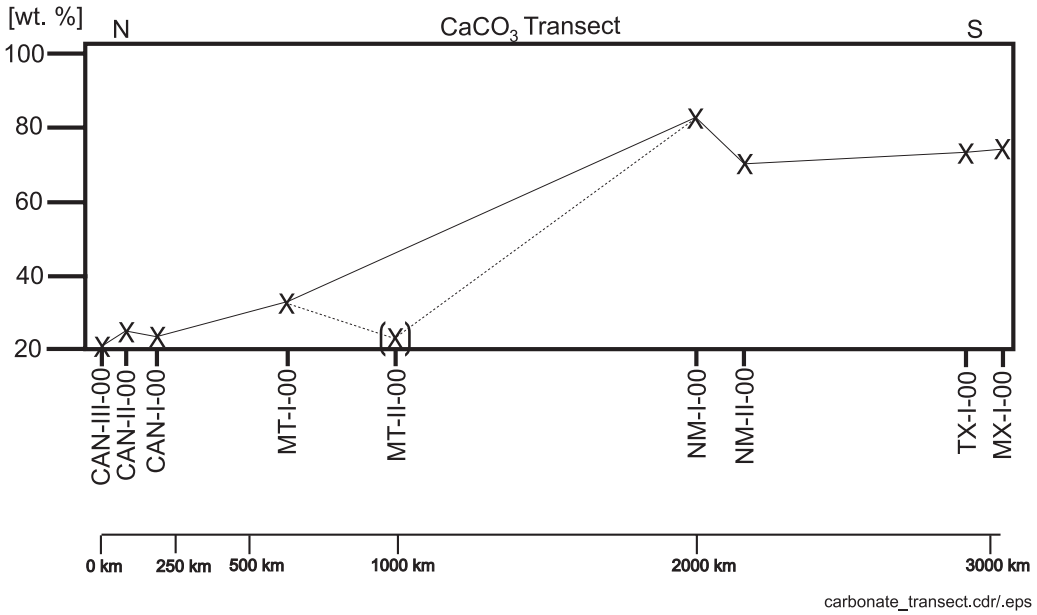

Figure 24: Average $CaCO_3$ data [wt. %] from north to south (to scale).

A general correlation between lithology and geochemistry can only be observed at the New Mexican and Texan sections. Here, $CaCO_3$ and TOC of limestones and shales correlate negatively; the limestones have higher carbonate- and lower TOC content than the shales.
The northern sections (CAN-II-00) do not indicate a cyclic variation of any of the three geochemical proxies close to that produced by Milankovitch parameters, except the carbonate content at section CAN-II-00. The values do vary with large amplitudes. It is possible that information was lost due to the relatively large sampling interval at this sections (3 m). Section CAN-I-00 shows variation of the $CaCO_3$ content with a period of about 122 ka, which is close to the eccentricity signal. The next two sections to the south (MT-I-00; NM-I-00) do all show large variation of one or more geochemical parameters, but these shifts occur highly irregular. This changes at NM-II-00, where a cyclicity of 36 cm for TOC and of 50 cm for $CaCO_3$ can be seen. These cyclic variations occur between 2 and 4 m in the section and give periodicities of 16 ka and 22 ka which indicate that these variations could have been produced by changes of the precessional parameter. Whereas the southernmost location in Northern Mexico does not show any resemblance between Milankovitch-type periodicities and the geochemical data, the Texan section shows a periodicity of ~96 cm for the $CaCO_3$ content, which could have been influenced by changes in obliquity (41 ka cycle).

The geochemical transects also suggest important oceanographic changes. Section MT-I-00 has the highest TOC value of all sections. It could have been located near an oceanic frontal system,

as proposed by FISHER et al. (1994) for the area near the Black Hills area in South Dakota. Another important indicator is the increase of the carbonate content south (~70-80 wt. %) of MT-I-00; north of MT-I-00 the carbonate values are around 20 wt. %.

The Cenomanian oceanic front in the WIS was first described as a classic facies change by BRAMLETTE and RUBY (unpublished data, available at the USGS, Denver, CO), but they did not interpret ist cause. MOORE (1949) pointed out that the continuous bentonites were deposited as a series of ash falls and can therefore be used as stratigraphic datum levels. After the facies change was correlated lithostratigraphically it was clear that the calcareous and the noncalcareous shales were deposited at the same time, but it was still not interpreted. Biofacies analysis (FISHER et al., 1994) of the abrupt facies change in southeastern Montana indicated that these changes record the boundary or oceanic front between two water masses with distinctly different paleoceanographic conditions. One water mass entered the seaway from the Arctic and the other from the Tethys/Proto-Gulf of Mexico. The southern water mass supported calcareous microplankton and calcareous benthic foraminifera as can be seen in carbonate content south of MT-I-00. The lack of calcareous microplankton in the northern seaway is due to ecologic exclusion, probably due to low salinity of the water mass. The high TOC values could be explained by a freshwater lid on the northern seaway which limited oxygenation of the bottom water and therefore enhanced preservation of organic matter. Therefore section MT-I-00 was probably located on the northern side of the oceanic front, mainly influenced by the fresher and cooler northern water mass from the Arctic region.

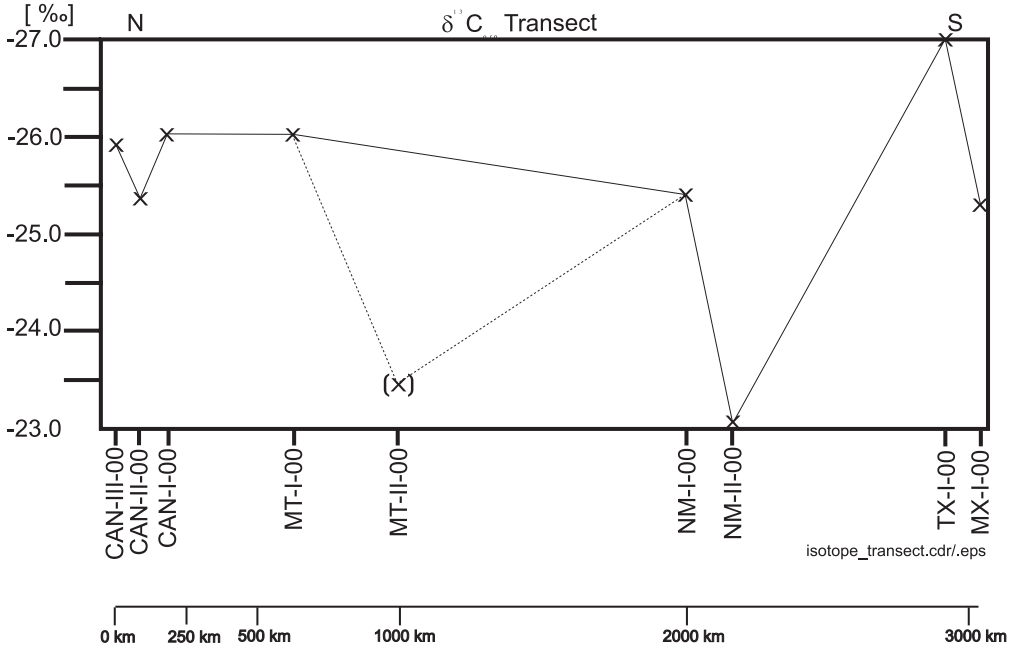

Figure 25: Average $\delta^{13}C_{org}$ data (‰) from north to south (to scale).

The $^{13}C_{org}$ data (see Figure 25) does not reflect a connection between isotopic fractionation and latitude. The average value for all sections is –25.6 +/-1.1 ‰. The independence of latitude and isotopic fractionation is supported by the fact that the sections with the heaviest (NM-II-00; -23.0 ‰) and the lightest (TX-I-00; -27.1 ‰) isotopic values are in sections next to each other, separated by only 750 km. The proximity between the heaviest and the lightest isotopic values reveals an interesting pattern. The paleogeography proposed by ROBINSON ROBERTS and KIRSCHBAUM (1995) in Figure 27 could give an explanation. If the proposed narrow gateway between the Western Interior Seaway and the Tethys is correct, these sections would have been influenced by different water masses. The New Mexican section was under the influence of the water of the seaway, whereas the Texan section would have been influenced by warmer and more saline subtropical waters of the Gulf of Mexico.
As described earlier, the C/T OAE (Oceanic Anoxic Event) is characterized by a large positive global carbon-isotope excursion in both carbonate and organic matter, caused by a major perturbation of the global carbon budget, most probably due to the extensive burial of organic matter in black shales (ARTHUR et al., 1987). The isotopic measurements of this study indicate lack of a positive excursion in the sections. The C/T excursion can only be detected at Burnt Timber Creek, Las Vegas, and Hot Springs but even at these four localities the amplitude of the excursion changes. These inconsistencies are probably due to the sampling of differing time slices. As can be seen in Figure 11, the isotopic excursion begins with a sharp rise towards more positive in the uppermost Cenomanian. In the Turonian values slowly get lighter gain. The isotopic data, together with biostratigraphic data, suggest that the sections at Thistle Creek, Big Horn River, Cone, Landfill, Emery Gap, and La Boca Canyon are already in the early Turonian. Another reason for changes of isotopic signature could be local effects on fractionation, which have been described for the C/T OAE (SCHLANGER et al., 1987).

7.5. Discussion – geochemical analyses

Cyclic variations in $CaCO_3$ and C_{org} (TOC) are commonly interpreted as a reflection of the interplay between terrigenous input, primary productivity, carbonate dissolution, and bottom-water oxygen content. Less directly they reflect weathering and surface runoff from land, upwelling, stratification, and carbon cycling, factors that may be influenced or controlled by climate cycles (EINSELE, 1982; ARTHUR et al., 1984; KAUFFMAN et al., 1991). The causes of cyclic variations are difficult to evaluate without climate modeling, because they are complicated by the fact that local and regional factors also effect sedimentation at a particular site.
The largest unknown in evaluating climate cycles is the sedimentation rate. The time assumed to be represented by cycle spacing is interpreted from assumptions of the sedimentation rate. If all other factors are constant, a high sedimentation rate produces cycles expanded in thickness and

low sedimentation rate produces the reverse. Sedimentary rocks are distorted representations of climate forcing and changes in sedimentation rate may play havoc with the basic assumption of time series analysis In addition, there is natural variability within the precessional and obliquity period (HERBERT, 1994).

Only the location at Thistle Creek reflects cyclical variation of all three geochemical parameters ($CaCO_3$ → 288 ka, TOC → 288 ka, and $\delta^{13}C_{org}$ → 266 ka; if sedimentation rate = 2.25 cm/ka), but here these geochemical cycles do not seem to reflect any relation to the known Milankovitch parameters. The Burnt Timber Creek section indicates a cyclicity of 120 ka in the $CaCO_3$ data. The geochemical cycles of the Canadian locations were probably constantly influenced by terrestrial runoff from western N-America because all of the Canadian sections, but they contain only very small amounts of terrestrial organic matter (MOESLE, 1995). Therefore dilution by detrital input is probably not the decisive factor for the formation of the geochemical cycles. Knowledge of the average sedimentation rate and it's variations within a section is important before the analysis and interpretation of Milankovitch cycles. The literature gives highly variable sedimentation rates for the Bridge Creek Interval ranging from 0.7 cm/ka in Colorado (SAGEMAN et al., 1998) and Nebraska (PRATT and THRELKHELD, 1984) up to 2.5, 2.8, and 1.5 cm/ka in Kansas, Arizona, and Colorado (PRATT and THRELKHELD, 1984). PROKOPH et al. (2001) suggests rates of 1.7 cm/ka for the reference section in Pueblo, Colorado and 3.0 cm/ka for Youngstown, central Alberta, a locality which is close to the Canadian sections studied here. PROKOPH et al. (2001) have shown cycles with wavelengths of ~3.0 and ~5.5 m at the Youngstown section; these are close to the 2.7 m cycle of $CaCO_3$ at Burnt Timber Creek and the 6.0 ($\delta^{13}C_{org}$) and 6.5 m (TOC, $CaCO_3$) cycles at Thistle Creek. These periodicities correspond to cycles of ~90 ka, 200 ka, and 217 ka, if they are calculated with a sedimentation rate of 3.0 cm/ka, the best current estimate based on new $^{40}Ar/^{39}Ar$ data. Therefore the $CaCO_3$ cycle at Burnt Timber Creek might reflect the short eccentricity cycle, whereas cycles at Thistle Creek may represent period doubling of the 100 ka eccentricity cycle.

In the south, assuming a sedimentation rate of 2.25 cm/ka the Las Vegas section shows cyclical variation of 16 ka (TOC data) and of 22 ka ($CaCO_3$ data), whereas the $CaCO_3$ data at the Hot Springs section in Texas has a periodicity of 42 ka. The other sections show variation of the geochemical proxies with time, but these are highly variable and not cyclic.

The general trend of decreasing TOC and increasing $CaCO_3$ from north to south indicates a strong dependence of the geochemical data on latitudinal climate forcing. This could have been caused by several effects: (1.) An overall increase in precipitation and/or lower evaporation in the north, resulting in higher surface runoff rates at high northern latitudes. This would lead to dilution of calcareous sediments by terrigenous material and/or to freshening of the water mass. It would exclude calcareous nannoplankton and therefore limit the formation of limestones.

The $\delta^{13}C_{org}$ signal on the other hand remains fairly constant, except at sections NM-II-00 and TX-I-00, which clearly differ from the mean (-25.55 ‰). The relatively constant values probably reflect the regional/global origin of the signal.
Why is the positive excursion developed more distinctly at some sections? The positive excursion is clearly developed at Burnt Timber Creek (CAN-I-00) and Las Vegas (NM-II-00) but is less distinct at Hot Springs (TX-I-00) and La Boca Canyon (MX-I-00). The other sections are either too young to show the excursion (Thistle Creek and Big Horn River), or the sample intervals were too large to record it (Emery Gap), or the samples were weathered (MT-II-00). Variation of the amplitude of the positive excursion between 2 and 6 ‰ is known for many sections at the C/T boundary worldwide, and is probably related to local factors which enhance or suppress the global signal.

7.6. Discussion – sedimentological and geochemical results

Using sedimentologic, paleontologic, and geochemical evidence, many authors (ARTHUR et al., 1984, 1985; Barron et al., 1985; PRATT et al., 1993) have argued for a combined terrigenous dilution-redox mechanism to explain the development of the Bridge Creek bedding couplets. The conceptual model described below should also apply to the sections in Texas and Mexico, but not to the higher northern latitude U. S. and Canadian sections (Montana and Alberta) where no bedding couplets can be recognized. Increased rainfall in the Sevier highlands to the west (highlands) increased both freshwater input to the seaway and erosion rates. This increased the delivery of fine-grained siliciclastics to the WIS. The increased terrigenous flux diluted the more constant carbonate flux, changing the nature of the accumulating sediment. The increased freshwater flux caused stratification of the water column, leading to lower benthic oxygen levels and increased C_{org} preservation. The result was deposition of laminated, C_{org}-rich shale or marlstone during wet periods. Alternately, drier periods with less fresh water input are characterized by a decreased supply of fine-grained sediment, a better-mixed water column, improved conditions for calcareous phytoplankton production and an increase in benthic oxygen levels resulting in deposition of more pure limestone. The driving force in this model is the modulation of climate by orbital influences to produce variations in precipitation over the land areas draining into the basin.
Other authors have argued that the planktonic microfossil record of the Western Interior basin does not support the interpretation of “freshened” surface waters during deposition of the clay-rich hemicycles. Instead, they proposed that changes in primary productivity in response to cycles of nutrient upwelling could account for the bedding couplets (EICHER and DINER, 1985, 1989). In this alternative conceptual model, orbital forcing led to increased evaporation at low latitudes,

causing the formation of warm, saline bottom waters in the seaway. These in turn displaced nutrient-rich deep waters, forcing them to the surface. Nutrient driven blooms of phytoplankton would occur along the northern margin of the Tethys sea and would have influenced the Western Interior basin through it's southern gateway. WATKINS (1989), however, argued that high productivity characterizes the clay- and C_{org}-rich hemicycles rather than the carbonate-rich phases. WATKINS suggested that the cycles reflect dilution of the carbonate flux by organic matter. ARTHUR and DEAN (1991) and RICKEN (1991, 1994) argued that patterns in bedding cycles may be understood in terms of the mixing of the three primary fluxes (Figure 26), detrital material (siliciclastic deposition), $CaCO_3$, and organic matter, as well as the degree of subsequent modification due to carbonate dissolution, C_{org} oxidation from biogenic activity and other diagenetic factors.

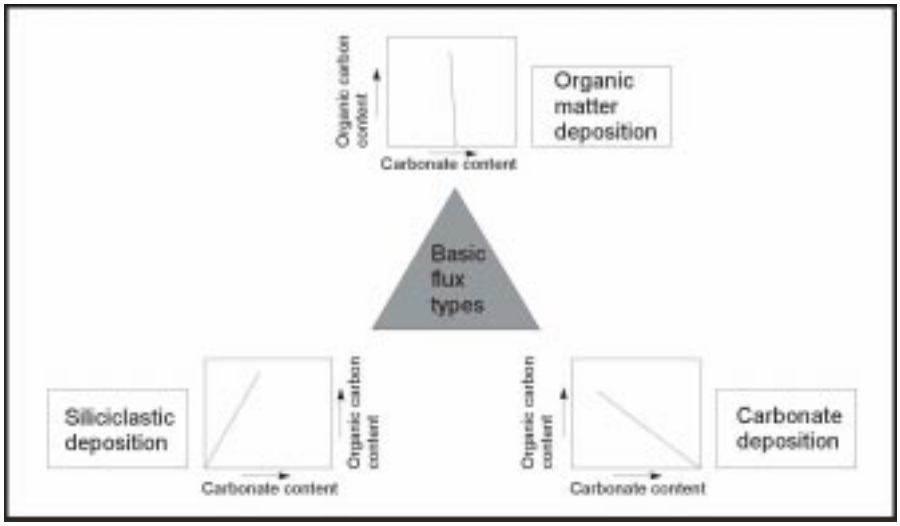

Figure 26: after RICKEN (1993): The "Three-Component-System".

Analyzing elemental, organic, and isotopic geochemical data, ARTHUR and DEAN (1991) concluded that the Bridge Creek bedding couplets were dominantly controlled by dilution of carbonate through orbitally forced changes in the terrigenous detrital flux, but that changes in the productivity of calcareous plankton played an important but secondary role. They also pointed out the need to understand the nature of the different fluxes to the sediment as well as the degree to which they represent dependant or independent variables. For example, the observed correlation between aluminum and C_{org} in the Bridge Creek Member was interpreted as reflecting a link of independent variables by a common forcing factor. They proposed an indirect relation, with higher freshwater input causing both an increase in detrital flux and enhanced water-column stratification leading to better preservation of C_{org}, rather than a direct relationship whereby C_{org} is adsorbed on clays so that a higher detrital flux would lead to enhanced C_{org} burial. SAGEMAN et al. (1998) concluded that the most important unanswered questions concerning Western Interior bedding cycles relate to the nature and origin of linkages:

1a) Is C_{org} production necessarily linked to carbonate production, and 1b) can changes in nannofossil and planktonic foraminiferal assemblages occur independently of changes in the noncalcareous phytoplankton and vice versa?
2) Are changes in C_{org} and carbonate production linked to oceanic nutrient cycles, to nutrient input from fluvial sources, or to a combination of both, and do they respond independently to these forcing factors?
3) Is C_{org} content primarily controlled by organic production, by preservation due to water column stratification and resulting oxygen deficiency, or to a combination of both?
4) Does the influence of orbitally forced changes in climate impart an overall coordination to multiple independent processes, and if so, how is it accomplished?
The bedding couplets of the Bridge Creek Limestone are complex and do not show consistently periodicities like other Cretaceous limestone/marlstone (shale) units (SCHWARZACHER and FISCHER, 1982). Nor do they show the uniform bedding characteristics of couplets interpreted as resulting from obliquity cycles (FISCHER et al., 1985) known from the sections in southern Texas and northern Mexico.
As pointed out by RICKEN (1994), LaFERRIERE et al. (1987), ARTHUR and DEAN (1991, and ELDER et al. (1994), the development of bedding cycles in Cretaceous rocks of the Western Interior basin reflects a highly sensitive depositional system. This system was influenced by minor changes in relative sea level and climate that periodically modulated the fluxes of organic matter, carbonate, and detrital material to the basin.
The sedimentology and sedimentary geochemistry across the sea level highstand interval at the C/T boundary suggest that the complex pattern of sedimentation in the central (New Mexico) and southern parts (Texas and Mexico) of the seaway, reflects constructive and destructive interference of different orbital cycles; precession, obliquity, and eccentricity. Specific cycles influenced different parts of the depositional system (SAGEMAN et al., 1997). With it's meridional configuration, the seaway spanned multiple climate zones, and was thus subject to changing latitudinal variations in climate forcing. This can clearly be seen in the different lithologies of the northern (marl/shale dominated) and southern parts (limestone/calcareous) of the seaway.

Causes of cyclic sedimentation:
In exploring the cause of the cyclic sedimentation observed in Cretaceous strata it is important to separate observation and interpretation. What cycles do we know from observation of the physical sediment record? How are they interpreted? What are they called? The list of types of cycles and their possible causes is very long, but some answers are presented below (Table 1).

1) -Carbonate/ clay cycles:

a) due to dilution of a constant flux of carbonate by variable flux of clay
("terrigeneous dilution cycles")

b) due to dilution of a constant flux of clay by a variable flux of carbonate

x) variable flux of carbonate due to changes in production rate

("carbonate productivity cycles")

y) variable flux of carbonate due to changes in dissolution rate

2) -Cyclic variations in C_{org} content:

a) due to dilution of a constant flux of C_{org} by variable flux of clay

b) due to dilution of a constant flux of clay by a variable flux of C_{org}

x) variable flux of C_{org} due to varying productivity of organic matter

("organic productivity cycles")

y) variable flux of C_{org} due to varying oxidation in water column

("redox cycles")

i) reflecting salinity stratification

ii) reflecting intensification of the oxygen minimum

3) -Clastic cycles (changes in grain size or mineral content)

a) due to changes in clastic sediment flux resulting from changes in

x) weathering

y) runoff

4) -Chert cycles (layer of chert nodules or beds of chert)

a) due to changes in supply of dissolved silica resulting from changes in weathering

b) due to changes in productivity of siliceous organisms

c) due to changes in ocean chemistry

5) -Light/dark cycles (changes in the "lightness" of the sediments

a) due to changes in carbonate content

b) due to changes in C_{org} content

6) -Flucuations in abundance of planktonic foraminifer and/or calcareous nannofossils

a) due to changes in productivity of one or both groups

("productivity/fertility cycles")

b) due to dissolution

("dissolution cycles")

7) -scour cycles (erosion surfaces)

a) due to fluctuations in the energy of bottom currents

Table 1: Cycles and their possible causes

One possible explanation for the shift from precessionally influenced sedimentation (New Mexico) to obliquity controlled sedimentation (Texas and Mexico) could lie in the paleogeographic configuration of ROBINSON ROBERTS and KIRSCHBAUM (1995) (see Figure 27). Their paleogeographic maps represent a distillation of many scientific papers since the turn of the last century.

They propose that a narrow gateway, located in southern New Mexico, separated the central part of the seaway from its southern segment (Texan and Mexican sections). This passage, which was about 200 km wide, restricted exchange between the Western Interior Seaway and Tethyan water masses. Obviously, these two water masses and their sedimentation systems were influenced by different Milankovitch forcing, but why they responded to different orbital forcings has not been clear.

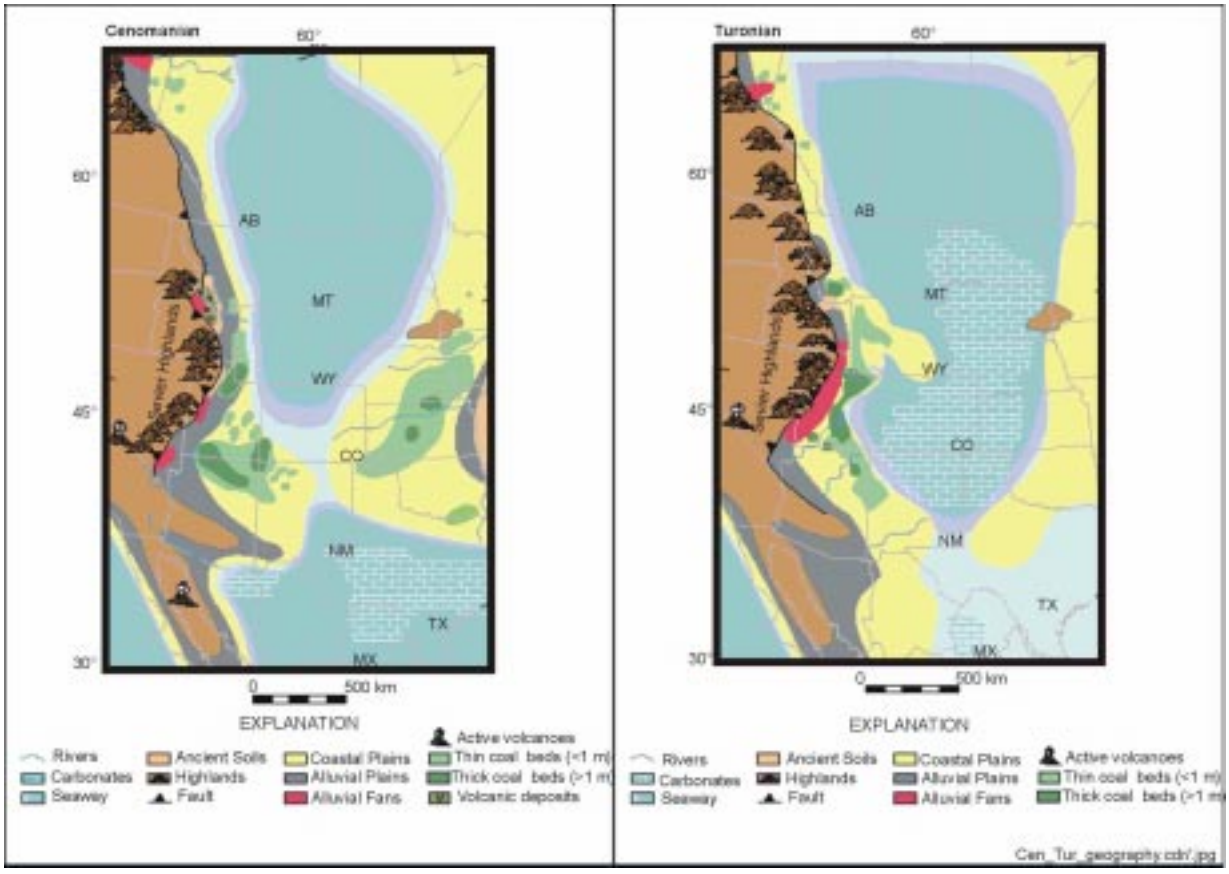

Figure 27: Regional paleogeography during the Cenomanian and the Turonian (peak transgression), including approximate position of the shorelines of the Western Interior Seaway (After ROBINSON ROBERTS and KIRSCHBAUM, 1995).

Possible mechanisms influencing the sensitivity of the sedimentary system to Milankovitch cycles could be:

1) - the volume of the water mass.
2) - physical (temperature) and chemical (salinity, oxygenation) properties of the water mass.
3) - meridional or latitudinal extent of the water mass.
4) - latitudinal position of the site of deposition.
5) - the size of the drainage basin.
6) - vegetation of the drainage basin.

7) - distance to paleo shoreline.
8) – relation between freshwater inflow and volume.

As mentioned earlier, the primary physical impacts of Milankovitch orbital changes on the Earth are insolation changes at the top of the atmosphere. These can be calculated and quantified in detail, but how these insolation changes are then translated into changes of the climate system and what kinds of positive or negative feedback mechanisms they initiate, is not well understood. Nor has it been clear precisely, how the climatic changes influence the sedimentary system.

8. Conclusions - Milankovitch controlled sedimentation

The sedimentation in the WIS was strongly influenced by variations in insolation due to variations of all three Milankovitch cycles; precession, obliquity, and eccentricity (100 and 400 ka). Another important parameter controlling sedimentation was the regional and local paleogeography. There is no general correlation between the geochemical and changing orbital parameters. Clear relations can be observed at four localities (CAN-III-00, CAN-I-00, NM-II-00, TX-I-00), although not in every geochemical proxy. Cyclicity of $CaCO_3$ can be seen at all four sections.

The general shift from non- or low calcareous sediments in the Alberta and Montana sections to highly calcareous sediments in New Mexico, Texas, and northern Mexico was primarily controlled by oceanographic and climatic factors.

The oceanic frontal system proposed by FISHER et al. (1994) to exist in the Black Hills region separated two distinctly different water masses. The northern water mass, coming from the Arctic (see Figure 28) had a low salinity (<33 ‰; FISHER et al., 1994) and a temperature of ~7-10°C (see Figures 30 and 31), which excluded calcareous microorganisms. The southern water with salinities in the range of 33-38 ‰ and temperatures between 18°-28°C (see Figures 30 and 31) supported an abundance of calcareous microplankton and calcareous benthic foraminifera. During the bridge Creek Interval the influence of water masses entering the WIS from the subtropical Tethys may have been less than previously thought, because the relatively narrow gateway (see Figure 27) restricted exchange between the central and southern parts of the Western Interior Seaway. The higher TOC values in the northern sections of the seaway could be explained by a consistent freshwater lid on the northern part of the seaway which limited oxygenation of the bottom water and therefore enhanced preservation of organic matter. This possibility seems reasonable if paleogeographic (Figure 28) and model calculations are taken into account (see chapter 9.4.2.)

If lithological and geochemical analyses of samples from the measured sections are taken into account, it appears that the Canadian sections (CAN-I-00 and CAN-III-00) are controlled by longer cycles (~266-288 ka and ~122 ka) than the southern sections in New Mexico (NM-I-00 → 27 ka and NM-II-00 → 16-22 ka), Texas (TX-I-00 → 42-44 ka), and Mexico (MX-I-00 → 40 ka). The Canadian sections do not form bedding couplets, but geochemical cycles can be recognized. A 2.7 m (~90 ka) cycle of $CaCO_3$ was measured at Burnt Timber Creek. Geochemical cycles of 6.0 m ($\delta^{13}C_{org}$→~200 ka) and 6.5 m (TOC, $CaCO_3$→~217 ka) were measured at Thistle Creek. The Canadian sections were calculated with a sedimentation rate of 3.0 cm/ka (PROKOPH et al., 2001). Therefore the $CaCO_3$ cycle at Burnt Timber Creek might reflect the short eccentricity cycle, whereas cycles at Thistle Creek may represent period doubling of the 100 ka eccentricity cycle.

In conclusion, the influence of different orbital parameters seems to control sedimentation at different parts of the WIS. A latitudinal dependence of the cycles from Milankovitch forcing does occur.

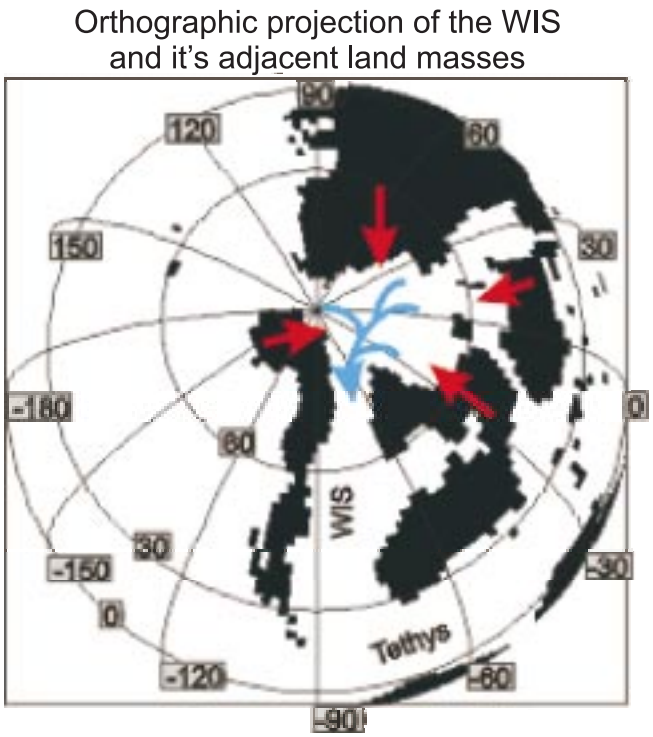

Figure 28: The WIS and it's adjacent land masses showing the important influence of the northern ocean as a source of low salinity water flowing into the seaway (red=runoff from continents; blue=water entering the northern WIS).

In order to solve the question which and above all, how Milankovitch cycles affected sedimentation more accurate information on sedimentation rates must be obtained. One way to explore the sensitivity of the sedimentary system to Milankovitch forcing is to determine or rule out possible mechanisms (Precipitation, wind, upwelling, runoff...) which could have produced cyclic sedimentation. Here, the use of GCM models can deliver crucial information, because parameters can be quantified to a certain degree, or even ruled out.

9. GCM-modeling

Climate models test the sensitivity of climate system to “external forcing”, such as variations in the solar insolation, and to changes in boundary conditions intrinsic to the Earth’s surface and atmosphere. However, climate is the result of complex interactions between the atmosphere, hydrosphere, cryosphere, biosphere, and the solid earth. These elements interact in complex ways, with each operating on a different time scale. The ultimate goal of Earth system models is to include all the components of the climate system, with each part interacting with the others in realistic ways. Earth system models have not yet fully achieved this level of sophistication, but their evolution toward more detailed treatment of climate processes and the inclusion of more subsystems result in increasingly accurate simulations that allow for the examination of the interactions between individual climate system components.
Several paleoclimate modeling studies have explored linkages between orbitally forced insolation variation and climate responses. PRELL and KUTZBACH (1992) have investigated the sensitivity of the Indian monsoon to orbital forcing parameters and implications for its evolution during the Late Cretaceous. CROWLEY et al. (1992, 1993) conducted a GCM study of Carboniferous interglacial climates. PARK and OGLESBY (1990, 1991) conducted GCM studies on the effect of orbital cycles on Late and Middle Cretaceous climate. VALDES et al. (1994) modeled Jurassic Milankovitch climate variations.

9.1. The GENESIS Climate System Model

GENESIS (Global Environmental Ecological Simulation of Interactive Systems) is a numerical climate system model designed specifically for paleoclimate research (POLLARD and THOMPSON, 1995, 1998; THOMPSON and POLLARD, 1995, 1997). GENESIS uses an Atmospheric General Circulation Model (AGCM) as its core component, coupled to a 50 m mixed bed slab ocean model and multilayer models of soil, snow and sea ice.
The GENESIS AGCM component is a heavily modified version of the NCAR Community Climate Model (CCM1) described by WILLIAMSON et al. (1987). Modifications and additions to CCM1 include diurnal cycle with solar radiation calculations performed every 1.5 model hours. It incorporates the solar radiation scheme of THOMPSON et al. (1987) performing delta-Eddington calculations for all atmospheric layers. The solar radiation calculations include multilayer, randomly overlapping clouds. The radiative effects of trace gasses (CO_2, CH_4, N_2O, and CFC´s) are treated explicitly, and the radiative effects of tropospheric aerosols can be included. Water vapor is advected in grid space by a semi-Lagrangian transport, as described in WILLIAMSON and RAUSCH (1989), RAUSCH and WILLIAMSON (1990), and WILLIAMSON (1990). Atmospheric

convection and planetary boundary layer mixing is simulated using an explicit subgrid scale plume model (ANTHES, 1977). The cloud parameterization is similar to that of SLINGO and SLINGO (1991), and uses stratus, anvil cirrus, and convective clouds. Atmospheric dynamics in GENESIS Version 2.0 include a gravity-wave drag parameterization (McFARLANE, 1987) and dynamic Courant spectral truncation in the upper stratosphere. The AGCM uses a gaussian, almost equispaced, latitude grid (WASHINGTON and PARKINSON, 1986). The AGCM resolutions for Version 2.0 are a spectral horizontal T31 grid (~3.75° latitude and longitude) and 18 vertical levels. The resolution of Version 1.02, which had been used previously for Triassic simulations by WILSON et al. (1994), HAY et al. (1994), HAY and WOLD (1998), was R15 (~4.75° latitude and longitude) with 12 vertical levels. Three of the 6 additional levels in Version 2.0 are in the planetary boundary layer. The gaussian AGCM grid is independent of the equispaced surface grid, with fields transferred between them by bilinear interpolation (AGCM to surface) or straightforward area averaging (surface to AGCM) at each time step. The equispaced surface grid, used by the Land Surface Transfer Scheme, and the soil, snow, sea-ice, and ocean models, has a resolution of 2° x 2°.

The Land Surface Transfer Scheme (LSX) serves as the interface between the atmosphere and the land surface including vegetation; it is based on the earlier models of BATS (Biosphere-Atmosphere Transfer Scheme; DICKINSON et al., 1986) and SiB (Simple Biosphere Model; SELLERS et al., 1986). LSX computes the exchanges of momentum, thermal energy, and water mass between the atmosphere and the land surface, accounting for the physical effects of vegetation, soil texture, and snow cover. Two vegetation layers or canopies, such as “trees” and “grass” can be specified at each grid point. LSX calculates the radiative and turbulent fluxes through these layers to the soil or snow surface. Rain or snow is intercepted by the vegetation and eventually drips or blows off. Given the conditions calculated by the AGCM above the upper canopy and the soil or snow conditions at the surface, LSX predicts vegetation temperatures, canopy air temperatures, and specific humidities. Prognostic fields are then passed back to the AGCM, allowing interaction between the surface and the atmosphere. The characteristics of the two vegetation layers--canopy heights, leaf area index, fractional cover, leaf albedo, and leaf orientation—are defined by the vegetation type specified at each point on the surface grid. GENESIS includes a six-layer soil model extending to a depth of 4.25 m Heat is diffused linearly and moisture non-linearly according to soil texture (CLAPP et al., 1986). Soil moisture is removed from rooted soil layers, according to transpiration rate. Ice within the soil is predicted, and the latent heat of fusion and amounts of ice and liquid water are accounted for explicitly. Surface runoff and subsurface gravitational drainage into the ground-water system are allowed to occur if precipitation minus evaporation exceeds the infiltration rate. Combined runoff and drainage is globally integrated and transferred uniformly to the ocean at each time step. Stochastic precipitation is supplied by single point LSX values instead of AGCM grid averages. Ponding of water at the

surface is allowed at grid points where the precipitation rate exceeds infiltration. The soil model also includes an explicit litter layer, non-local downward transport through near-surface microscopic channels, and hydrostatic pressure in saturated soil columns.
GENESIS Version 2.0 uses a three-layer model for snow cover on soil, ice sheet, and sea-ice surfaces. The vertical snow column is modeled by a standard finite-difference technique. Total snow thickness and fractional snow cover change according to melting and accumulation rates on the uppermost layer. Snow moisture content, percolation, and refreezing are modeled after LOTH et al. (1993).
A six-layer thermodynamic sea-ice model predicts the local melting and freezing of ice using standard finite difference techniques (SEMTNER, 1976). Heat is diffused linearly through the ice, with changes in total thickness controlled by melting or freezing of the top and bottom layers.
For surface climate simulations, the ocean is represented by a 50-m thermodynamic slab. The slab ocean captures the seasonal thermal capacity of the ocean's mixed layer. Poleward oceanic heat flux is defined as a linear diffusion down the local temperature based on present-day observations (COVEY and THOMPSON, 1989) and the zonal fraction of land and sea at a given latitude. A multiplicative of the diffusion coefficient can be prescribed.
The GENESIS prototype ocean model is driven by the surface climate simulated by the model system components listed above. The prototype oceanic general circulation model (OGCM) is a version of the SEMTNER and CHERVIN (1992) rigid lid, hydrostatic, Boussinesq primitive equation code modified by Esther Brady at NCAR to accelerate the deep levels to equilibrium following the method suggested by BRADY (1984). The ocean model has a horizontal resolution of 2° latitude by 2° longitude, and 20 vertical levels. It is capable of representing the major current systems, but not mesoscale eddies. Except for the deep acceleration and lower resolution, this model is the same as that used by WASHINGTON and MEEHL (1996) in coupled model transient CO_2 experiments.

9.2. Boundary conditions

Greenhouse gases and solar constant:
Boundary conditions for this study represent Cenomanian/Turonian forcing factors and paleogeographic conditions. For the climate simulations a solar constant of 98.62 % (1337.0 W/m^2) of the present value of 1365.0 W/m^2 was used. It is based on estimates of solar luminosity calculated from a standard model of solar evolution (GOUGH, 1981). Heat transport in the slab ocean model was prescribed with values similar to those of today.
Atmospheric CO_2 was specified as 1881.6 ppm which is 6x the preindustrial level of 313.6 ppm and about 5x the present value of 365 ppm. This value is within the range of estimated values of 1.5 and 9 times present for the Late Cretaceous (DeCONTO, 2000). BERNER (1994, GEOCARB

II) estimated the CO_2-values to be between 1.5 and 5 times present, based on a long-term geochemical carbon cycle model. CERLING (1991) calculated a Barremian to mid-Albian (Early Cretaceous) atmospheric CO_2 of 1500-3000 ppm, or about 4.4-9 times present, from the carbon isotopic composition of soil carbonate in paleosols. ANDREWS et al. (1995) applied Cerling's method to Maastrichtian paleosols from India, resulting in an estimate of 1300 (+/- 500) ppm. Concentrations of atmospheric CH_4 and N_2O were set at preindustrial levels, 0.800 ppm and 0.288 ppm, respectively.

Ocean salinity:
The ocean salinity can not be specified in a slab ocean model.

Vegetation type:
The vegetation type used for this model is "Type 6" (broadleaf trees with groundcover→ savanna) after DORMAN and SELLERS (1989).

Paleogeography:
The paleogeographic boundary conditions (land-sea distribution) were provided by the global paleogeographic reconstruction from BALUKHOVSKY and MIGDISOV (unpublished), mentioned in chapter 2.2.. The paleogeography, terrestrial elevations, and vegetation were interpolated to 2° x 2° resolution.

The model was allowed to spin up for 25 years during all five runs. The mean annual, seasonal, and monthly results were then calculated for years 15 through 25.

9.3. Model simulations

Five experiments (1 control run + 4 orbital runs) were carried out for this study. All the previous simulations which have been completed so far by other authors have changed all three orbital parameters (eccentricity, obliquity, and precession) to explore the effect of differences between total maximum and minimum forcings ("hot summer orbit/cold summer orbit approach"; CROWLEY et al., 1993; SLOAN and MORRILL, 1998).
For this study only the precessional parameter was changed for each run. In addition to the extremes used by CROWLEY et al. (1993), this study examines the influence of precessional changes through intermediate setups (orbital case A and C). Eccentricity was fixed during all orbital runs at a value of 0.05. This value was chosen because it is very close to the maximum of 0.07 and allows for maximum seasonality. Obliquity was fixed at the present value of 23.5°. All parameters were defined within a range of orbital values given by BERGER (1978).

Assuming that obliquity (ε) and eccentricity (e) remain constant over one precessional cycle, the northern hemisphere seasonal contrast is maximal when the summer solstice occurs at perihelion and minimal when it occurs at aphelion. The opposite is true for the southern hemisphere (BERGER and LOUTRE, 1994)

NOTE:
- DJF (Dec., Jan., Feb.→NH winter) and JJA (Jun., Jul., Aug.→NH summer).
- The celestial equator is the projection of the Earth's equator onto the sky.

Control run:
In order to eliminate on precessional effects the control run used an eccentricity of 0.00. This results in an circular orbit of the earth around the sun, so that seasonal precession has no climatological effect (precess. = ecc. * sin ϖ). In GENESIS, precession (PRECU) is defined as the prograde angle from perihelion to the vernal equinox. It differs from some other definitions by multiples of 90°.

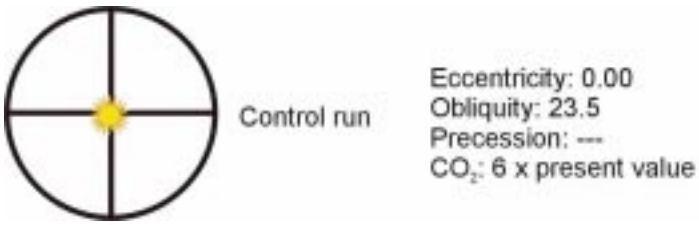

Figure 29: Parameters for control run.

Precession orbit case A:
For orbital case A, PRECU has a value of 0/360, meaning that the northern hemisphere vernal equinox (the date, near March 21, when night and day are the same length and the Sun crosses the celestial equator moving northward into the northern hemisphere) happens to be at perihelion and the northern fall equinox (the date, near September 22, when night and day are nearly of the same length and Sun crosses the celestial equator moving southward into the southern hemisphere) is at aphelion. This setup produces a intermediate forcing for the winter and summer months.

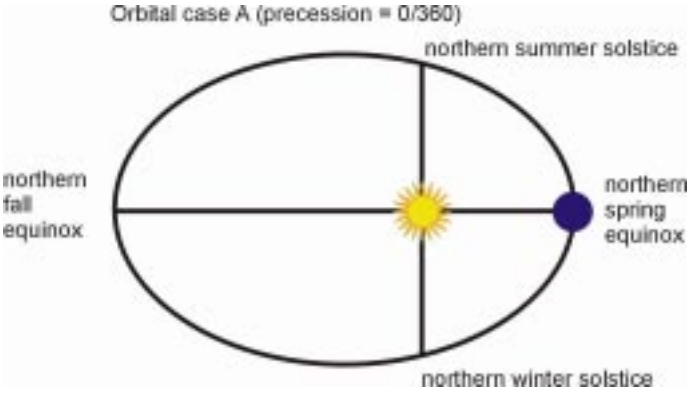

Figure 30: Setup of Orbital case A.

Precession orbit case B:
For orbital case B, PRECU was defined as 90. This puts the northern hemisphere winter solstice (longest night of the year) at perihelion and the northern hemisphere summer solstice (longest day of the year) at aphelion and therefore produces warmer than average winters and colder than average summers in the northern hemisphere. Opposite conditions, colder than average winters and warmer than average summers occur in the southern hemisphere.

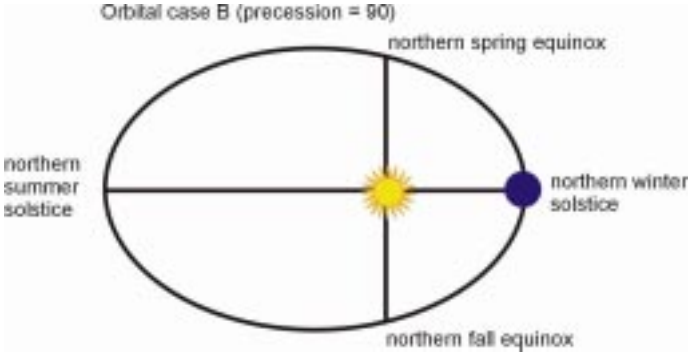

Figure 31: Setup of Orbital case B.

Precession orbit case C:
For orbital case C the precessional parameter was set as PRECU=180. This puts the northern hemisphere fall equinox at perihelion and the northern spring equinox at aphelion.

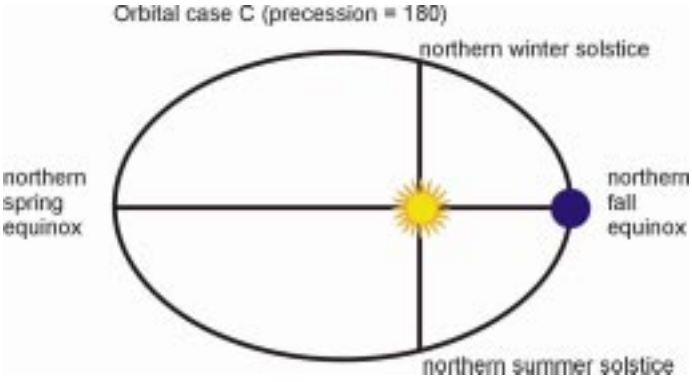

Figure 32: Setup of Orbital case C.

Precession orbit case D:
Orbital case D was run with PRECU= 270. Thereby the northern summer solstice coincides with perihelion and the northern winter solstice with aphelion which makes the summer warmer and the winter colder than average. In the southern hemisphere the summer is cooler and the winter is warmer than average.

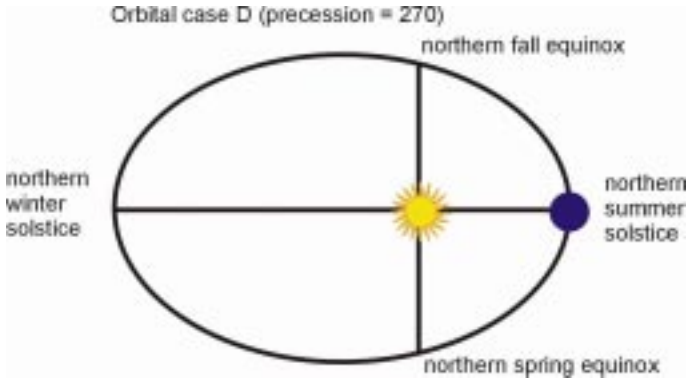

Figure 33: Setup of Orbital case D.

9.3.1. Model results: Control run

Temperature:
For the control run GENESIS predicts a global MAT (Mean Annual Temperature) of 20.66°C for model years 15 through 25, almost 6°C higher than the present day MAT of 15°C. Average temperatures around the north pole are slightly below freezing during the coldest months of the northern hemisphere winter (DJF = Dec., Jan., Feb.) (Figure 34). These temperatures correspond very well with those indicated by high-latitude floras (HERMANN and SPICER, 1996, 1997). During the austral winter (northern hemisphere summer) temperatures over Antarctica cool to an average of -12°C. The warmest temperatures occur between 30° north and south over the large continental interiors of Asia, Africa, and South America. During their hemispheric summers (Figure 34 and 35), temperatures in these regions reach more than 35°C. Over the ocean, the temperature is generally

equal to that of the sea surface, so that tropical sea surface temperatures during NH winter were as high as 32°C (present day: 28°C- max. 30°C). The highest temperatures were reached off the eastern coast of S-America and Africa.

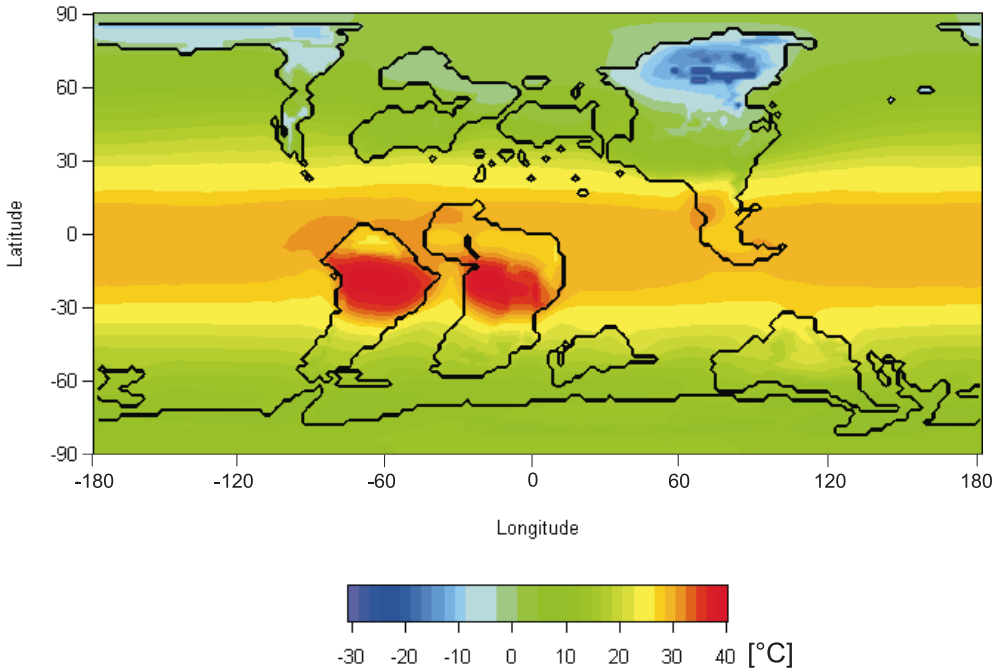

Figure 34: Temperature for Dec., Jan., Feb.; [°C].

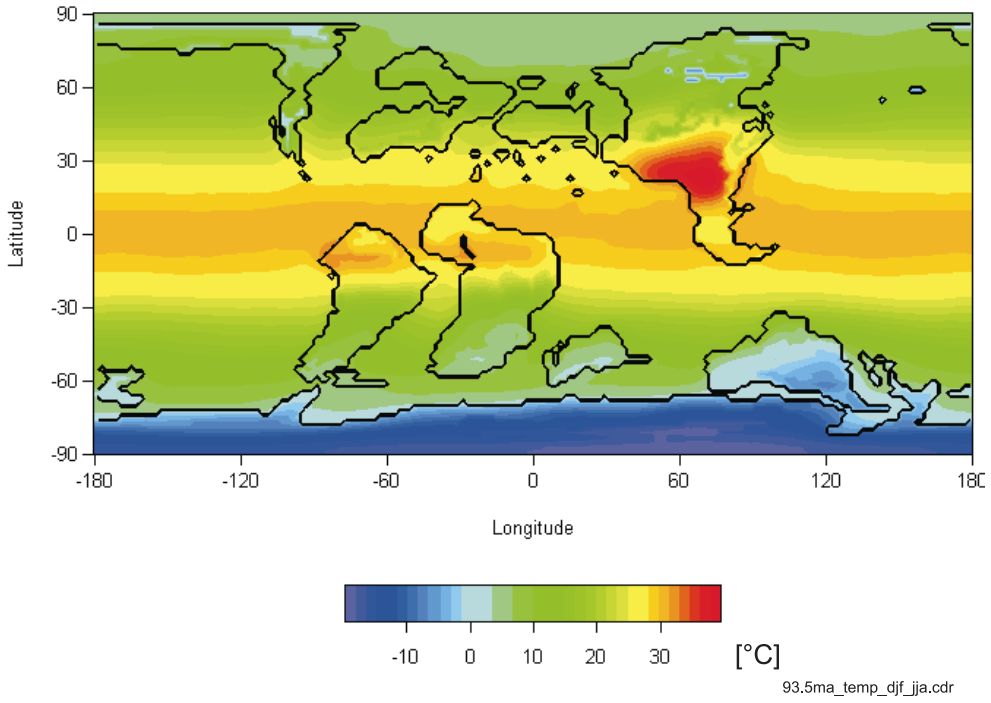

Figure 35: Temperature for Jun., Jul., Aug.; [°C].

Precipitation:

The precipitation pattern for this run shows relatively low precipitation for the regions north and south of 75° during northern hemisphere (NH) winter (Figure 36) and NH summer (Figure 37). Precipitation in these regions does not exceed 2 mm/day. The larger continental interiors of Asia, Africa, and South America are also zones of low precipitation with values of about 0-1 mm/day. They lie in desert latitudes. Highest precipitation occurs along the equator (up to 12 mm/day) and between 15° north and south, with values ranging from 4-7 mm/day. Another important feature is the establishment of zones of high precipitation between 30° and 60° north and south during their hemispheric winters. These zones weaken during their hemispheric summers. An explanation will be given in the “Atmospheric pressure systems” section below.

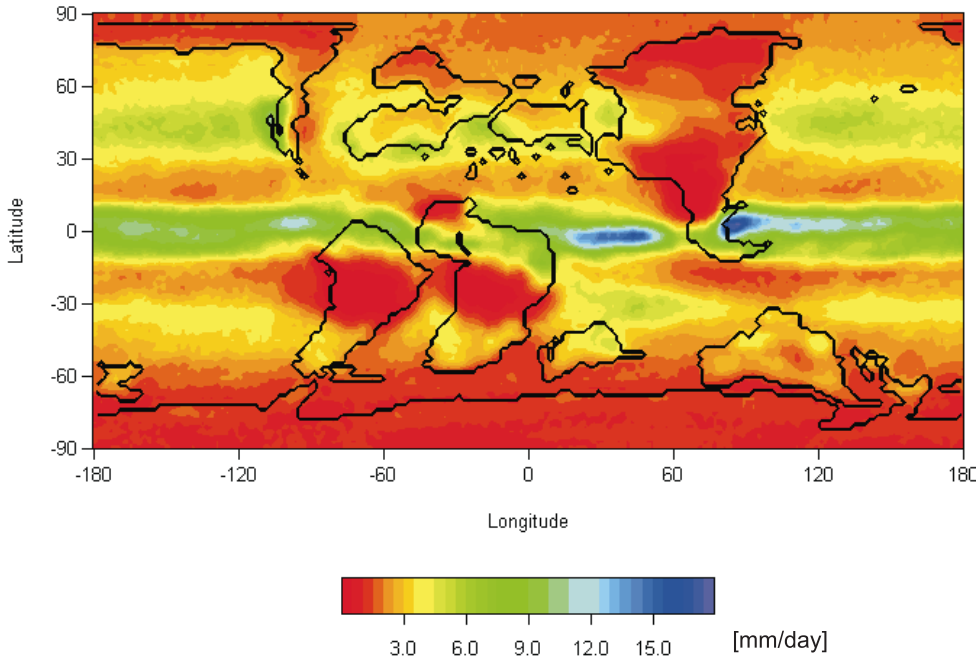

Figure 36: Precipitation for Dec., Jan., Feb.; [mm/day].

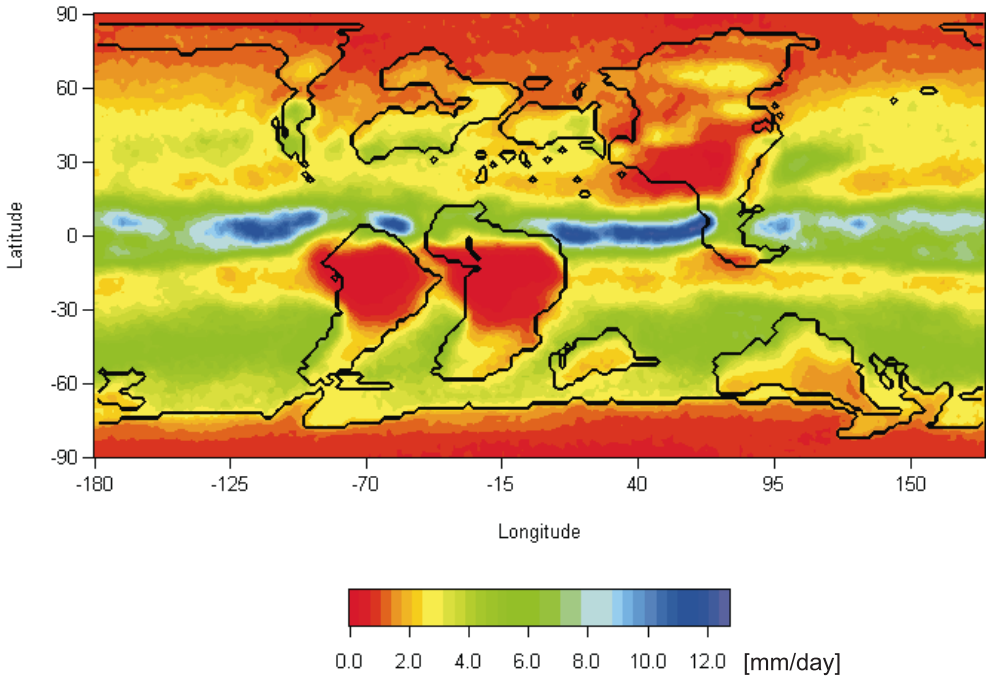

Figure 37: Precipitation for Jun., Jul., Aug.; [mm/day].

Atmospheric pressure system:

The air pressure systems for the Late Cenomanian-Early Turonian are strikingly different from those of today, shown in Figure 38 and 39, with polar lows (990-1005 hPa) during the hemispheric winters and relatively low pressure (1009-1016 hPa) during the summers. In the Arctic a very low pressure system forms during NH winter. Strong latitudinal high pressure zones develop around 30° north during boreal winter and 30° south during austral winter. Air Pressure in these zones is usually above 1020 hPa.

For better comparison, the present day pressure system is shown in Figure 40.

Wind systems:

The simulated wind systems shown in Figure 38 and 39 are also different from those of today, too. Due to the absence of polar highs during the winter, strong westerly wind belts develop between 50° and the high pressure zones at 30°. Changes for the southern hemisphere are similar;.

Another important difference lies in the strong trade winds, which developed during each hemispheric winter.

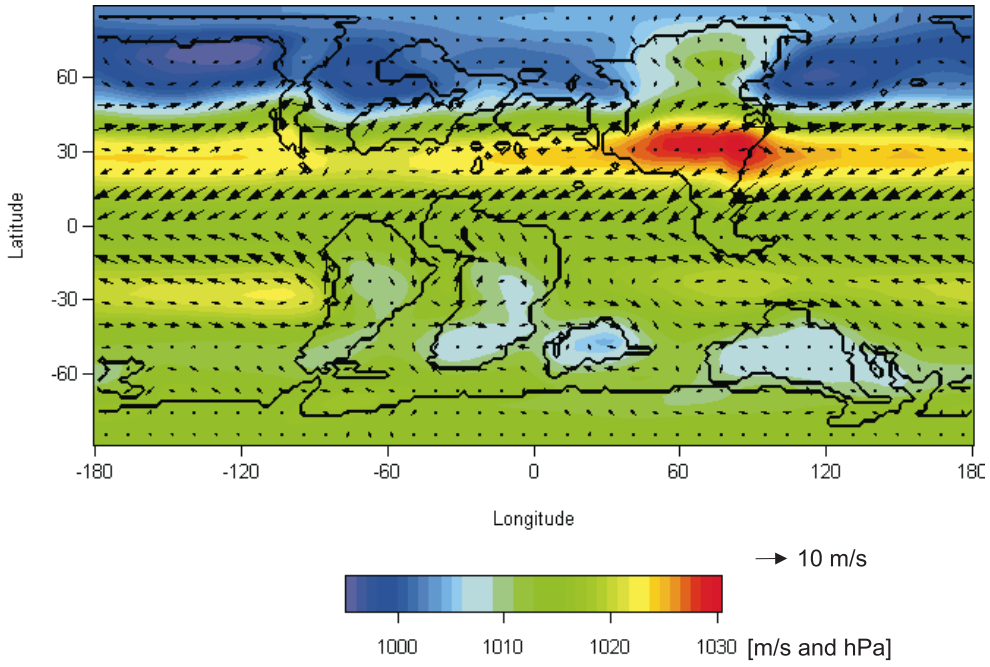

Figure 38: Wind speed and pressure at sea-level for Dec., Jan., Feb.; [m/s and hPa].

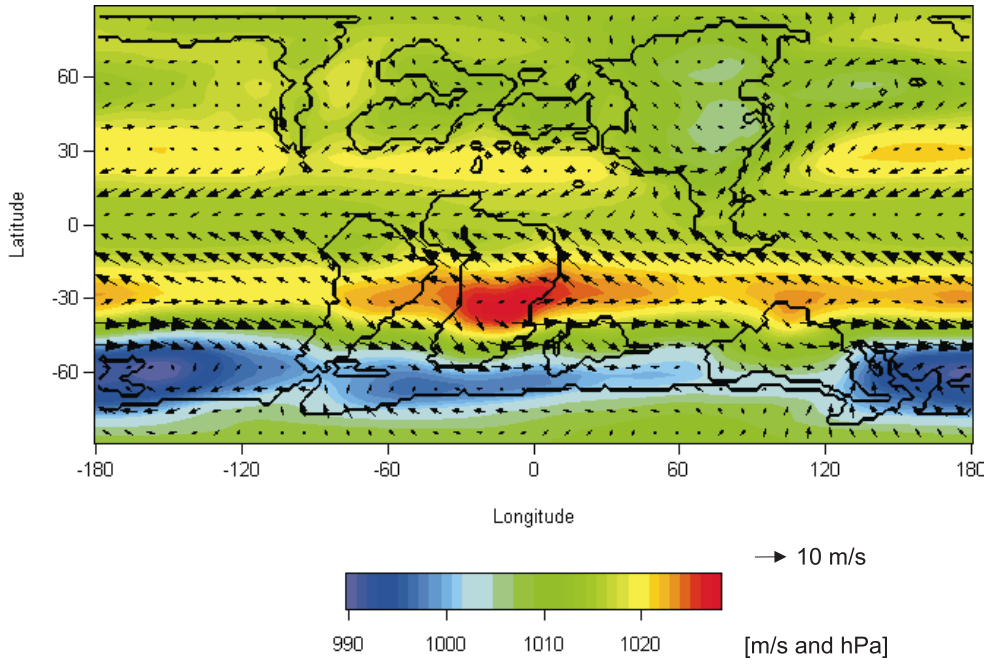

Figure 39: Wind speed and pressure at sea-level for Jun., Jul., Aug.; [m/s and hPa].

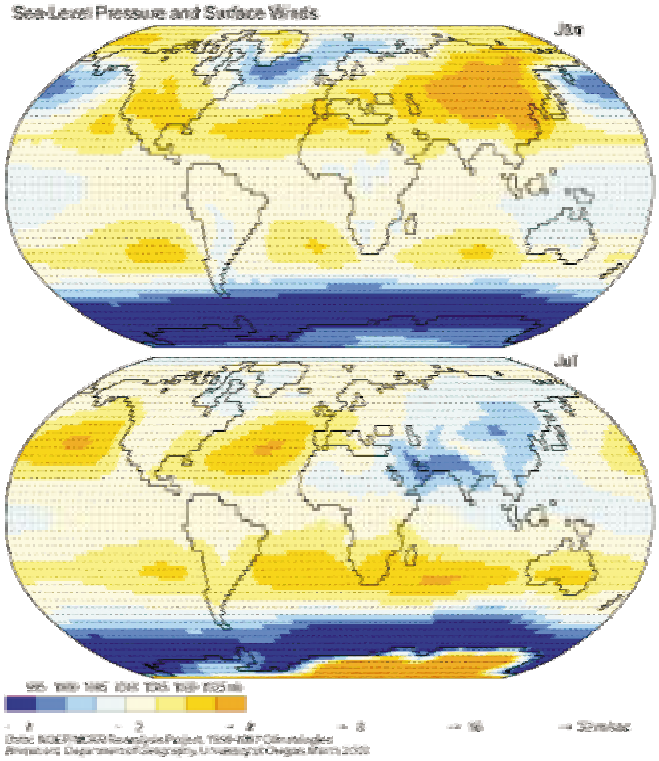

Figure 40: Present day wind speed (surface winds) and pressure at sea-level; [m/s and hPa].

Runoff:

For this study to runoff parameter have been analyzed, surface runoff (surface runoff rate; mm/day) and subsurface runoff (subsurface drainage rate; mm/day). Surface runoff is defined as the runoff (water) that travels over the soil surface to the nearest surface stream or as runoff of a drainage basin that has not passed beneath the surface since precipitation. However, subsurface runoff is defined as he runoff (water) infiltrating the surface soil and moving toward streams as ephemeral shallow perched ground water above the main ground-water level. It is usually considered part of direct runoff (LANGBEIN & ISERI, 1960).

Surface runoff from land:
Global surface runoff patterns for DJF (Figure 41) and JJA (Figure 42), as simulated by Genesis, predict that the highest surface runoff occurs north of ~40°N and south of ~40°S.

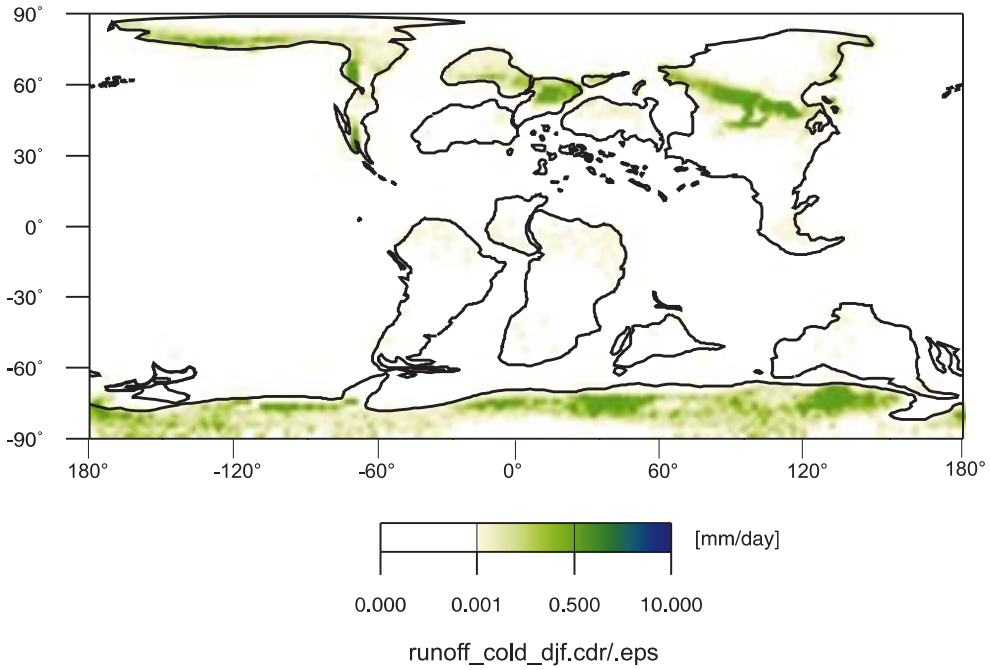

Figure 41: Surface runoff for Dec., Jan., Feb.; [mm/day].

During NH winter (Figure 41) maximum surface runoff occurs over Asia (max. 1.5 mm/day) and over eastern Antarctica (~ 2 mm/day). Notable surface runoff is limited to regions north of 30°N and south of 70°S. Australia, S-Asia, S-America, and Africa have no surface runoff (max. 0.005 mm/day).

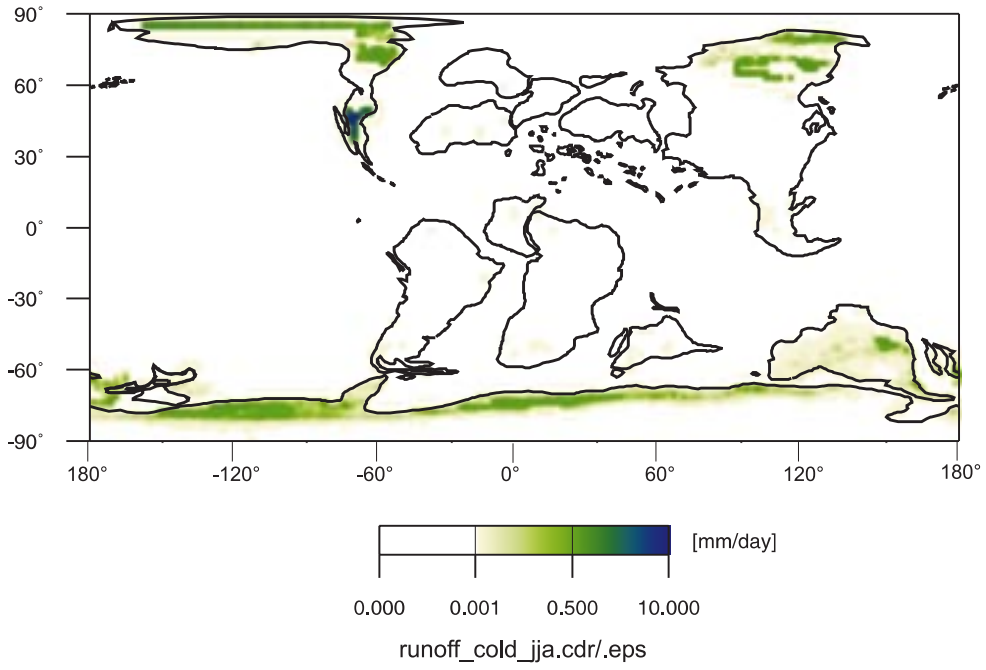

Figure 42: Surface runoff for Jun., Jul., Aug.; [mm/day].

The same picture emerges from surface runoff data for NH summer (Figure 42). Maximum runoff is predicted for eastern Antarctica, central WNA, northern WNA, and Asia. Globally, maximum is simulated off central WNA (Sevier Highlands) and reaches up to 7-9 mm/day.
The eastern craton of N-America, proto-Europe, central and southern Asia, S-America, and Africa do not show any notable surface runoff. Most of these regions do not have any surface runoff at all.

Subsurface runoff (Drainage):
Analysis of seasonal (DJF and JJA) subsurface runoff is shown in Figures 43 and 44. Subsurface runoff is called drainage in GENESIS. It is specified as the amount of water (mm/day) which gets infiltrated into the groundwater system. Groundwater is eventually returned through rivers. Its residence time is usually in the order of 5,000 years (PINNEKER, 1980).
The seasonal data do not show any significant changes in subsurface runoff, except at the southern tip of Asia where a decrease from ~15 mm/day to ~10 mm/day takes place between NH winter and summer. For the rest of the Cretaceous world, subsurface runoff remains almost the same. As already shown in the seasonal precipitation data, the regions where the formation of deserts took place can be distinguished. The subsurface runoff pattern is strongly correlated to precipitation. The simulations suggest desert-like conditions for central S-America, central Africa, south-central-Asia, and on Antarctica. The highest subsurface runoff was simulated for the N-American craton, Greenland, and Europe. Values are between 1.5-2.5 mm/day and slightly higher during the winter. The data for WNA do not show any significant variation throughout the year. Values generally shift around 1.5-2.5 mm/day.

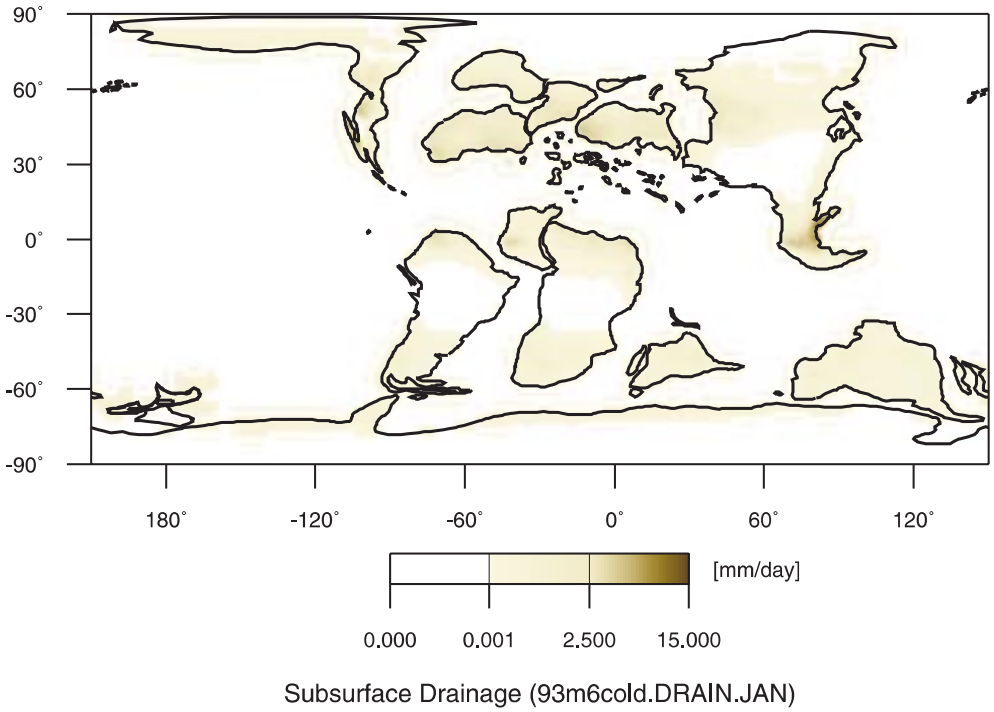

Figure 43: Subsurface runoff for Dec., Jan., Feb.; [mm/day].

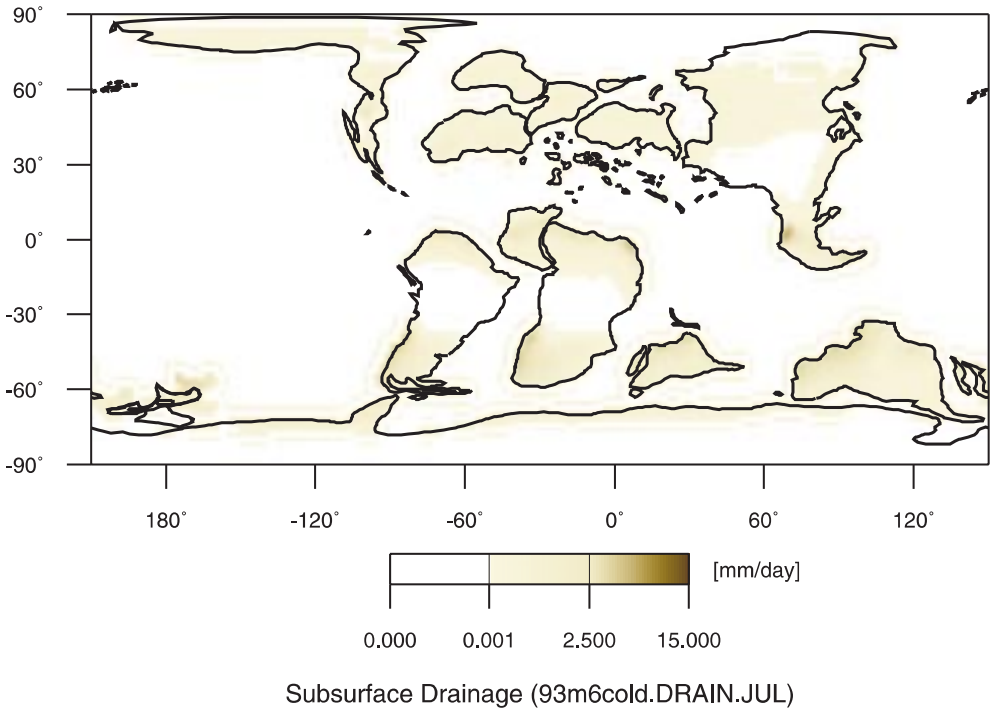

Figure 44: Surface runoff for Jun., Jul., Aug.; [mm/day].

9.3.2. Model results; Orbital cases A, B, C, D

Introduction:

The model results of the runs with changed orbital parameters are presented as difference plots. This means that the results of the control run were subtracted from the results of the orbital runs (ORBITAL RUN minus CONTROL RUN). Therefor, the results are presented as the deviation of the orbital run to the control run. Differences in temperature (ΔT), precipitation (ΔPrecip.), ΔRunoff (Surface runoff), and ΔDrainage (Subsurface runoff) have been compared. Each parameter has its own color scheme:

- ΔTemp.: blue (control run warmer than orbital run); red (orbital run warmer than control run).
- ΔPrecip.: red (control run wetter than orbital run); green (orbital run wetter than control run).
- ΔRunoff: red (control run has higher surface runoff than orbital run); blue (orbital run has higher surface runoff than control run).
- ΔDrainage: light green (control run has more subsurface runoff than orbital run); brown (orbital run has more subsurface runoff than control run).

The monthly data presented below show results of the:

1) control run
2) difference between orbital case A and the control run

3) difference between orbital case B and the control run
4) difference between orbital case C and the control run
5) difference between orbital case D and the control run

NOTE:
In the discussion below, the control run is considered to define reference conditions, and the precession experiments are discussed in terms of departure from these reference conditions.

9.3.3. Temperature; [°C]

Figures 45-56 show the differences in the results of the orbital runs compared to the control run.

Orbital case A:
For orbital case A, GENESIS predicts a global MAT of 20.82°C for model years 15 through 25.
With the vernal equinox coinciding with perihelion, a warmer than normal springtime and cooler than normal fall can be expected. This is also reflected by the model which suggests warming relative to the control run during March through June, with the greatest relative warming in May and June. Relative temperature increases, up to 4°C, occur over central-southern Asia, NW North America, central South America, and Antarctica. Lesser warming, around 0.5-2°C, occurs over the open ocean. The trend of warming relative to the control run continues over much of the globe into July, but relative cooling begins over the northern hemisphere land masses, reaching a maximum over Asia with temperature differences up to 2°C. The relatively cool conditions continue from August through December. The lower temperatures are more pronounced over the continents due to the lower heat capacity of land. Relatively lower insolation affects the oceans in September/October. Global temperatures for this simulation are cooler in December, with the greatest relative cooling over Antarctica (up to – 4°C). Finally, from January through March the relative cooling decreases and relative warming begins over Asia and Antarctica.
Generally, temperature differences over the WIS and the adjacent land masses are between 0.5-1°C, except in May/June when they are up to + 2°C, and during August/September, when they are up to – 2°C.

Orbital case B:
For orbital case B GENESIS predicts a global MAT of 20.80°C for model years 15 through 25.
This setup, with the NH winter solstice coinciding with perihelion generates a reduced seasonal insolation cycle in the northern hemisphere and an amplified cycle for the extreme seasons in the southern hemisphere. For months January through April the model predicts temperatures generally warmer than for the control run except north of 70°, where the changes are negligible due to the polar night. Close to the polar night the insolation approaches zero. Again, the relative warming is

greatest over Antarctica (up to 4°C). In April the model predicts the beginning of trend a of cooling for the NH relative to the control run, which is fully developed from May until August. The NH land masses cool between 2-4°C relative to the control run, whereas the ocean water only cools by ~1.5°C. The equatorial region remains unaffected from May until July, when the cooling reaches northern Africa and South America. With the beginning of September the NH begins to warm relative to the control run, starting in the continental interiors. The relative warming of Antarctica continues from January through August, when the southern hemisphere (SH) experiences winter. In October (springtime in the SH) the relative cooling of the SH reaches it's maximum (up to - 4°C). In November and December larger temperature changes are limited to continents, producing a mixed pattern. The WIS is largely unaffected by temperature changes greater than 1°C from January-May. In June a relative cooling of the North American continent, rather than of the seaway itself, starts. The relative cooling is greatest in July and August, with temperatures dropping over the seaway by 1.5 °C and over eastern and western North America by 2.0-2.5°C than in the control run.

Orbital case C:

This intermediate setup for winter and summer GENESIS predicts a global MAT of 20.91°C for model years 15 through 25.

This run is the opposite setup to run 93m6orba (case A), with fall and spring equinoxes coincide with perihelion and aphelion respectively; the forcing at the winter and summer solstices is "intermediate". Temperature changes predicted by GENESIS indicate a warming of the NH (~ + 0.5-1.5°C) and cooling of Antarctica (- 2.0-2.5°C) in January and February relative to the control run. This trend slows down in March and April with strong relative cooling of Asia and reverses in May and June when global cooling relative to the control run dominates, especially over the NH land masses (up to – 4°C over Asia). In July the pattern of temperature changes shifts again from a variable pattern towards global warming relative to the control run. This condition prevails from September until December. The relative warming begins in the NH continents and in Antarctica (~ + 2.0-3.8°C). With the end of NH summer and the beginning NH fall (September/October), ocean waters off S-America and Africa become warmer than the control run (~ + 0.5-1.0°C). Maximum relative warming of global oceans occurs in November and December; over the northern part of WIS temperatures are 1.0°C higher than the control run.

The WIS does not show the major changes seen in the continental interiors worldwide. The special situation of the WIS with the proto-Pacific, the Tethys, and the polar seas nearby allows only small variations in temperature. The values reached in August over the western part of N-America (+ 2.4°C) and in September/October over western N-America (+ 1.8-2.0°C) are the greatest relative warming predicted by all four orbital models discussed.

Orbital case D:

For orbital case D, GENESIS has simulated a global MAT of 20.96°C for model years 15 through 25.

The orbital setup of this run produces forcing opposite to orbital case B. The NH summer solstice coincides with perihelion and the NH winter solstice with aphelion. GENESIS predicts great temperature changes relative to the control run. The largest temperature changes compared to the control run are predicted for the larger continental interiors in both hemispheres. From December through April, GENESIS indicates a relative cooling of the SH. Compared to the control run, the largest temperature changes occur on Antarctica, in central Africa, and in central S-America. The cooling is strongest in January on Antarctica and in parts of Australia, when temperatures cool up to 4°C compared to the control run. The sensitivity of the climate system is greatest over the land masses. The relative temperature changes over the oceans are small (+/- 0.5°C). The relative cooling trend from December through April begins on the continents, whereas the southern ocean still warms in December. Greater response to orbital forcing occurs in the NH during May, June, and July, whereas temperatures changes in the SH are relatively small (~ +/- 1°C) compared to the control run. In June and July, all land masses of the NH warm up extremely, when compared to the control run. The relative warming reaches values between 3-4°C with intense warming of up to 4°C occurs in central Asia and Europe. Interestingly, the central regions of S-America and Africa also warm during NH summer. During June, the relative warming there is smaller than in the NH, but still evident (+ 1.5-2°C). The relative warming over Africa and S-America reaches maximum values during August, when temperature changes are as great as in the NH (up to + 4°C). Beginning in August this trend of relative warming of the SH becomes stronger, whereas the relative warming in the NH is smaller (~ 2°C). Generally, orbital case D predicts large seasonal contrasts of temperature changes relative to the control run, with the high northern latitudes warmer throughout the year.

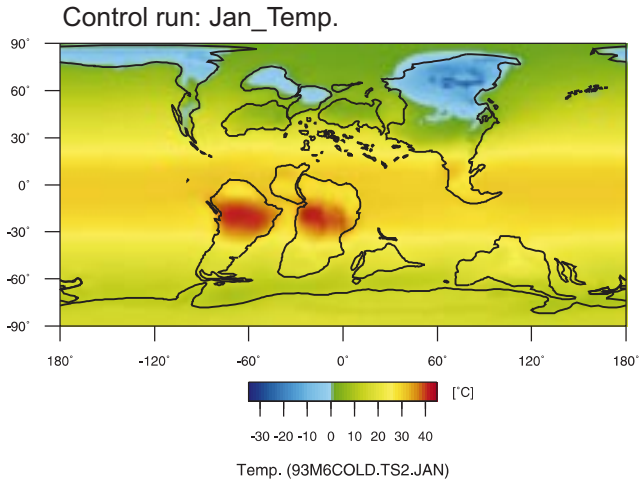

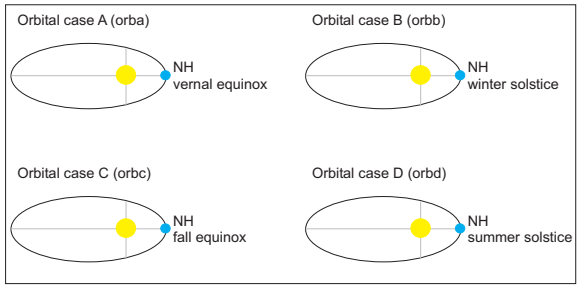

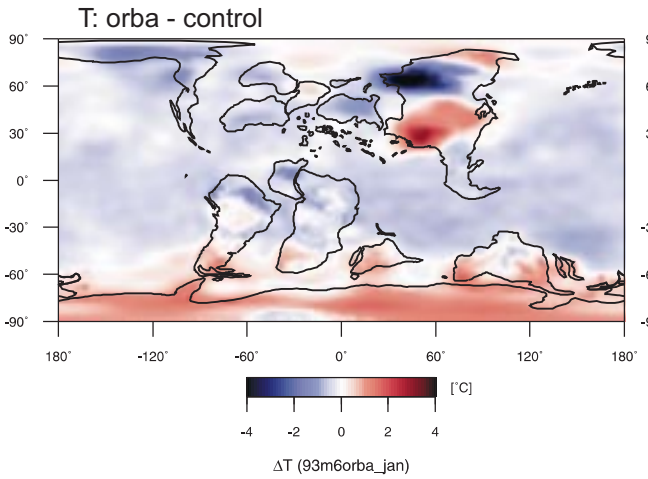

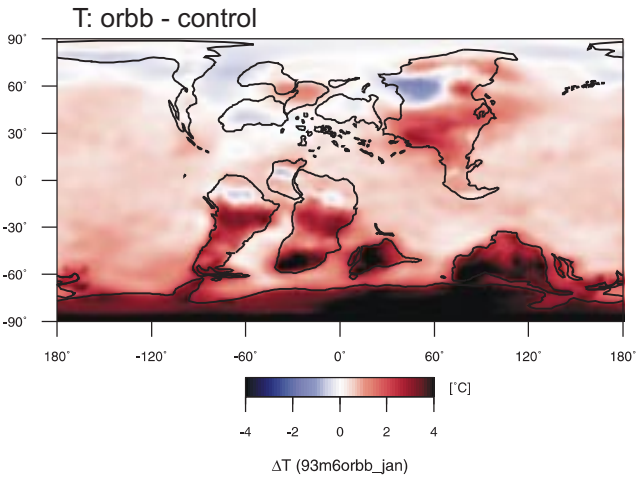

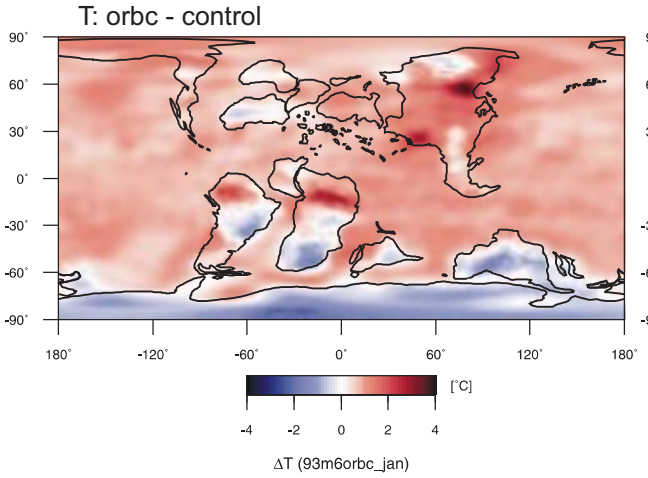

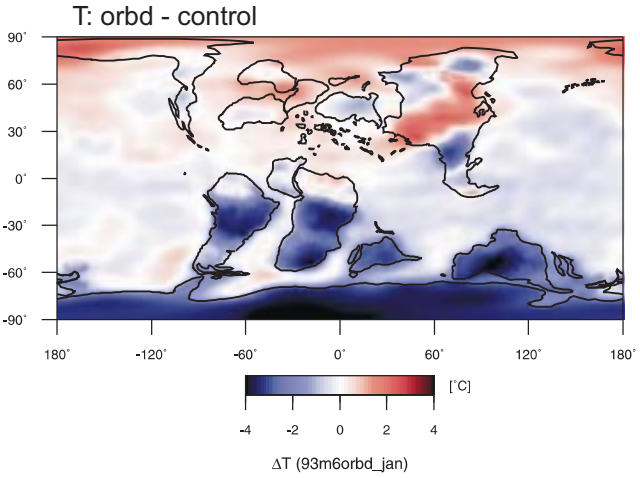

Figure 45: Model results for temperature in January; [°C].

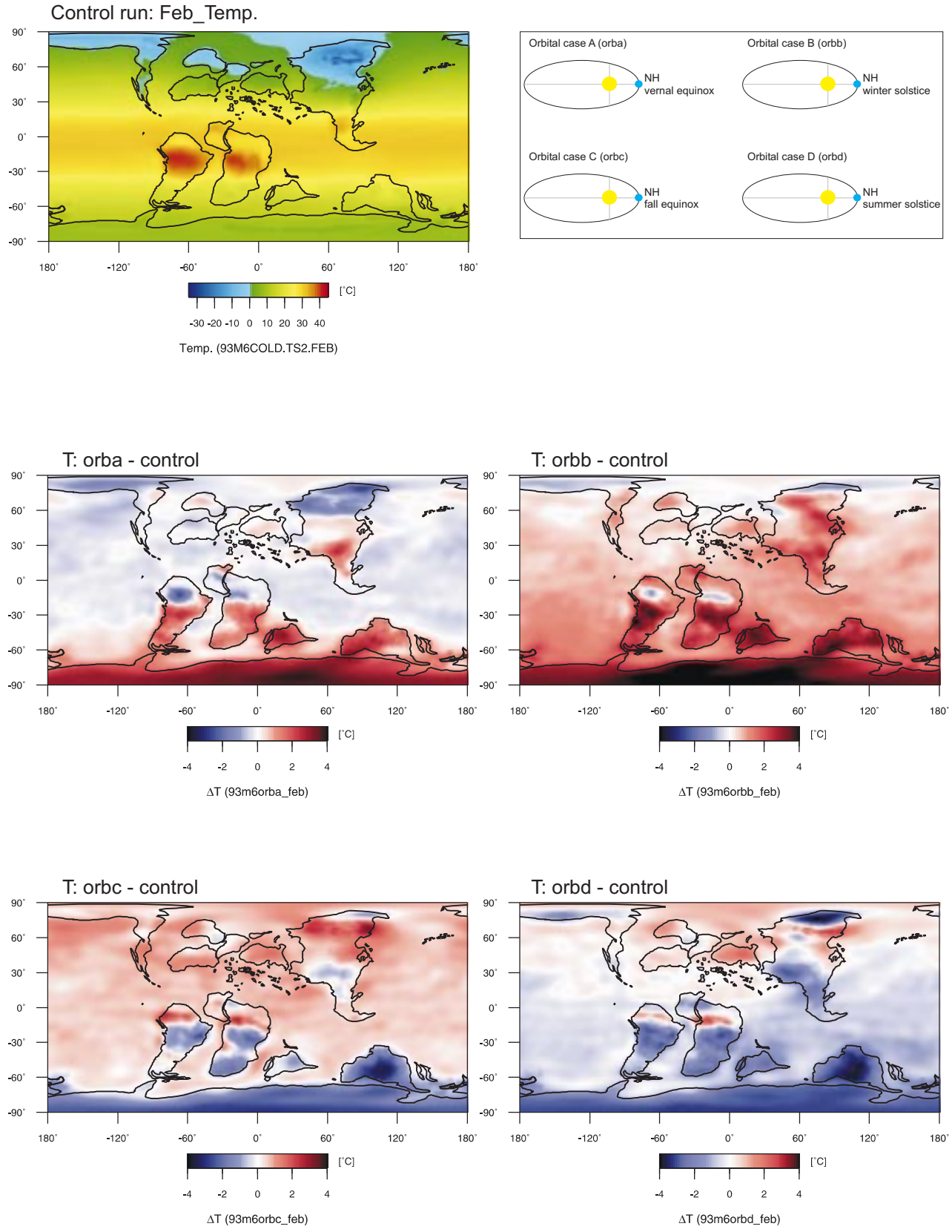

Figure 46. Model results for temperature in February; [°C].

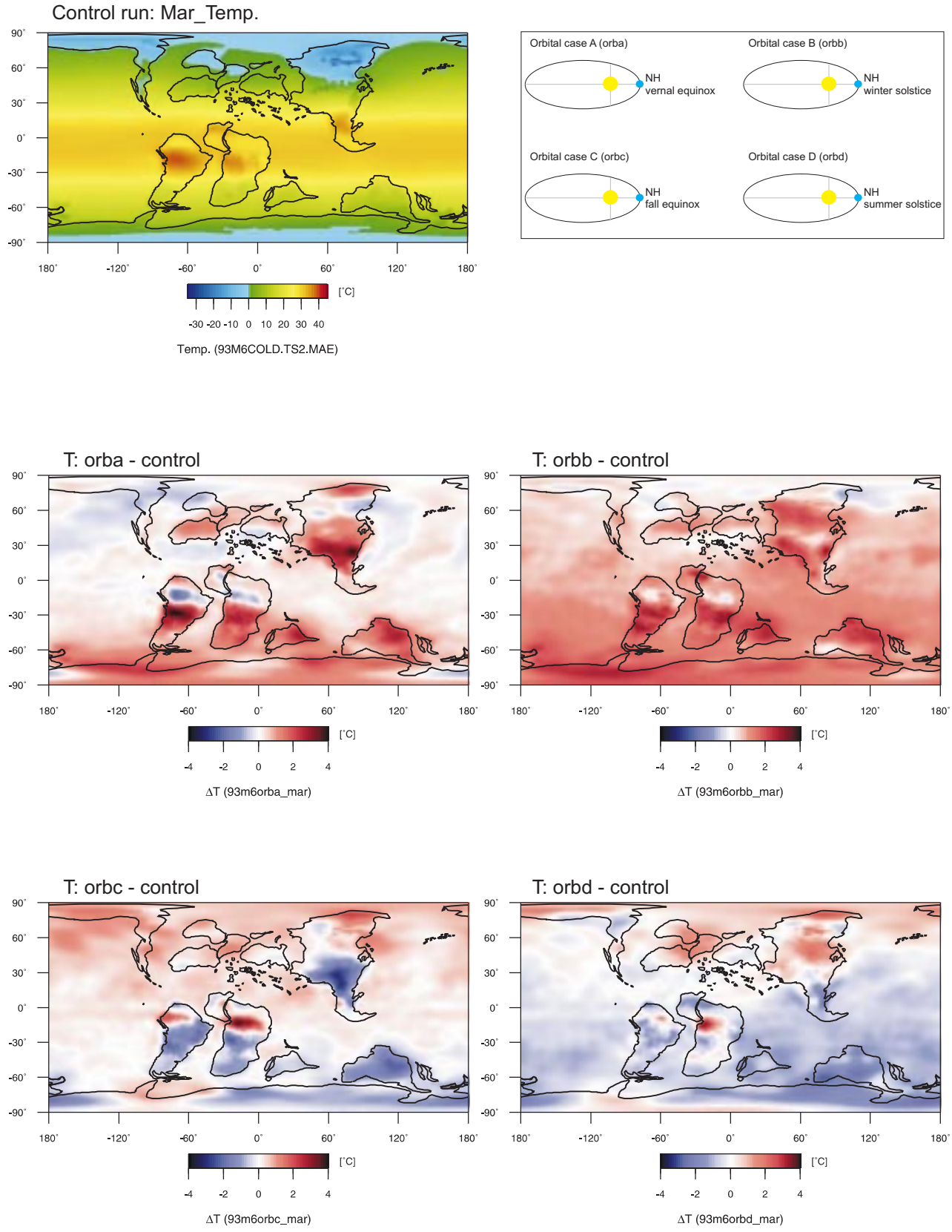

Figure 47: Model results for temperature in March; [°C].

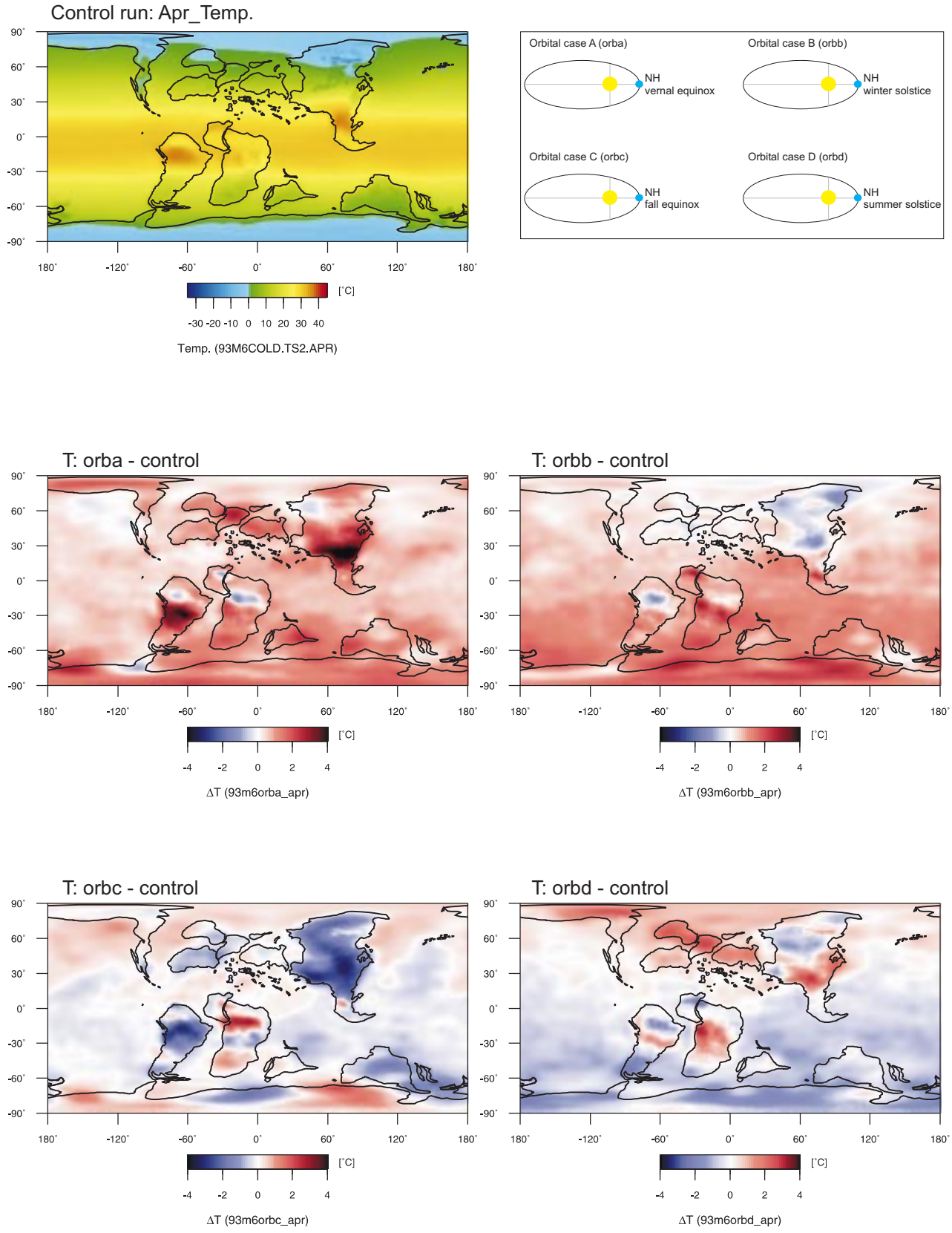

Figure 48: Model results for temperature in April; [°C].

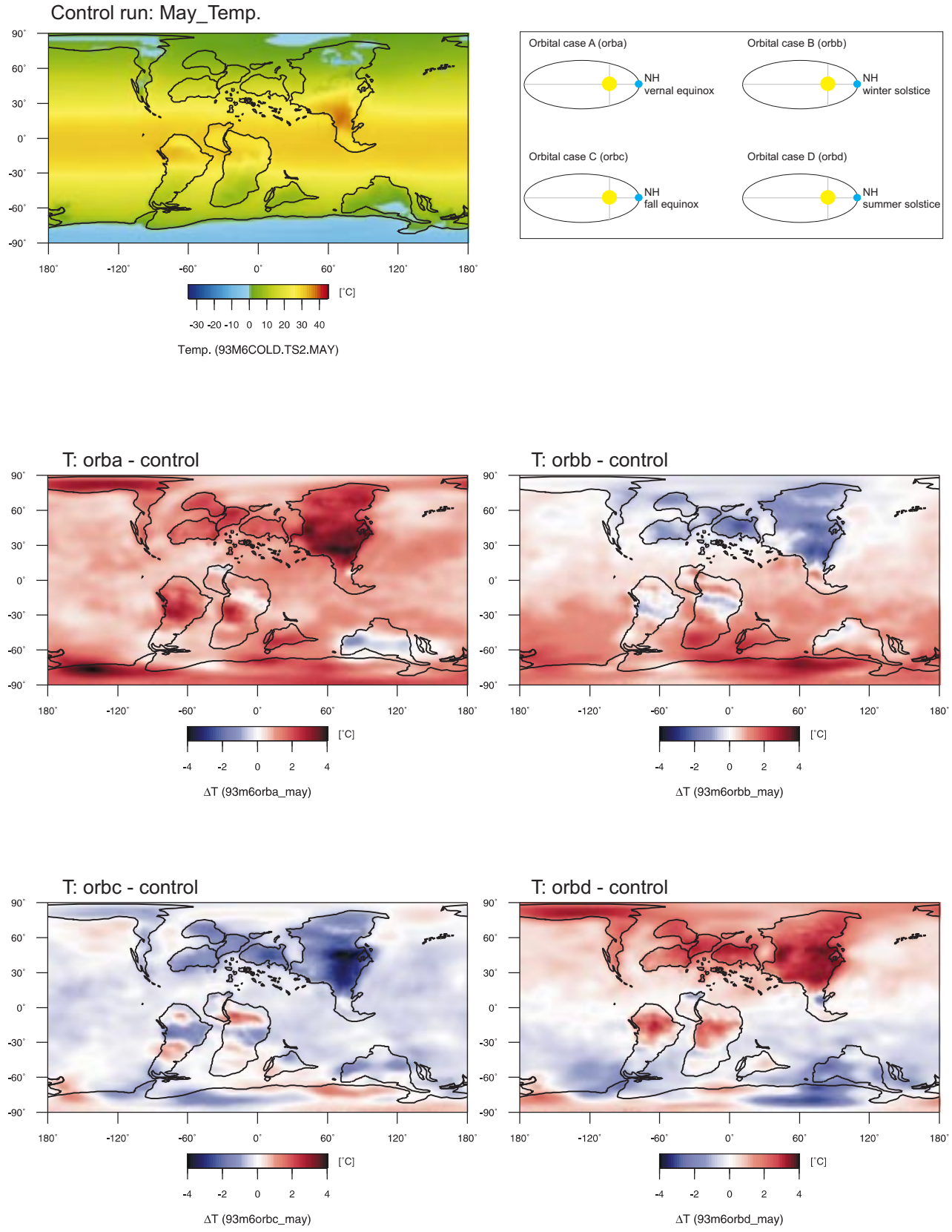

Figure 49: Model results for temperature in May; [°C].

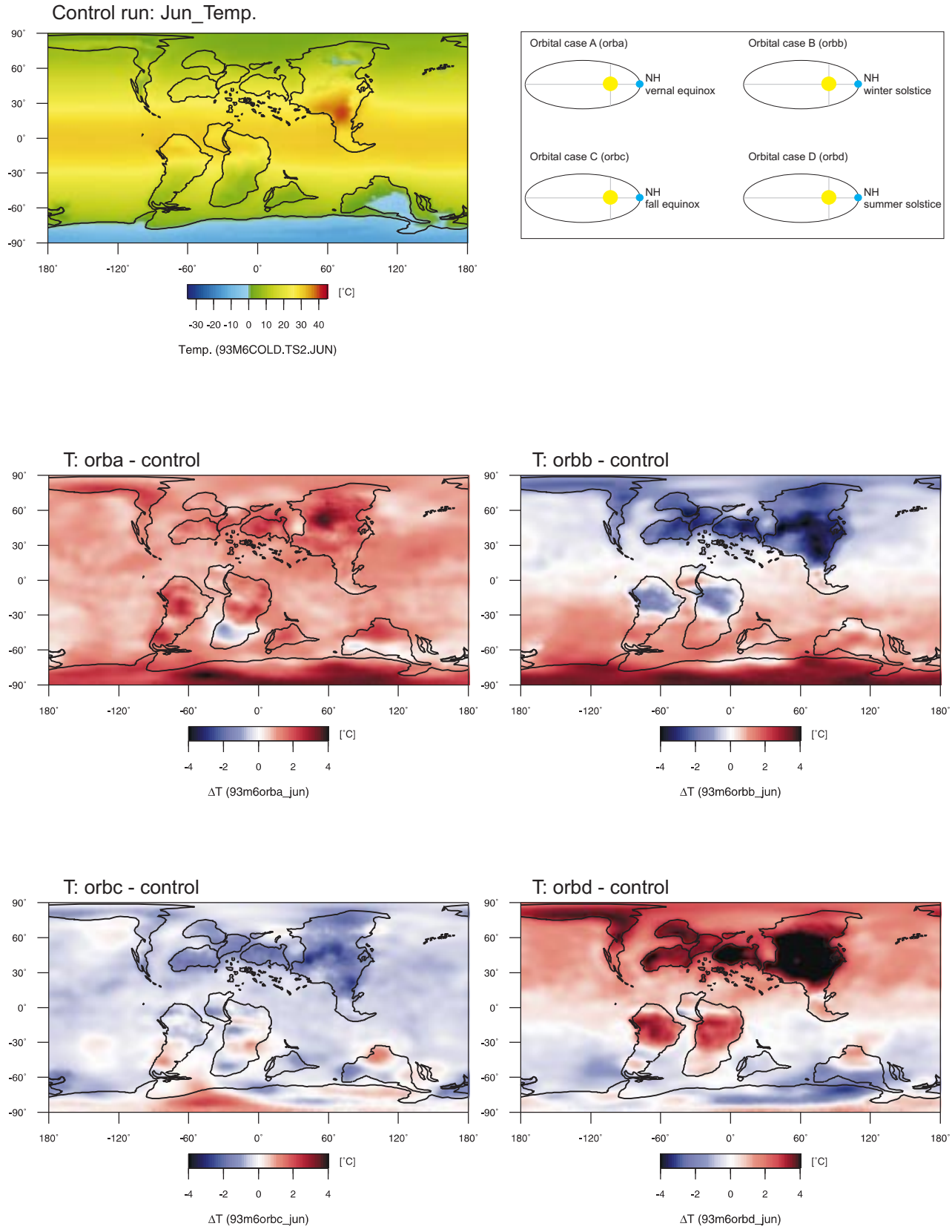

Figure 50: Model results for temperature in June; [°C].

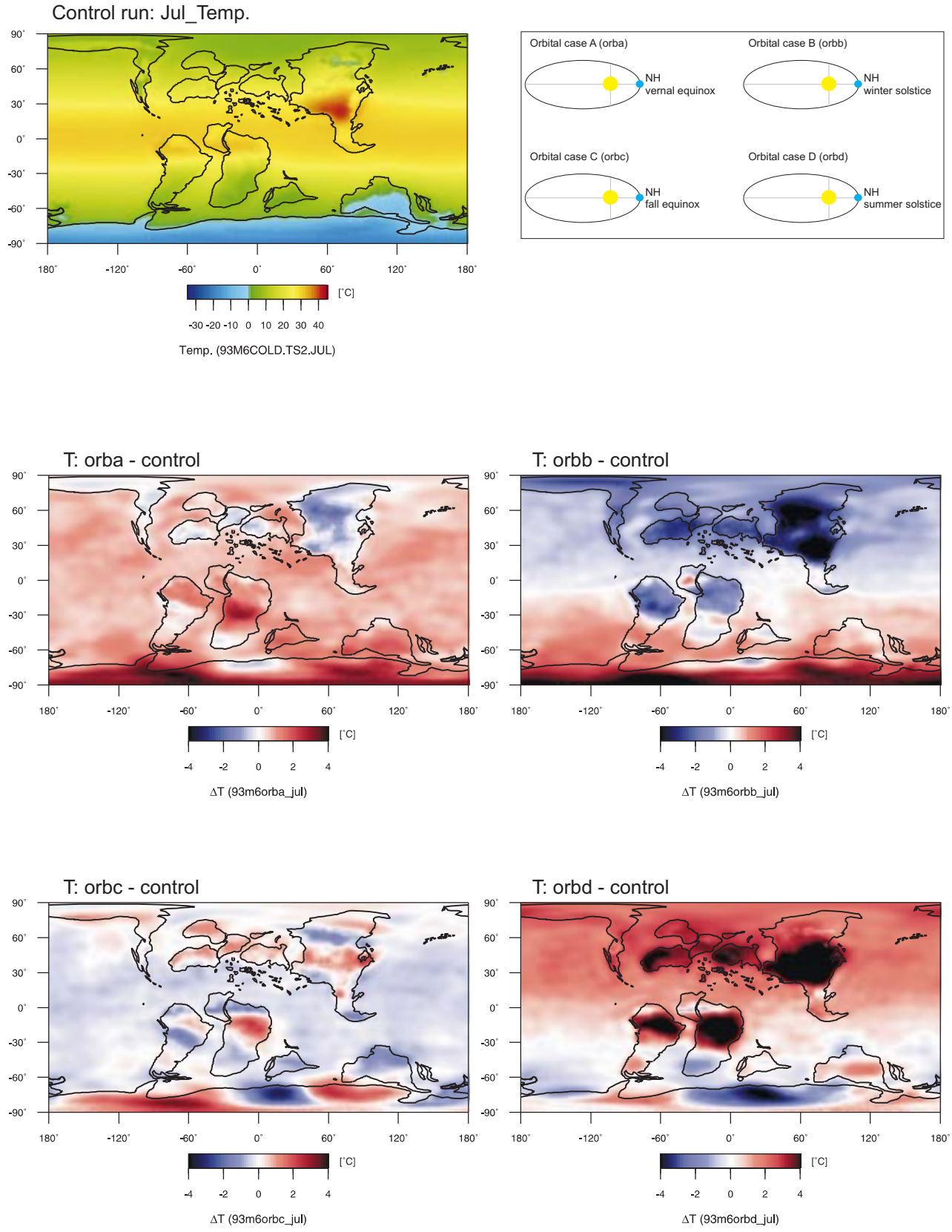

Figure 51: Model results for temperature in July; [°C].

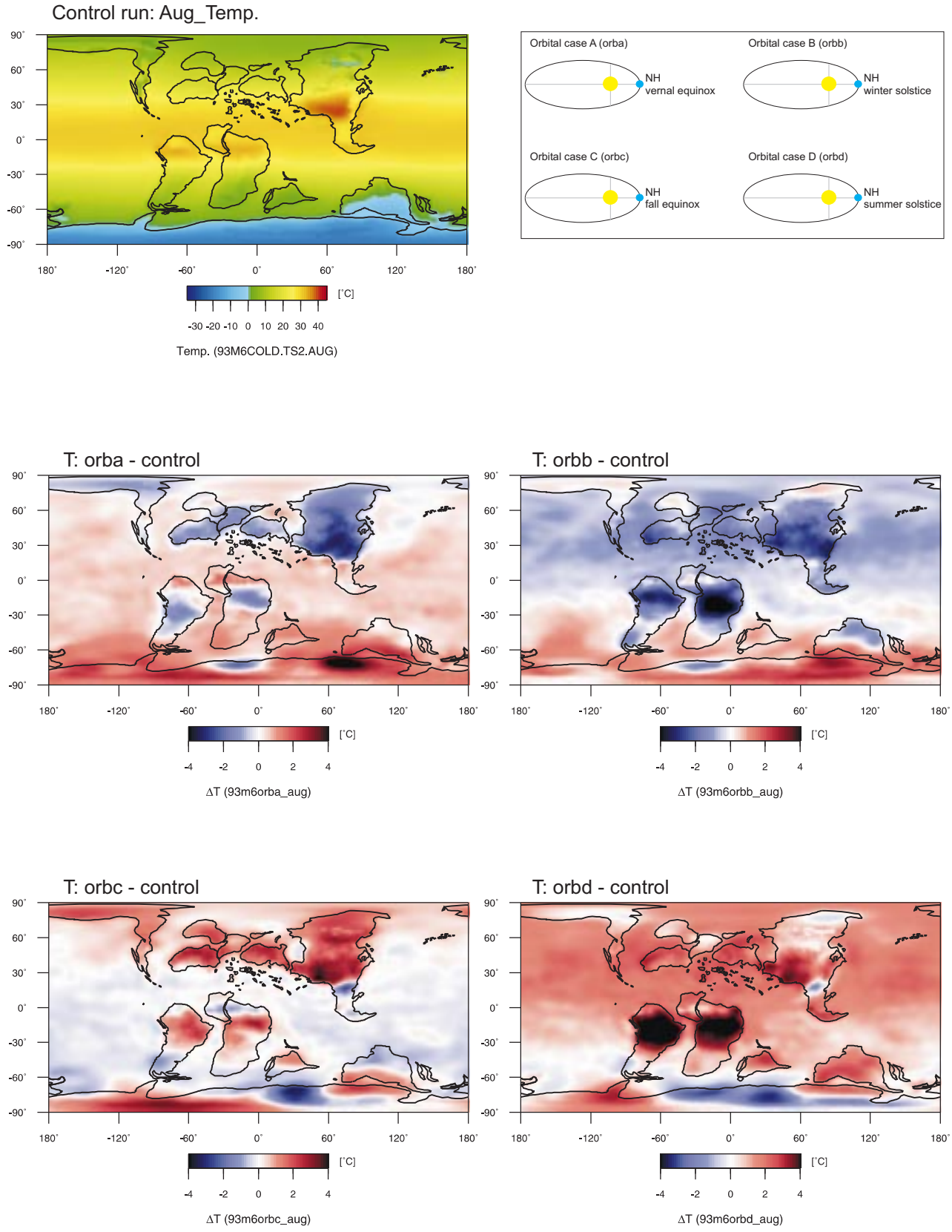

Figure 52: Model results for temperature in August; [°C].

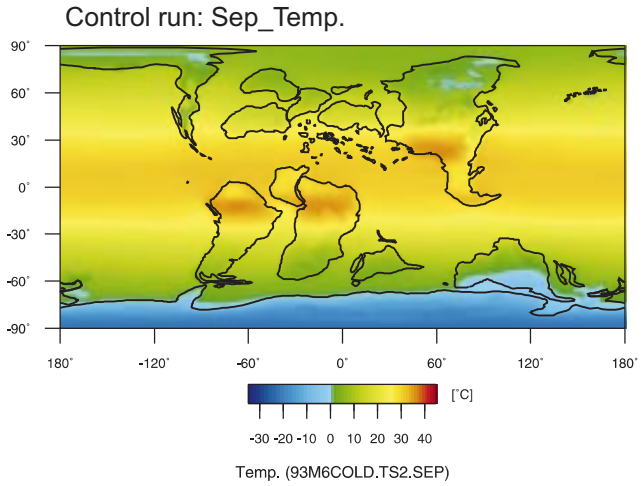

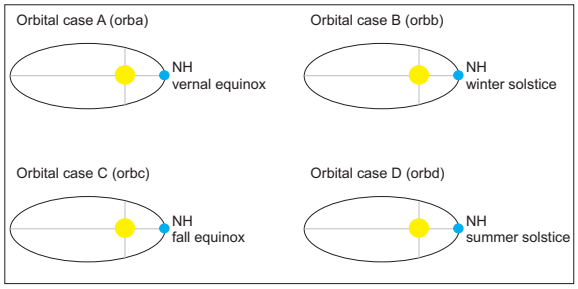

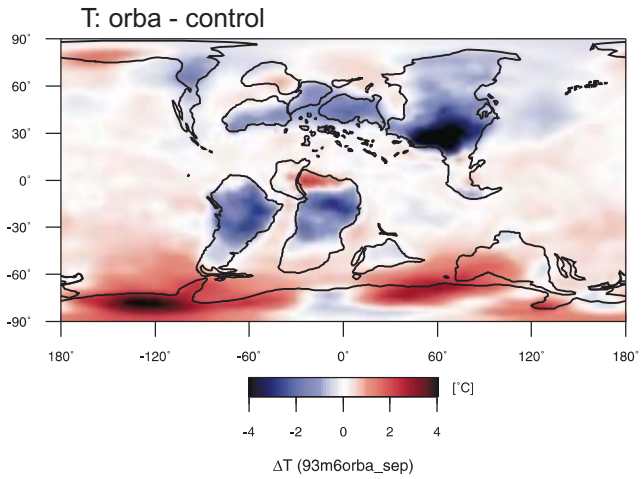

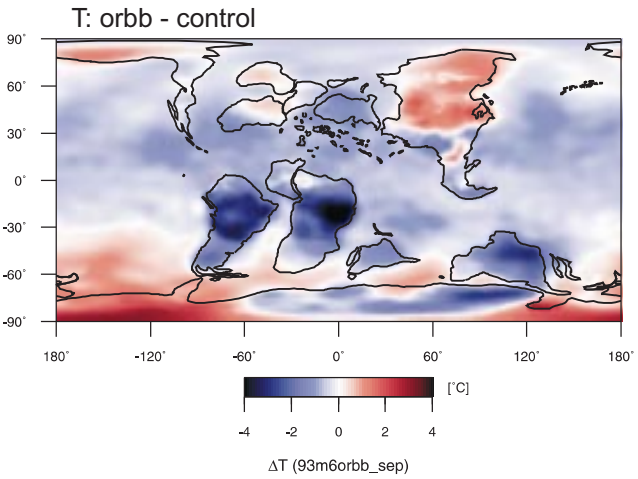

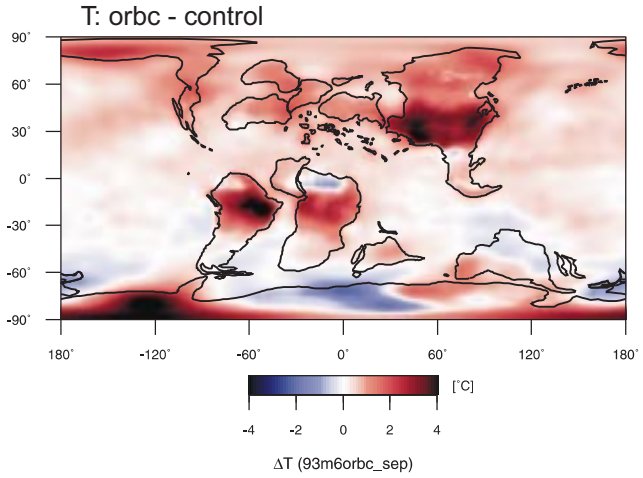

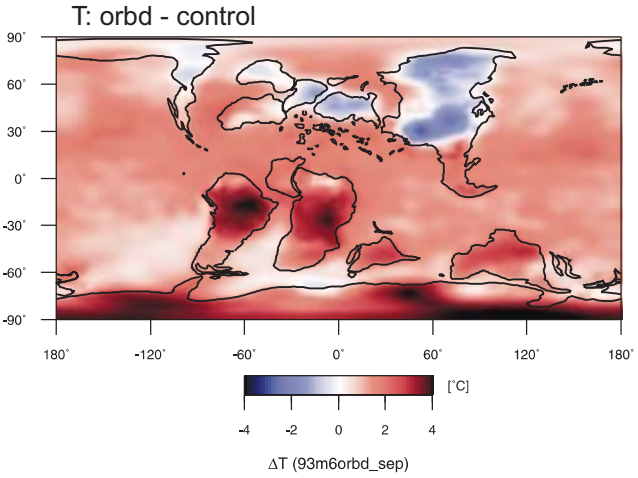

Figure 53: Model results for temperature in September; [°C].

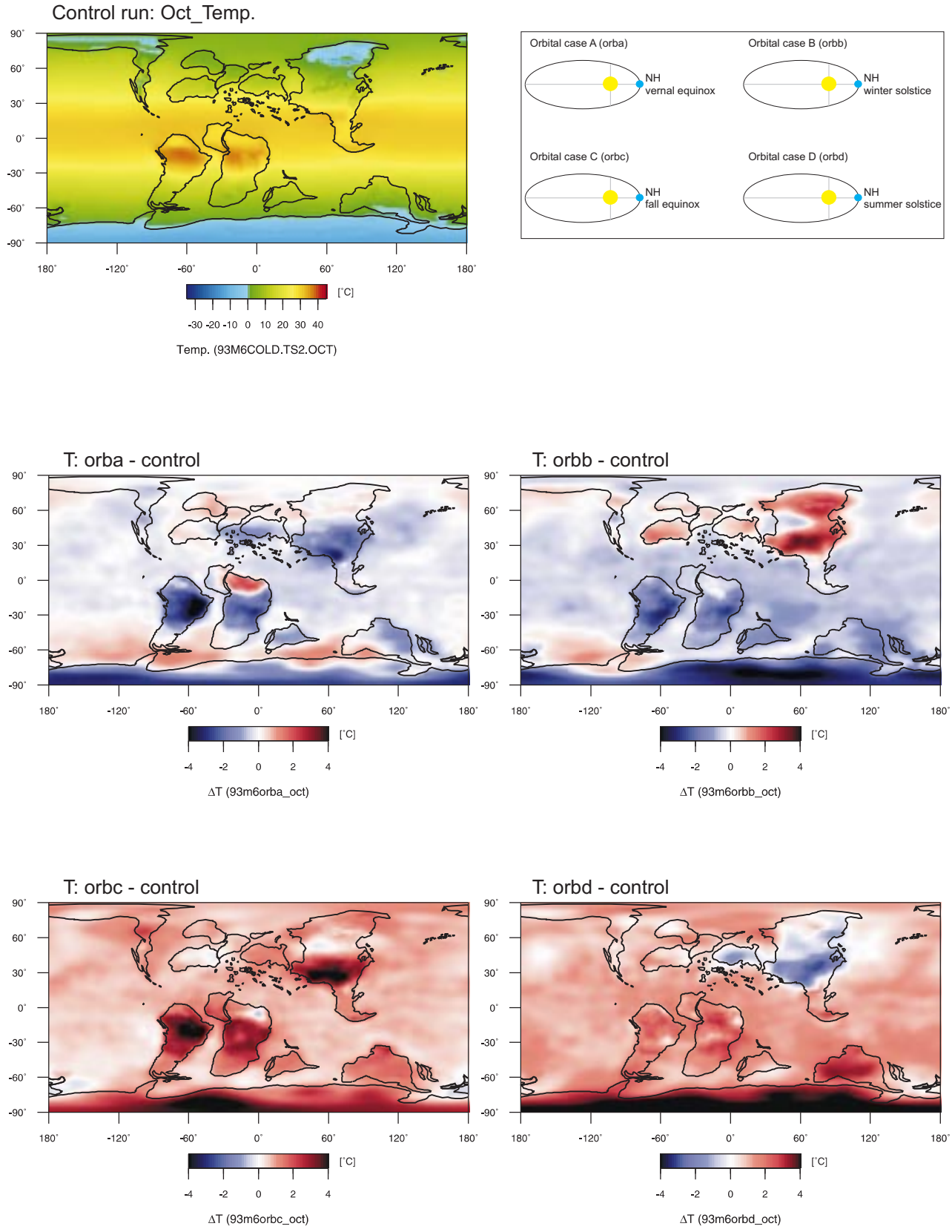

Figure 54: Model results for temperature in October; [°C].

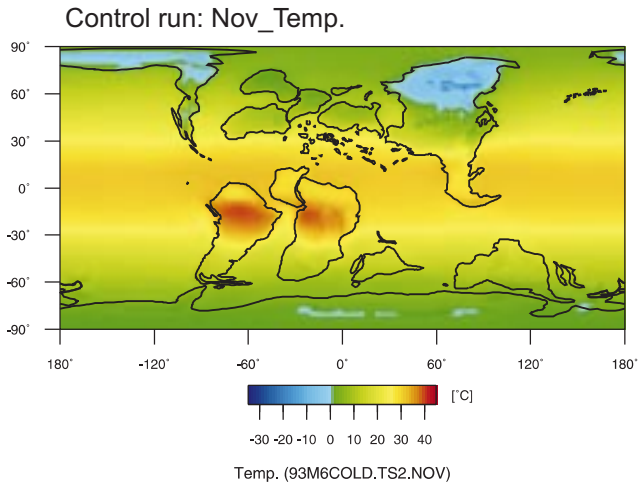

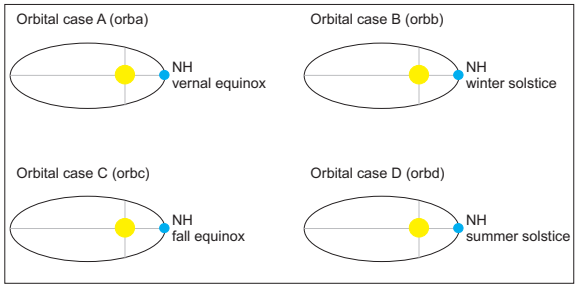

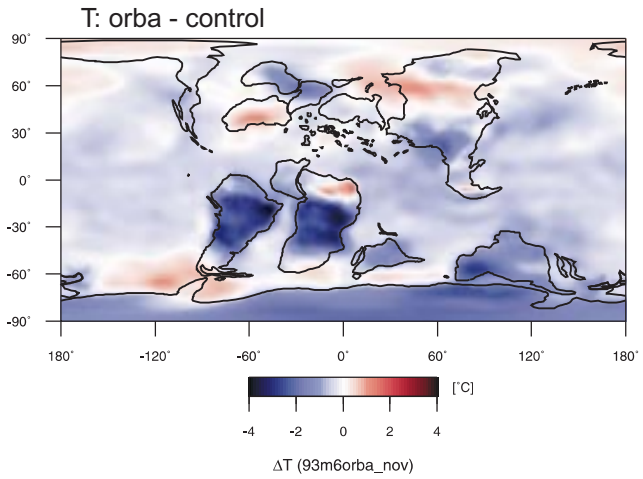

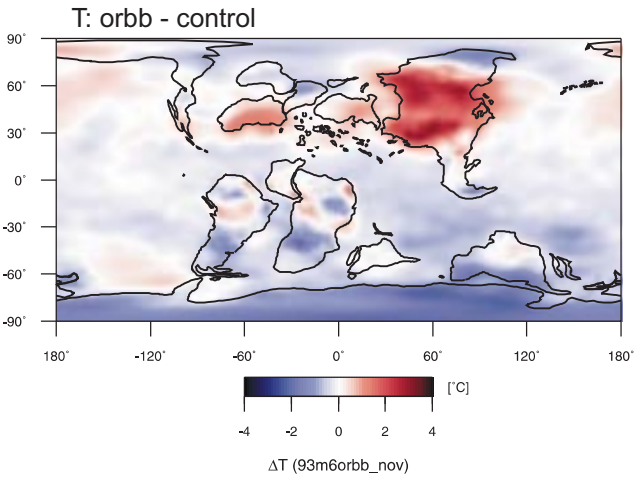

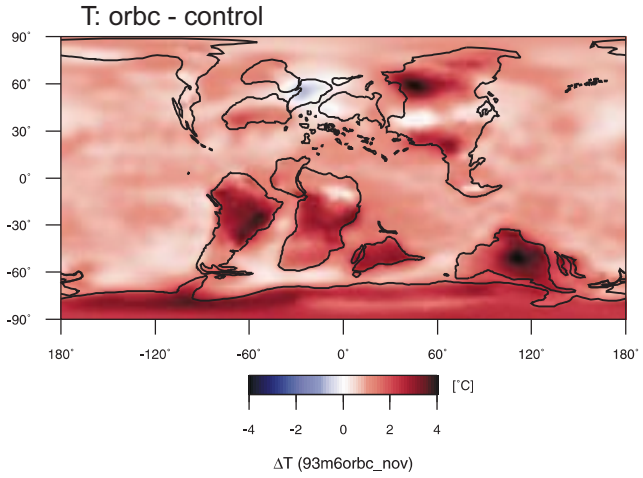

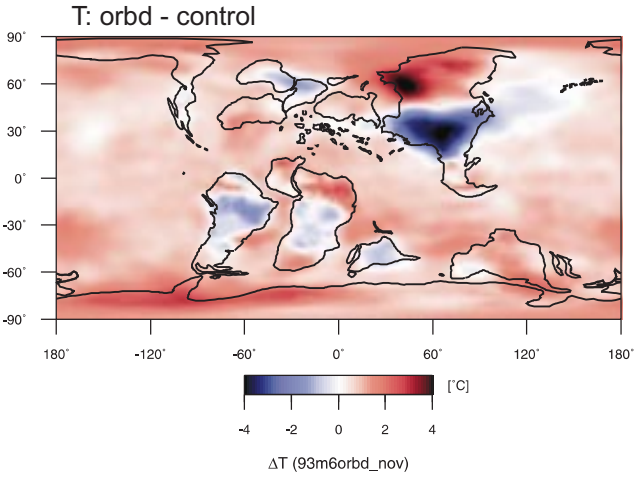

Figure 55: Model results for temperature in November; [°C].

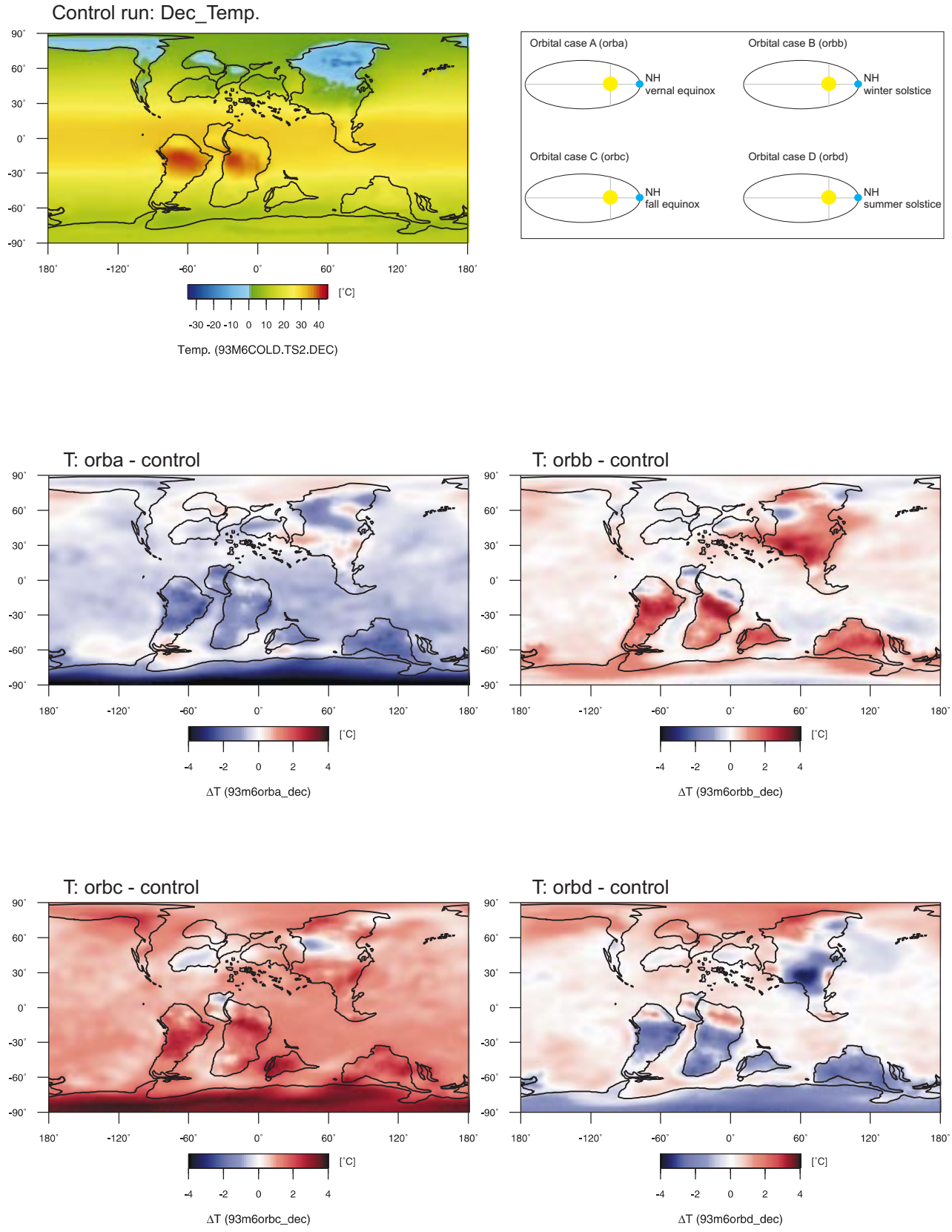

Figure 56: Model results for temperature in December; [°C].

9.3.4. Precipitation; [mm/day]

Figures 57-68 show the differences in the results of the orbital runs compared to the control run.

Orbital case A:
The largest changes in precipitation compared to the control run occur just north and south of the equator, in the paleo-ITCZ (Inter Tropical Convergence Zone). Smaller relative changes are predicted between ~40° North and South, but there are virtually no relative changes in the polar regions where precipitation is always low because of the cooler temperatures. Globally, the smallest changes compared to the control run occur in January on both sides of the equator. The continental response to this orbital setup relative to the control run is largest in northern Africa in March and April (+ 2-4 mm/day) and in September and October (- 2 mm/day). These relative increases (~30-50 %) and decreases (~40 %) reflect the great seasonality of the model. Another area with dramatic shifts of the precipitation pattern compared to the control run is off the western coast of southern Asia, where a relative increase of up to 8 mm/day (+ 100 %) occurs over a large part of eastern Tethys. A monsoonal precipitation pattern is predicted by the model for March, affecting both northern S-America and northern Africa, and for April, affecting only northern Africa. The WIS and the adjacent craton experience large changes from July through November, when precipitation increases (e. g. in August + 0.5-2.0 mm/day → up to 100 %) compared to the control run.
The correlation between changing temperatures and precipitation is poor. The largest relative temperature changes are on the continents whereas the largest changes in precipitation compared to the control run occur over the ocean. Western North America shows no significant changes in precipitation compared to the control run (<0.5 mm/day). Precipitation in the Sevier Highlands is 1.5-4 mm/day throughout the year, with the highest rainfall in the NH summer.

Orbital case B:
The overall pattern of increasing and decreasing precipitation resembles the previous model results. This substantial response (i. e. large sensitivity) to the precessional-driven forcing is largest along the equator. Usually changes North and South of the equator are the opposite; an increase in the NH is opposed by a decrease in the southern hemisphere. From January through June the model predicts widespread changes in the SH. The greatest changes in precipitation occur over northern Africa and northern South America. These regions experience conditions wetter than the control run, except from May through August (~ - 1 mm/day). A small monsoonal precipitation pattern becomes established over northern S-America and northern Africa from December through March. Other interesting features are the dry conditions in the southernmost part of the WIS and the westernmost Tethys region from October-December, with a maximum rainfall decrease in November (- 2.0-6.0 mm/day).

The WIS region shows no significant response to this orbital setup for most of the year but wetter conditions prevail in June and August over the westernmost part of eastern North America, with an increase of up to 1.5 mm/day. This is about 50 % more than the 3 mm/day of the control run. The Sevier Highlands in western North America show no significant changes in precipitation.

Orbital case C:

The relative precipitation changes predicted by the model show overall patterns similar to the previous simulations, with the largest variations taking place in the equatorial region and smaller effects towards the polar regions. When compared with the control run, the variations occur mostly over the oceanic regions with the exception that there are large seasonal contrasts over N-Africa. The control run predicts 5-9 mm/day of precipitation during March and April, but the precessional forcing of this orbit reduces that by 5-9 mm/day, turning parts of N-Africa into a arid region with no precipitation for about one fourth of the year. However, during September and October precipitation in this region increases by about 2.0 mm/day, over the 0.5-3.0 mm/day predicted by the control run. The pattern along the equator is variable, with “cells” of decrease and increase in opposite hemispheres on both sides of the equator relative to the control run. From July through November monsoon precipitation sets in over N-Africa due to strong warming of central Africa; this monsoon system is strongest in September and October.

The WIS and the surrounding land masses experience smaller relative fluctuations throughout the year. The relative increase over the Sevier Highlands along the western coast of the seaway is largest in June and August, ~ + 0.5-0.8 mm/day over the 2-4 mm/day (~ + 25 %) of the control run. The western portion of the North American craton shows an increase in February, May, and November of up to 1.2 mm/day in addition to the 3-4 mm/day (~ + 30%) of the control run.

Orbital case D:

The relative changes in the annual distribution of precipitation simulated for this orbital setup suggest that the sensitivity of the NH is larger during the second half of the year. From August through December changes relative to the control run occur primarily in the NH. Precipitation increases by up to 8 mm/day in the equatorial region as compared to the control run. The changes are strongest between N-Africa and southern Asia and west of northern S-America. Each of these bands of relatively increased precipitation is opposed by a zone of relative decrease in the same order of magnitude. Overall the NH shows increased precipitation relative to the control run. From January through July, changes relative to the control run are not larger than ~ 1 mm/day, except 10° north and south of the equator.

During the first six months of the year, the largest relative changes compared to the control run occur on the western flank of the Sevier Highlands. They increase up to 2 mm/day during January compared to the control run. That is an increase of about 30% compared to the control run.

Another month with a similar relative increase of precipitation over WNA is September, when an increase of ~ 3 mm/day is simulated. During the rest of the year, WNA shows only a small sensitivity to the precessional forcing produced by orbital case D.

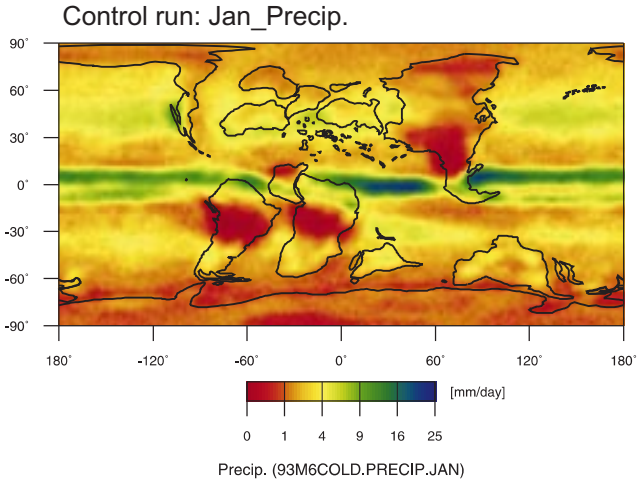

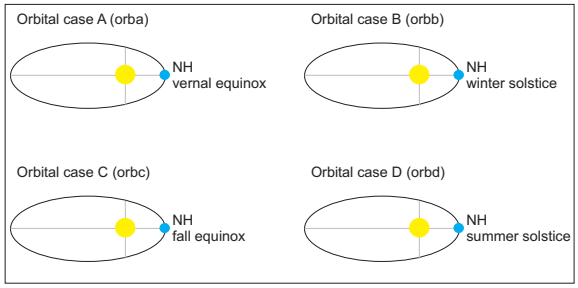

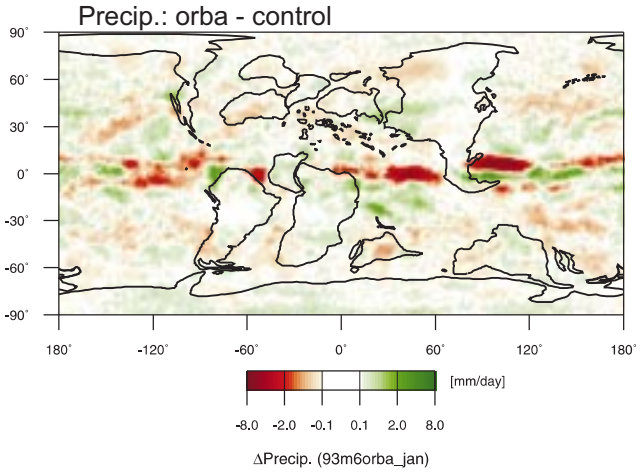

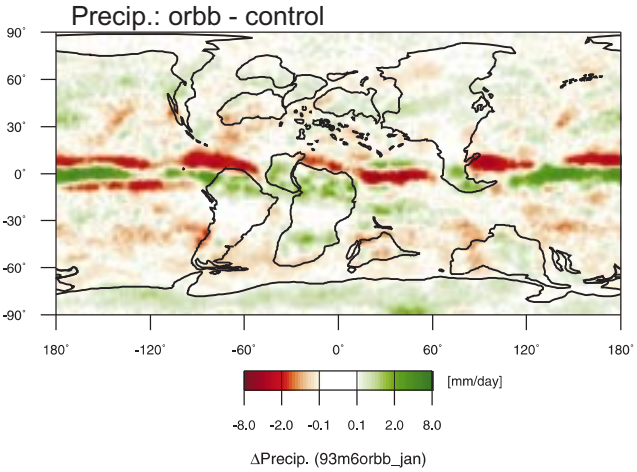

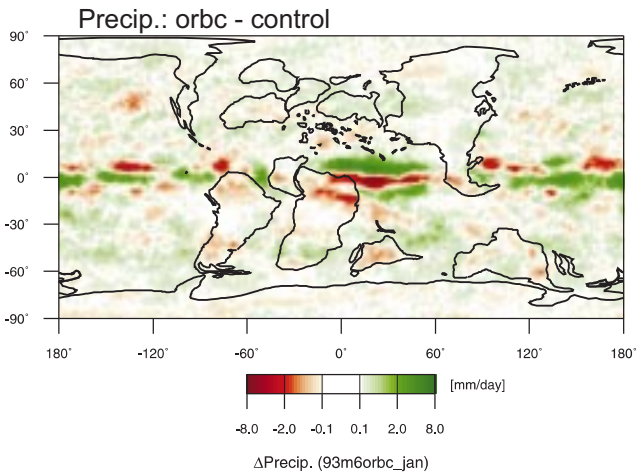

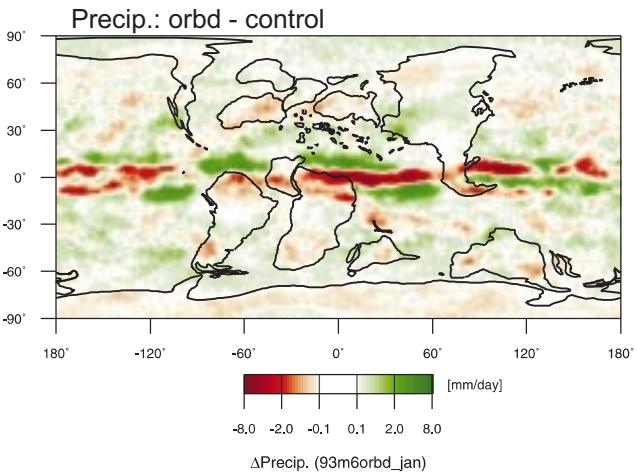

Figure 57: Model results for precipitation in January; [mm/day].

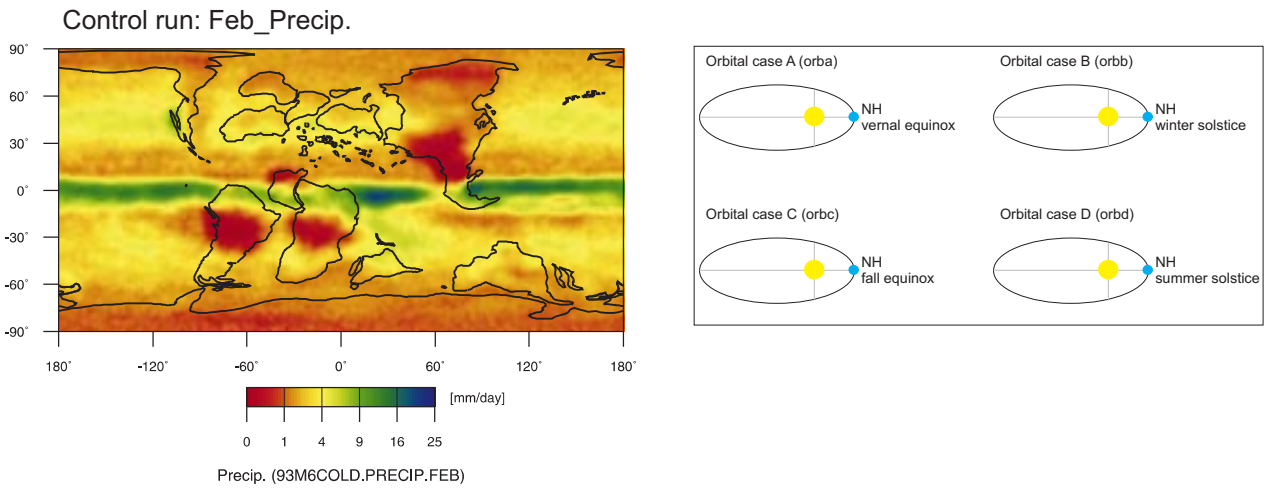

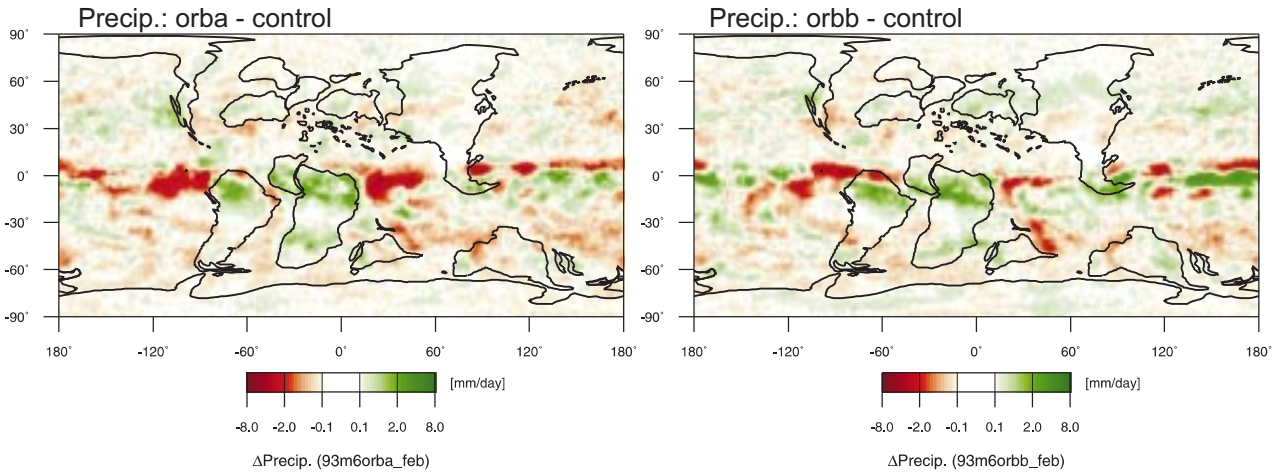

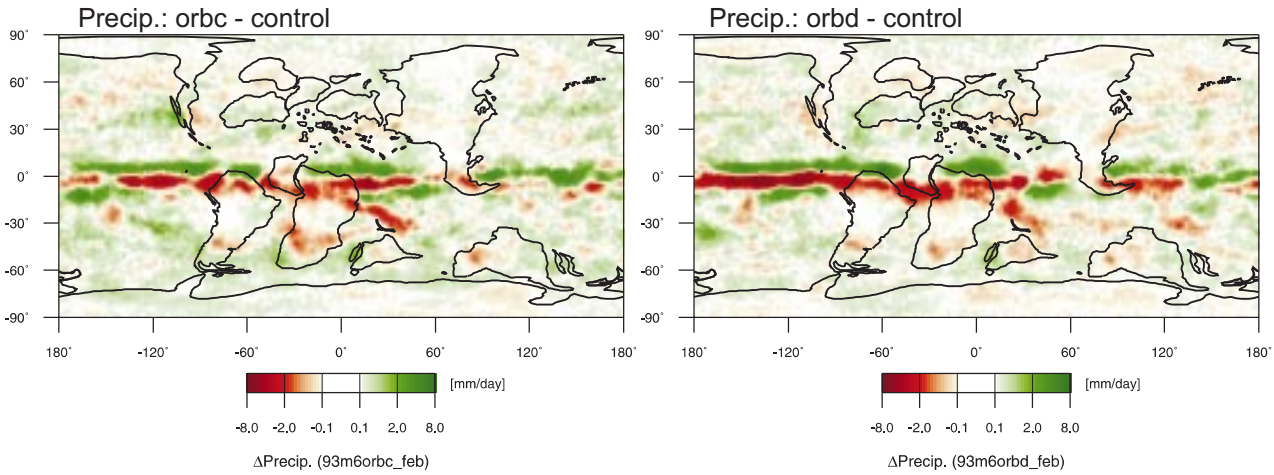

Figure 58: Model results for precipitation in February; [mm/day].

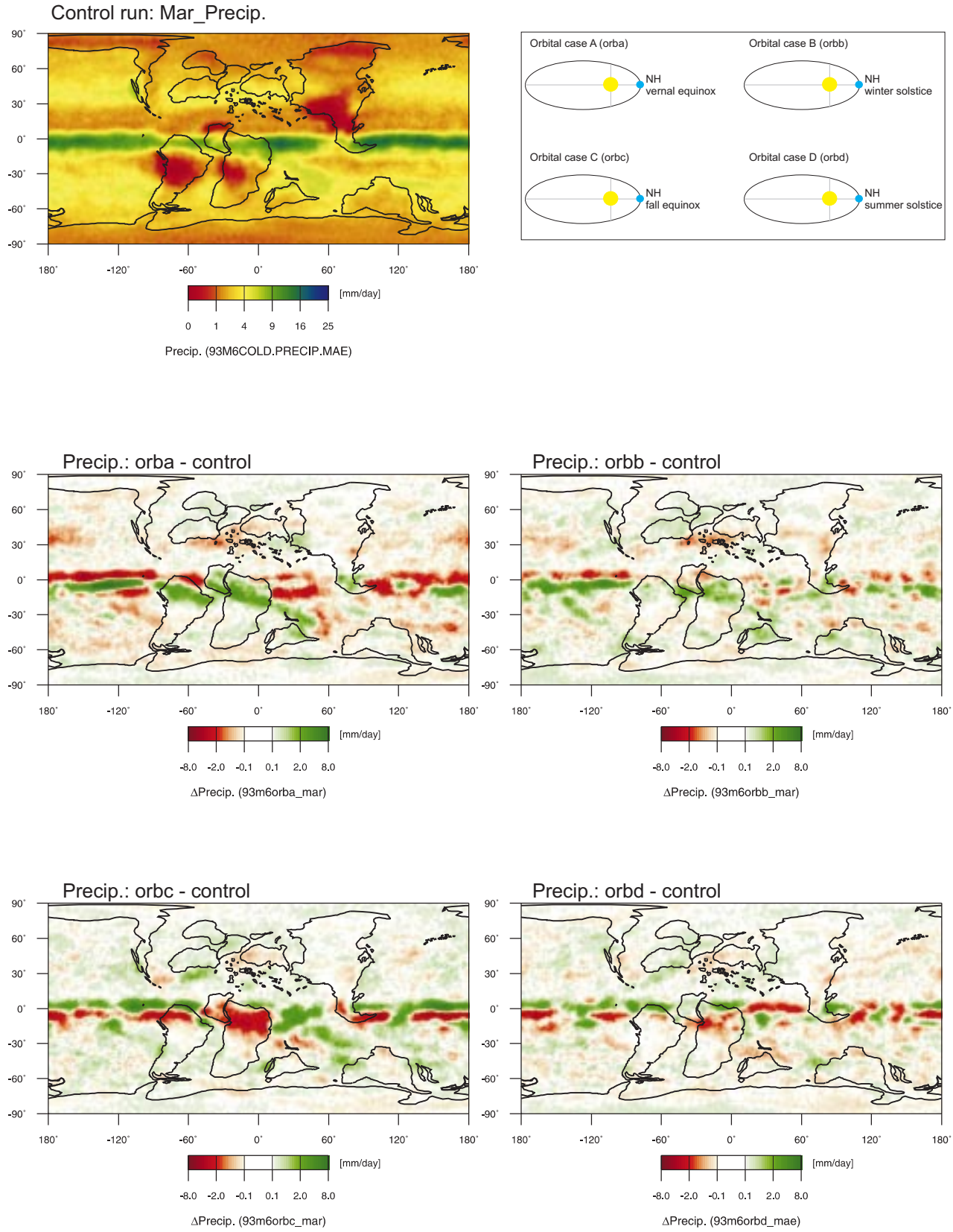

Figure 59: Model results for precipitation in March; [mm/day].

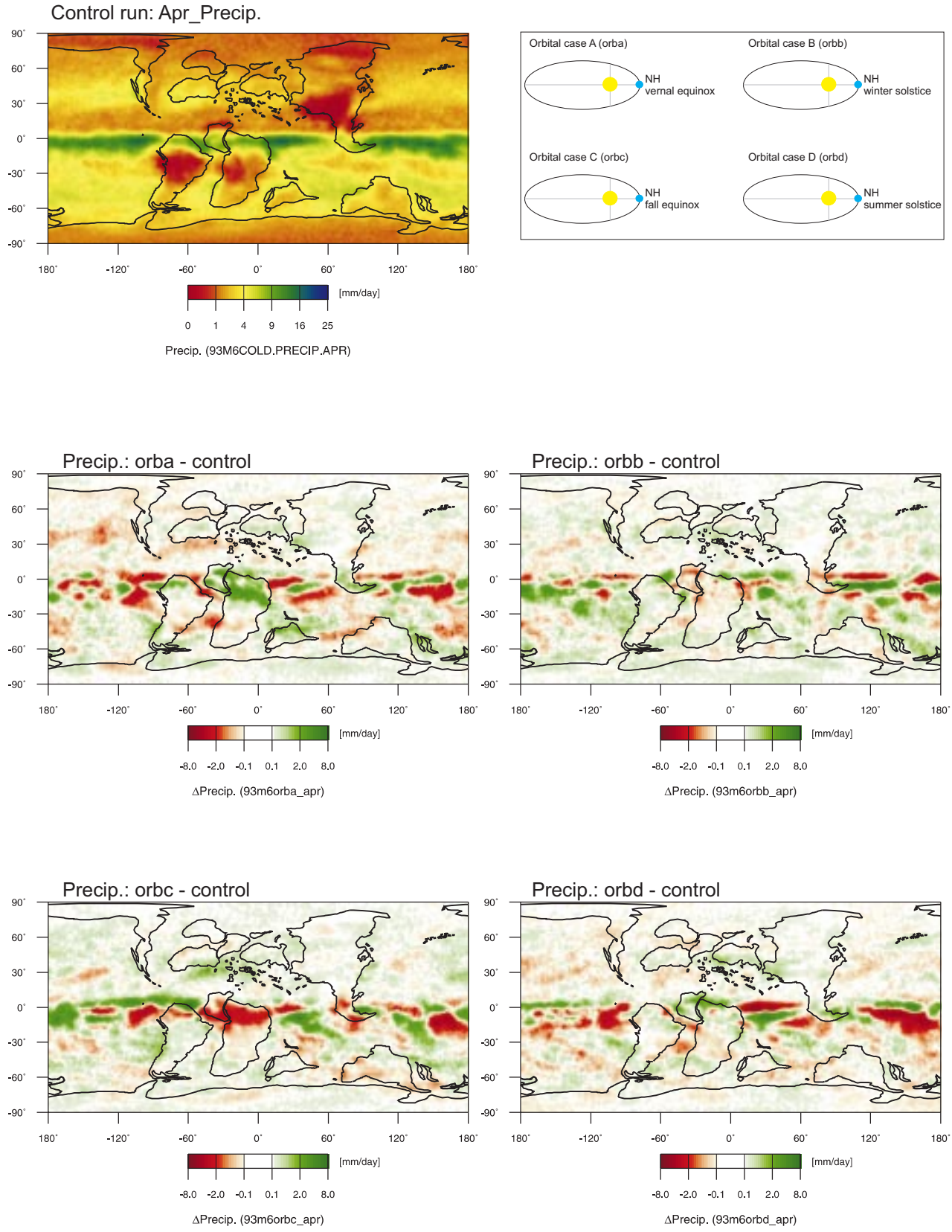

Figure 60: Model results for precipitation in April; [mm/day].

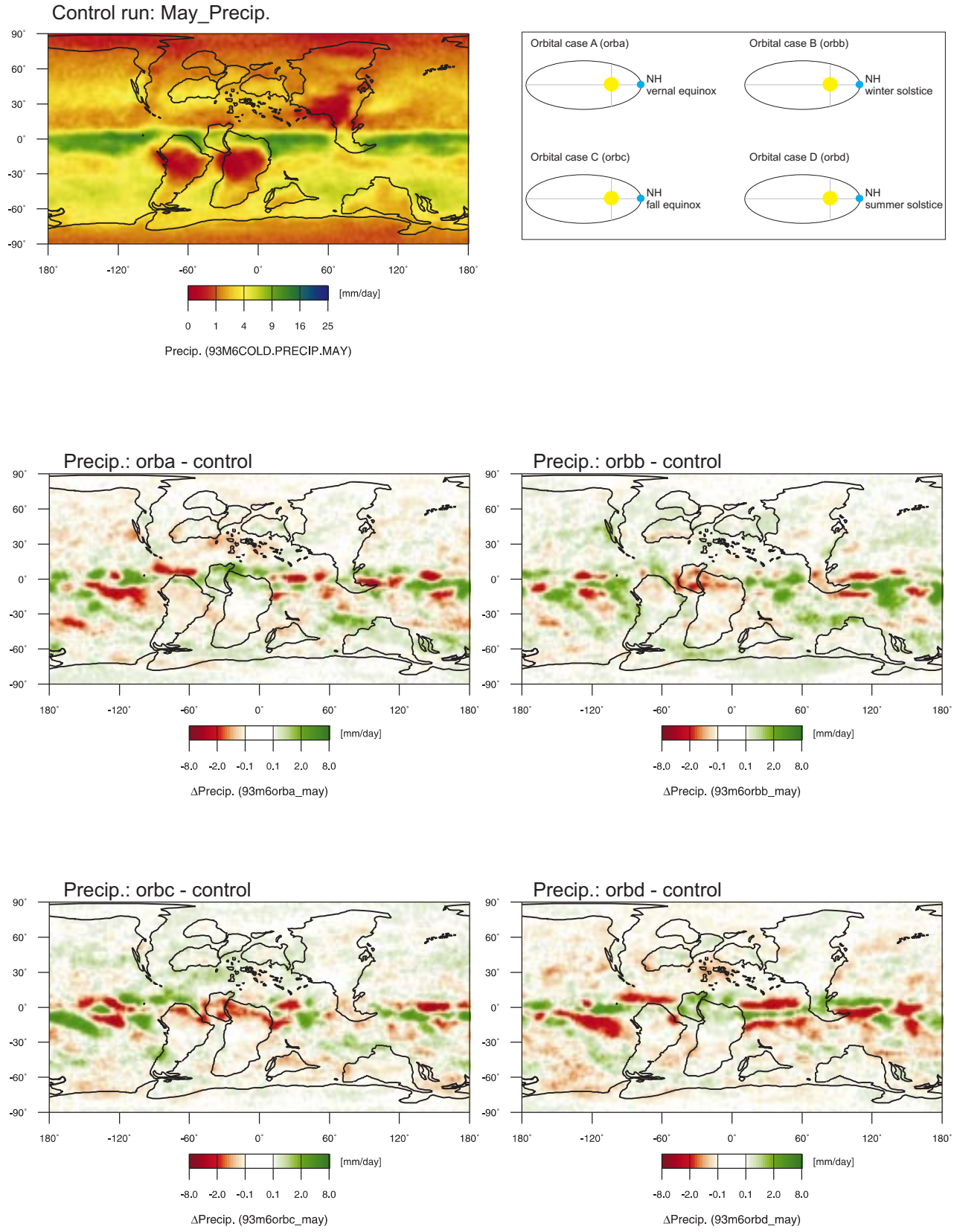

Figure 61: Model results for precipitation in May; [mm/day].

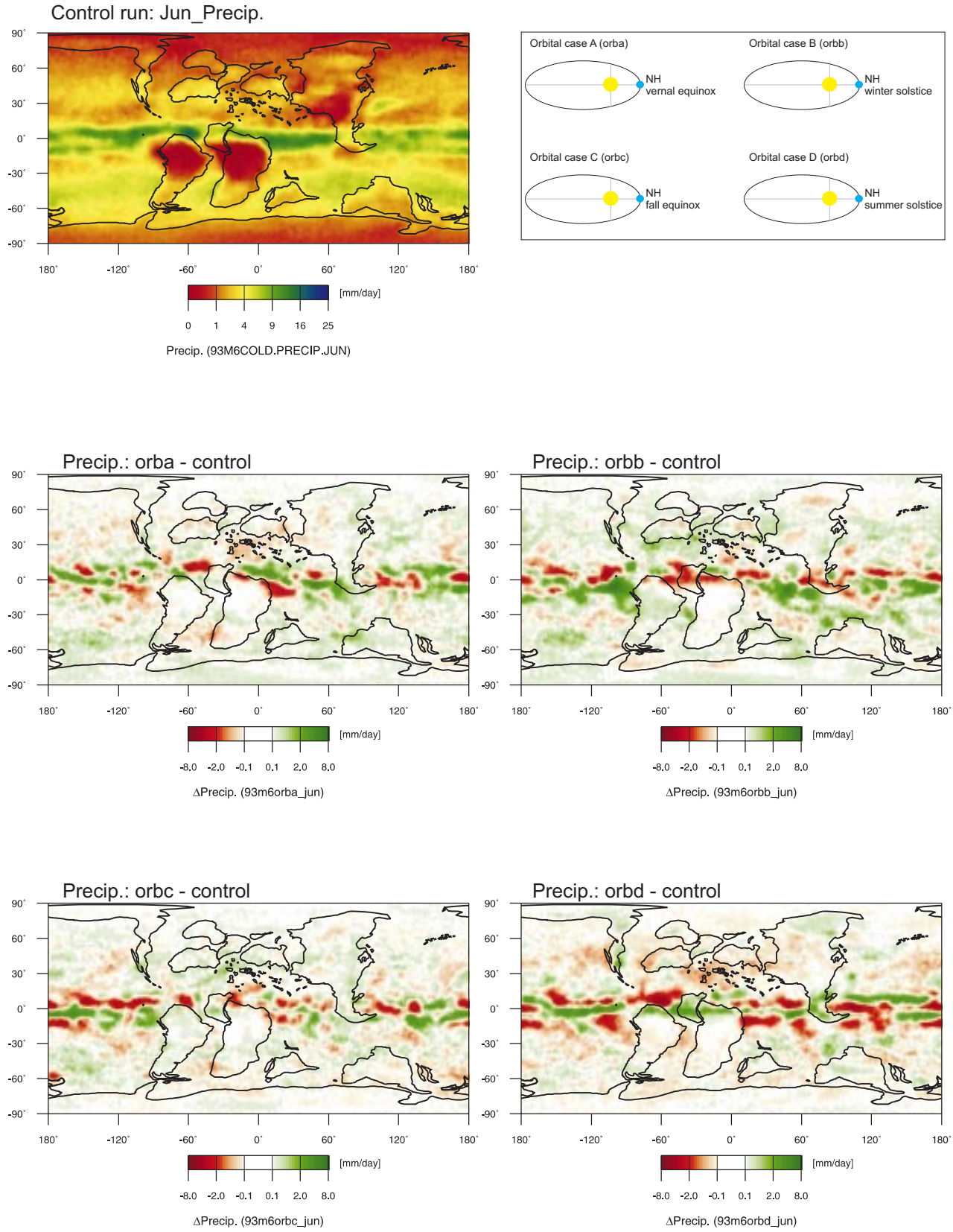

Figure 62: Model results for precipitation in June; [mm/day].

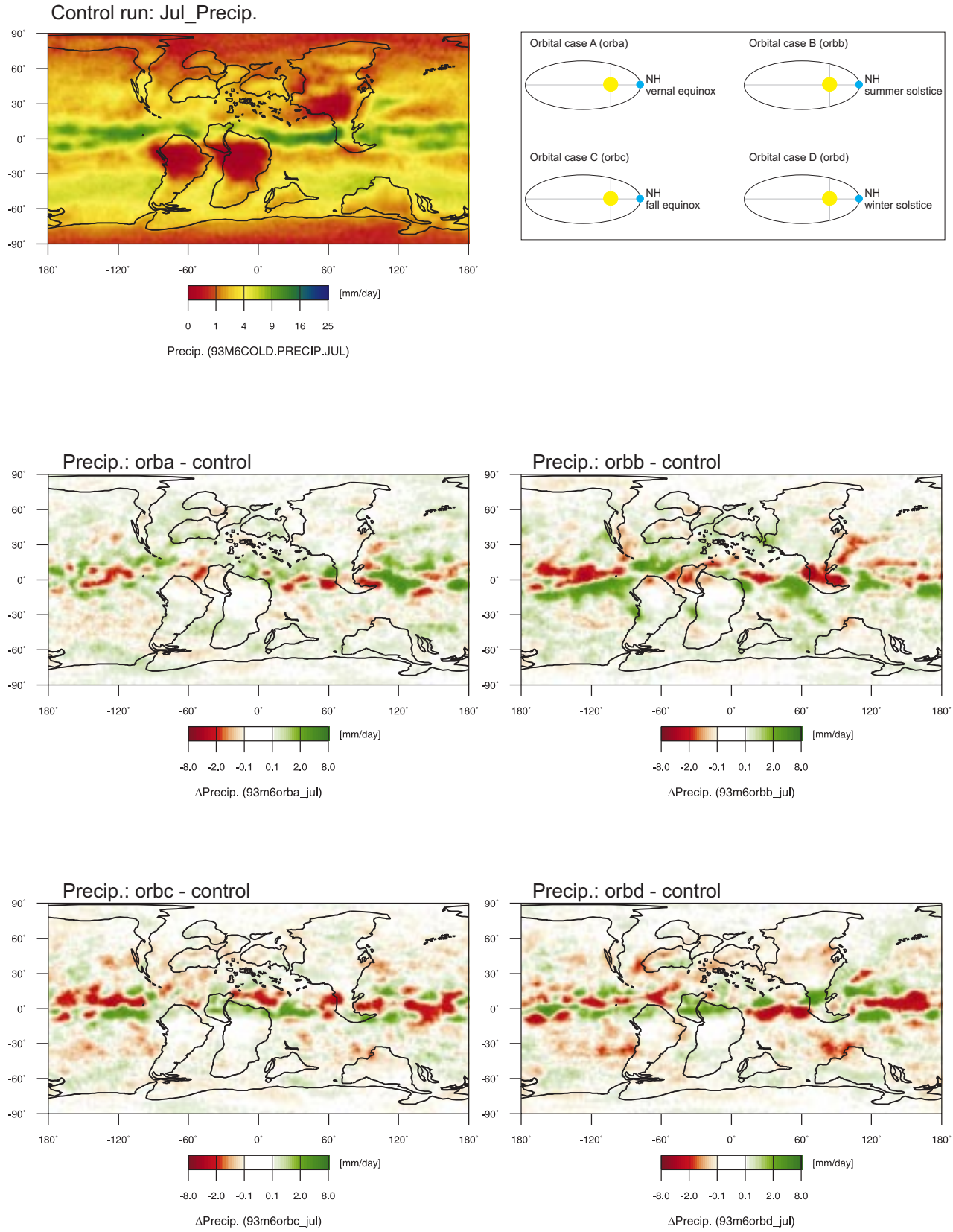

Figure 63: Model results for precipitation in July; [mm/day].

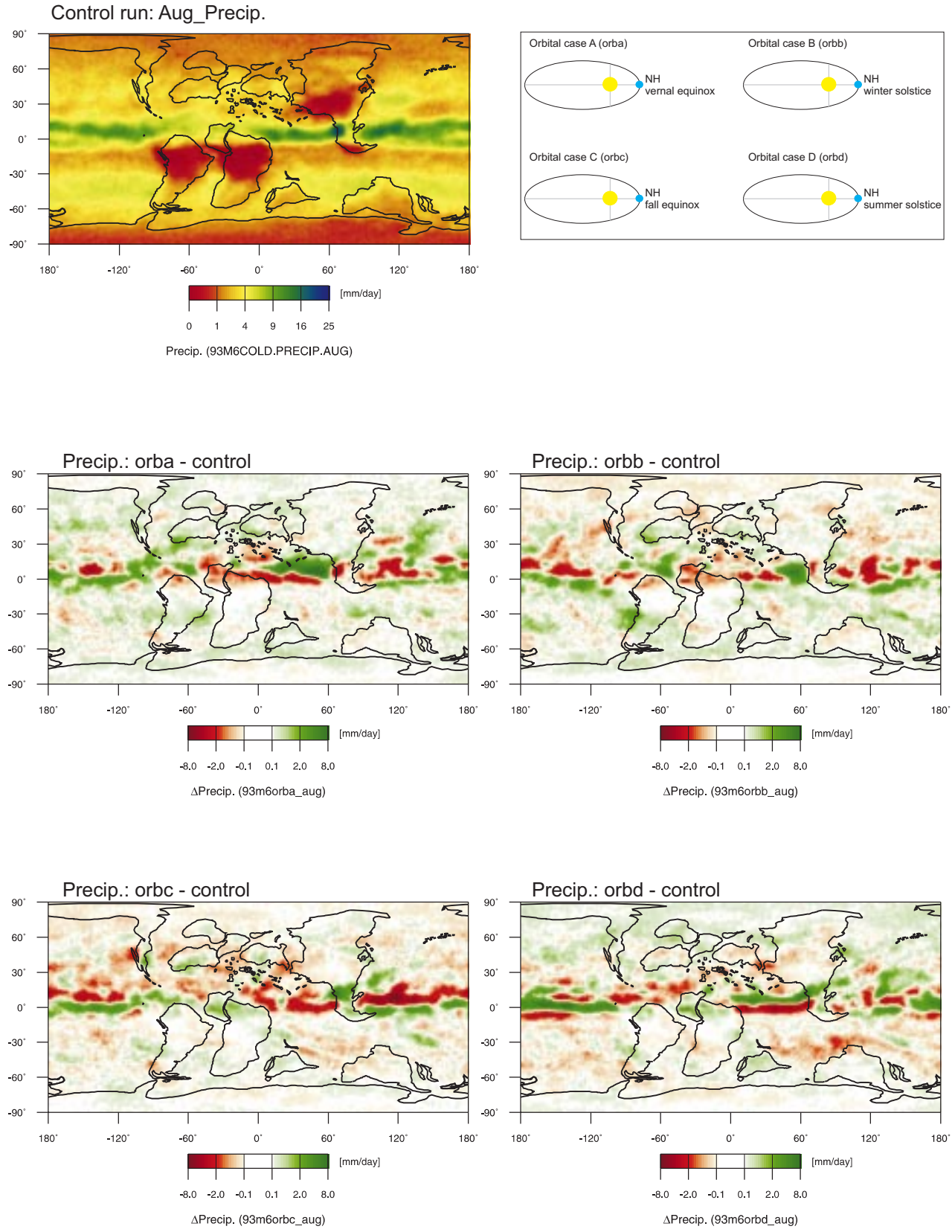

Figure 64: Model results for precipitation in August; [mm/day].

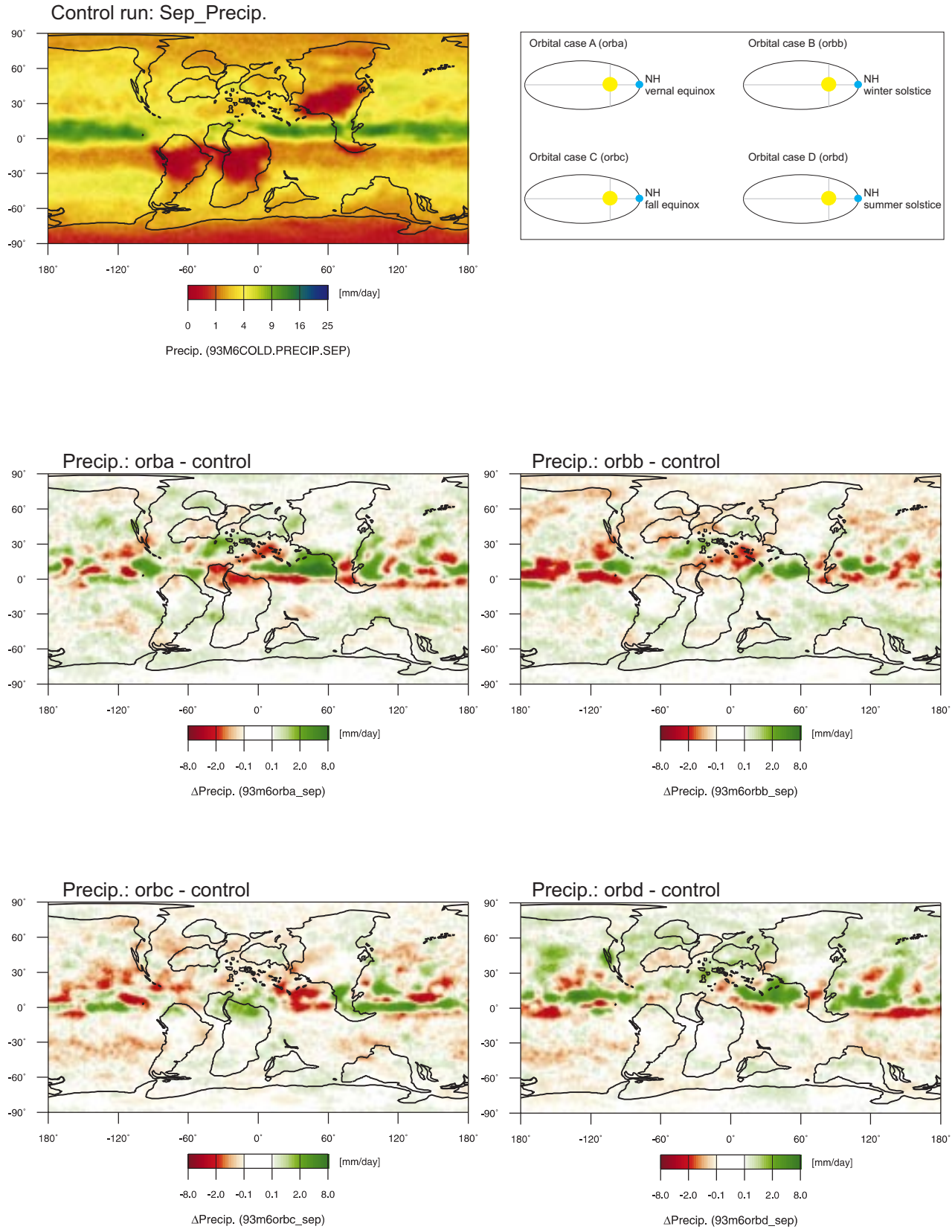

Figure 65: Model results for precipitation in September; [mm/day].

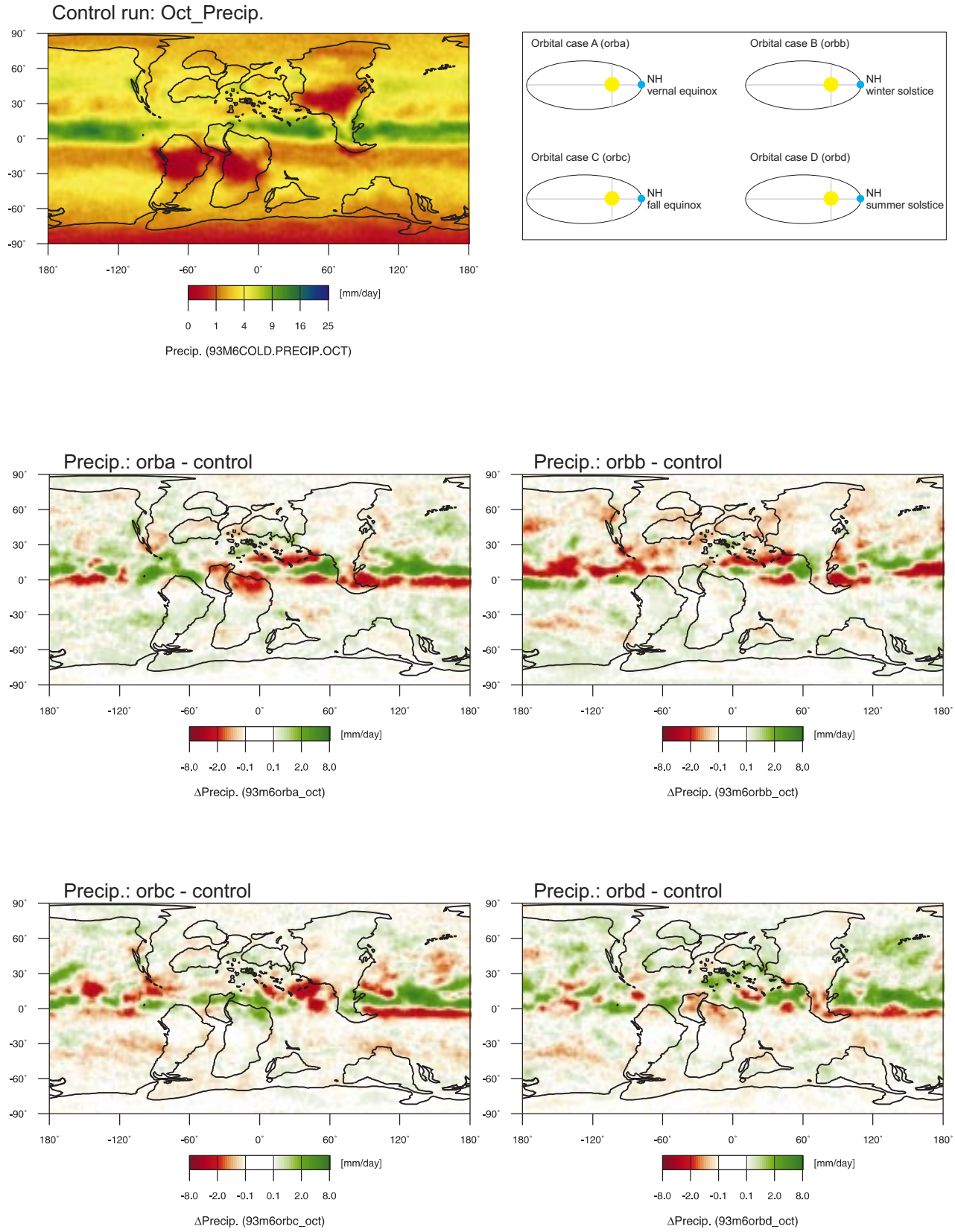

Figure 66: Model results for precipitation in October; [mm/day].

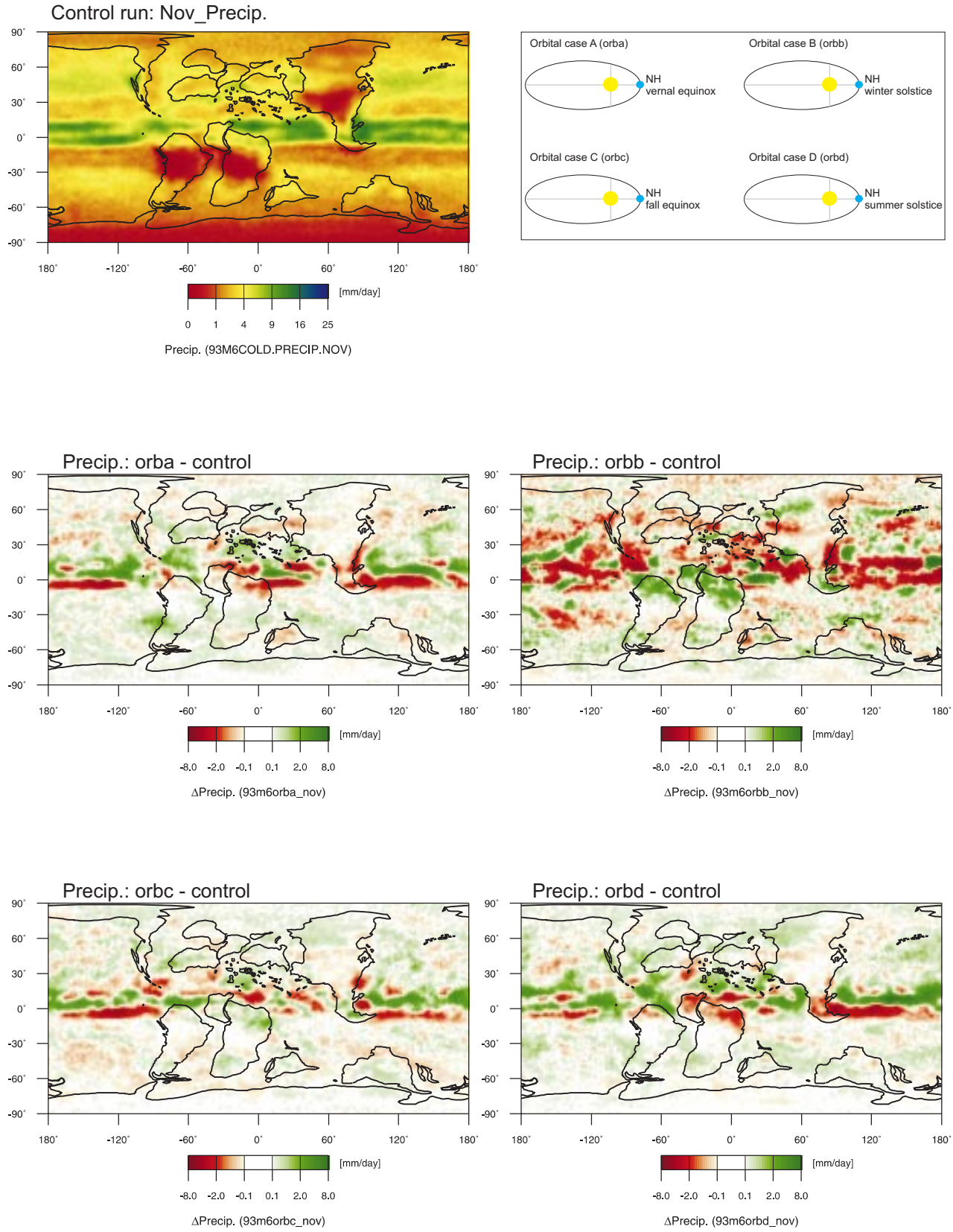

Figure 67: Model results for precipitation in November; [mm/day].

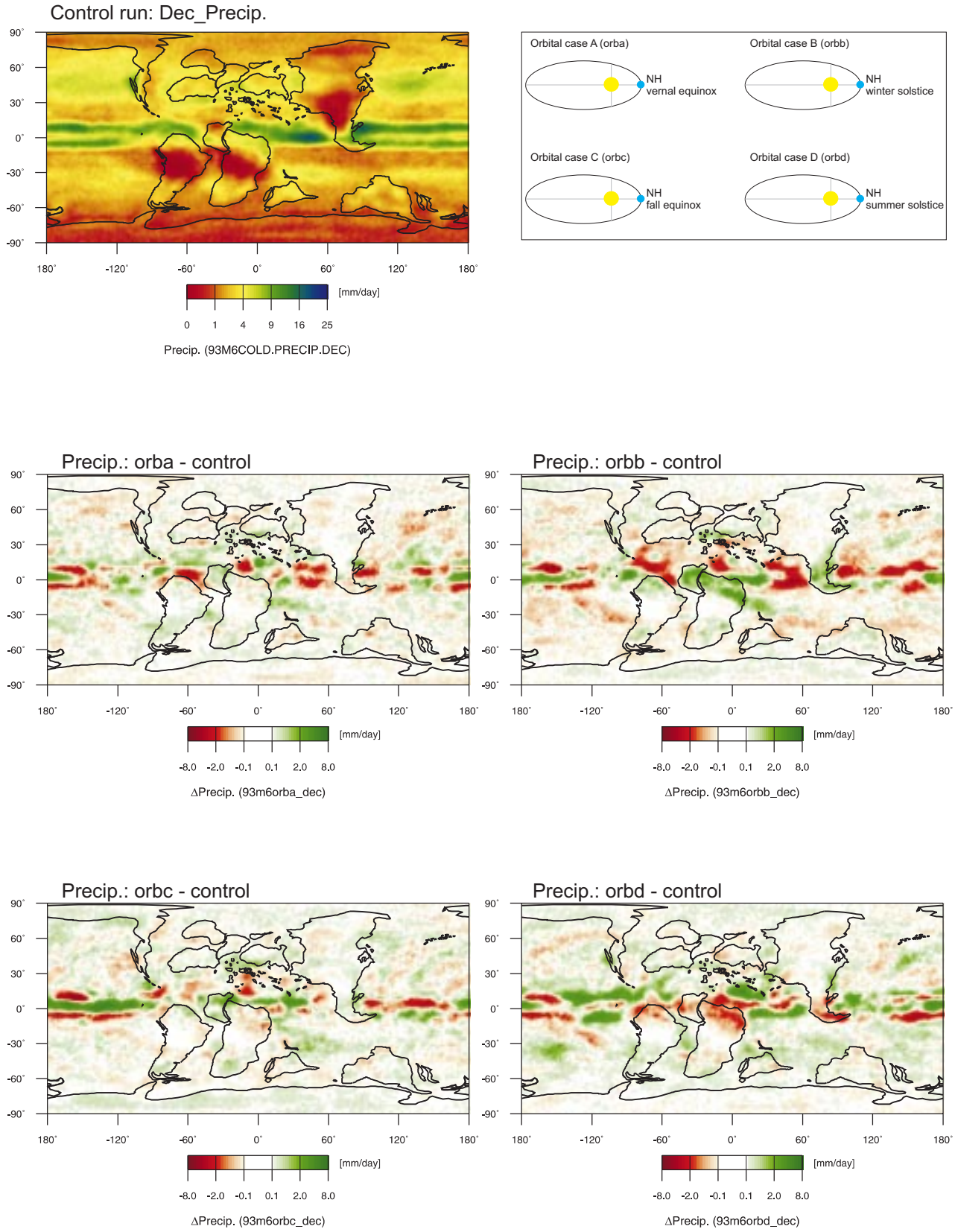

Figure 68: Model results for precipitation in December; [mm/day].

9.3.5. Surface runoff from land; [mm/day]

Figures 69-80 show the differences in the results of the orbital runs compared to the control run.
The overall distribution of surface runoff for runs with changing precessional forcing shows a distribution similar to the control run.

Orbital case A:
During orbital case A, as for all other orbital runs, regions with increased surface runoff are located next to regions with decreased surface runoff. Highly variable patterns persist throughout the year. The largest changes during orbital case A are predicted for April through June and November through December. During NH late spring and early summer, surface runoff over northern Asia decreases by up to 10 mm/day compared to the control run. In some regions this equals a 90-100% decrease. During November surface runoff changes due to orbital forcing are limited to Antarctica, where it decreases by ~70%. In December the conditions reverse; Antarctica shows increased surface runoff (~50-100%) on top of the already high surface runoff predicted for the control run (0.5-4.0 mm/day).

Orbital case B:
For orbital case B, changes were similar to those of orbital case A. There are no notable changes in the global distribution and magnitude of surface runoff changes. The only important differences were predicted for April, June, and July. During April the decrease over N-Asia is only 2-3 mm/day, which is only ~20% less than the control run. An important change was simulated for the Sevier Highlands of WNA, where a decrease of up to 9 mm/day (80-100%) compared to the control run occurred during June and July.

Orbital case C:
The setup for orbital case C produced surface runoff changes similar to those of the two previous runs. The global distribution of surface runoff remains unchanged. The data for June show a large increase in surface runoff over N-Asia (~7 mm/day), whereas the Sevier Highlands show a decrease of ~7-8 mm/day compared to the control run. For October, there is a global increase in surface runoff, especially on N-Asia, WNA, and Antarctica (up to 5-6 mm/day). During December the distribution of surface runoff changes is the opposite of orbital case A, with a decrease on Antarctica and an increase on northern WNA.

Orbital case D:
From January through April, surface runoff results simulated for orbital case D show only marginal changes when compared to the control run. During these months, relative changes in surface runoff are limited to middle- to high northern latitudes and high southern latitudes. Changes relative

to the control run do not exceed +/- 0.2 mm/day. In May, changes relative to the control run increase in the NH. An increase in relative surface runoff was simulated for the Sevier Highlands, northern WNA, and the northern parts of central Asia. Surface runoff in those regions increases by ~ 5 mm/day over the ~ 10 mm/day simulated for the control run. The trend of increasing surface runoff in the NH reverses in June and July when surface runoff begins to decrease compared to the control run. The decrease is greatest over WNA and reaches up to 5 mm/day in the southern Sevier Highlands. From August through September changes relative to the control run are again marginal, generally about ~ 0.2 mm/day. From October through December, major relative changes in surface runoff take place in the SH, whereas the NH is largely unaffected. Relative changes on Antarctica increase by ~ 3 mm/day during October. In November, northern Antarctica shows a decrease of up to 2-3 mm/day, whereas the southern polar region still shows a minimal increase of ~ 0.2 mm/day. In December there are no major changes relative to the control run.

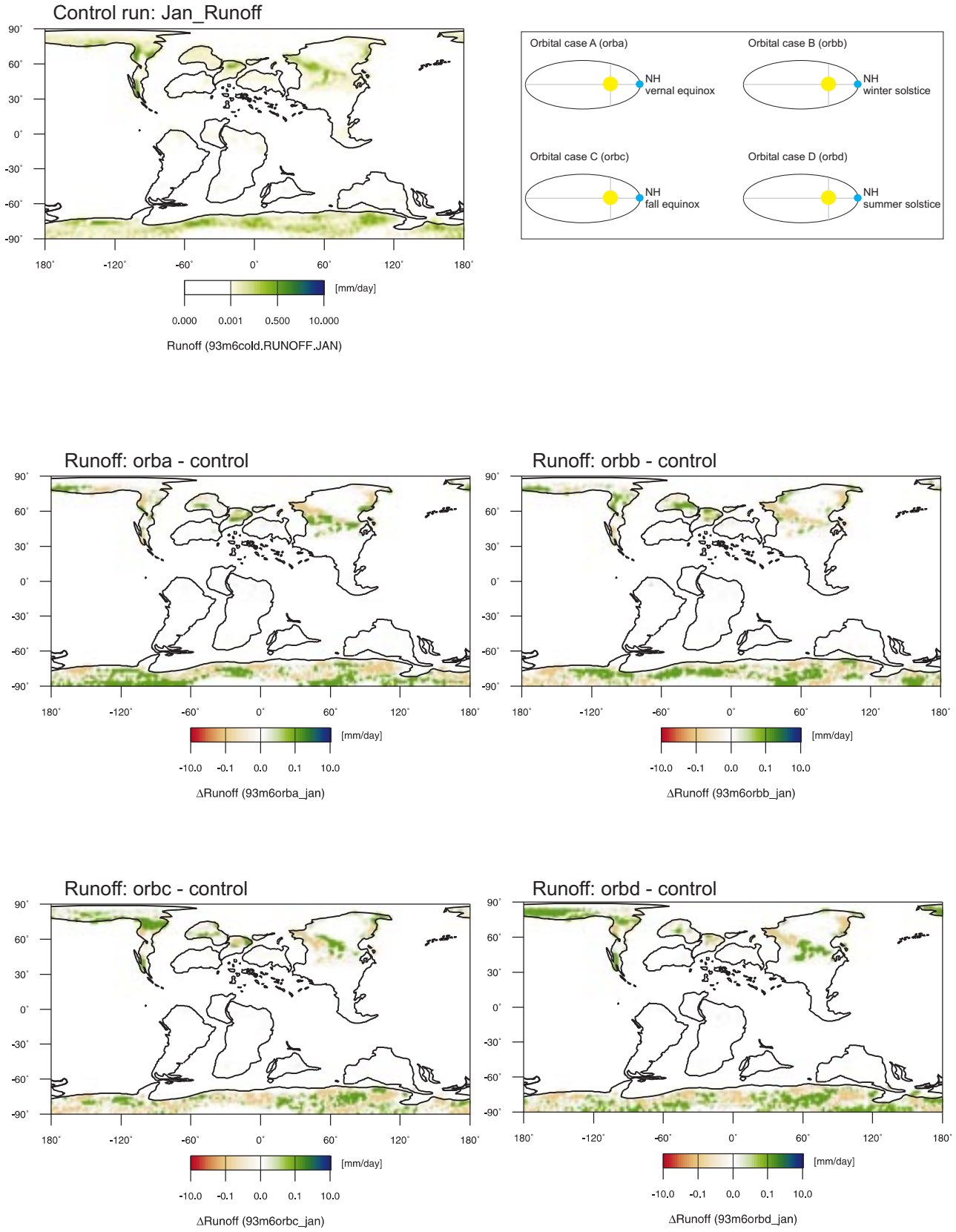

Figure 69: Model results for surface runoff from land in January; [mm/day].

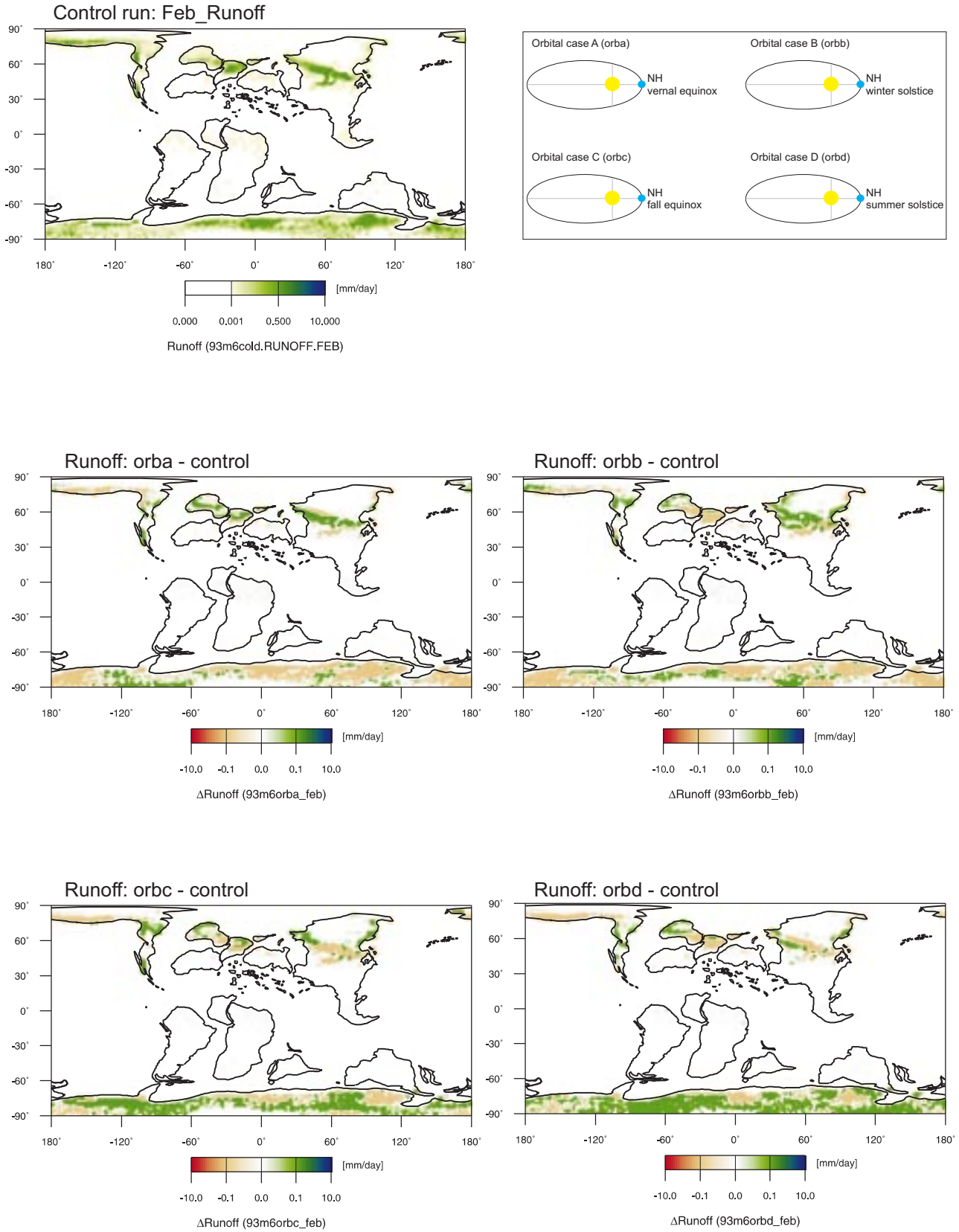

Figure 70: Model results for surface runoff from land in February; [mm/day].

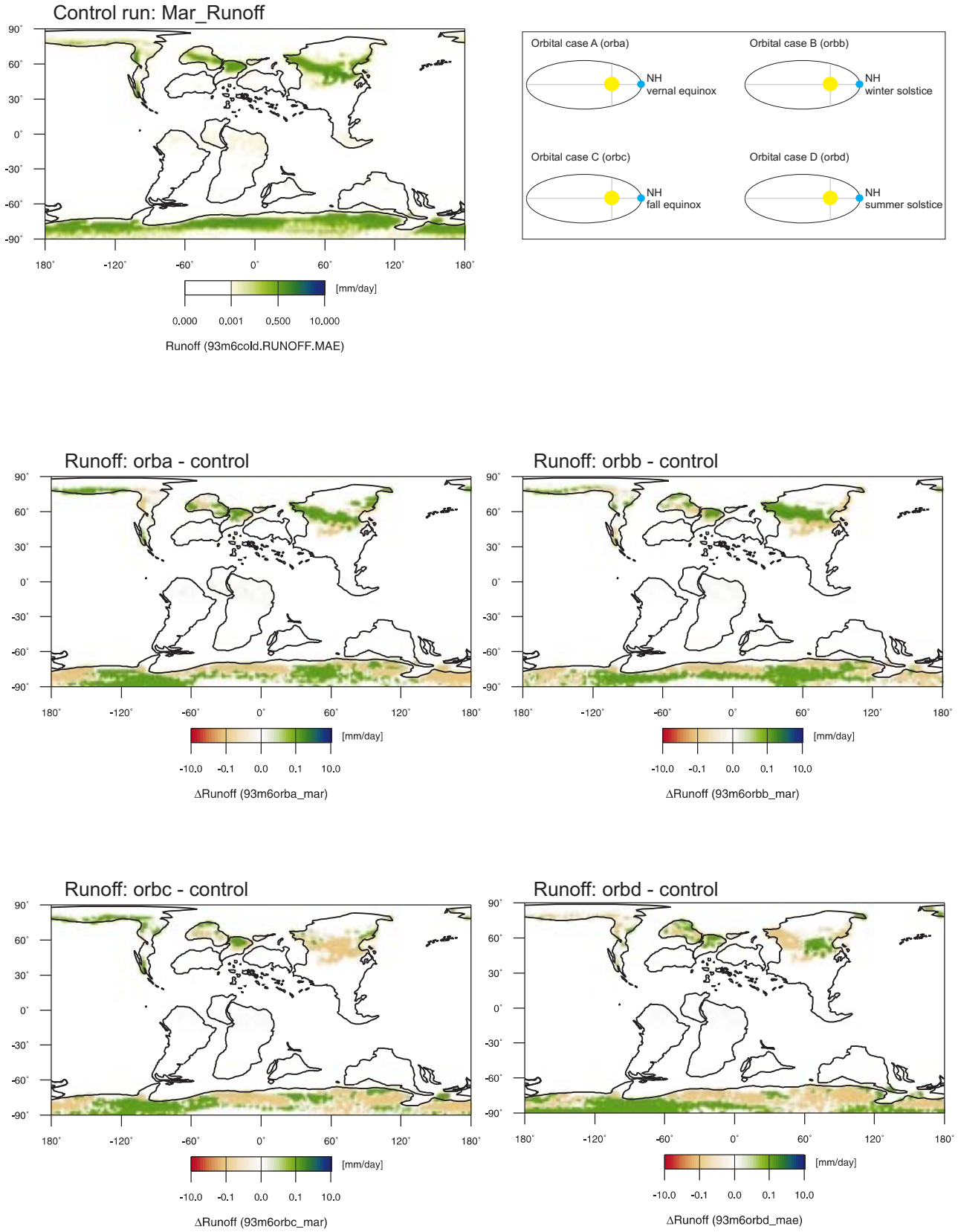

Figure 71: Model results for surface runoff from land in March; [mm/day].

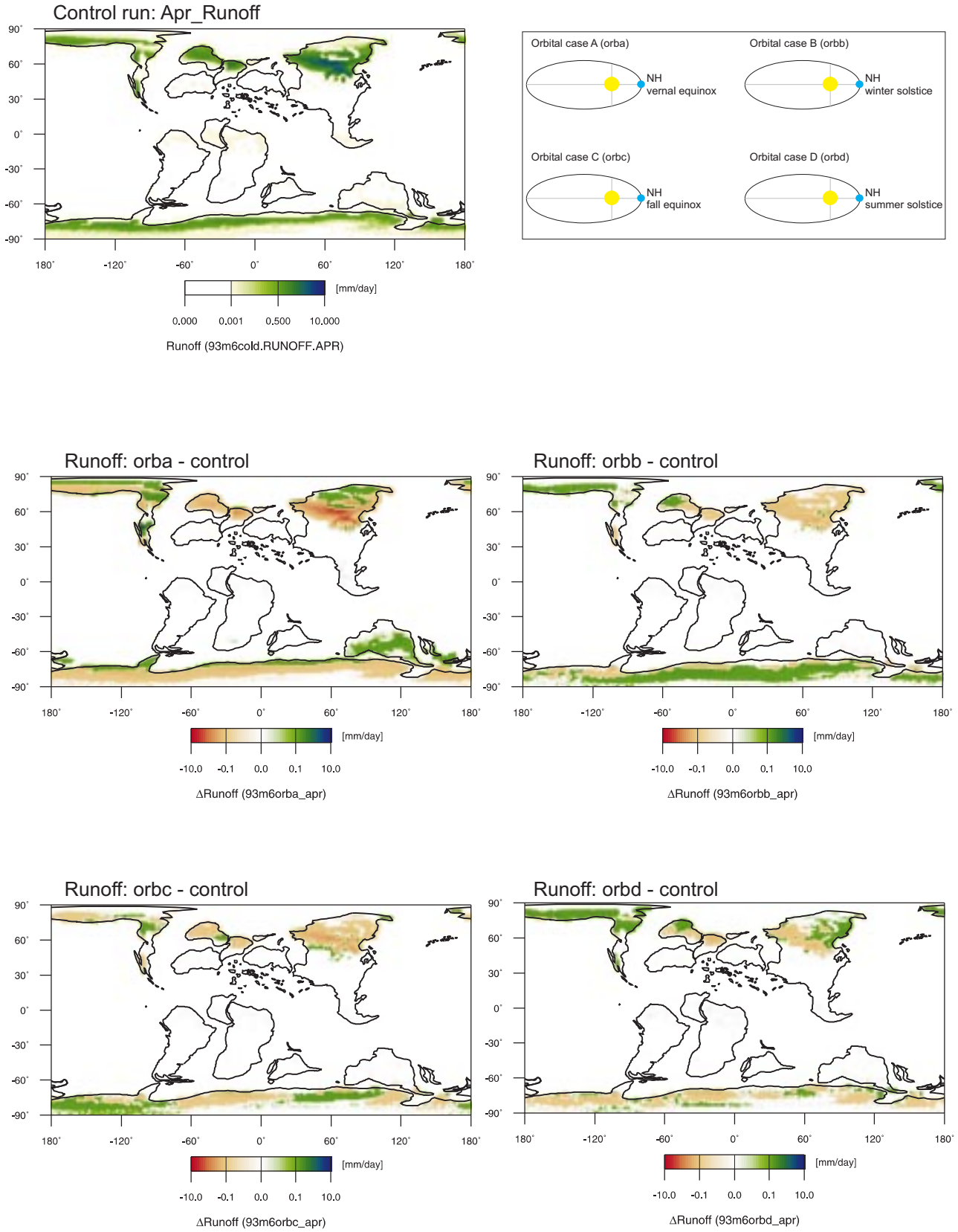

Figure 72: Model results for surface runoff from land in April; [mm/day].

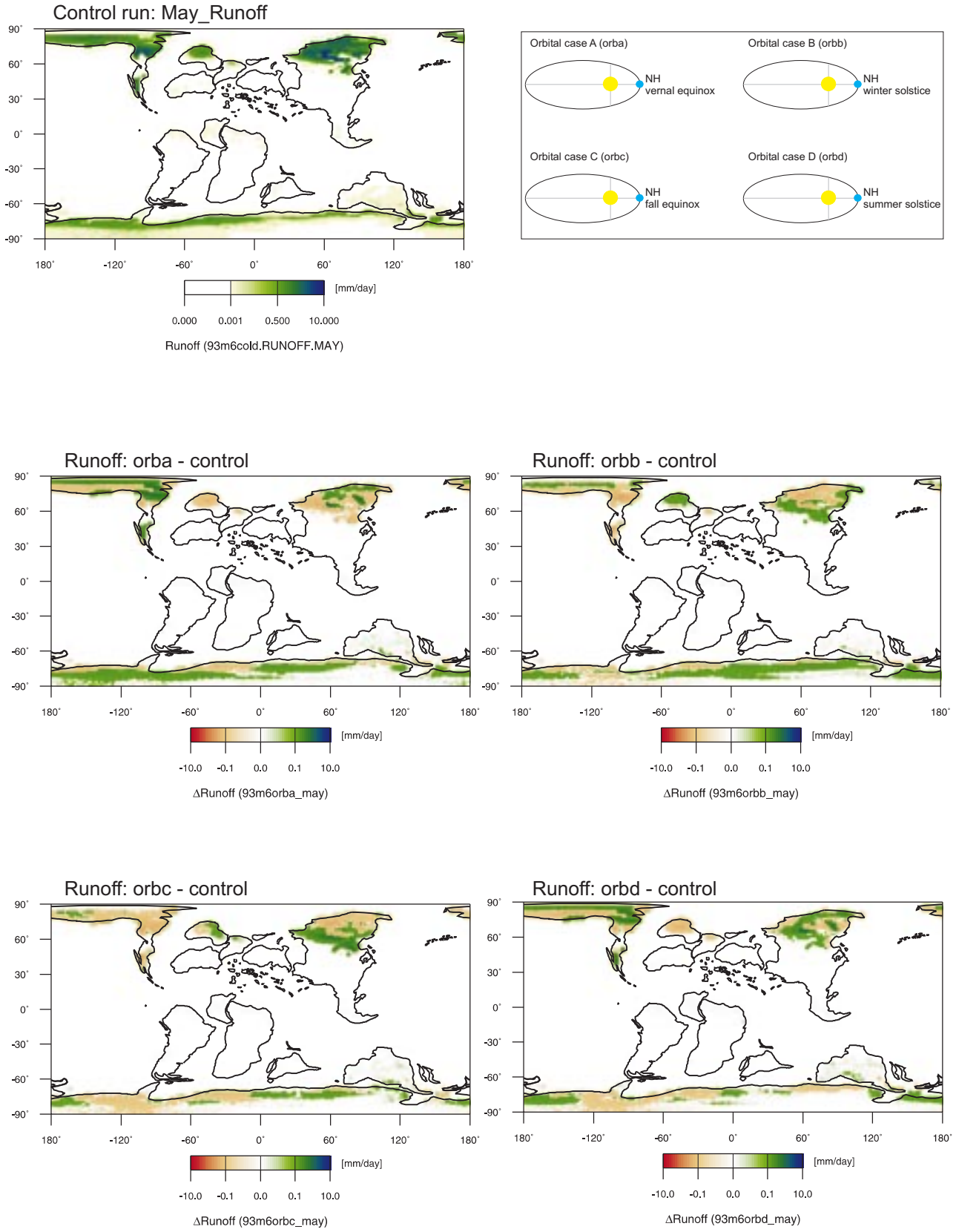

Figure 73: Model results for surface runoff from land in May; [mm/day].

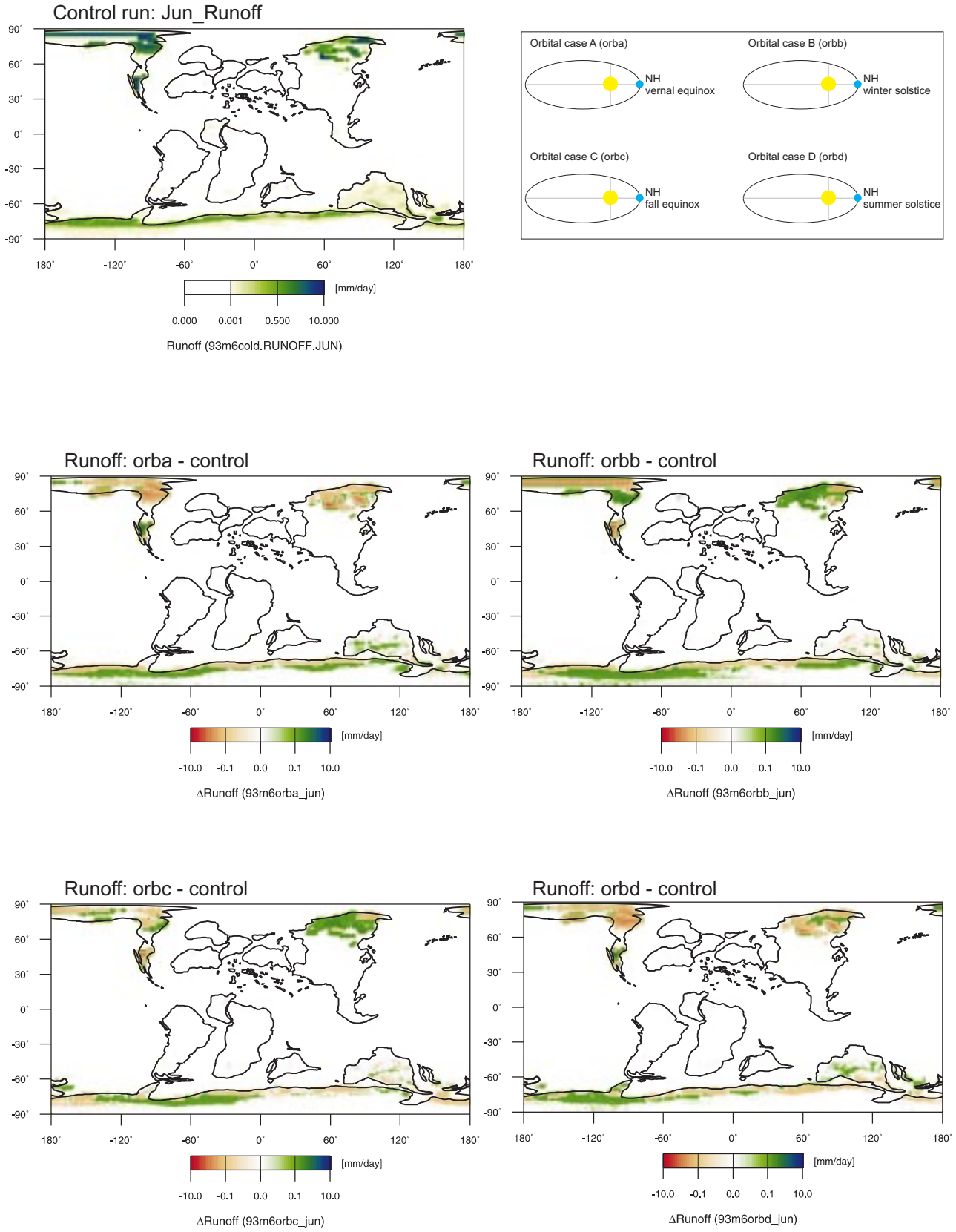

Figure 74: Model results for surface runoff from land in June; [mm/day].

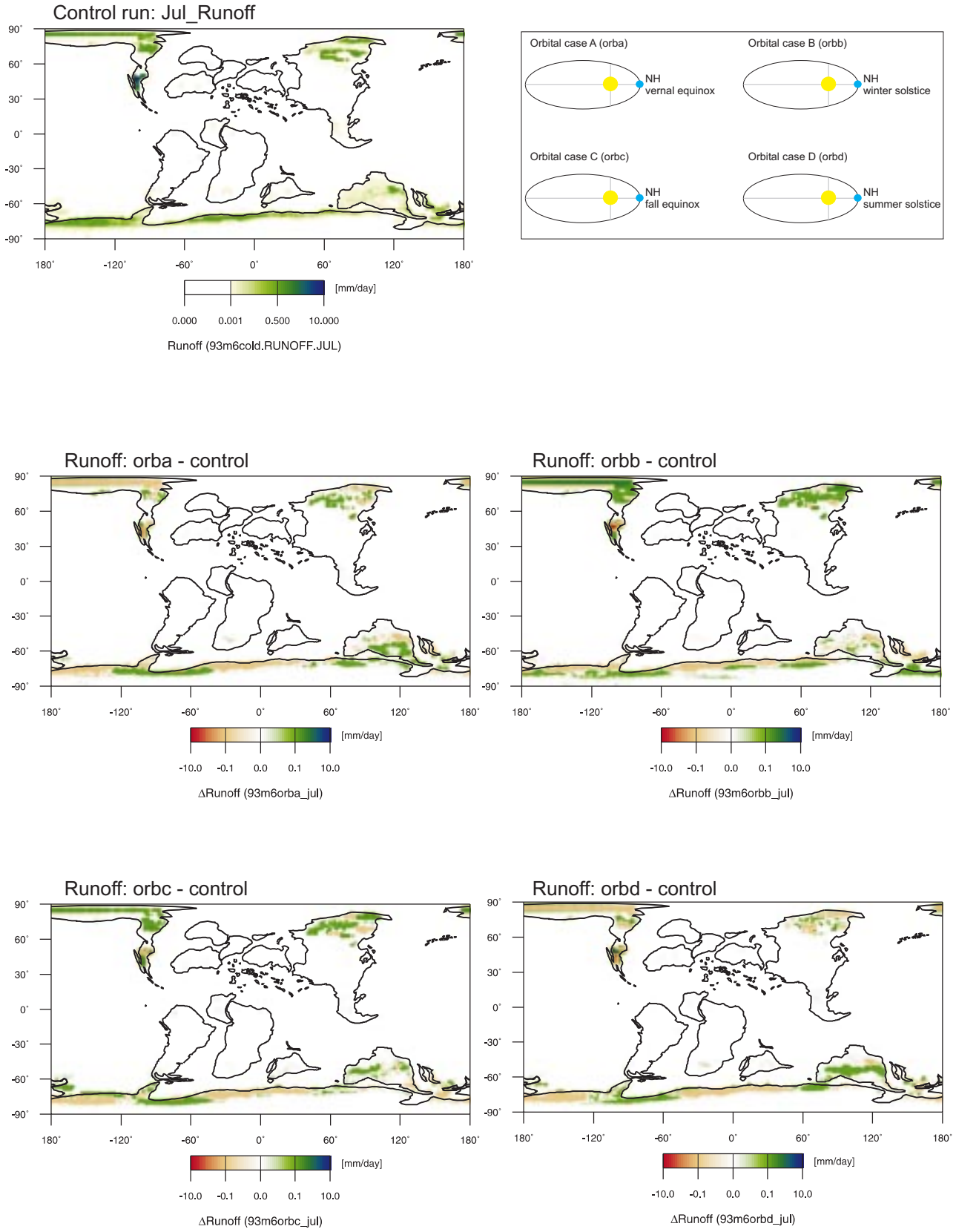

Figure 75: Model results for surface runoff from land in July; [mm/day].

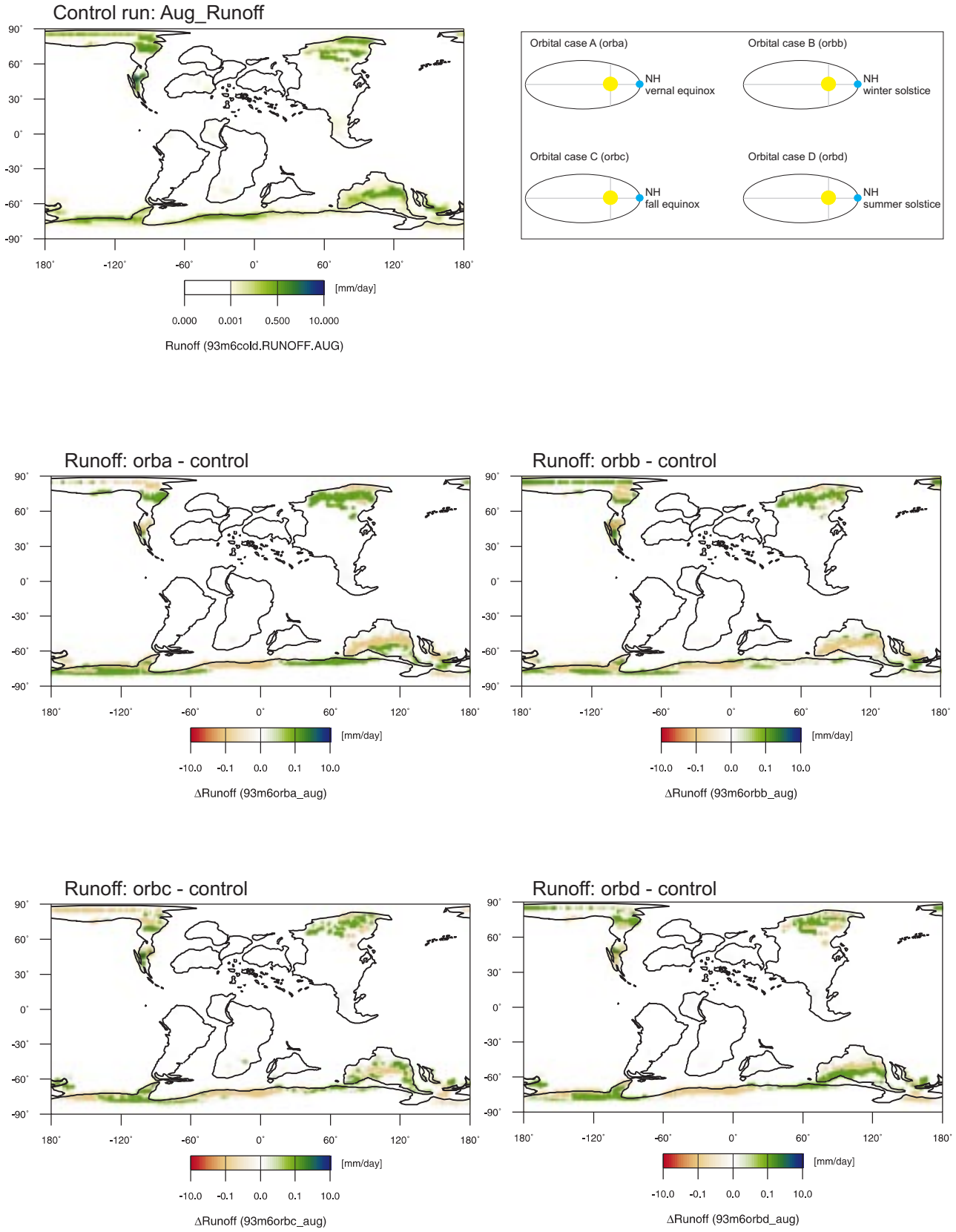

Figure 76: Model results for surface runoff from land in August; [mm/day].

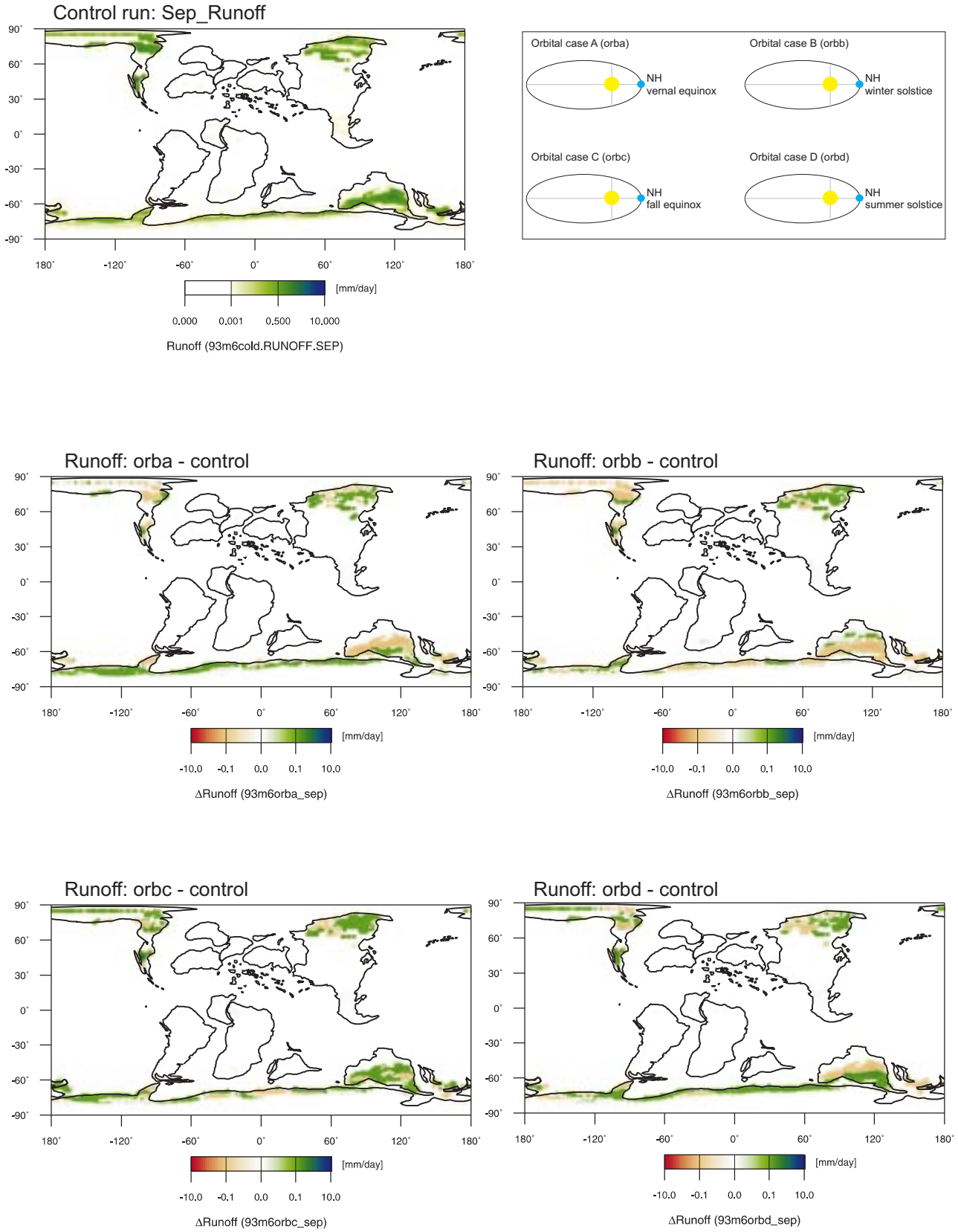

Figure 77: Model results for surface runoff from land in September; [mm/day].

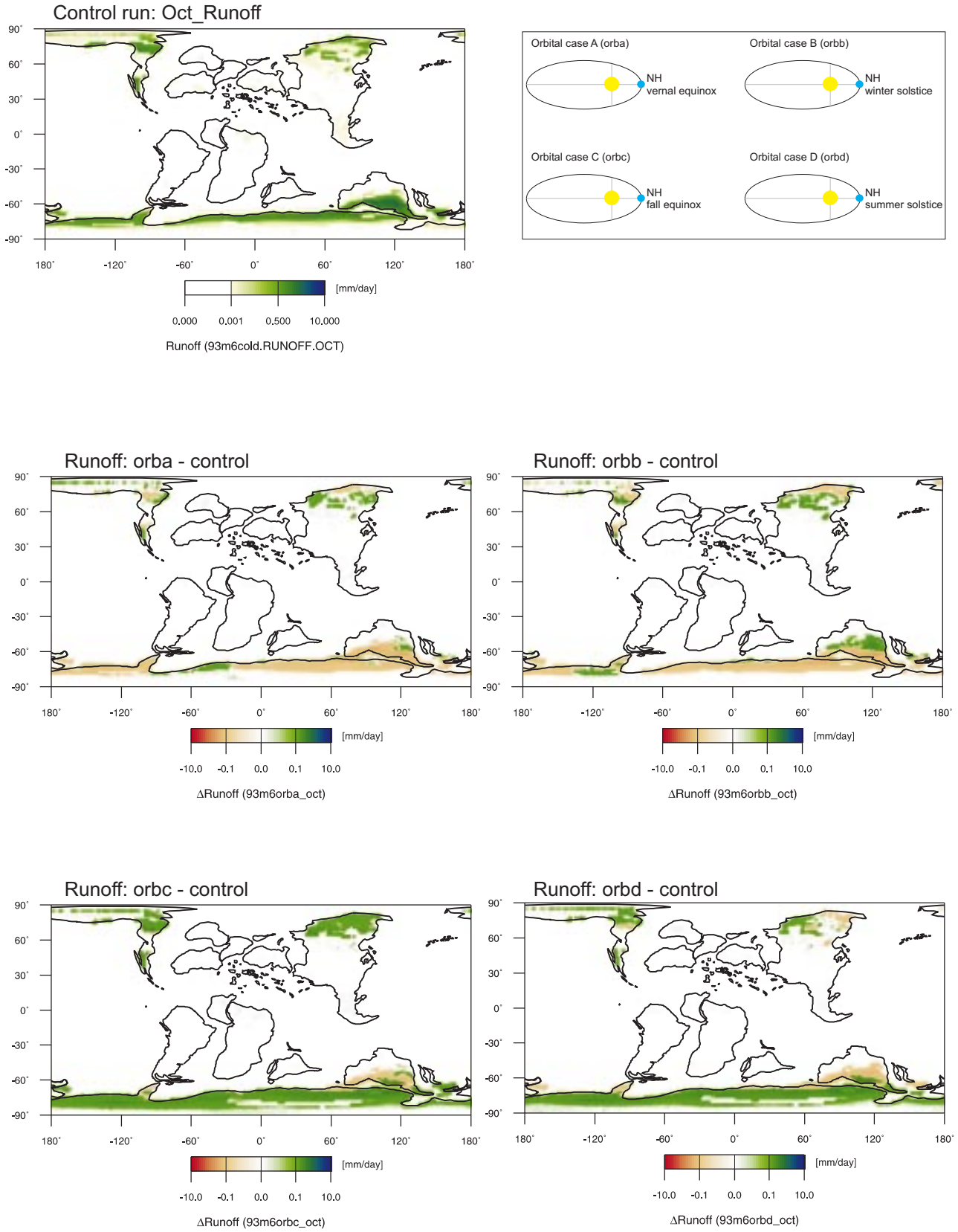

Figure 78: Model results for surface runoff from land in October; [mm/day].

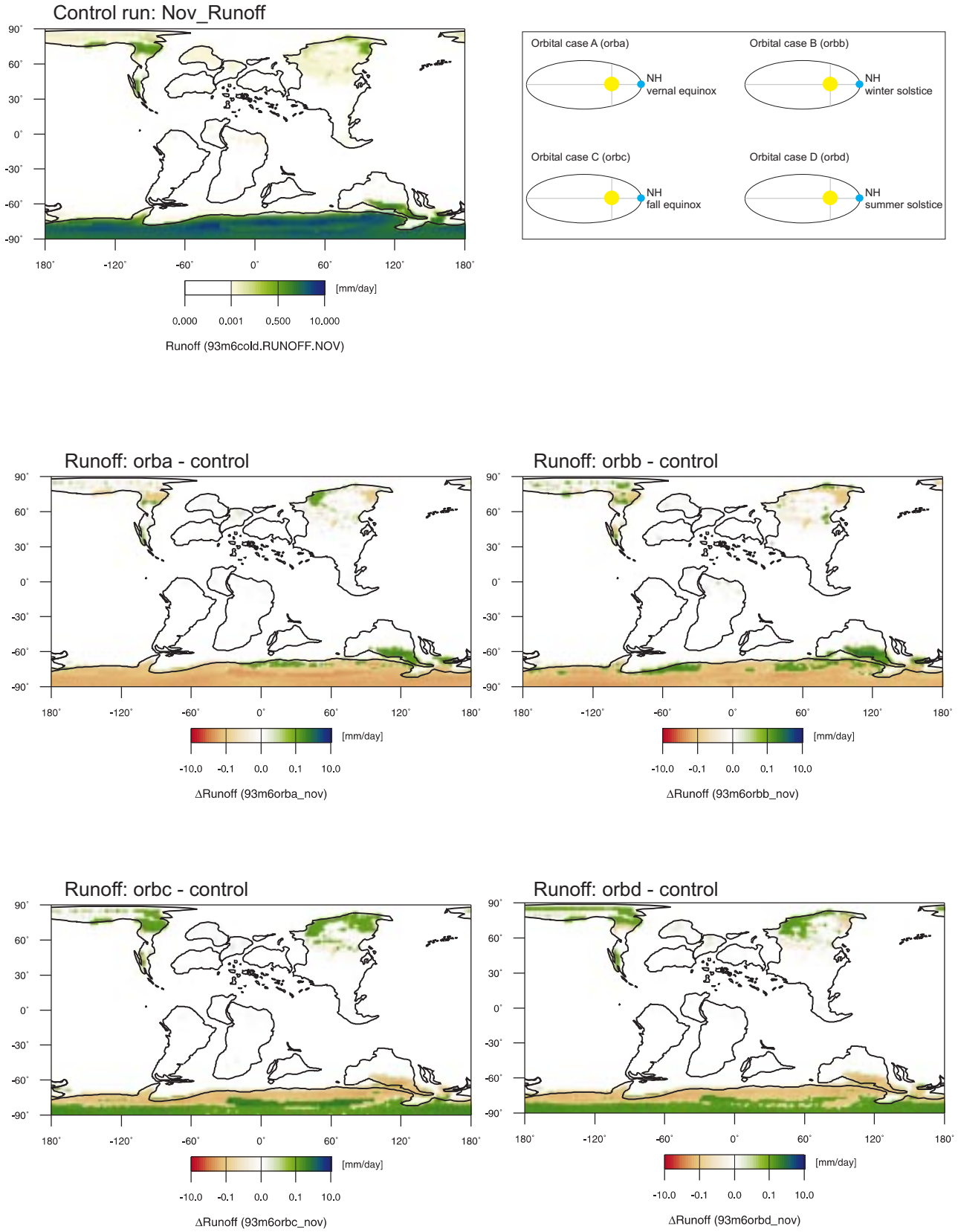

Figure 79: Model results for surface runoff from land in November; [mm/day].

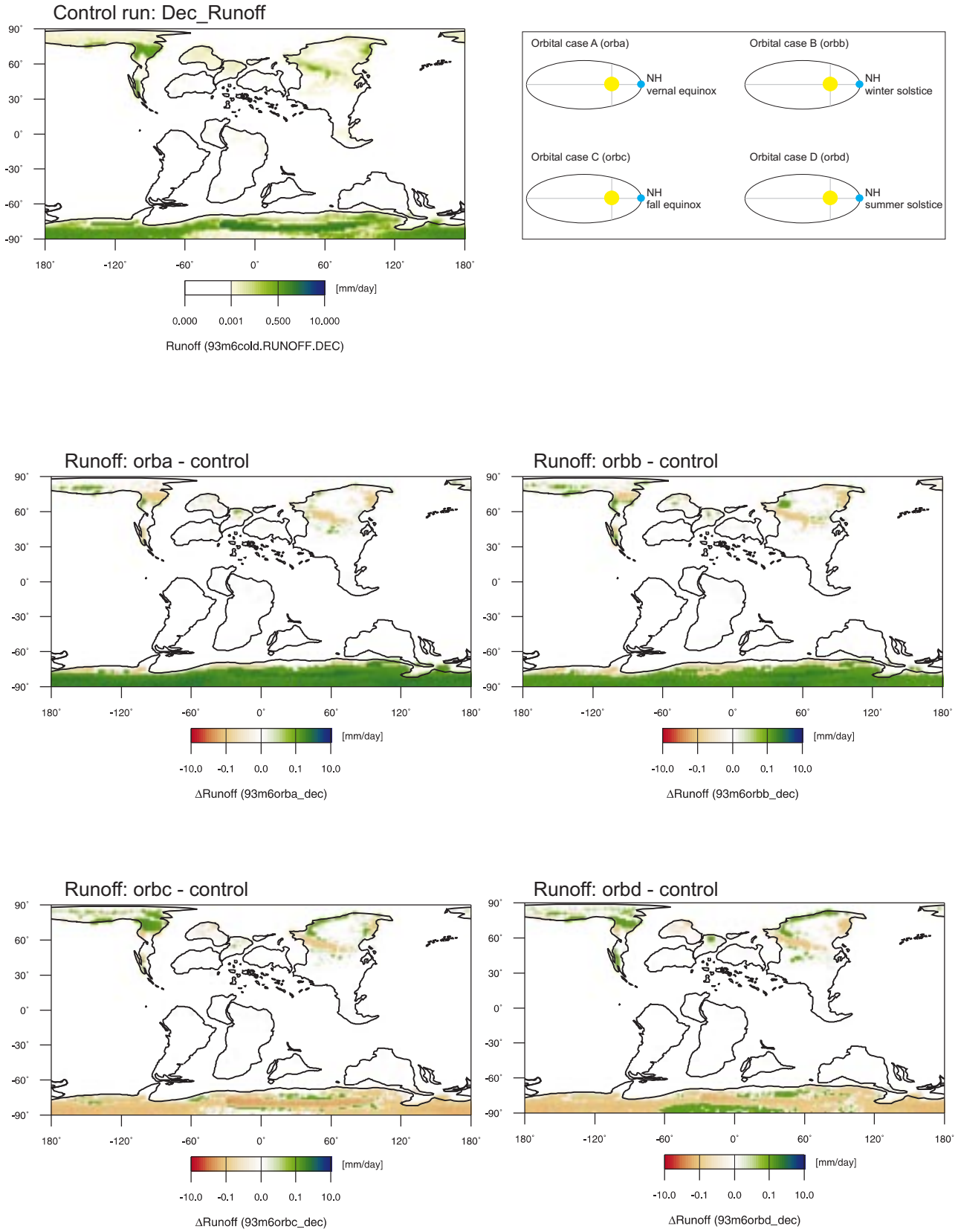

Figure 80: Model results for surface runoff from land in December; [mm/day].

9.3.6. Subsurface runoff (Drainage); [mm/day]

Figures 81-92 show the differences in the results of the orbital runs compared to the control run.

The overall pattern of subsurface runoff (drainage) remains unchanged throughout the year during the control run. Neither the distribution, nor the overall magnitude of the subsurface runoff varies. However, dramatic changes were simulated for changing precessional forcing.

Orbital case A:
The simulations for orbital case A indicate that the largest changes relative to the control run occurred along the northern and southern margins of the Tethys. The largest sensitivity to precessional forcing is in N-Africa and at the southern tip of Asia. The largest response in N-Africa occurs in April and May, when subsurface runoff increases in some regions by ~4 mm/day, an increase of ~100 % compared to control run. For most of the year changes are in the range of ~ +/- 0.4 mm/day. Generally, the northern hemisphere shows an increase in subsurface runoff during the year, whereas the southern hemisphere seems to respond seasonally or to show a variable pattern. Changes on WNA never exceed (Oct., Nov., Dec.) 0.5 mm/day. For the rest of the year changes in subsurface runoff are marginal or absent.

Orbital case B:
The monthly distribution of subsurface runoff does change from orbital case A to orbital case B. There is an increase of about 0.5-1.5 mm/day on N-Africa relative to the control run. Changes over WNA never exceed 0.6 mm/day throughout the year. Globally, the smallest changes occur in northern hemisphere summer and fall. During this time the largest difference to the control run is predicted to be 0.5 mm/day, in Europe. Antarctica shows slightly increased subsurface runoff along the its margin, but values never exceed 0.25 mm/day.

Orbital case C:
As expected, this setup produced results opposite to orbital case A. This is clearly recognizable from March through June and from October through December. Changes range between 0.5-1.0 mm/day. Maximum variation is reached during April over northern S-America, where values increase to ~5 mm/day. Another region which is sensitive to orbital forcing is southernmost Asia, where subsurface runoff increases by as much as 4 mm/day (September) and decreases by as much as 1.5 mm/day. Generally, subsurface runoff over WNA increases throughout the year, but values never exceed 0.6 mm/day.

Orbital case D:

Relative changes of subsurface runoff occur in the same regions as in the three previous orbital cases. Compared to the control run, there are no changes in subsurface runoff for Antarctica, central S-America, central Africa, and northern and central Asia. Only relatively small changes, not exceeding +/- 1 mm/day are indicated for the NH. The greatest changes occur in southern S-America, northern Africa, and the southernmost tip of Asia. Changes relative to the control run decrease from January through April, with a maximum of ~ - 3-4 mm/day in February. Beginning in May, the equatorial land masses show a trend towards increasing subsurface runoff compared to the control run. The greatest increase is reached in southern Asia during August (+ 6 mm/day). Increasing subsurface runoff persists in those regions until September. Globally, relative changes of +/- 1 mm/day were predicted for October. From November through December, subsurface runoff relative to the control run increases up to 1.5 mm/day in the NH, whereas changes in the SH are again limited to the equatorial region.

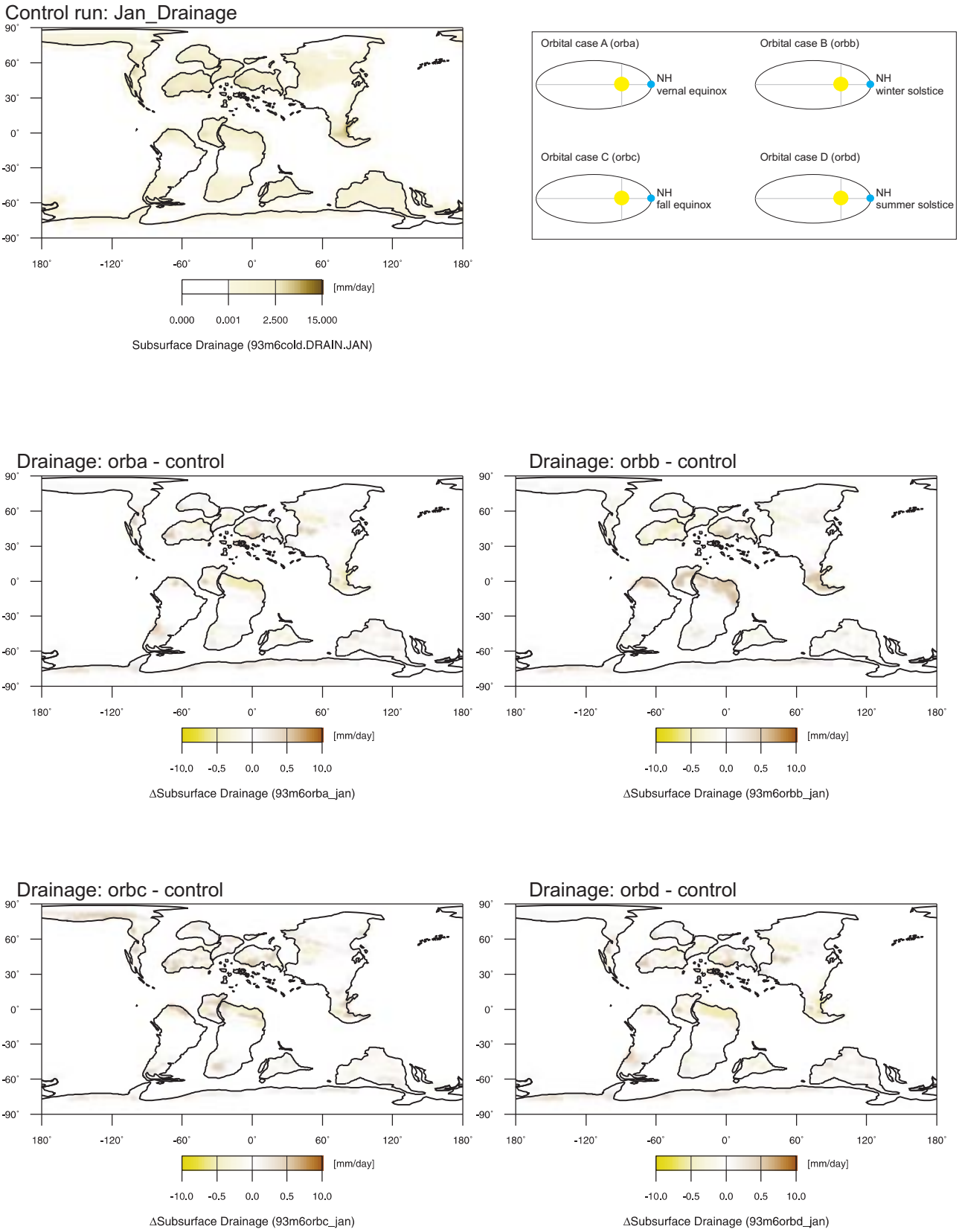

Figure 81: Model results for subsurface runoff (drainage) in January; [mm/day].

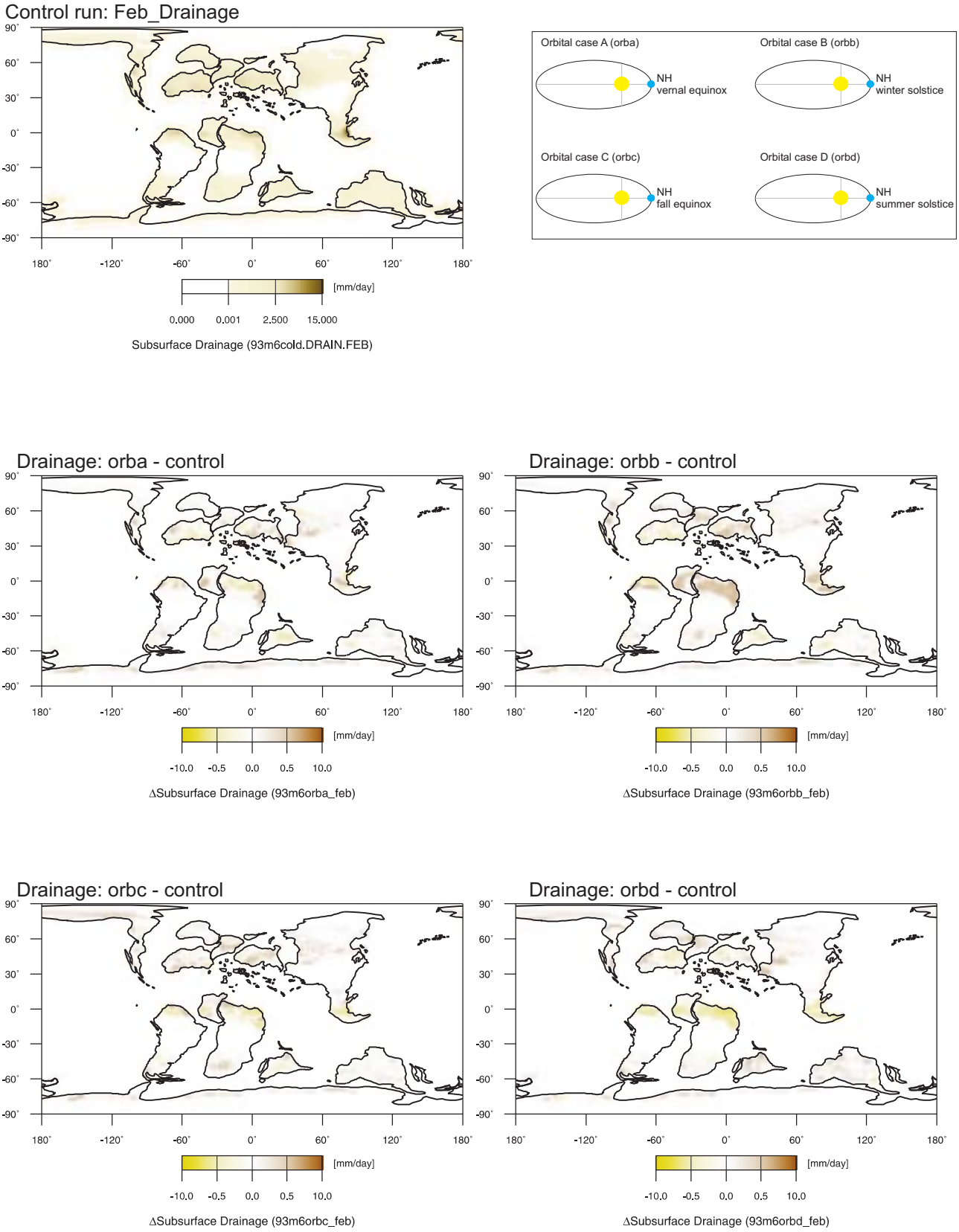

Figure 82: Model results for subsurface runoff (drainage) in February; [mm/day].

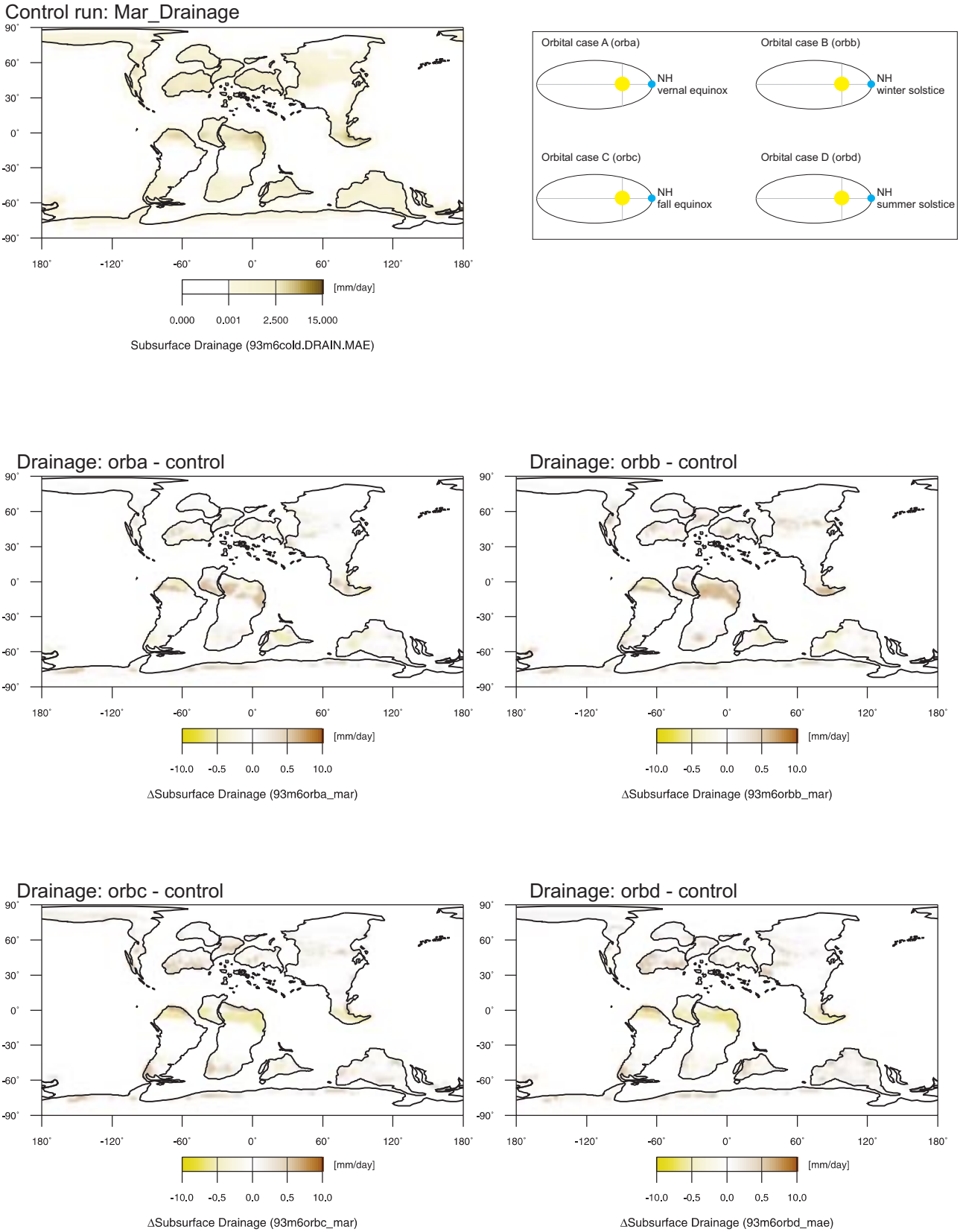

Figure 83: Model results for subsurface runoff (drainage) in March; [mm/day].

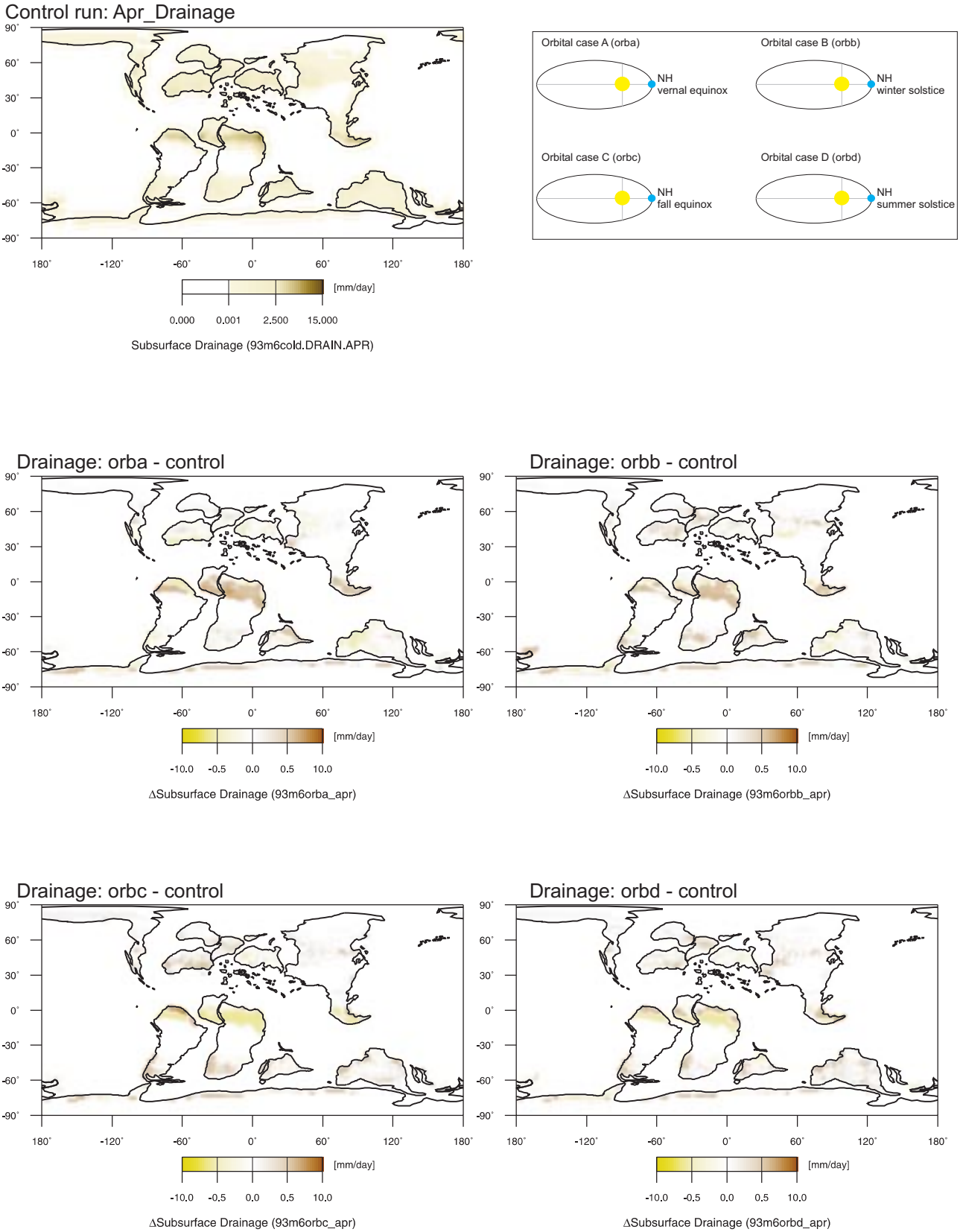

Figure 84: Model results for subsurface runoff (drainage) in April; [mm/day].

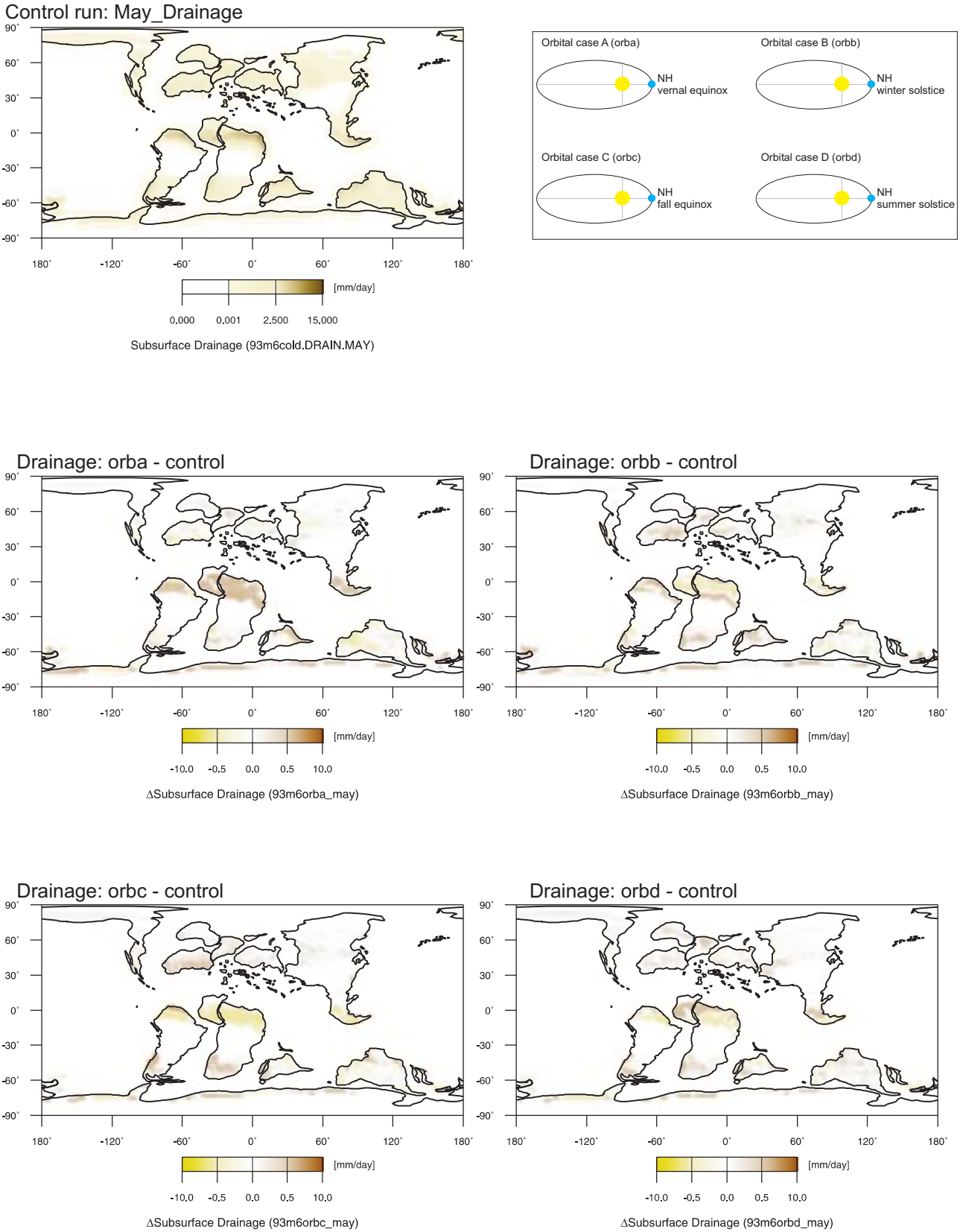

Figure 85: Model results for subsurface runoff (drainage) in May; [mm/day].

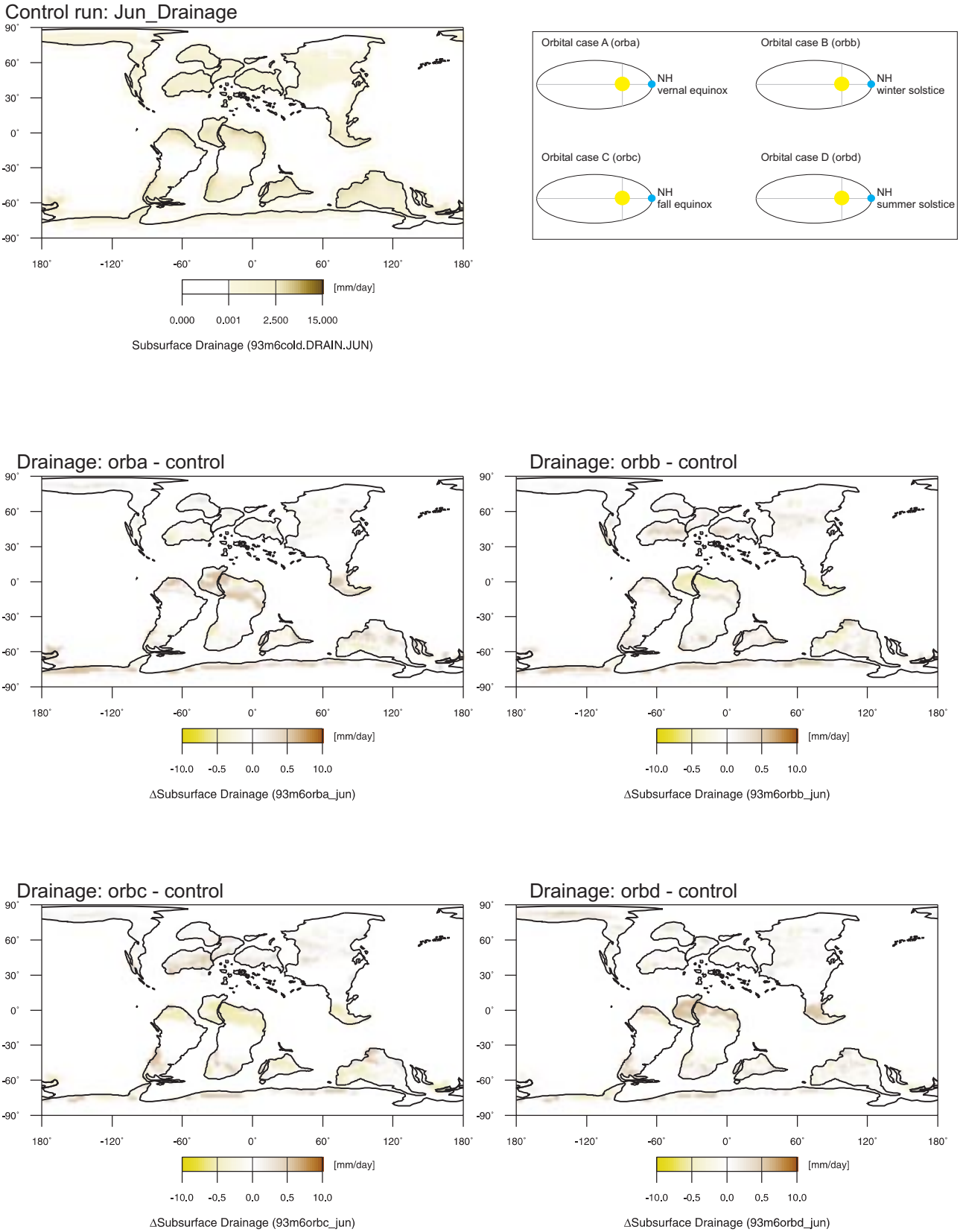

Figure 86: Model results for subsurface runoff (drainage) in June; [mm/day].

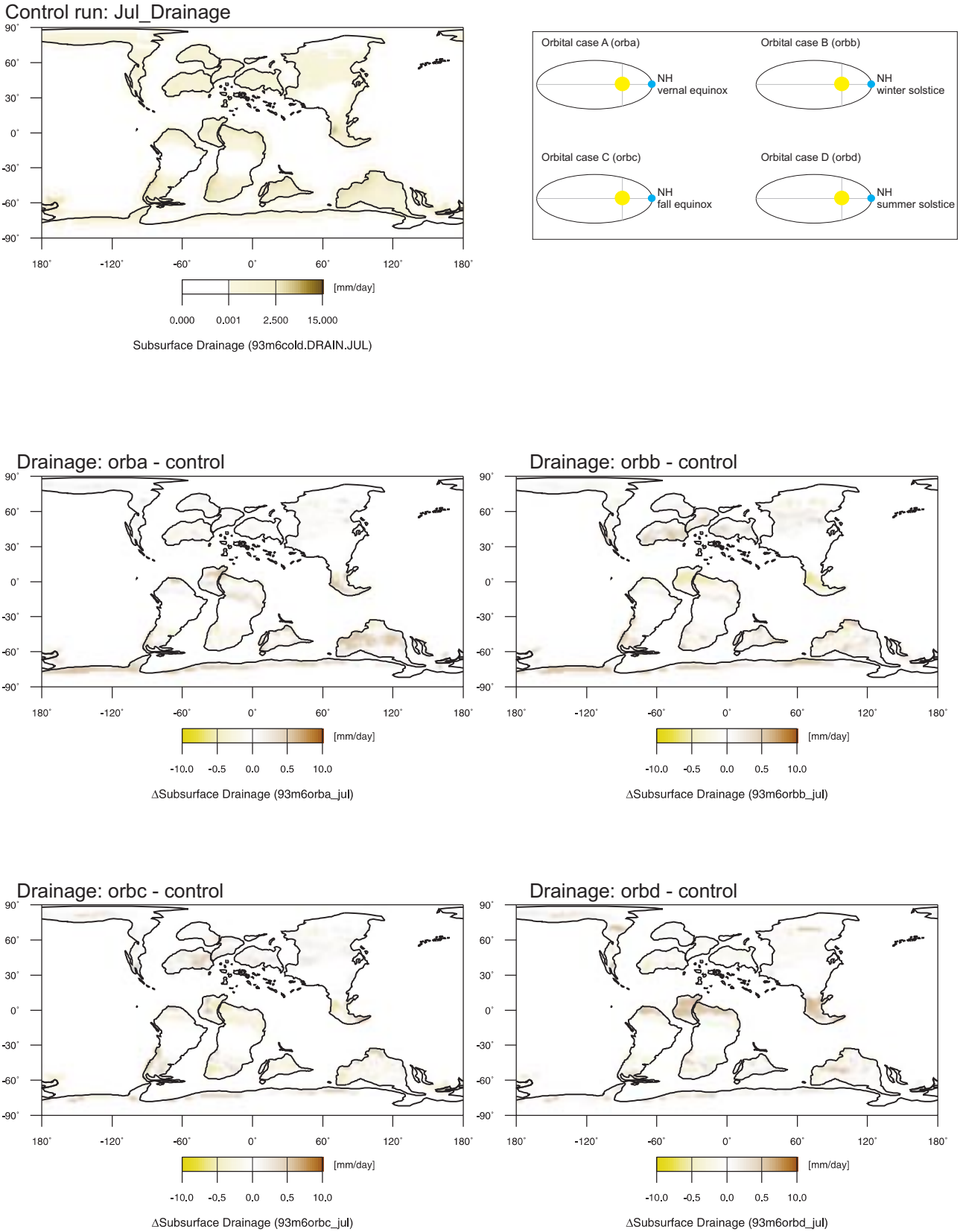

Figure 87: Model results for subsurface runoff (drainage) in July; [mm/day].

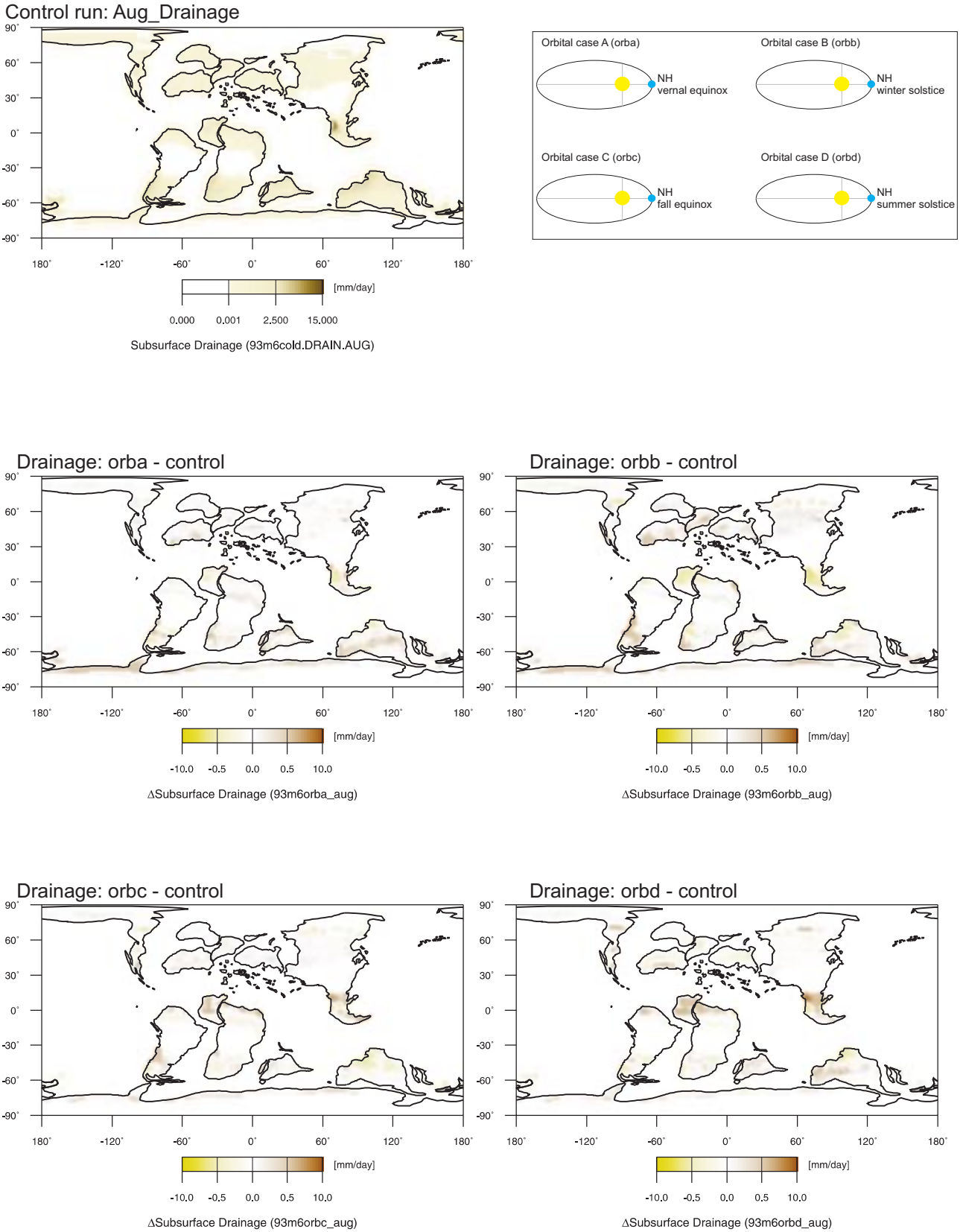

Figure 88: Model results for subsurface runoff (drainage) in August; [mm/day].

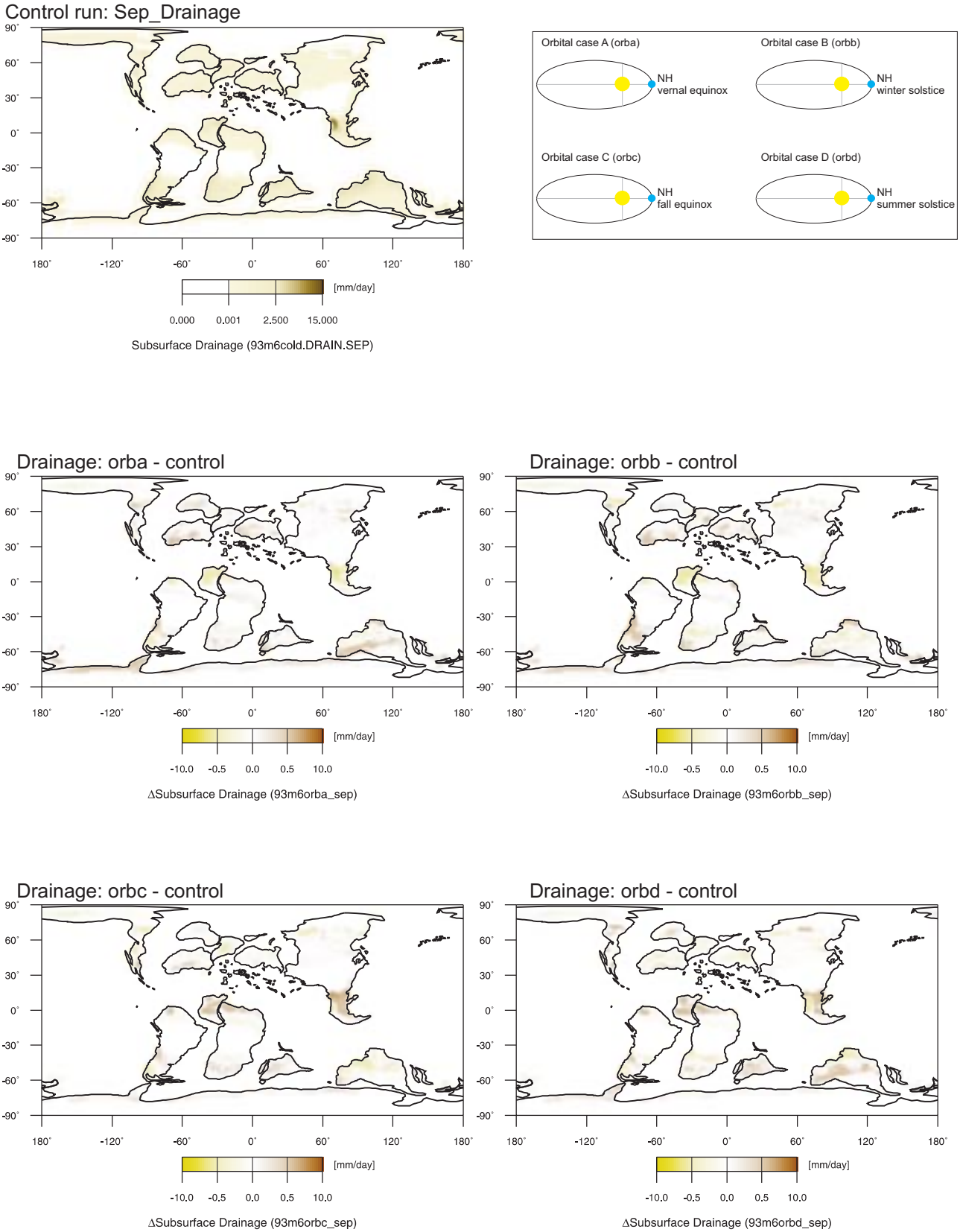

Figure 89: Model results for subsurface runoff (drainage) in September; [mm/day].

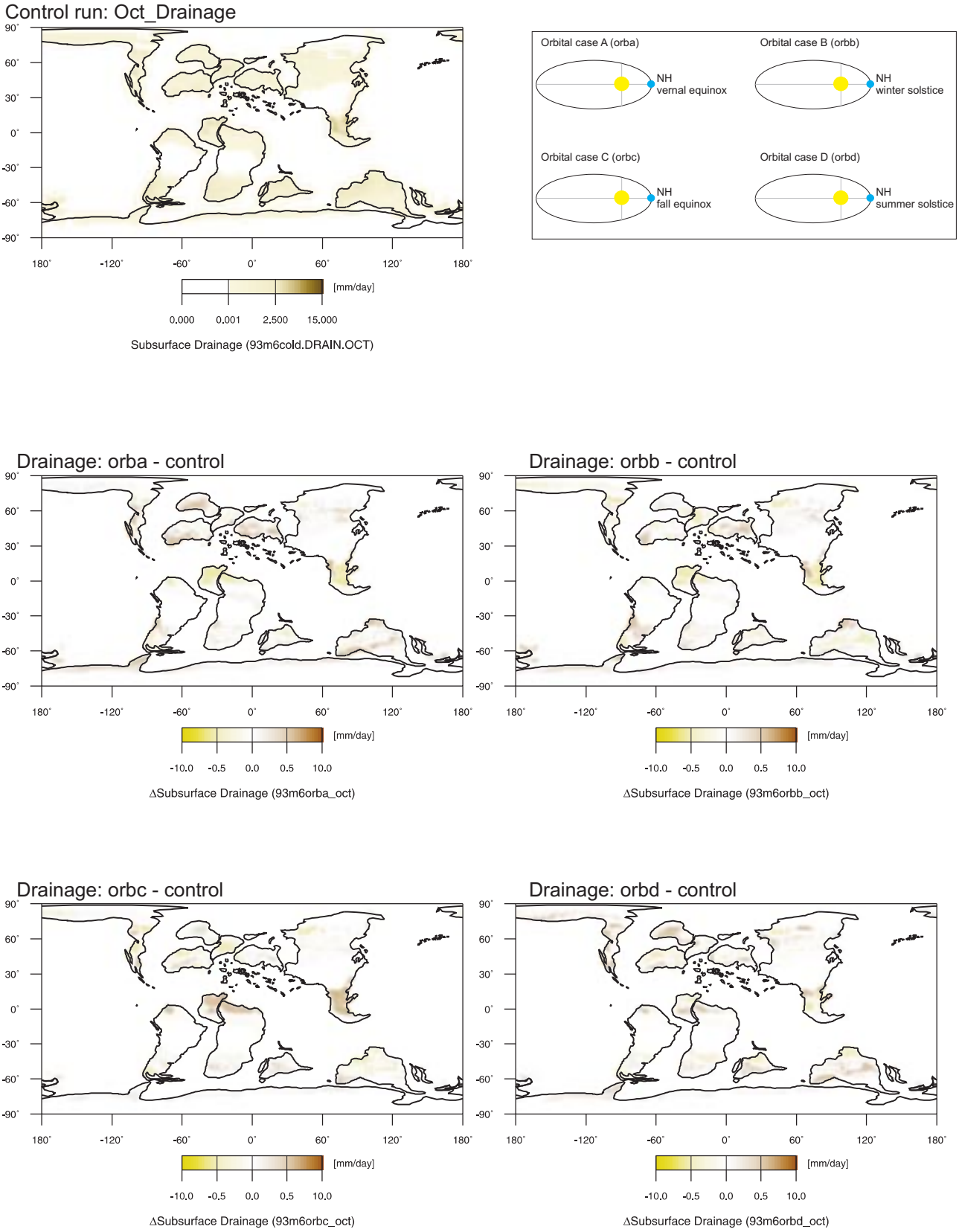

Figure 90: Model results for subsurface runoff (drainage) in October; [mm/day].

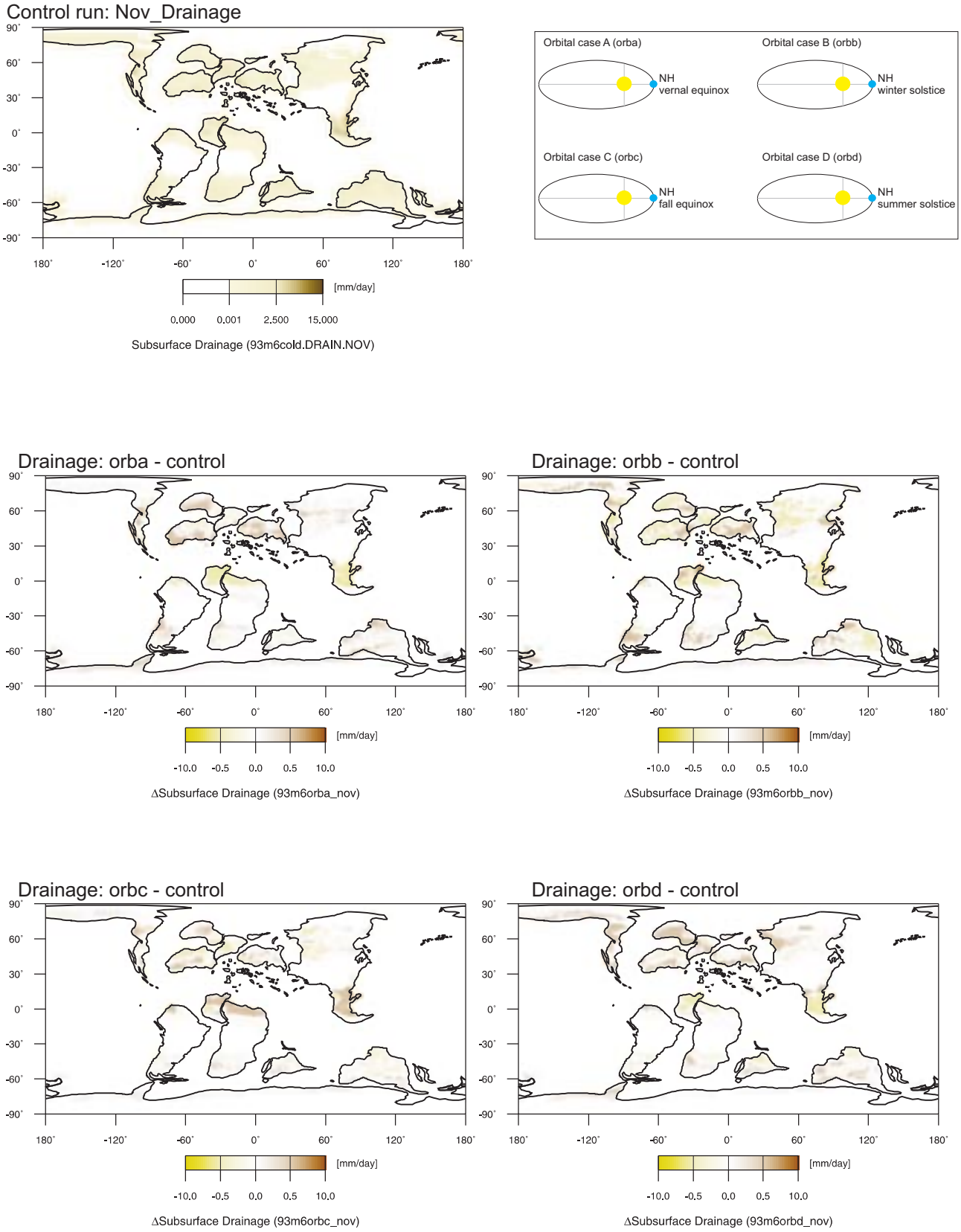

Figure 91: Model results for subsurface runoff (drainage) in November; [mm/day].

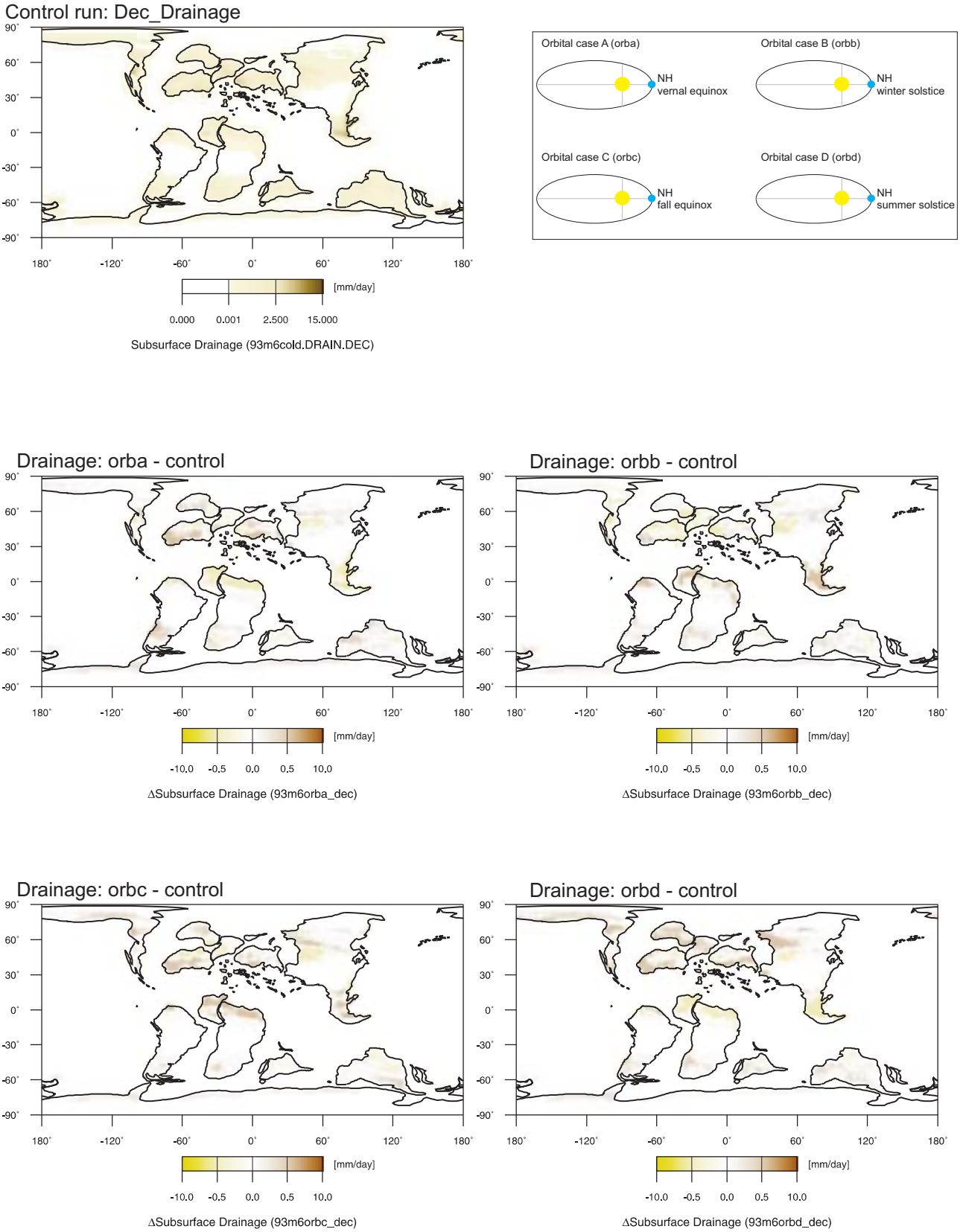

Figure 92: Model results for subsurface runoff (drainage) in December; [mm/day].

9.4. 10 year average, seasonal, and monthly data

Ideally, “climate” is a 30 year average of data (BUDYKO, 1974).However, because the forcing of climate models is identical from one year to the next, and because computational expenses are high, it is customary to take the average of model output for 10 years to represent the climate. For this study, all data were averaged from model years 15 through 25.
To understand how the sedimentary couplets in the WIS formed, three different data sets were evaluated: 1) For an impression of the long-term stability of the climate system, mean annual data for the different runs are compared; 2) To explore the climate in greater detail, the data for extreme seasons Dec.-Jan.-Feb. and Jun.-Jul.-Aug. are analyzed, 3) For a detailed evaluation of possible mechanisms monthly data are examined.

9.4.1. Meridional data (global), 10 year average and seasonal

Temperature:
The simulated global mean annual temperatures for the five models are 20.66°C (control run), 20.82°C (orbital case A), 20.80°C (orbital case B), 20.91°C (orbital case C), and 20.96°C for orbital case D. These MAT values indicate a low sensitivity to precessional forcing compared to the control run (Figure 93 and 94).

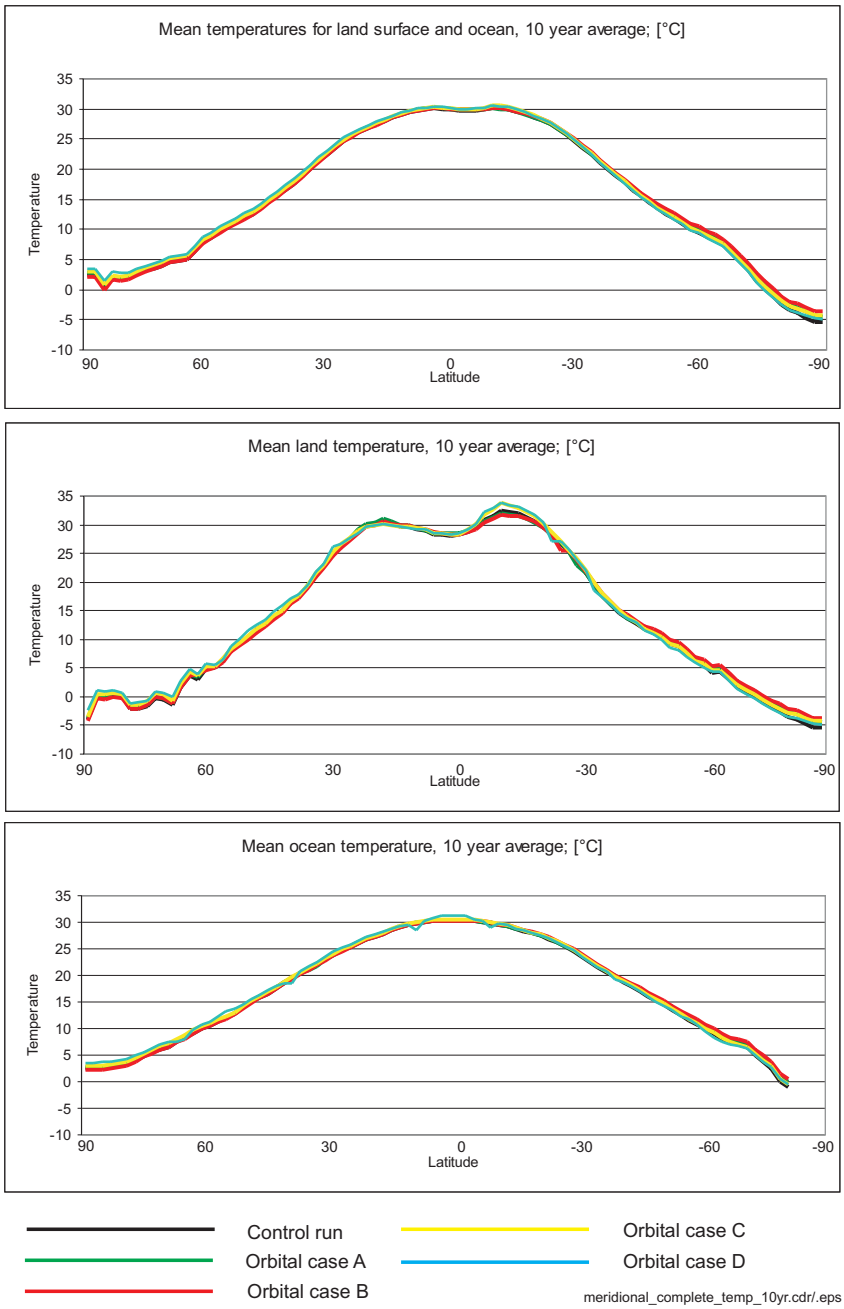

Figure 93: Meridional temperature (global) plots for land surface/ocean (top), land surface (middle), and ocean (bottom), 10 year average; [°C].

Global mean annual temperatures are shown in Figure 93, as combined land surface and ocean data (top), land surface data only (middle), and ocean data only (bottom). The large changes resulting from seasonal insolation forcing do not appear in the global annual means because any increase in summer temperature is offset by a decrease in winter temperature, resulting in a very small mean annual response to precessional orbital forcing.

The seasonal temperature data for winter (DJF) and summer (JJA) are shown in Figure 94, and indicate a larger seasonal sensitivity to orbital forcing. The models predict differences for the meridional temperature gradients of up to 4°C for land and ocean surface temperatures between 75-90°S during NH winter. The largest differences occur on the continents at ~30°N during NH

summer between orbital case B and orbital case C. The simulations indicate that land masses show larger seasonal changes of temperature than the ocean during winter and summer, as expected because of the lower heat capacity of land.

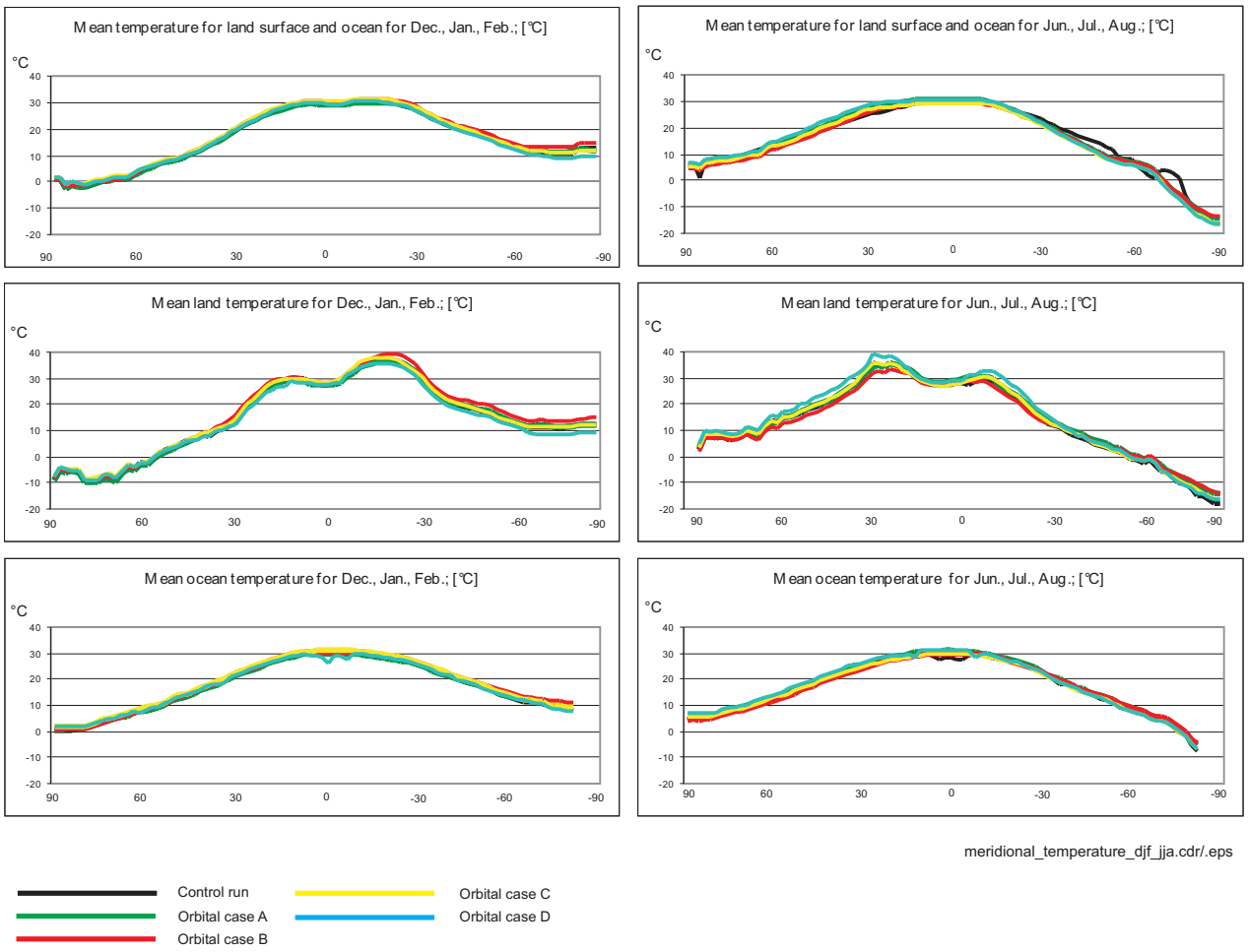

Figure 94: Meridional temperature (global) plots for land surface/ocean (top), land surface (middle), and ocean (bottom), DJF (figure on the left) and JJA (figure on the right); [°C].

Although, Figure 94 suggests that northern hemisphere summer temperatures (JJA) are more sensitive to precessional forcing, the differences are only marginal.

Precipitation:

The 10 year average of mean annual precipitation values predicted by the GENESIS simulations shows a higher sensitivity to changes of the precessional parameter than the temperature data. As seen in Figure 95 the largest changes occur in the equatorial region and between 30-60°N and 30-60°S.

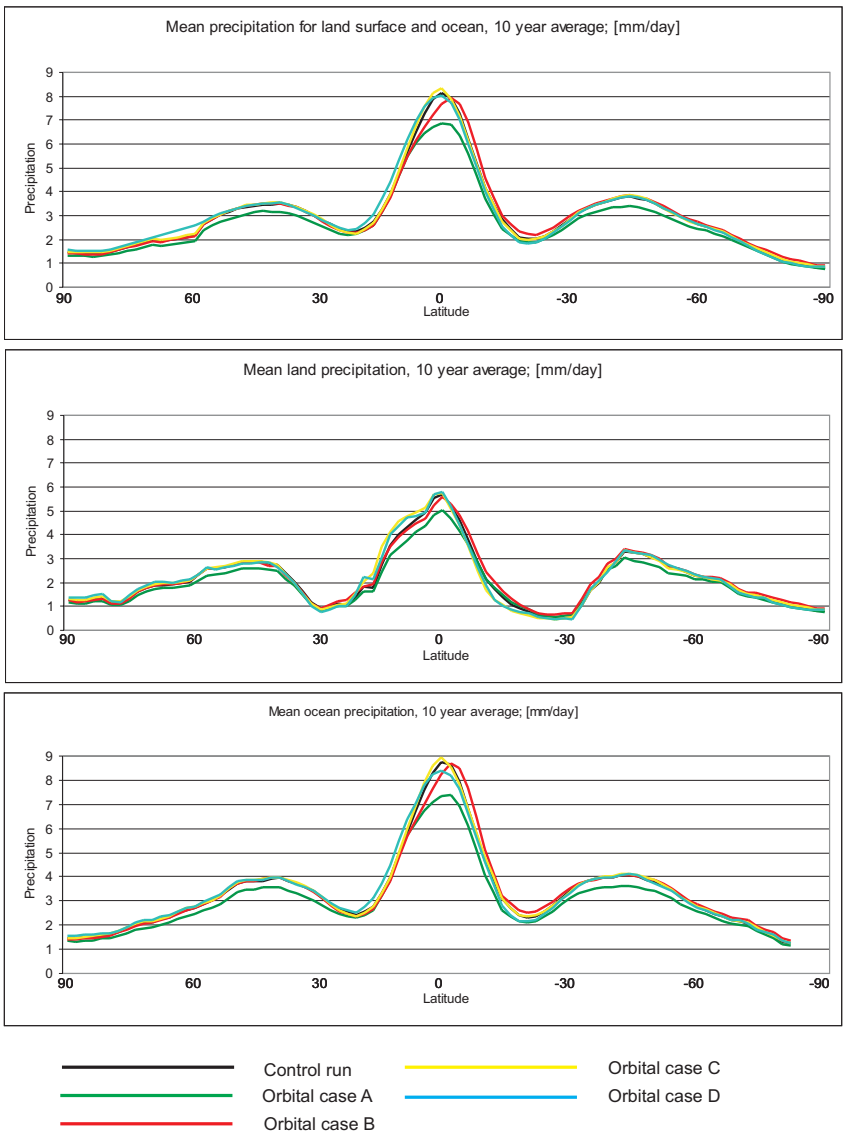

Figure 95: Meridional precipitation (global) plots for land surface/ocean (top), land surface (middle), and ocean (bottom), 10 year average; [mm/day].

Differences in the mean annual precipitation (land surfaces and ocean) reach a maximum of 1.6 mm/day between orbital case A and orbital case C, which have opposite precessional forcing at the equinoxes. The changes in mean annual precipitation over land reach values of about 0.4 mm/day between 30-60° N and S. The responses to changes in orbital forcing are greatest over the combined land and ocean surfaces (top) and over the ocean (bottom). The amplitude of the changes in the equatorial region is smallest in the “land only” data (max. 0.8 mm/day).
To summarize, these data for mean annual precipitation show that the equatorial region is most sensitive to changes of the precessional parameter. The precipitation differences in the equatorial region reach ~22%, whereas changes between 30-60°N and S are only ~13%.

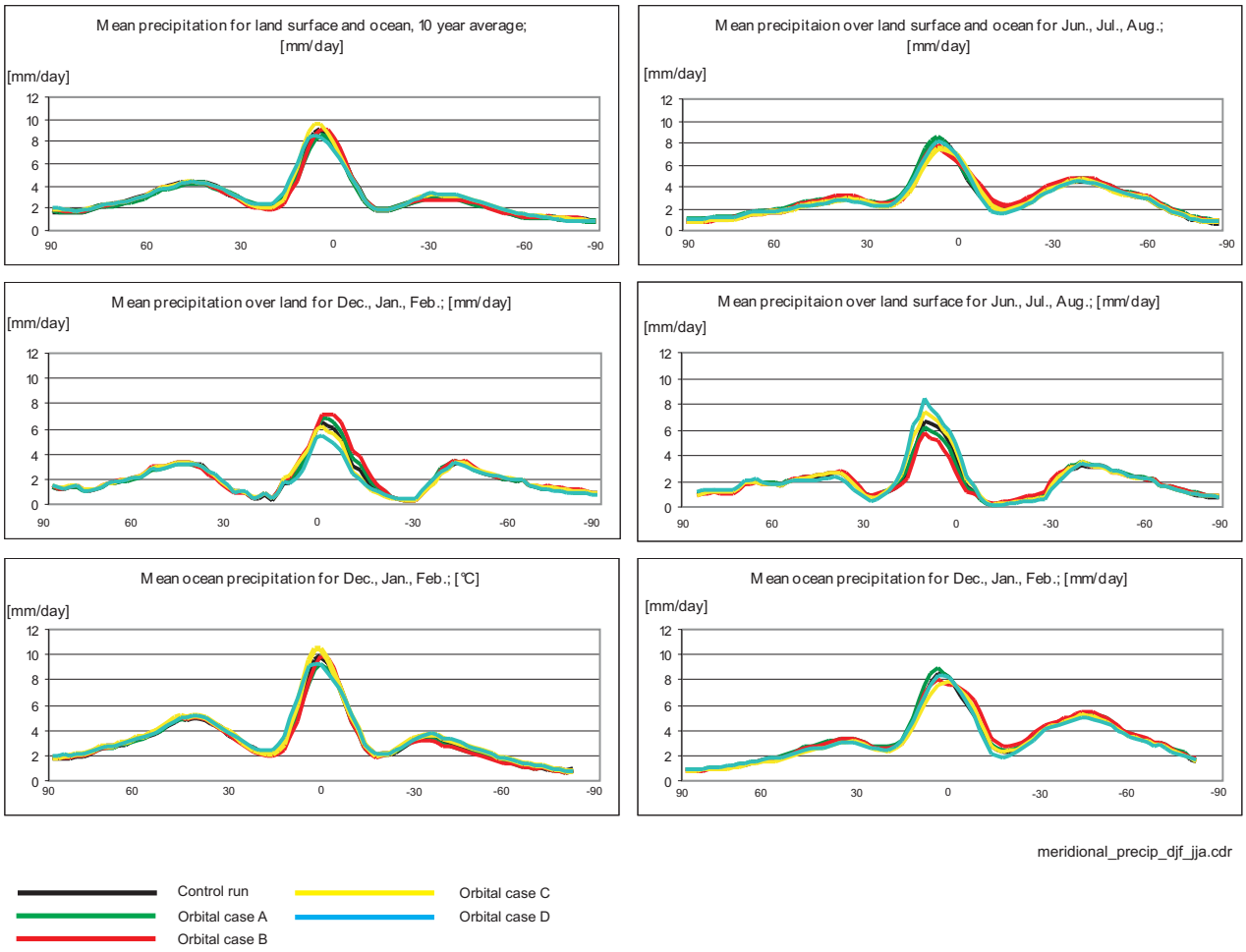

Figure 96: Meridional precipitation (global) plots for land surface/ocean (top), land surface (middle), and ocean (bottom), DJF (figure on the left) and JJA (figure on the right); [mm/day].

The seasonal (DJF and JJA) precipitation data (Figure 96) show patterns similar to the mean annual data. The largest changes, ~1.9 mm/day, occur on the continents in the equatorial region during NH summer. The seasonal changes between 30-60°N and S are marginal ~0.3 mm/day. It is interesting to note that the largest precipitation differences north and south of the equator do not necessarily occur between runs with opposite forcing. This is the case for the diagrams showing land surface/ocean and ocean values. On a seasonal basis, the largest changes in the continental precipitation pattern are produced during NH summer between orbital case B (red curve) and orbital case D (blue curve, with differences as large as 2.5 mm/day. This value corresponds to ~690 mm/year, which is close to the present total annual amount of precipitation of the city of Hamburg/Germany (714 mm/year).

9.4.2. Monthly data; WIS and adjacent continents between 25-61°N and 55-121°W

The results presented above indicate that MAT's produced by the model simulations are not a good indicator for changes resulting from insolation forcing. The averaging of monthly temperature and precipitation values over a year or over the three month summer and winter seasons obscures differences of the high and low values. In contrast, the monthly data for temperature, precipitation, and surface runoff show significant changes. Monthly data for the land masses of WNA and the western part of the N-American craton were analyzed to determine whether they can explain changes observed in the sediments of the seaway. The focus is on WNA because the Sevier Highlands are thought to be the major source of surface runoff and detrital sediment for the Western Interior Seaway.

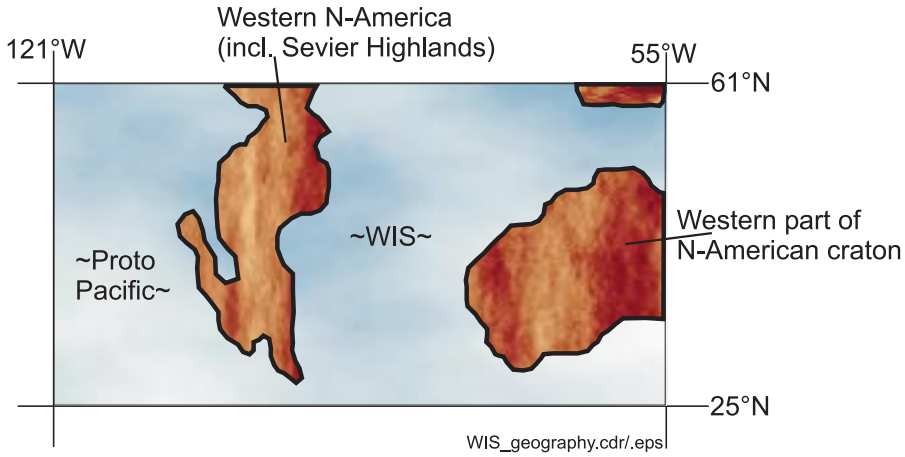

Figure 97: The WIS and it's adjacent land masses (25-61°N/55-121°W).

The analyses of temperature, precipitation, and surface runoff for the region of the Western Interior have been calculated from data representing the area between 25-61°N and 55-121°W (Figure 97). Only continental temperature, precipitation, and surface runoff data were used for the plots below (Figure 98 and 99).

Temperature:
The simulated monthly temperature changes for land in the study area show significant differences in response to the different forcings. Temperature differences reach up to 2.0°C over western North America (WNA) and up to 3.3°C over the western part of the N-American craton. Variations in response to orbital forcing over the western part of the N-American craton are largest during the summer (~3.3°C) and relatively small during spring, fall, and winter (max. ~1°C). The same general shape of the temperature curves can be seen for western North America. The only difference is the magnitude of temperature response during summer, which is greater by a factor of ~1.7 over the craton. The largest differences are predicted to be between orbital cases B and C. Generally,

temperatures are about 5-7°C cooler over WNA than they are over the craton due to the high mountains (Sevier Highlands: 1,000-3,000 m) which cover most of WNA. Temperature changes over WNA are smaller because it is a relatively narrow land mass surrounded by the proto-Pacific, Tethys, WIS, and Arctic sea. These large water masses dampen temperature changes caused by orbital forcing. The larger temperature changes (~3.3°C; orbital case B/orbital case C) over the N-American craton reflect the fact that it was a larger land mass with greater continentality.

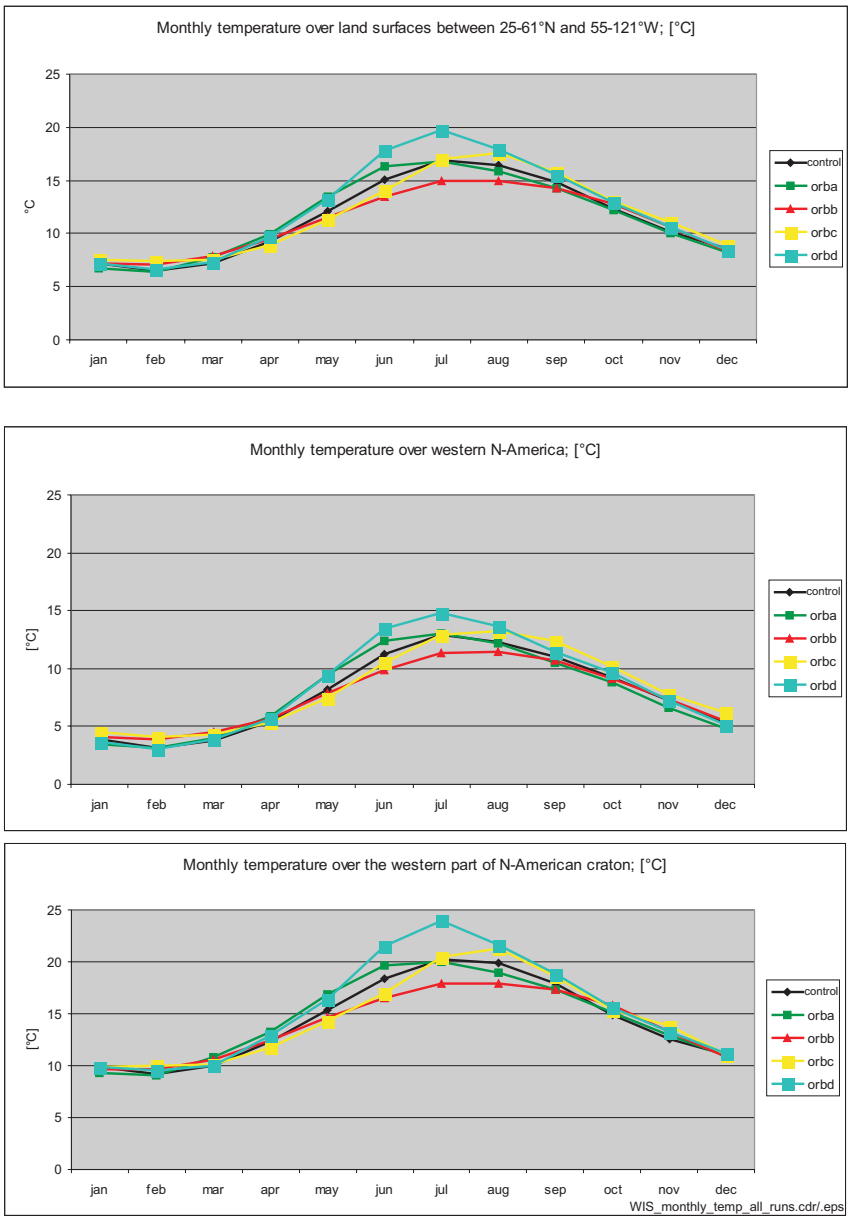

Figure 98: Monthly land surface temperature data for the WIS region between 25-61°N and 55-121°W. All land surfaces (top), Sevier Highlands (middle), western part of N-America (bottom).

Precipitation:

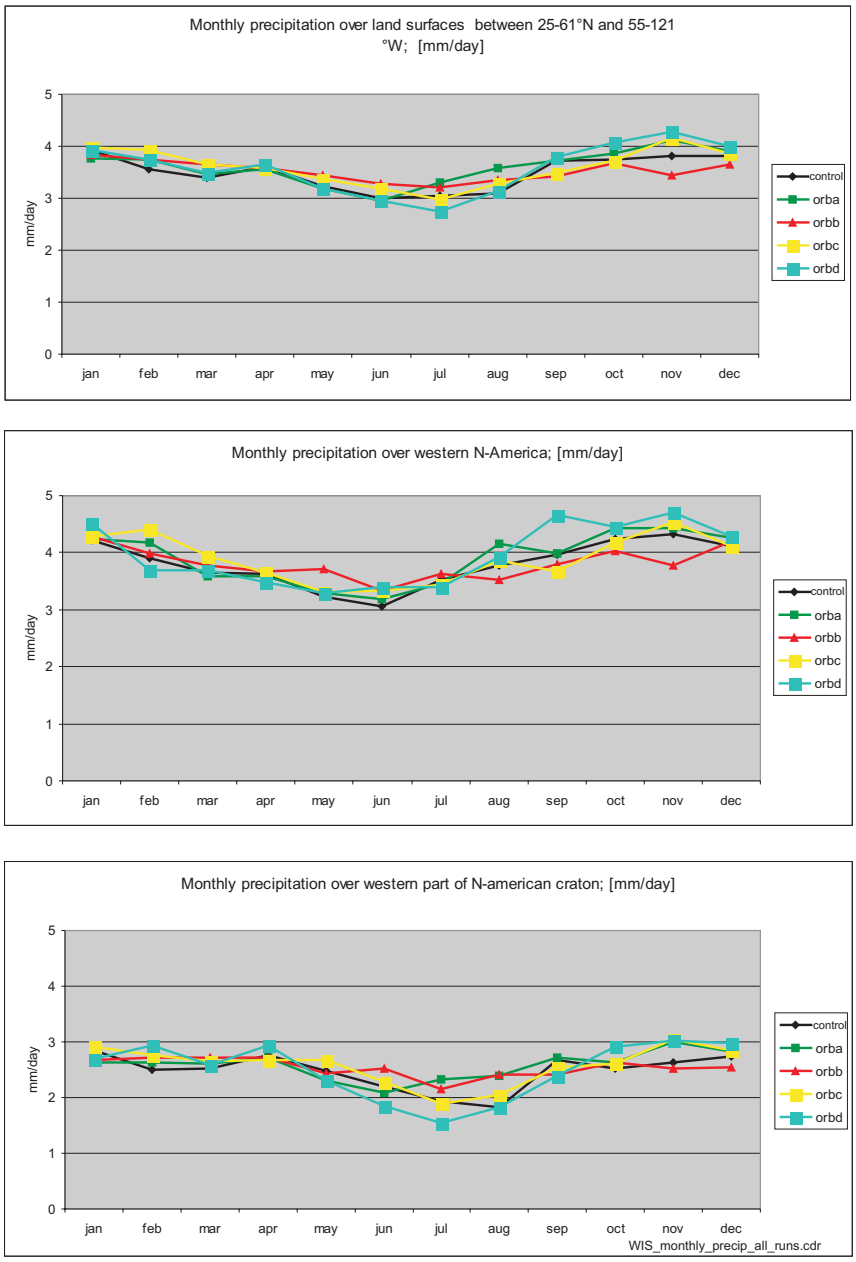

Figure 99: Monthly land surface precipitation data for the WIS region between 25-61°N and 55-121°W. All land surfaces (top), WNA (middle), western part of N-America craton (bottom).

Simulated continental precipitation (Figure 99) in the study area suggests a generally uniform precipitation pattern throughout the year for all runs. Highest precipitation occurs from October through February and the lowest values occur during NH summer (June and July). The largest precipitation difference is between orbital cases B and C during NH summer. It reaches up to 0.8 mm/day (~290 mm/yr) over WNA and 0.5 mm/day (~180 mm/yr) over the western part of the craton. The annual average precipitation over WNA is about 4 mm/day and slightly below 3 mm/day over the western part of the craton. It is important to note that due to the prevailing westerlies (north of ~30°N in NH winter) most of the precipitation over WNA falls on the western flank (windward side) of the Sevier Highlands, where

precipitation is about 3-5 times higher than on the leeward side of the mountain range. The decrease in precipitation is attributable to the weakening of the westerlies during NH summer. Maximum precipitation changes over the course of a year reach 25-35%.

Figure 100: Monthly land surface precipitation data for the northern (43°-61°N; top) and southern (25°-41°N; bottom) part of WNA; [mm/day].

As shown in Figure 100, continental precipitation varied in magnitude and annual distribution between the northern and southern parts of WNA. Monthly average precipitation was about 1 mm/day higher in the south (average ~4.4 mm/day) than in the north (average ~3.6 mm/day). The annual variability was simulated to be larger in the north (max. 2 mm/day for orbital case C) than in the south (max. 1.2 mm/day for orbital case C). Another difference is the variability between all orbital runs which is smaller over northern WNA. This indicates a stronger sensitivity of the climate system in the south, with a more balanced annual distribution in the north. No seasonal signal can be seen in the south, whereas precipitation in the north is lowest in the summer and highest in the winter.

Surface runoff from land; WNA:

In order to answer the question whether orbitally forced changes in surface runoff could have produced the bedding couplets of the WIS, monthly surface runoff (mm/day) off WNA was evaluated.

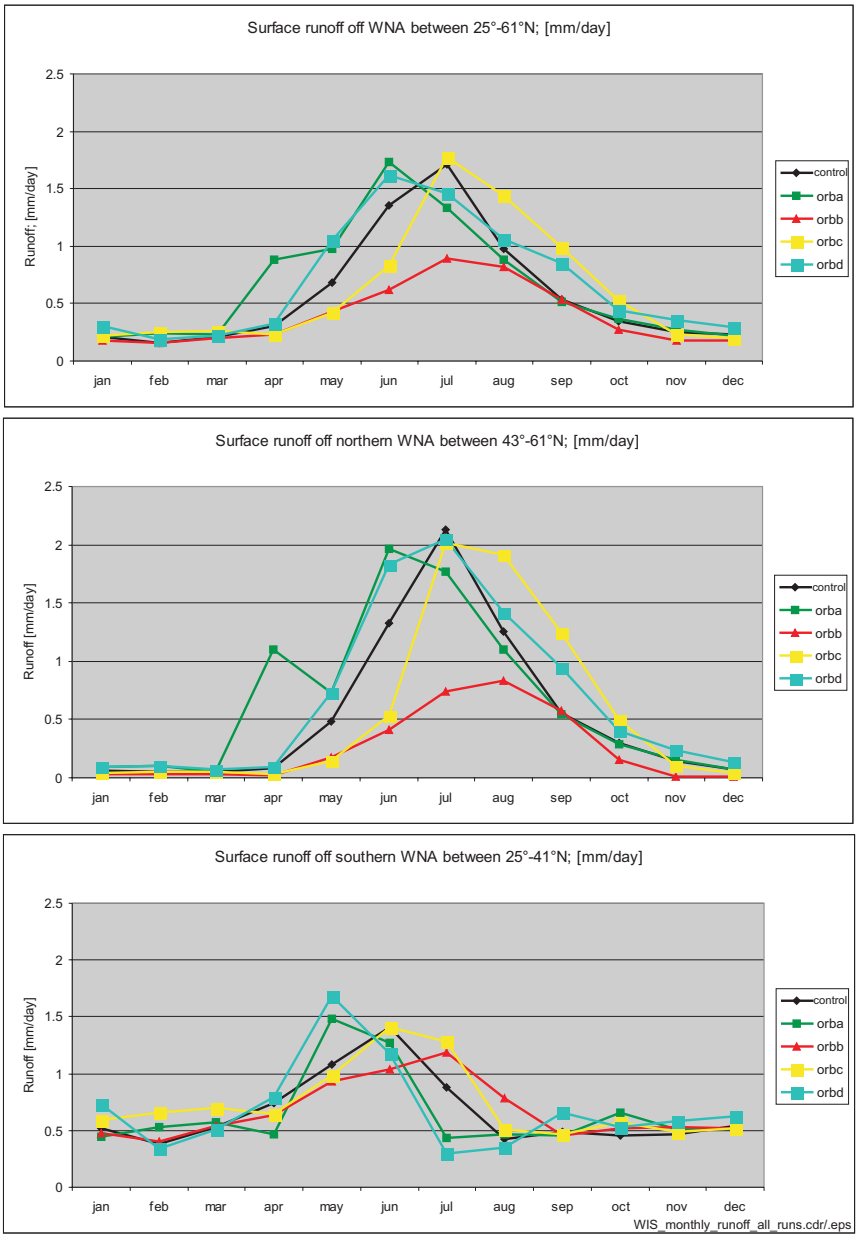

Figure 101: Surface runoff off Western North America (WNA) between 25-61°N and 93-107°W (top), off the northern portion between 43°-61°N (middle), and off the southern portion between 25°-41°N (bottom); [mm/day].

Only surface runoff from WNA was considered because surface runoff off the western part of the N-American craton did not add large volumes of freshwater to the WIS. Surface runoff from the craton did not exceed 0.15 mm/day, and this value was reached only during February of orbital case A.

Surface runoff is a function of precipitation, evaporation, transpiration, and infiltration rate into the groundwater system (THOMPSON and POLLARD, 1997). Precipitation, evaporation, and transpiration depend on temperature. Precipitation is also a function of the availability of moisture sources, and evaporation and transpiration are a function of wind speed, turbulence, soil type and plant physiology. The infiltration of moisture into the groundwater system is controlled by the nature of the vegetation, soil development and geological materials (HAY, 1998). Generally, the suspended load of rivers is related to surface runoff whereas the dissolved load is related to subsurface runoff (drainage). Surface runoff is calculated by GENESIS, but it is returned to the ocean across the nearest coastline rather than through more realistic rivers. This study analyses the runoff results because surface- and subsurface runoff can affect many processes that can be recorded by deep-sea sediments (DEAN and GARDNER, 1986; RAYMO et al., 1988; FROELICH et al., 1992; SLOAN et al., 1997).

The results for surface runoff presented in Figure 101 show its monthly distribution for WNA as a whole (25°-61°N), and for the northern (43°-61°N) and southern portions (25°-41°N). The simulated surface runoff from WNA suggests a strong sensitivity to precessional forcing, especially from May through July (southern portion) and from June through August (northern portion). The general distribution and magnitude of surface runoff during model runs A and C, representing “intermediate forcing” (equinoxes at perihelion and aphelion), and orbital case D (northern summer solstice at perihelion) strongly resemble surface runoff predicted for the control run. Three month-long peaks of surface runoff (~1.75 mm/day) from WNA are indicated, two in June (orbital cases A and D) and one in July (orbital case C). These three months with maximum surface runoff could be associated with increased clastic sediment input and possible carbonate dilution, greater freshwater flux to the surface water and perturbation of vertical ocean mixing regimes, and/or increased input of nutrients from continental sources to the surface ocean. If detrital sediment load were a linear function of runoff, the times with peak surface runoff from northern WNA should produce bedding couplets which show a 1:6 ratio of the limestone and shale units, meaning that the shales are six times as thick as the limestones. The ratio is calculated with average sedimentation rates of 1.5 cm/ka for the limestones and 3.0 cm/ka for the shales. The ratio of 1:6 is close to the 1:5 ratio measured for the bedding couplets of Bridge Creek Limestone at section NM-I-00, but the ratio is not consistent throughout the Bridge Creek Limestone.

A comparison between surface runoff off the northern and southern half of WNA reveals two interesting features. 1) Three peaks during NH summer (orbital cases A, C, and D) are well established in the northern portion, where maximum surface runoff is about 20% (~2.1 mm/day) higher than in the southern portion (~1.7 mm/day). 2) There is a time lag in sensitivity to precessional forcing between the north and south; surface runoff maxima occur one month earlier in the southern half (May and June) than in northern half (June and July).

Variations of surface runoff between the individual orbital runs reach 110% between cases B and D from northern WNA. Surprisingly, precipitation and surface runoff correlate negatively on WNA; the highest surface runoff occurs during times when precipitation is lowest (summer). This reflects that in the simulation the precipitation in summer occurs in short, intense storms. In GENESIS, concentration of precipitation in a short period of time produces surface runoff because the infiltration rate of precipitation into the soil has an upper limit and when this limit is exceeded the additional precipitation becomes surface runoff. These times with peak runoff could be expected to erode large volumes of sediment.
The sedimentary significance of the concentration of precipitation into short periods of time was first recognized by FOURNIER (1960), who proposed that an uneven distribution of precipitation through the year increases erosion.

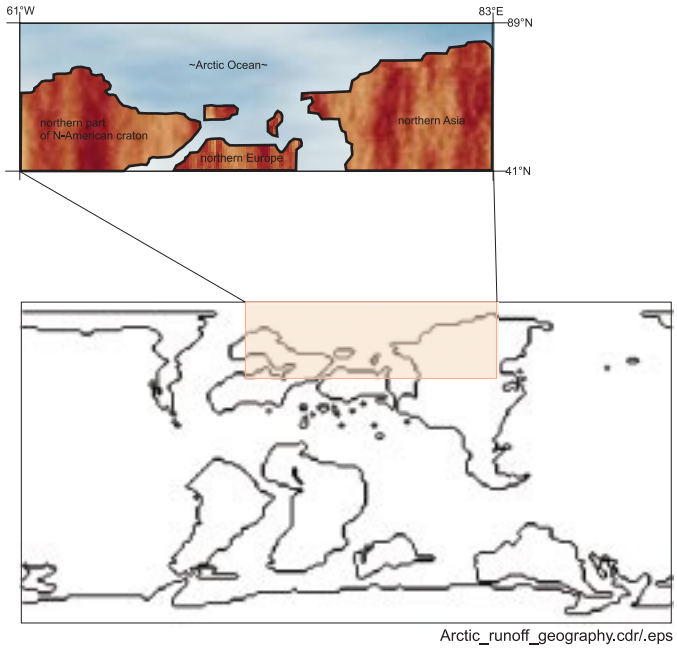

Figure 102: The Arctic Ocean and it's adjacent land masses (45-89°N/61°W-83°E).

Land surface runoff; N-Asia, N-Europe, and northern part of N-American craton:

Land surface runoff from N-Asia, N-Europe, and the northern part of the N-American craton into the Arctic Ocean (Figure 102) shows little sensitivity to precessional forcing (Figure 103). The general distribution and magnitude of surface runoff from these areas is almost identical for all four orbital runs and the control run. The lack of response to precessional forcing in the Arctic is accompanied by a lack of response to changes in eccentricity. The shape and magnitude of land surface runoff from this region does not change between e=0.0 (control run) and e=0.05 (orbital runs). This stability of surface runoff from land surrounding the Arctic is in agreement with the assumption of FISHER et al. (1994), that a stable oceanic front formed in WIS and migrated only a

few 10's of kilometers north and south over millions of years. If the northern water mass in the seaway had a low salinity, land surface runoff into the Arctic Ocean could have been the source of that excess freshwater.

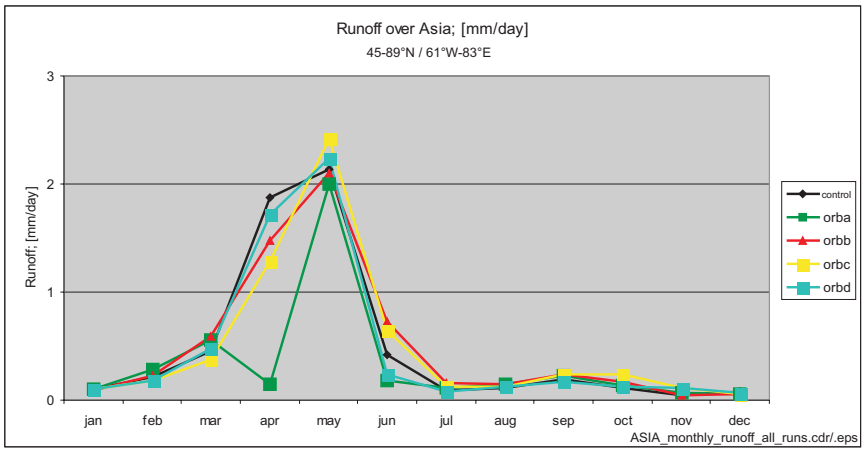

Figure 103: Land surface runoff into the Arctic Ocean from N-Asia, N-Europe, and northern part of N-American craton; [mm/day].

Although the average surface runoff data from the continents into the Arctic does not change during the precession cycle, WNA (Figure 101) shows significant variability.

Subsurface runoff from land; WNA:

The results for subsurface runoff presented in Figure 104 show the monthly distribution of subsurface runoff (mm/day) for WNA as a whole (25°-61°N), and for the northern (43°-61°N) and southern portions (25°-41°N). The simulated subsurface runoff from WNA indicates only small intra-annual variation. Variation between the control and the four orbital runs does not exceed 15%, and sensitivity to precessional forcing is not evident. The annual distribution is similar to that of precipitation, which indicates the strong connection between those two parameters. Mean annual values for subsurface runoff range from 3.8 to 4.0 mm/day for WNA as a whole, and from 3.6 to 3.7 mm/day in the northern part. The largest annual variation between the climate simulations was predicted for the southern portion, where values vary from 4.2 to 4.6 mm/day.

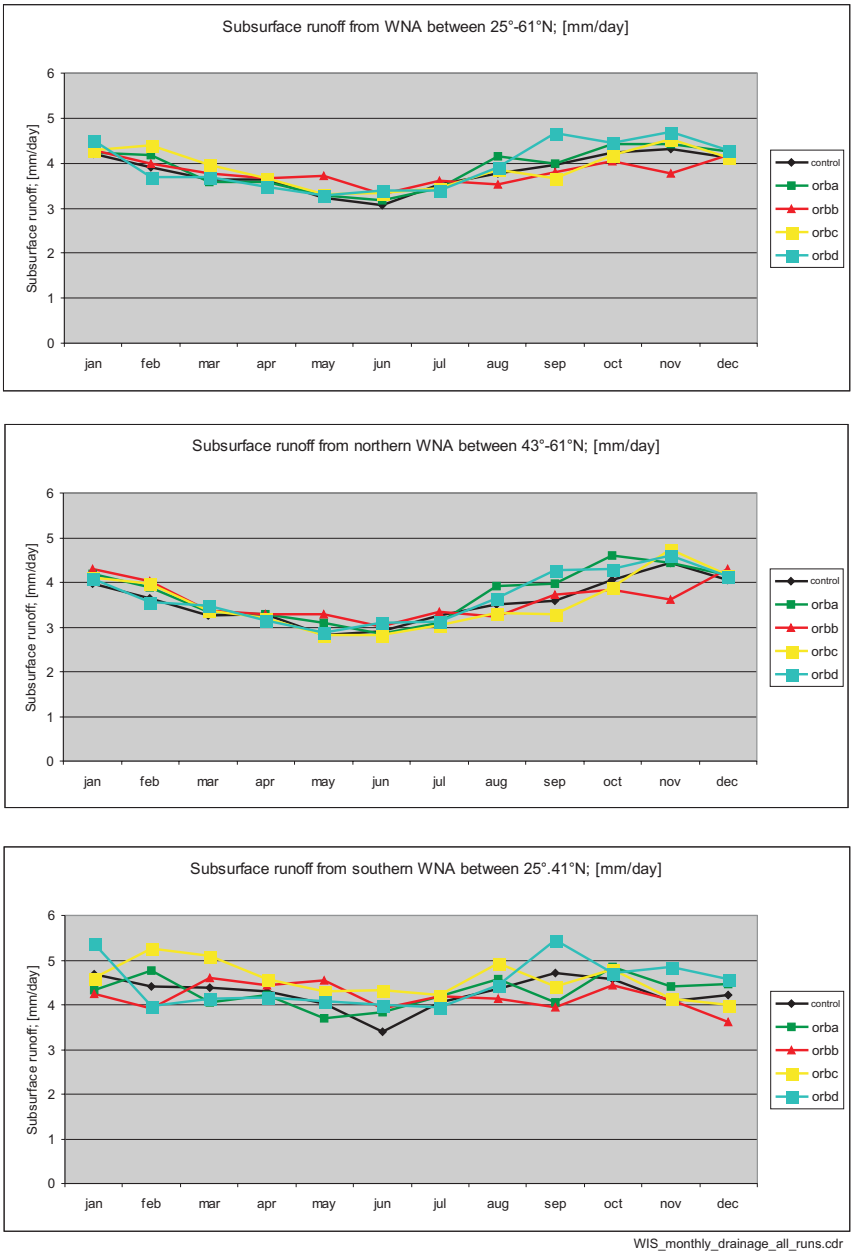

Figure 104: Subsurface runoff off Western North America (WNA) between 25-61°N and 93-107°W (top), off the northern portion between 43°-61°N (middle), and off the southern portion between 25°-41°N (bottom); [mm/day].

River discharge:

River discharge is the sum of the surface runoff and subsurface runoff, expressed as volume per unit time. The river discharge by month is given as m^3/s and is calculated as follows:

$$\text{River discharge } [m^3/s] = \frac{\text{Annual average subsurface runoff x Area of the drainage basin}}{\text{Monthly surface runoff x Area of the drainage basin}}$$

Today, 2/3 of the river discharge comes from the surface runoff and only 1/3 is added by subsurface runoff as groundwater flow into the streams. However, the model simulations for the late Cretaceous have shown that about 6/7 of the freshwater entering the seaway is coming from subsurface runoff and only 1/7 from surface runoff.

Figure 105: River discharge from Western North America (WNA) between 25-61°N and 93-107°W (top), off the northern portion between 43°-61°N (middle), and off the southern portion between 25°-41°N (bottom); [mm/day].

RIVER DISCHARGE; [m3/s]

Orbital case	Region of WNA	River discharge; [m3/s]	Ratio surf. runoff/subsurf. runoff
orba	north + south	121,399	1:6
	north only	65,719	1:6
	south only	57,680	1:7
orbb	north + south	111,814	1:10
	north only	57,744	1:14
	south only	56,567	1:6
orbc	north + south	119,893	1:6
	north only	61,482	1:6
	south only	61,690	1:6
orbd	north + south	123,450	1:6
	north only	65,422	1:5
	south only	60,332	1:6

River_discharge.cdr/.eps

Table 2: River discharge from WNA during different orbital forcing. Data are for the northern and southern part of WNA as a whole, for the northern part only and for the southern part; [mm/day].

NOTE:
The residence time of groundwater in the system is about 5000 years. Because groundwater is such an important component of Cretaceous rivers, their flow is largely dependant on infiltration into the groundwater system that occurred 5000 years earlier. In this study, the subsurface runoff data show no sensitivity to orbital forcing, so this effect is not considered.

9.5. Discussion -model results

9.5.1. Control run

The control run, forced by the average solar boundary conditions provided some interesting results about the mean state of the Cretaceous climate system assuming 5 times present CO_2.
Using the boundary conditions described in chapter 9.3.1. GENESIS predicts a pattern of atmospheric pressure systems strikingly different from that of today. The largest differences are in the polar regions, particularly for the NH winter. At present, high pressure persists throughout the year in the Arctic. The high is most strongly developed during NH winter (~1015-1024 hPa) and is slightly weaker during NH summer (~1005-1010 hPa). Today, the Antarctic also has a permanent high, located over eastern Antarctica. It is strongest during SH winter (~1020-1030 hPa) and weakens slightly during SH summer (~995-1015 hPa). The climate simulations for the Late Cretaceous show a polar low (990-1005 hPa) over the Arctic Basin during NH winter and simultaneously a weak high over Antarctica (1009-1016 hPa). During NH summer a high developed over the Arctic and Antarctica (1015-1017 hPa). During the hemispheric winter strong

latitudinal highs with pressures usually above 1020 hPa develop around 30° north (boreal winter) and 30° south (austral winter).
The wind systems also differ from those of today. Due to the polar low or weak polar highs during each hemispheric winter, strong wind belts develop between 50° and the high pressure zones at 30°. During the northern hemisphere winter strong stable westerly winds develop in the northern hemisphere. Changes in the southern hemisphere are less than in the NH. Another important difference lies in the strong trade winds of the northern- and southern hemisphere. Today, the trade winds are strongest during the hemispheric summer. In the Late Cretaceous simulation they are strongest during the hemispheric winter. Overall, the winds were more variable in the Late Cretaceous simulation than at present.
These changes suggest very different global atmospheric and oceanic circulation systems. Analysis of the ODSN database (Ocean Drilling Stratigraphic Network; an initiative of GEOMAR-Research Center for Marine Geosciences / Kiel and the Geological Institute of the University Bremen) has shown that during most of the Cretaceous, Paleocene, Eocene and Early Oligocene calcareous plankton species were cosmopolitan, extending to high latitudes in the southern Atlantic and Indian Oceans (HAY et al., 2001). Today their biogeographic range is sharply limited by the subtropical and polar frontal systems of the high latitude oceans. Their cosmopolitan distribution in the Late Mesozoic and early Cenozoic implies that there were no effective subtropical and polar fronts in the ocean. The subtropical and polar frontal systems are forced by the curl of the wind stress where the westerly winds reach their maximum velocities. The lack of these frontal systems implies that either the westerlies were displaced poleward over land areas or were so unstable or weak as to be unable to force the frontal systems into existence. Such conditions would be most likely if the polar regions were sites of low or alternating rather than persistent high atmospheric pressure, and there were seasonally two rather than three atmospheric cells per hemisphere.
The climate of the control run shows weak high pressure systems in the polar regions in the respective hemispheric summers and only very weak polar highs or even lows in the winters. In effect, this simulation produces an unstable two-cell/three-cell hemisphere atmospheric circulation. Well defined westerly winds, capable of forcing the frontal systems into existence developed only during the winter in each hemisphere. Summers are characterized by a much more diffuse circulation controlled by local climate factors. The effect of these changing wind systems is to destabilize the boundaries in the oceanic circulation and to prevent the formation of stable frontal systems. These conditions would allow the paleobiogeographic limits of the calcareous plankton to extend much further poleward than they do today.

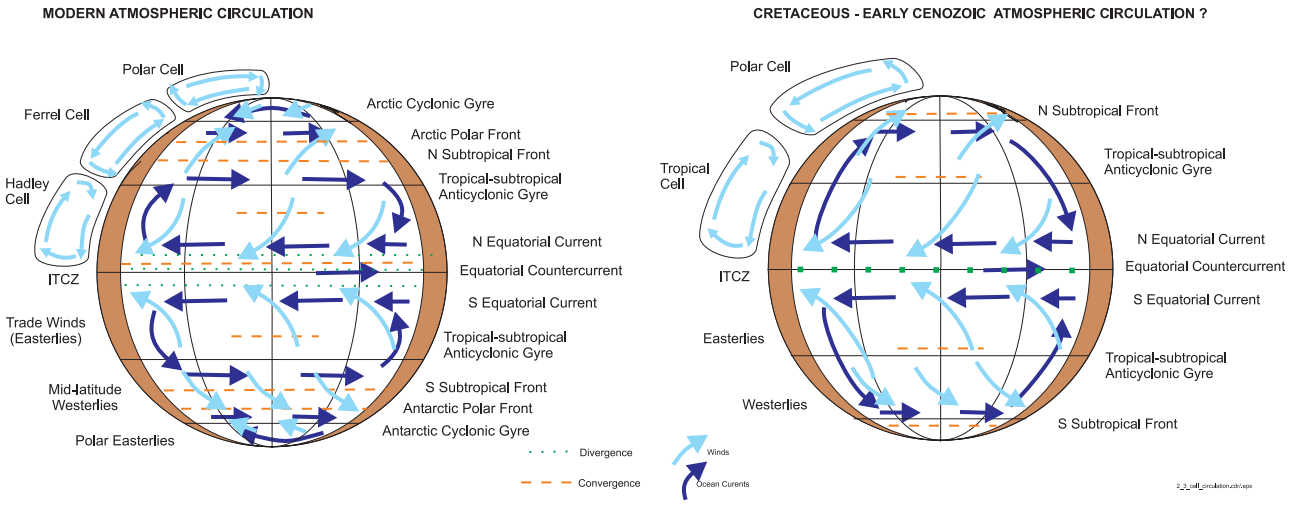

Figure 106: Modern and possible Cretaceous/early Cenozoic atmospheric circulation (HAY et al., 2001b)

Two alternative atmospheric circulation patterns are shown schematically above (Figure 106). The modern atmospheric circulation is more complex than shown in this schematic diagram, but surface ocean currents reflect its long-term integral as a three-cell/hemisphere system. The alternative two-cell/hemisphere circulation should be possible under the condition of warm poles; it has been generated by climate models for other planets (WILLIAMS, 1998a, b). However, it had not been successfully simulated by numerical climate models for the Earth except when warm sea surface temperatures were specified (HUBER and SLOAN, 1999).

9.5.2. Orbital runs

The goal of this study was to understand how the variability of continental- and ocean-related climate processes in a Cretaceous greenhouse world, as driven by the changes during one complete precessional cycle, could affect the sedimentation in the Western Interior Seaway. Solar insolation at the top of the atmosphere is the external driving force for the climate system and its changes during the precession of the equinoxes forms the basis of the sensitivity tests presented in this study. All modeling results represent response to the temporal and spatial distributions of solar insolation forcing.

The Earth's climate is usually defined with respect to patterns of long-term averages of temperature and precipitation. Determinant aspects of temperature are the annual temperature range, seasonal (winter and summer) temperature range, and the mean monthly temperature. Temperature over land is mainly controlled by: 1) insolation, 2) degree of continentality, 3) elevation, and 4) vegetation. Precipitation has two aspects of importance, the mean annual rainfall amount and its distribution during the year. Precipitation is primarily controlled by: 1) temperature,

2) global atmospheric convergence/divergence patterns, 3) orography, and 4) distance from a moisture source.
Another parameter evaluated in this study is surface runoff, which is dependant on precipitation, evaporation, transpiration by vegetation, and infiltration into the soil. It has a large effect on mechanical erosion and the mass of suspended load in the rivers. The fourth parameter analyzed in this study is subsurface runoff (drainage). Subsurface runoff is defined as precipitation, snow melt, or other water that infiltrates the surface and flows in underground hydraulic systems. For this study the simulated subsurface runoff was calculated because it contributes large amounts of freshwater into the seaway. Subsurface runoff provides most of the dissolved load of rivers, but is has no effect on mechanical erosion and the mass of suspended load in the rivers.

The global distribution of land masses and its response to orbital forcing is very important in any study about the climate system. At present, the seasonal hemispheric response to orbital forcing depends mainly on obliquity and precession, but not on eccentricity. This is because today the eccentricity of Earth's orbit around the Sun is small (e=0.0167) and aphelion and perihelion differ from the mean Sun-Earth distance by less than 2%. The global average insolation on Earth in July (aphelion) is 6.40% (BERGER, 2001) less intense than it is in January (perihelion). Surprisingly, July is presently Earth's warmest month. The average temperature of Earth at aphelion is about 2.3°C higher than it is at perihelion; today the Earth is warmer when it is farther from the Sun. This is due to the lower heat capacity of land.
The heat capacity (specific heat x density) of the solid earth is much less than that of water. The specific heat of most earth materials is about ¼ that of water, so that, although they have a density 2 to 3 times that of water, their heat capacity is lower. Further, heat can be transmitted in solid materials only by conduction, so that the seasonal temperature differences rarely penetrate to depths of more than 1m soil or rock. In contrast, the ocean surface waters, mixed by the wind, provide a heat sink that is often 100m or more thick.
Today, land is concentrated in the NH (100,345 x $10^3 km^2$), whereas there is more water and less land (48,559 x $10^3 km^2$) in the SH (BAUMGARTNER and REICHEL, 1975). During the month of July the "land-crowded" northern half of the Earth is tilted toward the Sun and receives higher insolation. Northern continents, warmed by the aphelion Sun, elevate the average temperature of the entire globe. Six months later, in January, the situation is reversed as Earth faces the sun with it's water-dominated southern hemisphere. The extra energy Earth receives in January is taken up by the ocean mixed layer with its high specific heat and heat capacity. The southern summer in January, at perihelion, is therefore cooler than northern summer in July, at aphelion. There is another notable difference between summers in the two hemispheres, their duration. Following Kepler's 2nd Law, planets move more slowly through their orbit at aphelion than they do at perihelion. As a result, northern summer on Earth is 2 to 3 days longer than southern summer,

which gives the Sun even more time to warm the northern continents. All of these factors contribute to making July Earth's warmest month at present (PHILLIPS, 2001).

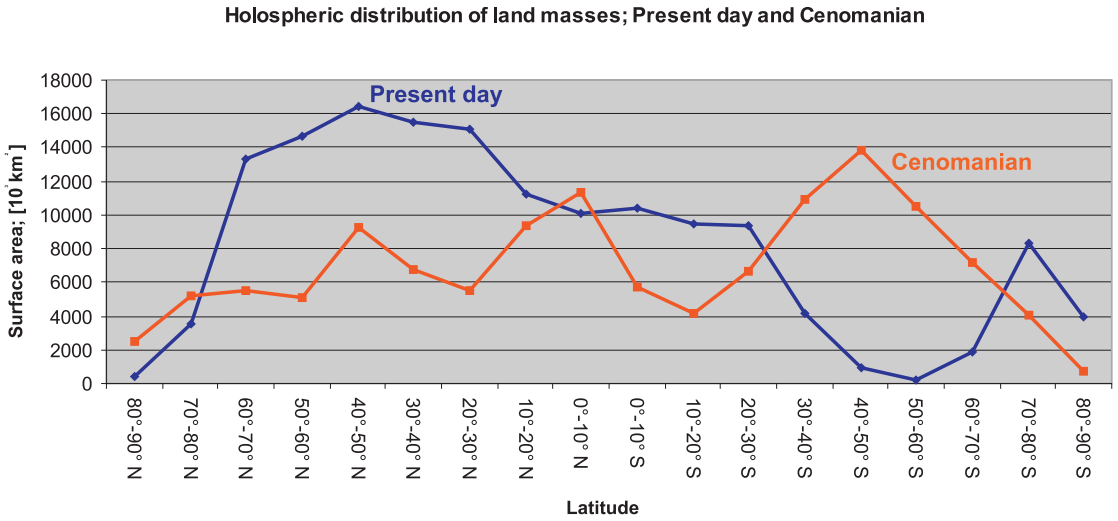

Figure 107: Holospheric distribution of land masses [$10^3 km^2$] during the Cenomanian. Data from BAUMGARTNER and REICHEL, 1975.

During the Cretaceous there was a more even distribution of land masses between the northern- and southern hemispheres. Approximately 60,237 x $10^3 km^2$ were in the NH and 63,820 x $10^3 km^2$ in the SH. But the land masses were not evenly distributed between the poles (Figure 107).Most of the land area was located between 40-50°S, a situation very different from the present day configuration, where most of the continents are between 20°N and 70°N. Previous climate simulations have shown that the Cretaceous distribution of land would have produced a different seasonal mean temperature on Earth compared with today even if greenhouse gas concentrations and the land-ocean ratio had been the same.

BARRON and WASHINGTON (1982a, b) conducted five sensitivity experiments in order to explore possible mechanisms for the mid-Cretaceous global warmth (100 Ma). The experiments were performed using mean annual solar insolation. A baseline experiment compared the results of simulations for the present with the Cretaceous paleogeography of BARRON et al. (1981a). For each of the five sensitivity experiments leading from the present to Cretaceous paleogeography, one geographic variable was changed. The results of each experiment was compared with the results of the preceding experiment. The first experiment used present-day geography and topography and explored the effect of changing the albedo of the surfaces of Antarctica and Greenland from snow-covered to snow-free. The effect was to increase the global average temperature 0.8°C and to raise the temperature of Antarctica by 10-15°C. The second experiment was to remove the topography from the present-day continents to explore the effect of relief on the climate. The global average temperature increased 1.1°C although the temperature of present

lowland areas decreased 1-7°C; the temperature of Antarctica increased by 15°C. The third experiment moved the flat continents to their Cretaceous positions, but keeping present-day shorelines. This produced the largest change, an increase of 3.1 °C in global average temperature. The greatest difference was in the northern polar region, where temperatures increased 21°C. The fourth experiment changed the shorelines to reflect the higher sea-level of the mid-Cretaceous. Although it was expected that the much greater area of epicontinental seas would result in significant warming, the global average temperature actually decreased by 0.1°C. The fifth experiment added Cretaceous topography; the global average temperature decreased 1.1°C, exactly offsetting the effect of removing topography from the present land areas carried out in the second experiment. Comparing the simulation with mid-Cretaceous geography directly to the simulation for the present, BARRON and MOORE (1994) cited a global average temperature increase of 4.8°C for the Cretaceous. Tropical temperatures increased 2°C, the North Pole 15°C, and the South Pole became 39°C warmer than in the simulation for the present-day.
For orbital case B (NH winter at perihelion), which is the run closest to the present day orbital configuration average temperatures on Earth were 2.6°C warmer at perihelion than at aphelion. These results were expected, because the relatively uniform distribution of the continents at the C/T boundary favors a “normal” response of Earth’s climate system to precessional forcing.

This study has shown that the interpretation of seasonal data (DJF and JJA) alone does not fully describe the effects of orbital forcing on the climate and sedimentary system. In order to test climatic and sedimentological sensitivity to orbital forcing, the evaluation of monthly data is essential. Analysis of these simulations also shows that the largest climatic effects do not necessarily occur during maximum and minimum forcing, when winter or summer solstices were at perihelion or aphelion. Instead, the simulations indicate large changes when the equinoxes coincide with perihelion or aphelion (orbital case A and C). Previous model approaches, where only seasonal data (DJF and JJA) and cold summer/warm summer simulations have been investigated, may have missed important information.
There is no obvious dependence between the amplitude of temperature changes and precipitation on WNA in these simulations. However, the correlation between temperature and surface runoff over WNA is very good, indicating direct relation between those two parameters. The model simulations indicate that the largest effect of precessional forcing on temperature takes place over the continental interiors, whereas the largest response of precipitation is over the open ocean, especially in the equatorial Tethys. The response of land surface- and ocean precipitation to precessional forcing in the tropics varies by as much as 18% between orbital cases A and C.

9.6. Hypotheses to explain the formation of bedding couplets in the WIS

Detailed clay-mineral studies of the Bridge Creek bedding cycles in the Greenhorn Formation by PRATT (1981, 1984) showed that these cycles were the result of varying supply of terrigenous material from the basin margin, diluting the biogenic carbonate flux. PRATT further suggested that during the wetter parts of the Greenhorn cycles, when carbonate was diluted with terrigenous clay, a surface layer of lower salinity water developed and caused stratification of the water column. The density-stratified water column resulted in oxygen-deficient bottom water which, in turn, resulted in enhanced preservation of organic matter in the sediments. Basin stratification with less saline surface waters during the carbonate-poor parts of the Greenhorn cycles was further substantiated by studies of oxygen-isotopic values and faunal composition by BARRON et al. (1985). These studies suggested that changes in the Earth's precession and obliquity altered the patterns of precipitation, particularly along the northern margin of the Tethys. During the times of increased precipitation, freshwater surface runoff from the Sevier Highlands to the west of the seaway increased. These climate changes had two effects: 1) the increase in the influx of terrigenous clastics diluted the rain of biogenic carbonate debris. 2) the salinity of the surface water was lowered, creating a density-stratified basin. The increased supply of clastic debris reduced the carbonate content and increased the overall sedimentation rate. Variations in the supply of terrigenous debris from WNA was largest in the central part of the WIS (this study: NM), where the bedding cycles are well developed. However, variation of the precession of the equinoxes caused smaller fluctuations in the south (this study: TX, MX), whereas changes in the supply of terrigenous debris were smallest in the northernmost sections (this study: CAN, MT). Sections in Canada and Montana experienced continuous influence of terrestrial debris and were not affected by changes in its supply.

The more clay-rich sediments deposited during the wetter intervals contained greater quantities of less-degraded, hydrogen-rich organic matter. Higher biologic productivity in the surface waters may have been caused by a greater supply of land-derived nutrients during wet intervals (PRATT et al., 1993).

EICHER and DINER (1985) proposed an alternative hypothesis, that the primary bedding cyclicity (couplets) in the Bridge Creek Interval reflects climatically-controlled variations in carbonate productivity. They argued that the Bridge Creek Interval was deposited in a pelagic setting, far from shore. Periodic freshwater input to the seaway would have deposited fine-grained detrital sediment at a high rate, much more like that in a near shore setting than in a pelagic setting. The estimated rate of pelagic sedimentation (after EICHER and DINER, 1985; 1-2 cm/ka) for the Bridge Creek Interval does not appear to be compatible with the existence of a freshwater lid on the WIS during deposition of the marlstone beds. Instead, the carbonate sedimentation rate favors the productivity model for the observed rhythmic sedimentation. Productivity cycles could develop through changes

in the a) the intensity of upwelling, b) riverine nutrient flux, or c) surface water salinity (MACLEOD et al., 2001).

Note that the proposed Milankovitch cycles with periods at 400, 100 ka; 41 ka; and 23 and 19 ka are the dominant ones observed in the sedimentological record, but bedding couplets or geochemical cycles are unlikely to be simple 21, 41, 100, and 400 ka signals, because: a) there are numerous quasi-periods within the Milankovitch bands, b) the orbital forcing-climate/ocean system response is complex and non-linear, c) sediments rarely preserve all fluctuations of the climate system, d) periods of Milankovitch cycles could have changed through time, and e) other cycles such as autocycles and sub-Milankovitch cycles are likely to be present in the stratigraphy. Thus it is simplistic to look for simple sets of 5 precession cycles per 1 eccentricity cycle (5:1 “bundles”) as tests of Milankovitch forcing.

These two models are usually cited in discussions of the interpretation of Milankovitch forced bedding- or geochemical cyclicity in the Western Interior Seaway of North America. The precession simulations support the EICHER and DINER (1985) hypothesis. The formation of bedding couplets was probably not influenced by changes in precipitation along the northern margin of the Tethys ocean as proposed by BARRON et al. (1985), but by changes in surface runoff from the Sevier Highlands. Changes of temperature clearly reflect changes in insolation during the course of a year and correlate positively with the surface runoff data in the study area.

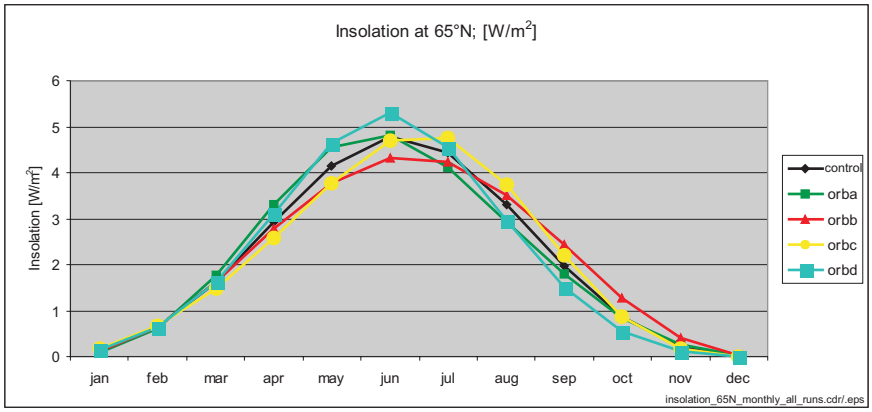

Figure 108: Monthly insolation at the top of the atmosphere at 65°N; [W/m^2]. Atmospheric resolution is 3.75°x3.75°.

Paleo-elevations and paleo-latitudes of WNA; [meter]

	western WNA			eastern WNA								
	107°W	105°W	103°W	101°W	99°W	97°W	95°W	93°W	91°W	89°W	87°W	85°W
89°N	0	0	0	0	0	0	0	0	0	0	0	0
87°N	0	0	0	0	0	0	0	0	0	0	0	0
85°N	1000	1000	1000	1000	1000	1000	1000	1000	1000	1000	1000	200
83°N	200	200	200	200	1000	1000	1000	1000	1000	1000	200	200
81°N	200	200	200	200	1000	1000	1000	1000	1000	1000	1000	1000
79°N	200	200	200	200	200	200	200	200	1000	1000	1000	1000
77°N	1000	1000	1000	1000	1000	1000	200	200	200	200	200	200
75°N	0	0	200	1000	1000	1000	1000	1000	1000	1000	1000	1000
73°N	0	0	0	1000	1000	1000	1000	1000	1000	1000	1000	1000
71°N	0	0	0	1000	1000	1000	1000	1000	1000	1000	1000	1000
69°N	0	0	1000	1000	1000	200	1000	1000	1000	1000	1000	200
67°N	0	200	1000	1000	200	200	200	1000	1000	1000	1000	0
65°N	0	200	1000	1000	200	200	200	200	1000	0	0	0
63°N	0	0	1000	1000	200	200	200	200	0	0	0	0
61°N	0	0	0	1000	200	200	200	0	0	0	0	0
59°N	0	0	0	0	0	200	200	0	0	0	0	0
57°N	0	0	0	0	1000	200	200	1000	0	0	0	0
55°N	0	0	0	200	1000	1000	1000	0	0	0	0	0
53°N	0	0	200	200	200	1000	1000	1000	0	0	0	0
51°N	0	0	1000	1000	1000	1000	3000	1000	0	0	0	0
49°N	0	0	3000	1000	1000	3000	3000	1000	0	0	0	0
47°N	500	0	3000	3000	3000	1000	0	0	0	0	0	0
45°N	500	0	3000	3000	1000	0	0	0	0	0	0	0
43°N	0	500	0	3000	1000	0	0	0	0	0	0	0
41°N	0	500	0	3000	1000	1000	0	0	0	0	0	0
39°N	0	200	1000	3000	1000	1000	0	0	0	0	0	0
37°N	0	0	1000	3000	1000	1000	0	0	0	0	0	0
35°N	0	0	500	3000	1000	1000	0	0	0	0	0	0
33°N	0	0	0	3000	0	1000	0	0	0	0	0	0
31°N	0	0	0	0	0	1000	0	0	0	0	0	0
29°N	0	0	0	0	0	0	1000	0	0	0	0	0
27°N	0	0	0	0	0	0	0	0	0	0	0	0
25°N	0	0	0	0	0	0	1000	0	0	0	0	0

elevations_WNA.cdr/.eps

Table 3: Table shows general topography in terms of the average paleo-elevation in each 2° x 2° grid cell for western North America from BALUKHOVSKY and MIGDISOV (unpublished) and KAUFFMAN (pers. comm.).

The simulations suggest that the formation of bedding couplets in the central and southern portion of the Western Interior Seaway was primarily controlled by the topography of WNA (Table 3) and sensitivity of the surface runoff regime to precessional forcing. WNA can be divided into two parts: a high southern region extending from about 27°-49°N (TX and MX sections) and a low northern region between 51°-63°N (NM, (CO), CAN and MT sections). Bedding couplets closely related to changes of the precessional parameter were also found in southern Colorado, about 100-200 km north of the New Mexican sections (FLOEGEL and RIPS, unpublished diploma thesis, see Figure 1 for location of these sections). These two regions were characterized not only by different relief but also by the shape of their drainage basins. The southern part of WNA had an area of about 1,009,000 km^2. It was narrow and dominated by the steep relief of the Sevier Highlands with elevations up to 3000 m. Varying input of large amounts of terrigenous material could be transported into the central and southern seaway from this mountainous region. This allowed terrigenous dilution of the carbonate content during times of increased surface runoff, but the sensitivity to changes of the precessional parameter was low. The northern part of WNA had an area of ~1,292,000 km^2, but was characterized by a low relief (200-1000 m). Due to the higher

surface runoff in the northern region, the amount of sediments transported by rivers to the WIS was larger. The sensitivity of surface runoff to precessional forcing was higher than in the south.
A surprising result of these simulations for WNA was the fact that precipitation and surface runoff correlate negatively (northern part) or not at all (southern part), whereas surface runoff and temperature correlate positively. Surface runoff was simulated to reach the highest values when precipitation was lowest (northern part). Precipitation and subsurface runoff show the same annual distribution, whereas GENESIS simulated peaks in surface runoff during NH summer, when temperatures were high, resulting in convective storms in the study area. Convective storms would have the effect of sudden short-time increases of precipitation which can not be seen in the mean monthly data. Not all of those large volumes of precipitation can infiltrate into the groundwater system, due to a saturation of the soil. As a result, the excess volumes of water become surface runoff with high erosivity. Another contributor to surface runoff is melt water from snow in the mountains of WNA. The surface runoff peaks in April (northern WNA, orbital case A) and May (southern WNA, orbital case A) could be attributed to the spring melt water. The models predict average snow heights accumulations up to 10 m (annual average) on the highest (southern) parts of the Sevier Highlands. The $\delta^{18}O$ values of DETTMAN and LOHMANN (2000) had suggested that snow melt must have been an important component of the freshwater system and the simulations support this idea.

In addition to the topographic differences affecting the detrital load of rivers, the sediments were also deposited under different oceanographic conditions. The reason for the different response of the sedimentary system to orbital forcing between the New Mexican (precession) and the Texan-Mexican (obliquity) sections could be related to the narrow gateway between the WIS and the Tethys in southern New Mexico, proposed by ROBINSON ROBERTS and KIRSCHBAUM (1995). The sedimentary systems north and south of this gateway were influenced by very different water masses: the enclosed meridional WIS and the “open ocean” system of the Tethys. The sediments deposited beneath these two water masses record different orbital cycles (precession and obliquity), but the surface runoff data suggest that the precession signal should also be present in the southern sections. Only small changes of the climatic and topographic conditions occurred north and south of the gateway. Either global scale signals overprinted the precessional signal in the south, or the cycles in Texas and Mexico may be precession rather than obliquity cycles. This problem can only be solved with better age control and more reliable estimates of sedimentation rates for the Texan and Mexican sections.

Recognizing its diverse topographic and oceanographic properties, the WIS can be divided into three units (Table 4). The sedimentary system of each unit reacted differently to changes of the climate system.

Unit Paleolatitude	Climatic, topographic, and oceanographic conditions
Northern unit 51°-71°N	- rel. low precipitation (~3.6-3.7 mm/day, annual average) - large annual variability of precip. - rel. high runoff (~0.3-0.7 mm/day, annual average) - rel. low relief (200-1000 m) - rel. large amount of sediment to the WIS (by rivers) - rel. low saline water (<24 per mil ???) in the WIS - water temperature of 10-15°C in the WIS - rel. large time lag between erosion and sedimentation - very low sensitivity to precessional forcing
Central unit 41°-51°N	- rel. high precipitation (~4.2-4.6 mm/day, annual average) - small annual variability of precip. - rel. high runoff (~0.3-0.7 mm/day, annual average) - rel. steep relief (1000-3000 m) - high sediment load of rivers - rel. high saline water (33-38 per mil) in the WIS - water temperature of 15-25°C in the WIS - rel. short time between erosion and sedimentation - highest sensitivity to precessional forcing
Southern unit 27°-41°N	- rel. high precipitation (~4.2-4.6 mm/day, annual average) - small annual variability of precip. - rel.high runoff (~0.6-0.7 mm/day, annual average) - rel. steep relief (1000-3000 m) - high sediment load of rivers - rel. high saline water (33-35 per mil) in the WIS/Tethys - water temperature of 20-27°C in the WIS/Tethys - more open oceanic conditions - rel. short time between erosion and sedimentation - rel. low sensitivity to precessional forcing

WIS_three_units.cdr/.eps

Table 4: The WIS can be divided into three different units, according to varying climatic, topographic, and oceanographic conditions.

The reasons why the Canadian sections did not develop any bedding couplets were of climatic, topographic and oceanographic origin. The permanent low salinity inflow from the Arctic Ocean, fed by surface runoff from N-Asia, N-Europe, and northern part of N-American craton, freshened the northern part of the WIS. In combination with the cool water temperatures, this led to ecologic exclusion of calcareous microplankton. Due to low sensitivity to changes of the precession of the equinoxes, no sedimentary couplets formed.

The sections in Montana were at paleolatitudes of ~45-47°N. Although they belong to the central unit, their proximity to the oceanic frontal systems interfered with the formation of bedding couplets. Similar mechanisms as proposed for the Canadian sections prevented the formation of

limestone/shale interbedding. Climatically, the Montana sections should belong to the central unit, but due to the oceanographic conditions, they are influenced by mechanisms responsible for sedimentation in the northern unit.

The central unit, containing the New Mexican and the sections in Colorado (FLOEGEL and RIPS, unpublished diploma thesis) was influenced by different factors. Changes in precession could produce bedding couplets because the sensitivity of the sedimentary system to changes of the climate system was higher. The more direct response was due to the narrow, steep drainage basins of WNA, which translated the large changes in surface runoff into changes in the sediment supply. Creeks and rivers could deliver their high terrestrial sediment load directly to the seaway without major losses in flood plains or coastal plains. Carbonate deposition was enhanced by high salinity water and higher temperatures. These factors allowed for the development of bedding couplets.

The southern unit, containing the Texan and New Mexican sections was controlled by climate mechanisms similar to the central unit, but being open to the Gulf of Mexico it experienced oceanographic conditions. The southern seaway water masses were related to those of the “open-ocean”, and apparently responded to changes in obliquity, rather than to the precession of the equinoxes. One mechanism which has been proposed for the rhythmicity of the Agua Nueva Formation (MX) and for the Ernst Member of the Boquillas Formation (TX) is periodic carbonate dissolution (ARTHUR and DEAN, 1991; DIESTER-HAASS, 1991). Microfacies analysis has shown that the Agua Nueva Formation formed under upper bathyal environment conditions. The lysocline was shallower during the Cretaceous, because of the widespread carbonate deposition as chalk in shallow seas. The lysocline may have been even shallower along continental margins, as it is today. These authors have shown that in younger pelagic sequences the most common cause of carbonate cyclicity is changing chemical characteristics of the deep waters. EINSELE and RICKEN (1991) have shown that during the late Quaternary the position of the lysocline oscillated by 500 m in the equatorial Pacific and by 1000 m in the central Indian Ocean, due to complex interaction between carbonate accumulation and dissolution. The lysocline has experienced a constant fluctuation in response to periodical climatic and sea level changes. Carbonate rich beds formed when deposition took place above the lysocline, but when deposition was below the lysocline dissolution diminished the production of carbonate, and relatively carbonate-poor layers developed. Therefore, it has been proposed by LONGORIA (1998) that fluctuations of the depth of the lysocline caused the periodical changes in the carbonate dissolution rate which formed the rhythmic limestone and marl couplets.

9.7. Implications of the orbital runs

9.7.1. River discharge and its effect on the freshwater balance of the WIS

The even annual distribution and the low sensitivity to changes of the precession of the equinoxes indicates that there is probably no connection between subsurface runoff and the cyclic formation of bedding couplets. However, the effect of subsurface runoff on the fresh water balance of the WIS is very large compared to the effect of surface runoff, because the mean annual subsurface runoff is six to seven times larger than surface runoff. The annual distribution shows that subsurface runoff in the southern part (~4.4 mm/day) of WNA is about 0.7 mm/day higher than in the northern part (~3.7 mm/day). River discharge (subsurface- plus surface runoff) from WNA is ~3,757 km^3/yr. About 1,974 km^3/yr come from the northern part and ~1,863 km^3/yr from the southern part. This large constant input of freshwater from WNA and the inflow from the Arctic Ocean (Figure 102) was probably adequate to establish a permanent low salinity lid on the WIS, at least over the northern part.

	Area of water surface; [km^2]	Area of drainage basin; [km^2]	River discharge ; [km^3/yr]	Volume of water mass; [km^3]	Thickness of freshwater added annually; [m/yr]
Black Sea	461,000	1,874,904	353	573,945	~0.77
Arctic Ocean present day	14,700,000	22,350,000	5,140	16,700,000	~0.35
WIS north and south	11,600,000	2,300,515	3,757	2,900,000	~0.32
WIS north only	5,459,862	1,291,667	1,974	1,364,966	~0.36
WIS south only	6,092,119	1,008,848	1,863	1,523,030	~0.31

Blacksea_WIS.cdr/.eps

Table 5: Comparison of the present day Black Sea and the Cretaceous WIS (VLADIMIROV, 1999; ALYUSHINSKAYA and IVANOV, 1978).

A modern analog to the northern part of the WIS might be the Black Sea. Although it lies in a region where evaporation exceeds precipitation, its fresh water balance is dominated by the large

land area and volume of water which drains into it through a few rivers (50% from the Danube alone). The fresh water balance is responsible for freshening the surface layer to about 17‰ whereas the deep waters are about 35‰. These salinity differences control the Black Sea marine ecosystem. Changes in the fresh water input have a significant impact on salt and water balances, particularly in the shallow, biologically highly productive north-western region. Low salinity surface outflow from the Black Sea and high salinity bottom inflow of Mediterranean water through the Bosphorus are controlled by the width and depth of the strait, and are critical elements maintaining the unusual hydrography and ecosystems of the Black Sea. The fresh water balance of the Black Sea is usually negative from July to October when river inflow is minimal, but reverses during the rest of the year. In some years the fresh water balance is also negative in January, June, November, and December. The strongest positive balance of fresh water occurs from February through May. The total annual river discharge into the Black Sea (353 km^3/yr) is ~1/10 of that of the WIS, equal to a layer 0.77m thick. The area of the drainage basin (1,874,904 km^2) is about 20% smaller than that of the WIS. The volume of the Black Sea is ~547,000 km^3 compared to the ~875,000 km^3 of the WIS.

Another modern analogue might be the Arctic Ocean, which is not as restricted from the open ocean as the Black Sea. There are major ocean water fluxes through the Greenland-Spitsbergen gap, the Bering Strait, and the Arctic Archipelago. Salinities of the open Arctic Ocean range between 28-35‰, but are less on the shelves. The inflow of surface- and subsurface runoff add the equivalent of a ~0.35m thick layer of freshwater to the Arctic Ocean each year. The Arctic Ocean is characterized by a large seasonal cycle of fresh water input against a background of climatically significant interannual and decadal timescale variations. Today, the Arctic Ocean has an area of 14,700,000 km^2 and river discharge of ~5,140 km^3/yr. This would a add layer with a thickness of 0.35m each year.

River discharge from WNA into the WIS is simulated to be the equivalent to a layer about 0.32m thick, about half of that of the Black Sea. This large inflow suggests that a reduced salinity layer would have existed in the WIS if the connections to the open ocean were restricted. The northern connection to the open ocean was through the Arctic Ocean which received major fresh water inflow from eastern N-America, Europe and Asia. During Cenomanian/Turonian times, the Arctic Ocean had an area of at most 3×10^6 km^2. Then, as today, a large part of Asia, Europe, Greenland, and North America drained into it. Surface runoff into the Arctic Ocean was simulated to be 3,375 km^3/yr for orbital case A, 5,054 km^3/yr for orbital case B, 4,962 km^3/yr for orbital case C, and 4,727 km^3/yr for orbital case D. Annually, these volumes of surface runoff should have added thicknesses of 1.10m, 1.70m, 1,65m, and 1,60m of fresh water to the Arctic Ocean. The subsurface runoff is not yet included in those numbers. These constant very large fresh water inflows would easily be able to maintain a salinity below 25‰, as suggested by FISHER et al. (1994). Due to higher river discharge from northern WNA and exchange with the low salinity Arctic

Ocean, the low salinity surface waters were probably thicker in the north. The lack of calcareous benthic foraminifera indicates that the low salinity waters reached the floor of the seaway.

9.7.2. Mechanical erosion and sediment discharge by rivers

Surface runoff from land is responsible for the mechanical erosion of terrigenous detritus. It is the surface runoff which erodes loose material and provides the suspended and fraction load of rivers. The major factors controlling erosion are: a) area of the drainage basin, b) large-scale relief, c) local relief, d) geologic conditions in the drainage basin, and e) climate (SUMMERFIELD and HULTON, 1994; ALLEN, 1997; HAY, 1998; HOVIUS, 1998; HARRISON, 2000). Vegetation also plays a major role; in a frequently cited paper, LANGBEIN and SCHUMM (1958) noted that the spacing between plants and degree of exposure of the soil to precipitation are important factors in erosion and surface runoff. They indicated that the most rapid erosion occurs where precipitation supports only sparse plant cover, so that bare soil is exposed between the plants and roots do not bind all of the soil. Unfortunately, the model runs described here did not include an interactive vegetation model, so this effect can not be evaluated.
The sedimentary significance of the concentration of precipitation into short periods of time was first recognized by FOURNIER (1960), who proposed that an uneven distribution of precipitation through the year increases erosion. The Oxford Sediment Flux Database (ALLEN, 1997; HOVIUS, 1998) shows that this also true for surface runoff.
Another important parameter in determining the amount of sediment delivered to the sea is the competence of rivers. Competence refers to the largest particle a river can carry in suspension, and is indicative of the total amount of sediment it can carry. Increased flow in a river enhances its ability to carry large amounts of sediment downstream. Competence is high when the river transports large volumes of water and when its gradient is high.
Cretaceous rivers were very different from those of today. Today, about 2/3 of the amount of water of a river comes from surface runoff and only 1/3 from the groundwater system. The model simulations indicate that during the Cretaceous the ratio of surface runoff/subsurface runoff varied between 1:6 and 1:14 during the 4 orbital models. Totally different from the 2:1 ratio observed today. Only ~7-17% of the river discharge is contributed by surface runoff, but it was surface runoff that generated the suspended load of the rivers. This study has shown that surface runoff from WNA is strongest in June, July, and August. This concentration of runoff, due to increased occurrence of intense convective storms would have resulted in increased mechanical erosion of detrital material on land. Due to the constant large volume river discharge throughout the year, competence of the Cretaceous rivers must have been high, and they would have been able to transport any detrital material they received into the seaway.

Bedding couplets could only form where variations in the surface runoff regime took place and where the sensitivity to orbital forcing was high.

10. Summary and conclusions

A multidisciplinary investigation of early Late Cretaceous conditions in the Western Interior Seaway of North America (WIS) was carried out in order to test it's sensitivity to changes of one of the Earth's orbital parameters, the precession of the equinoxes. The aim was to explore possible mechanisms for the formation of cyclic bedding sequences seen in large parts of the central and southern WIS, comparing sedimentological, paleontological, and geochemical methods with the results of the paleoclimate simulations.
Focussing on the Cenomanian/Turonian (C/T) boundary interval, nine sections were measured and analyzed geochemically for TOC, $CaCO_3$, and $\delta^{13}C_{org}$. These sections represent a North-South transect, extending from southern Canada (Alberta) through northern Mexico (Nuevo Leon).

Assuming reasonable rates of continuous sedimentation (2.25 cm/ka), the stratigraphic sections studied show Milankovitch-like periodicities, but bedding couplets can not be seen in all of the sections. The sections in Canada and Montana do not show any lithological cyclicity. Bedding couplets only form in the central and southern part of the seaway. Of the sampled sections, NM-I-00 is the northernmost section which shows a lithological cyclicity of ~27 ka, whereas location NM-II-00 shows bedding couplets probably related to a 22 ka cycle. Further south, the duration of the cycles increases almost by a factor of two, with a mean cyclicity for section TX-I-00 of 44 ka and 40 ka for section MX-I-00.
Although the lithological couplets may not be visible, some of the sections show geochemical cyclicity closely related to Milankovitch parameters. The northernmost location at Thistle Creek (CAN-III-00) which shows a cyclicity of 266-288 ka for the $\delta^{13}C_{org}$, TOC and $CaCO_3$ parameters. An assumption of lower sedimentation rates would indicate a cyclicity close to 400 ka, which could have been produced by changes in Earth's eccentricity. The next section to the south (CAN-II-00) does not indicate a cyclic variation close to that produced by Milankovitch parameters, but CAN-I-00 shows variation of the $CaCO_3$ content with a period of about 122 ka, which is close to the eccentricity signal. The next two sections to the south (MT-I-00; NM-I-00) both show large variation of one or more geochemical parameters, but the changes are highly irregular. At NM-II-00 periodicities of 16 ka and 22 ka have been proposed, indicating that variations of the precessional parameter influenced sedimentation. The Texan section shows a periodicity of the $CaCO_3$ parameter close to the 42 ka obliquity cycle, whereas the Mexican section does not show any geochemical cyclicity.
The resemblance between Milankovitch-type periodicities in the Earth's orbital elements and Late Cretaceous rhythmic bedding sequences at the C/T boundary in the WIS strongly suggests an orbital influence on sedimentary regimes during non-glacial times.

The different signals in New Mexico (precession), and in Texas and Mexico (obliquity) may be related to the response of the sedimentary system in two different water masses. A narrow gateway between the WIS and the Tethys, located in southern New Mexico probably blocked large-scale water exchange between the two sedimentary systems allowing them to respond differently to the climatic changes caused by varying orbital parameters.

A reference paleoclimatic model was simulated by a control run with a circular orbit (eccentricity=0), an obliquity of 23.5°, and 5 x present day CO_2.The control run predicts a global MAT of ~20.7°C, almost 6°C higher than the present day MAT, with average temperatures around the north pole only slightly below freezing during the coldest months of the northern hemisphere winter. The simulated high-latitude temperatures correspond very well with those indicated by analysis of paleo-flora. During the austral winter temperatures over Antarctica cool to an average of -12°C. The warmest temperatures occur between 30° north and south over the large continental interiors of Asia, Africa, and South America. During their hemispheric summers, temperatures in these regions reach more than 35°C. As a rule, the surface air temperature over the ocean closely approximates that of the sea surface. Tropical sea surface temperatures off the eastern coast of S-America and Africa during NH winter were as high as 32°C (present day: 28°C- max. 30°C). The precipitation pattern for the control run shows relatively low precipitation for the regions north of 75°N and south of 75°S during each hemispheric winter. Precipitation in these regions does not exceed 2 mm/day. The larger continental interiors of Asia, Africa, and South America lie in desert latitudes and have very low precipitation values of 0-1 mm/day. Highest precipitation occurs along the equator (up to 12 mm/day) and between 15° north and south, with values ranging from 4-7 mm/day. Zones of high precipitation become established between 30° and 60° north and south during their hemispheric winters, but weaken during their hemispheric summers. Due to the absence of polar highs during the winter, strong westerly wind belts develop between 50° and the high pressure zones at 30°. Strong trade winds developed during each hemispheric winter. The results of the control run suggest global atmospheric and oceanic circulation systems that were very different from today.
Analysis of the distribution of calcareous plankton species has shown that they were cosmopolitan during the Cretaceous. This distribution implies that there were no effective subtropical and polar fronts in the ocean. The lack of these frontal systems implies that either the westerlies were displaced poleward over land areas or were so weak as to be unable to force the frontal systems into existence. Such conditions would be most likely if the polar regions were sites of seasonal low or weak atmospheric pressure rather than the persistent highs. This would imply that there were seasonally two rather than three atmospheric cells per hemisphere. This pattern was simulated in the control run. These conditions could have extended the paleobiogeographic limits of the

calcareous plankton further poleward than today. A two-cell/hemisphere circulation (HAY, 2001) should be possible under the condition of warm poles presented in this study.

The results of the four orbital runs suggest that orbital-scale temperature, precipitation, surface runoff, and subsurface runoff variability interpreted from sediments may reflect orbitally modulated changes in monthly temperature, precipitation, surface runoff and subsurface runoff rather than mean annual changes of these parameters.

This study has shown that the influence of precessional Milankovitch cycles and the resulting solar radiation distribution at the top of the atmosphere can produce significant seasonal variations in temperature and precipitation, and in particular in surface runoff from land. Temperature sensitivity to orbital forcing is evident in the large continental interiors (Antarctica, Asia, S-America, Africa) at middle and high latitudes, whereas precipitation responds primarily over the continents (S-America, Africa) and oceans at low and middle latitudes. Global surface runoff changes induced by precessional forcing show a completely different pattern. Significant changes were found only north of 25°N and south of 45-50°S. The largest changes occur on WNA, the northern part of the N-American craton, northern Asia, Australia, and Antarctica. A reduced sensitivity was simulated for small regions in S-America and Africa, but the amount of surface runoff occurring on these two continents was low, ~0.01 mm/day at the maximum. Changes in the distribution of subsurface runoff do not contribute to mechanical erosion , but have a large effect on chemical erosion. The largest response to changes of the precessional parameter is simulated between 25°S and 50°N. Changes are largest in northern S-America, N-Africa, WNA (Sevier Highlands), and on the southernmost tip of Asia. No subsurface runoff was produced in the desert regions of northern and central Asia, central S-America, central Africa, and on Antarctica. The even annual distribution and the low sensitivity to changes of the precession of the equinoxes indicates that there is probably no mechanism connecting subsurface runoff and the cyclic formation of bedding couplets. However, the effect of subsurface runoff on the freshwater balance of the WIS is very large compared to the effect of surface runoff. The mean annual subsurface runoff is six to seven times larger than surface runoff. Subsurface runoff in the southern part of WNA is simulated to be 15% higher than in the northern part.

It might be anticipated that the precessional signal seen in the sediments would reflect an increase and peak in surface runoff when perihelion is at the NH summer solstice. Perhaps surprisingly, the opposite seems to be true. There is high surface runoff in summer during all orbital configurations and low surface runoff when NH winter is at perihelion (orbital case B). Instead of being due to a spike of surface runoff at one orbital configuration, the precession signal is produced by the elimination of high summer surface runoff when perihelion occurs during NH winter.

The Cenomanian/Turonian WIS can be divided into three units controlled by different climatic, topographic and oceanographic factors:
1) A northern unit (51°-71°N; AB and MT), where bedding couplets did not develop, had a permanent low salinity lid and relatively cool water temperatures. This led to ecologic exclusion of calcareous microplankton. The response of surface runoff to changes of the precessional parameter is very low. In addition, the topographic conditions of northern WNA allowed for relatively large amounts of terrigenous material entering the seaway.
2) The central unit (41°-51°N; CO and NM) responded to changes of the precessional parameter with the formation of bedding couplets had more normal warm marine conditions. Due to the narrow and steep drainage basin, changes of the surface runoff regime were translated directly to varying sediment loads of creeks and rivers. Interference of terrestrial processes, such as fluvial sedimentation in coastal plains was low. At the same time carbonate production was enhanced by more normal saline water and higher temperatures. These two factors allowed for the development of bedding couplets.
3) The southern (27°-41°N; TX and MX) unit was controlled by similar mechanisms as the central unit, but being open to the Gulf of Mexico had different oceanographic conditions. The latter must have been responsible for the change from precessional- to obliquity controlled sedimentation. Sensitivity to changes of the precession of the equinoxes is lower than for the central unit. The properties of the water mass resembled more that of an “open-ocean” water mass, which was probably controlled by changes in obliquity. One possible mechanism could have been periodic carbonate dissolution, produced by fluctuations of the depth of the lysocline, which caused the periodical changes in the carbonate dissolution rate, which in turn formed the rhythmic limestone and marl couplets. The position of the lysocline was shallower during times of global warmth, because of the more widespread carbonate deposition.

Model simulations such as these may be applied to the sampling strategy and interpretation of the sedimentary record. This study demonstrates the feasibility of using climate model results to identify regions of high sensitivity to orbital forcing. In addition the results can be used to evaluate the impact of parameters such as precipitation and surface runoff on the sedimentary record. Ideally, this study should be followed up with modeling experiments investigating the effect of obliquity changes, in order to define the effect of the full spectrum of orbital-scale variability on processes related to sedimentation. With a plausible fresh water balance for the WIS its role in global circulation could be investigated with an appropriate ocean model.

11. Acknowledgements

First of all, I want to thank Prof. William W. Hay who has guided my research during this thesis. I am especially grateful that he was not “just” my supervisor, but a friend. Bill, I will always remember our time in France. I also want to thank my co-supervisor Prof. Wolf-Christian Dullo for his helpful contributions to this study. Special thanks are due to my friend Dr. Robert M. DeConto (University of Massachusetts, Amherst, MA), who introduced me to the troubles and secrets of climate modeling and gave me all the computing time needed to complete this study. I would also like to thank Dr. Emanuel Söding (GEOMAR, Kiel), who helped me with just everything, including all the “small” computer problems, which needed to be fixed to complete this thesis.

There are a great number of friends and colleagues at GEOMAR and at many institutions in the United States who I thank for their help and discussions during this study. It would be difficult to name all of the people who have contributed to this dissertation, but I would especially like to thank: Prof. J. F. Longoria (Florida International University, Miami, FL) for analyzing the thin sections and smear slides of the Texan and Mexican sections, Dr. C. Collom (Mt. Royal College, Calgary, AB) for his exceptional help in Canada with the biostratigraphy of the Canadian sections during the field season, Prof. C. Johnson & Prof. E. G. Kauffman (Indiana University, Bloomington, IN) for their helpful discussions and friendship, Dr. R. M. Leckie (University of Massachusetts, Amherst, MA) for providing the largest part of the samples from section MT-II-00, Dr. Rüdiger Stein (AWI, Bremerhaven) and Uli Wand (AWI, Potsdam) for the isotopic analyses, and A. & Dr. C. N. Wold (Estes Park, CO) for drink, food, housing, and friendship.

I am also grateful to Dr. D. A. Lopez (The Montana Bureau of Mines and Geology, Billings, MT), Prof. A. G. Plint (University of Western Ontario, London, ON), Don Corrick and Carol Purchase (National Park Service, Big Bend NP, TX), Dr. C. Duncan (University of Massachusetts, Amherst, MA), A. MacConnell (University of Massachusetts, Amherst, MA), W. Stinnesbeck (Universität Karlsruhe), W. E. Dean Jr. (U. S. Geological Survey, Denver, CO), Dr. G. Hoffman (New Mexico Bureau of Mines & Mineral Resources, Sorocco, NM), Dr. M. Elrick (University of New Mexico, Albuquerque, NM), Dr. J. R. Morrow (University of Northern Colorado, Greeley, CO.), and Prof. L. M. Pratt (Indiana University, Bloomington, IN).

Special thanks to Uwe Hentschke, Felix “Hiwi” Studt, Bettina Domeyer, Dagmar Rau, Jutta Pagel, and Karin Wießjahn.

I would also like to thank the Deutsche Forschungsgemeinschaft for funding this study (HA 2891/3-1 and HA 2891/3-2).

Very important contributions to this thesis came from the “Betriebssportgruppe Dart” (Toby, thanks for the expression). Without you guys, this thesis would have been a lot less amusing and stimulating (?).Thanks to Claudia Didié, Carolyn Wegner, Jan Helmke, Tobias “Toby” Mörz, Stefan Nees, and Emanuel “Manu” Söding.
After all this research, one question remains unsolved and mysterious:

“Kreisklasse oder Weltklasse”

My parents deserve special thanks for just everything during the last 31 years.
Last but not least, thanks to my girlfriend, Nicole for her “PATIENCE” during the last 12 years.

12. References

ADHÉMAR, J. A. (1842): Révolutions de la mer, déluges périodiques. Carilian-Goeury & Dalmont, Paris.

AGASSIZ, L. (1828): On the erratic blocks of the Jura. Edinburgh New Philos. Journal, 24, p. 176-179.

ALLEN, P. A. (1997): Earth Surface Processes. 1st edition. Blackwell Science. Oxford. pp. 404.

ALYUSHINSKAYA, N. M. and IVANOV, V. V. (1978): Water inflow from land. In: Korzun, V. I., ed., World Water Balance and Water Resources of the Earth. Studies and Reports in Hydrology 25, United Nations Educational, Scientific and Cultural Organization (UNESCO). p. 568-574.

ANDREWS, J. E., TANDON, S. K., and DENNIS, P. E. (1995): Concentration of carbon dioxide in the Late Cretaceous atmosphere. Journal of the Geological Society of London, 152, p. 1-3.

ANTHES, R. A. (1977): A cumulus parameterization scheme utilizing a one-dimensional cloud model. Monthly Weather Review, 105, p. 921-941.

ARMSTRONG, R. L. and WARD, P. (1993): Late Triassic to earliest Eocene magmatism in the North American Cordillera: Implications for the Western Interior Basin. In: Caldwell, W. G. E. and Kauffman, E. G., eds., Evolution of the Western Interior Basin. Geological Association of Canada Special Paper 39, p. 49-72.

ARTHUR, M. A. and DEAN, W. E. (1991): An holistic geochemical approach to cyclomania: Examples from Cretaceous pelagic limestone sequences. In: Einsele, G., Ricken, W., and Seilacher, A., Cycles and events in stratigraphy. Springer-Verlag, Berlin, p. 126-166.

ARTHUR, M. A. and SCHLANGER, S. O., (1979): Cretaceous “oceanic anoxic events” as causal factors in development of reef-reservoired giant oil fields: American Association of Petroleum Geologists Bulletin, 63, p. 870-885.

ARTHUR, M. A., DEAN, W. E., BOTTJER, D., and SCHOLLE, P. A. (1984): Rhythmic bedding in Mesozoic-Cenozoic pelagic carbonate sequences; the primary and diagenetic origin of Milankovitch-like cycles. In: Berger, A., Imbrie, J., Hays, J. D., Kukla, G., and Saltzman, B., eds., Milankovitch and Climate, pt. 1. Amsterdam, Reidel Publishing Company, p. 191-222.

ARTHUR, M. A., SCHLANGER, S. O., and JENKYNS, H. C. (1987): The Cenomanian-Turonian oceanic anoxic event, II. Paleoceanographic controls on organic-matter production and preservation. In: Marine Petroleum Source Rocks, Brooks, J. and Fleet, A. J., eds., Geological Society Special Publication No. 26, p. 401-420.

ARTHUR, M. A., DEAN, W. E, and PRATT, L. M. (1988): Geochemical and climatic effects of increased marine organic carbon burial at the Cenomanian/Turonian boundary, Nature 335, p. 714-717.

ARTHUR, M. A., DEAN, W. E., POLLASTRO, R. M., SCHOLLE, P. A., and CLAYPOOL, G. E. (1985): A comparative geochemical and mineralogical study of two transgressive pelagic limestone units, Cretaceous Western Interior Basin U. S.. In: Pratt, L. M., Kauffman, E. G., and Zelt, F., eds., Fine-grained Deposits and Biofacies of the Cretaceous Western Interior Seaway: Evidence of Cyclic Sedimentary Processes, Field Trip Guidebook No. 4: Tulsa, Society of Economic Paleontologists and Mineralogists, p. 16-27.

ARTHUR, M. A., BRUMSACK, H.-J., JENKYNS, H. C., and SCHLANGER, S. O., (1990): Stratigraphy, geochemistry, and paleoceanography of organic carbon-rich Cretaceous sequences. In. Ginsburg, R. N. and Beaudoin, B., eds., Cretaceous, Resources, Events, and Rhythms: Background and Plans for Research. Dordrecht, the Netherlands, Kluwer Academic Publishers, p. 75-119.

BARRON, E. J. (1983): Warm equable Cretaceous, the nature of the problem. Earth Science Reviews, 19, p. 305-338.

BARRON, E. J. and WASHINGTON, W. M. (1982a): Atmospheric circulation during warm geologic periods: Is the equator-to-pole surface-temperature gradient the controlling factor. Geology, 10, p. 633-636.

(1982b): Cretaceous climate: A comparison of atmospheric simulations with the geologic record. Palaeogeography, Palaeoclimatology, Palaeoecology, 40, p. 103-133.

(1985): Warm Cretaceous climates: High atmospheric CO_2 as a plausible mechanism. In: Sundquist, E. T. and Broecker, W. S., eds., The carbon cycle and atmospheric CO_2: Natural variations Archean to present. Geophysical Monograph, 32, p. 546-553.

BARRON, E. J., THOMPSON, S. L., and SCHNEIDER, S. H. (1981): An ice-free Cretaceous? Results from climate model simulations. Science, 212, p. 501-505.

BARRON, E. J., ARTHUR, M. A., and KAUFFMAN, E. G. (1985): Cretaceous rhythmic bedding sequences: A plausible link between orbital variations and climate. Earth Planetary Science letters, v.72, p. 327-340.

BARRON, E. J., FAWCETT, P. J., PETERSON, W. H., POLLARD, D., and THOMPSON, S. L. (1995): A simulation of mid-Cretaceous climate. Paleogeography, 10, p. 953-962.

BASS, N. W. (1926a): Geologic investigations in western Kansas, with special reference to oil and gas possibilities; Geology of Ellis County; Geology of Hamilton County; Geologic structure of the Dakota sandstone; Structure and limits of the Kansas salt beds; Kansas, State Geol. Survey, Bull. 11.

BAUMGARTNER, A. and REICHEL, E. (1975): The world water balance-mean annual global, continental and maritime precipitation, evaporation and run-off. Elsevier Scientific Publishing Company. Amsterdam. pp.179.

BEATTY, J. K. (1990): The New Solar System, 4th ed. Cambridge, Petersen, C. C.; and Chaikin, A. (eds.). England: Cambridge University Press, p. 105.

BEERBOWER, J. R. (1966): Cyclotherms and cyclic depositional mechanisms in alluvial plain sedimentation. Kansas State Geological Survey Bulletin 1, p. 31-42.

BERGER, A. L. (1977): Support for astronomical theory of climatic change. Nature 269, p. 44-45.

(1978): Long-term variations of daily insolation and Quaternary climatic changes, Journal of Atmospheric Sciences 35, p. 2362-2367.

(1980):The Milankovitch astronomical theory of paleoclimates; a modern review. Vistas in Astronomy. 24, Part 2, 103-122. 1980.

(1981): The astronomical Theory of paleoclimates. In: Berger, A. L., ed., Climatic Variations and Variability: Facts and Theories. Reidal, Dordrecht, The Netherlands, p. 501-525.

(1984): Accuracy and frequency stability of the Earth's orbital elements during the Quaternary. In: Berger, A. L., Imbrie, J., Hays, J., Kukla, G., Saltzman, B., eds., Milankovitch and Climate. Reidal, Dordrecht, The Netherlands, p. 3-39.

(1987a): Long-term variations of caloric insolation resulting from the Earth's orbital elements. Quaternary Research 9, p. 139-167.

(1992): Astronomical theory of paleoclimates and the last glacial-interglacial cycle. In: Methods and concepts in European Quaternary stratigraphy; proceedings of a session of INQUA, Subcommission for European Quaternary Stratigraphy and Long Terrestrial Records Working Group. Quaternary Science Reviews. 11, p. 571-581.

(2001): Where astronomy and geology meet: From ice ages to global warming. Louis Schlichter lectureship, Institute of Geophysics and Planetary Physics, UCLA.

BERGER, A. and TRICOT, C. (1986): Global climatic changes and astronomical theory of paleoclimates. In: Cazenave, A., ed., Earth Rotation: Solved and Unsolved Problems, D. Reidel Publ. Company, Dordrecht, Holland, p. 111-129.

BERGER, A. and LOUTRE, M. F. (1994): Long-term variations of the astronomical seasons. In: Topics in Atmospheric and Interstellar Physics and Chemistry, Boutron, C., ed., Les Editions de Physique, Les Ulis, France, p. 33-61.

BERGER, W. H. and HERUGA, J. C. (1992): Reading the sedimentary record of the ocean's productivity. In: Falkowski, P. G. and Woodhead, A. .D., eds., Primary Productivity and Biogeochemical Cycles in the Sea. Plenum Press, New York, p. 455-485.

BERGER, W. H., BONNEAU, M. C., PARKER, F. L. (1982): Foraminifera on the deep-sea floor: lysocline and dissolution rate. Oceanologica Acta, 2, p. 249-257.

BERNER, R. A. (1992): Paleo-CO_2 and climate. Nature 358, 114 p..

(1994): Geocarb II: a revised model of atmospheric CO_2 over Phanerozoic time. American Journal of Science, 294, p. 56-91.

BERNER, R. A., LASAGA, A. C., and GARRELS, R. M. (1983): The carbonate-silicate geochemical cycle and its effect on atmospheric carbon dioxide over the past 100 million years. American Journal of Science, 283, p. 641-683.

BLACKWELDER, E. (1915): Post-Cretaceous history of the mountains of central western Wyoming. Journal of Geology, 23, p. 97-117, 193-217, 307-340.

BOTTJER, D. J. (1986): Campanian-Maastrichtan chalks of SW Arkansas: petrology, paleoenvironments and comparison with other N American and European chalks. Cretaceous Research, 7, p. 161-196.

BOTTJER, D. J., ARTHUR, M. A., DEAN, W. E., HATTIN, D. E., and SVARDA, C. E. (1986): Rhythmic bedding produced in Cretaceous pelagic carbonate environments: sensitive recorder of climatic cycles. Paleoceanography, 1, p. 467-481.

BRADLEY, R. S. (1985): Quaternary Paleoclimatology: Methods of Paleoclimatic Reconstruction, Allen & Unwin, 472 p..

BRALOWER, T. J. (1988): Calcareous nannofossil biostratigraphy and assemblages of the Cenomanian-Turonian boundary interval: Implications for the origin and timing of oceanic anoxia. Paleoceanography 3, 275-316.

BROECKER, W. S. (1995): The glacial world according to Wally, revised edition. Eldigio Press, Palisades, New York, 318 p.

BROECKER, W. S & DENTON, G. H. (1990): What drives glacial cycles ? Scientific American, January 1990, p. 49-56.

BRYAN, K. (1984): Accelerating the convergence to equilibrium of ocean climate models. Journal of Physical Oceanography. 14, p. 666-673.

BUDYKO, M. I. (1974): Climate and Life. Academic Press, pp. 508.

CALDWELL, W. G. E. (1984): Early Cretaceous transgressions and regressions in the southern Interior Plains. In: The Mesozoic of Middle North America. D. F. Stott and D. J. Glass (eds.). Canadian Society of Petroleum Geologists Memoir 9, p. 173-203

CERLING, T. (1991): Carbon dioxide in the atmosphere: Evidence from Cenozoic and Mesozoic Paleosoils. American Journal of Science, 291, p. 377-400.

CLAPP, R. B., COVEY, C., THOMPSON, S. L., and HORNBERGER, G. M. (1986): Empirical equations for some soil hydrologic properties. Water Resources Research, 14, 601-604.

CLAYTON, J., MUDGE, M., R., LUBECK, Sr. C., and DAWS, T., A., (1983): Hydrocarbon source rock evaluation of the disturbed belt, northwestern Montana, in Powers, R.B., ed., Geologic studies of the Cordilleran thrust belt - 1982: Rocky Mountain Association of Geologists, 2, p. 817-830.

COBBAN, W. A., ERDMANN, C. E., LEMKE, R. W., and MAUGHN, E. K. (1959): Revision of Colorado group on Sweetgrass arch, Montana. American Association of Petroleum Geologists Bulletin, 43, p. 2786-2796.

COTILLON, P. (1985): Les variations à différentes échelles du taux d'accumulation sédimentaire dans les séries pélagiques alternantes du Crétacé inférieur, conséquences de phénomènes globaux. Bull. Soc. Géol. France, 8, p. 59-68.

CRAIG, H. (1957): Isotopic standards for carbon and oxygen and correction factors for mass spectrometric analysis of carbon dioxide. Geochim. Cosmochim. Acta, v. 12, p. 133-149.

CROLL, J. (1864): On the physical cause of the change of climate during geological epochs. Philosophical Magazine, 28, p. 121-137.

(1875): Climate and time in their geological relations. Appleton, New York

CROWLEY, T. J. (1998): Significance of tectonic boundary conditions for paleoclimate simulations. In: Tectonic boundary conditions for climate reconstructions, Crowley, T. J. and Burke, K., eds., p. 3-20.

CROWLEY, T. J. and NORTH, G. R. (1991): Paleoclimatology. Oxford University Press, 339 p..

CROWLEY, T. J., KIM, K.-J., MENGEL, J., and SHORT, D. (1992): Modeling 100,000-year climate fluctuations in pre-Pleistocene time series. Science, 255, p. 705-707.

CROWLEY, T. J., YIP, K.-J., and BAUM, S. K. (1993): Milankovitch cycles and Carboniferous climate. Geophysical Research Letters, 20, p. 1175-1178.

DARWIN, C. (1842): Notes on the effects produced by ancient glaciers of Caernaronshire, and on the boulders transported by floating ice. London, Edinburgh, Dublin, Philosophical Magazine, 21, p. 180-188.

DEAN, W. E. and GARDNER, J. V. (1986): Milankovitch cycles in Neogene deep-sea sediments. Paleoceanography, 1, p. 539-553.

DEAN, W. E., ARTHUR, M. A., and CLAYPOOL, G. E. (1986): $^{13}C/^{12}C$ of organic carbon in Cretaceous black shales: influence of source, diagenesis, and environmental factors. Marine Geology, 70, p. 119-157.

DeCELLES, P. G., GRAY, M. B., RIDGWAY, K. D., COLE, R. B., SVRIASTAVA, P., PEQUERA, N., and PIVNIK, D. A. (1991): Kinematic history of a foreland uplift from Paleocene synorogenic conglomerate, Beartooth Range, Wyoming and Montana,. Geological Society of America Bulletin, 103, p. 1458-1475.

DeCONTO, R. M. (2000): Late Cretaceous climate, vegetation, and ocean interactions. In: Huber, B. T., MacLeod, K. G., and Wing, S. L., eds., Warm climates in earth history, p. 275-296.

DE GRACIANSKY, P. C., DEROO, G., HERBIN, J. P., MONTADERT, L., MÜLLER, C., SCHAAF, A., and SIGAL, J. (1984): Ocean-wide stagnation episode in the late Cretaceous. Nature, 308, p. 346-349.

DEINES, P. (1980): The isotopic composition of reduced organic carbon. Elsevier, Amsterdam, p. 329-406.

DETTMAN, D. L. and LOHMANN, K. C. (2000): Oxygen isotope evidence for high-altitude snow in the Laramide Rocky Mountains of North America during the Late Cretaceous and Paleogene. Geology, 28, no. 3, p. 243-246.

DICKINSON, R. E., HENDERSON-SELLERS, A., KENNEDY, P. J., and WILSON, M. F. (1986): Biosphere-atmosphere transfer scheme (BATS) for the NCAR community climate model. Boulder, Colorado, National Center for Atmospheric Research (NCAR), NCAR Technical Note NCAR/TN-275+STR, 69 p..

DIESTER-HAASS, L. (1991): Rhythmic carbonate content variations in Neogene sediments above the oceanic lysocline. In: Einsele, G., Ricken, W., and Seilacher, A., Cycles and events in stratigraphy. Springer-Verlag, Berlin, p. 94-109.

DORMAN, J. L. and SELLERS, P. J. (1989): A global climatology of albedo, roughness length and stomatal resistance for atmospheric general circulation models as represented by the simple biosphere model (SiB). American Meteorological Society. 28, p. 833-855.

DYMAN, T. S., (1987): A review of the geology and petroleum resource potential of north-central Montana: U.S. Geological Survey Open-File Report 87-450G, 30 p.

EICHER, D. L. (1969): Paleobathymetry of the Cretaceous Greenhorn Sea in eastern Colorado. American Association of Petroleum Geologists Bulletin, 53, p. 1075-1090.

EICHER, D. L. and DINER, R. (1985): Foraminifera as indicators of water mass in the Cretaceous Greenhorn Sea, Western Interior. In: Pratt, L. M., Kauffman, E. G., and Zelt, F. B., eds., Fine-grained deposits and biofacies of the Cretaceous Western Interior Seaway: Evidence of cyclic sedimentary processes. Society of Economic Paleontologists and Mineralogists, Second Annual Midyear Meeting, Golden, Colorado, Field Trip No. 9, p. 60-71.

EICHER, D. L. and DINER, R. (1989): Origin of the Cretaceous Bridge Creek cycles in the Western Interior, United States. Palaeogeography, Palaeoclimatology, and Palaeoecology, 74, p. 127-146.

EICHER, D. L. and WORSTELL, P. (1970): Cenomanian and Turonian foraminifera from the Great Plains, United States. Micropaleontology, 16, p. 269-324.

EINSELE, G. (1982): Limestone-marl cycles (periodicities): Diagnosis, significance, causes – A review. In: Einsele, G. Seilacher, A., eds., Cyclic and Event Startification. Springer Verlag, New York, p. 8-53.

EINSELE, G. and RICKEN, W. (1991): Limestone-marl alternations; an overview. In: Cycles and events in stratigraphy. Einsele, G., Ricken, W., and Seilacher, A., eds., Springer Verlag. Berlin, p. 23-47.

ELDER, D. L., GUSTAFSON, E. R., and SAGEMAN, B. B. (1994): Basinwide correlation of parasequences in the Greenhorn Cylothem, Western Interior, U. S.. Geological Society of America Bulletin, v. 106, p. 892-902.

EMERSON, S. and BENDER, M. (1981): Carbon fluxes at the sediment-water interface of the deep sea: calcium carbonate preservation. Journal Marine Research, 39, p. 139-162.

EMILIANI, C. & GEISS, J. (1959): On glaciations and their causes. Geologische Rundschau, 46, p. 576-601.

EPIS, R. C. and CHAPIN, C. E. (1975): Geomorphic and tectonic implications of the post-Laramide, late Eocene erosion surface in the Southern Rocky Mountains. In: Curtis, B. F., ed., Cenozoic history of the Southern Rocky Mountains. Geological Society of America Memoir 144, 30, p. 45-74.

FISCHER, A. G. (1980): Gilbert-bedding rhythms and geochronology. In: Yochelson, E. I., ed., The scientific ideas of G. K. Gilbert. Geological Society of America Special Publication 183, p. 93-104.

(1993): Cyclostratigraphy of Cretaceous chalk-marl sequences. In: Caldwell, W. G. E. & Kauffman, E. G., eds., Evolution of the Western Interior Basin. Geological Association of Canada, Special Paper 39, p. 283-295.

(1998): Preface. In: Barrera, E. and Johnson, C. C., eds., Evolution of the Cretaceous Ocean-Climate System. Boulder, Colorado, Geological Society of America, Special Paper 332, p. vii-viii.

FISCHER, A. G., HERBERT, T., and PREMOLI-SILVA, I. (1985): Carbonate bedding cycles in Cretaceous pelagic and hemipelagic sediments. In: Pratt, L. M., Kauffman, E. G., and Zelt, F. B., eds., Fine-grained deposits and biofacies of the Cretaceous Western Interior Seaway: Evidence of cyclic sedimentary processes. Society of Economic Paleontologists and Mineralogists, Field trip guidebook No. 4, Tulsa, p. 1-10.

FISHER, C. G., (1991): Calcareous nannofossil and foraminifera definition of an oceanic front in the Greenhorn Sea (late middle through late Cenomanian), northern Black Hills, Montana and Wyoming: paleoceanographic implications [Ph. D. thesis]. Boulder, University of Colorado, 341 p..

FISHER, C. G., HAY, W. W., and EICHER, D. L. (1994): Oceanic front in the Greenhorn Sea (late middle through late Cenomanian). Paleoceanography, vol. 9, no. 6, p. 879-892.

FISHER, A. G. and HAY, W. W. (1999): Calcareous nannofossils as indicators of mid-Cretaceous paleofertility along an ocean front, U. S. Western Interior. In: Barrera, E. and Johnson, C. C., eds., Evolution of the Cretaceous Ocean-Climate System. Boulder, Colorado, Geological Society of America, Special Paper 332, p. 161-180.

FLOEGEL, S. and RIPS, M. (1998): Rekonstruktion der paläo-ozenographischen Verhältnisse an der Wende Cenoman/Turon im Western Interior Seaway, entlang einer Nord-Süd-Traverse, Foothills, Colorado Front Range. Unpublished Diploma Thesis. University of Göttingen, Germany.

FOURNIER, F. (1960): Climat et l'érosion. Presses Universitaires de France, Paris. UNESCO, 7 Place Fontenoy, 75700 Paris, France.

FRITZ, P. & FONTES, J. CH. (1989): Handbook of Environmental Isotope Geochemistry, 3, The Marine Environment, A. Elsevier Science Publishers B. V., 425, Amsterdam.

FROELICH, P., BLANC, V., MORTLOCK, R., CHILLRUND, S., DUNSTAN, W., UDOMKIT, A., and PENG, T.-H. (1992): River fluxes of dissolved silica to the ocean were higher during glacials: Ge/Si in diatoms, rivers, and ocean. Paleoceanography, 7, p. 739-767.

FRUSH, M. P. and EICHER, D. L. (1975): Cenomanian and Turonian foraminifera and paleoenvironments in the Big Bend region of Texas and Mexico. Special Paper - Geological Association of Canada. 13, Cretaceous System in the Western Interior of North America, p. 277-301.

GALE, A. S., JENKYNS, H. C., KENNEDY, W. J., and CORFIELD, R. M. (1993): Chemostratigraphy versus biostratigraphy: data from around the Cenomanian-Turonian boundary. Journal of the Geological Society London. 150, 29-32.

GALE, A. S., SMITH, A. B., MONKS, N. E. A., YOUNG, J. A., HOWARD, A., WRAY, D. S., and HUGGETT, J. M. (2000): Marine biodiversity through the Late Cenomanian-Early Turonian: palaeocenographic controls and sequence stratigraphic biases. Journal of the Geological Society, London, 157, p. 745-757.

GARDNER, J. V. (1982): High-resolution carbonate and organic-carbon stratigraphies for the late Neogene and Quaternary from the western Caribbean and eastern equatorial Pacific. In: Prell, W. L., Gardner, J, V. et al., Initial Reports DSDP 68, Washington (US Government Print Office), p. 347-364.

GILBERT, J. K. (1895): Sedimentary measurement of Cretaceous time. Journal of Geology, 3, p.121-127.

GOUGH, D. O. (1981): Solar interior structure and luminosity variations. Solar Physics, 74, p. 21-34.

HANCOCK, J. M. and KAUFFMAN, E. G. (1979): The great transgressions of the Late Cretaceous. Journal of the Geological Society, 136, p. 175-186.

HAQ, B., HARDENBOHL, J., and VAIL, P. R. (1987): Chronology of fluctuating sea level since the Triassic (250 million years ago to present). Science, 235, p. 1156-1167.

HARRIES, P. J. (1993): Dynamics of survival following the Cenomanian-Turonian (Upper Cretaceous) mass extinction event. Cretaceous Research, 14, p. 563-583.

HARRISON, C. G. A. (2000): What factors control mechanical erosion? Int. Journal of Earth Sciences, 88, p. 752-763.

HAY, W. W. (1996): Tectonics and climate. Geologische Rundschau, 85, p. 409-437.

(1998): Detrital sediment fluxes from continents to oceans. Chemical Geology, 145, p. 287-323.

HAY, W. W., EICHER, D. L., and DINER, R. (1993): Physical oceanography and water masses in the Cretaceous Western Interior Seaway. In: Caldwell, W. G. E. & Kauffman, E. G., eds., Evolution of the Western Interior Basin. Geological Association of Canada, Special Paper 39, p. 297-318.

HAY, W. W., DeCONTO, R. M. & WOLD, CH. N. (1997): Climate: Is the past the key to the future ? Geol. Rundschau 86, p. 471-491.

HAY, W. W., DeCONTO, R. M. & WOLD, CH. N, WILSON, K. M., VOIGT, S., SCHULZ, M., ROSSBY-WOLD, A:, DULLO, W.-C., RONOV, A. B:, BALUKHOVSKY; A. N. and SÖEDING, E. (1999): An alternative global Cretaceous paleogeography. In: Barrera, E. and Johnson, C. C., eds., Evolution of the Cretaceous Ocean-Climate System. Boulder, Colorado, Geological Society of America, Special Paper 332, p. 1-47.

HAY, W. W. and WOLD, C. N. (1998): The role of mountains and plateaus in a Triassic climate model. In: Crowley, T., and Burke, K.,eds., Tectonic boundary conditions for climate reconstructions. Oxford, United Kingdom. Oxford University Press, p. 116-143.

HAY, W. W., THOMPSON, S. L., POLLARD, D., WILSON, K. M., and WOLD, C. N. (1994): Results of a climate model for Triassic Pangaea. Zentralblatt für Geologie und Paläontologie, Teil I, v.1992 11/12, p. 1253-1265.

HAY, W. W., DeCONTO, R. M., FLOEGEL, S. and SOEDING, E. (2001b): ODSN data explained by low atmospheric pressure at the poles during times of equable climate. Poster presentation, Kolloquium des DFG-Schwerpunktprogramms ODP/DSDP, 2001, Karlsruhe.

HAYS, J. D., IMBRIE, J. & SHACKLETON, N. J. (1976): Variations in the Earth’s orbit: Pacemaker of the ice ages. Science 194, p. 1121-1132.

HERBIN, J. P., MONTADERT, L., MÜLLER, C., GOMEZ, R., THUROW, J., and WIEDMANN J. (1986): Organic-rich sedimentation at the Cenomanian-Turonian boundary in oceanic and coastal basins in the North Atlantic and Tethys. In: Summerhayes, C. P. and Shackleton, N. J., eds., North Atlantic Paleoceanography. Geological Society Special Publication No. 21, p. 389-422.

HERBERT, T. D. (1994): Reading orbital signals distorted by sedimentation: Models and examples. In: deBoer, P. L. and Smith, D. G., eds., Orbital forcing and cyclic sequences, Oxford, International Association of Sedimentologists, Special Publication Number 19, p. 483-507.

HERMANN, A. B. and SPICER, R. A. (1996): Paleobotanical evidence for a warm Cretaceous Arctic Ocean. Nature, 390, p. 330-333.

(1997): New quantitative paleoclimate data for the Late Cretaceous Arctic: evidence for a warm polar ocean. Palaeogeography, Palaeoclimatology, Palaeoecology, 128, p. 227-251.

HOFMANN, P., RICKEN, W., SCHWARK, L., and LEYTHAEUSER., D (1999): Coupled oceanic effects of climatic cycles from late Albian deep-sea sections of the North Atlantic. In: Barrera, E. and Johnson, C. C., eds., Evolution of the Cretaceous Ocean-Climate System. Boulder, Colorado, Geological Society of America, Special Paper 332, p. 143-159.

HOVIUS, N. (1998): Controls on sediment supply by large rivers. In: Shanley, K. W. and McCabe, P. J., eds., Relative role of eustasy, climate, and tectonism in continental rocks. SEPM Special Publication 59, p. 3-16.

HUBER, M., and SLOAN, L.C. (1999): Warm climate transitions: A general circulation modeling study of the Late Paleocene Thermal Maximum (~56 Ma). Journal of Geophysical Research, 104, p. 16,633-16,655.

IMBRIE, J. & IMBRIE, J. Z. (1980):Modeling the climate response to orbital variations. Science 107, 943-953.

JABLONSKY, D. (1991): Extinctions: a paleontological perspective. Science, 253, p. 754-757.

JELETZKY; J. A. (1970): Cretaceous macrofauna. In: Douglas, R. J. W., ed., Geology and economic minerals of Canada (fifth edition). Canada Geological Survey, Economic Geology Report 1, p. 649-662.

JENKYNS, H. C., 1980: Cretaceous anoxic events-from continents to oceans: Journal of the Geological Society of London, 137, p. 1-17.

JENKYNS, H. C., GALE, A. S., and CORFIELD, R. M. (1994): Carbon- and oxygen-isotope stratigraphy of the English Chalk and Italian Scaglia and its palaeoclimatic significance. Geol. Mag. 131, p. 1-34.

JORDAN, T. E. (1981): Thrust loads and foreland basin evolution, Cretaceous western United States. American Association of Petroleum Geologists Bulletin, 65, p. 2506-2520.

KAUFFMAN, E. G. (1977): Geological and biological overview: Western Interior Cretaceous Basin. In. Kauffman, E. G., ed., Cretaceous Facies, Faunas, and Paleoenvironments across the Western Interior Basin. Mountain Geologist, 14, No. 3 & 4, p. 75-99.

(1984): Paleobiogeography and evolutionary response dynamic in the Cretaceous Western Interior Seaway of North America. In: Westermann, G. E. G., ed., Jurassic-Cretaceous Biochronology and Paleogeography of North America. Geological Association of Canada, Special Paper 27, p. 273-306.

(1985):Cretaceous evolution of the Western Interior Basin of the United States. In: Pratt, L. M., Kauffman, E. G., and Zelt, F. B., eds., Fine-grained deposits and biofacies of the Cretaceous Western Interior Seaway: Evidence of cyclic sedimentary processes. Society of Economic Paleontologists and Mineralogists, Second Annual Midyear Meeting, Golden, Colorado, Field Trip No. 9, p. IV-XIII.

(1988): Concepts and methods of high-resolution event startigraphy. Annual Rev. Earth Planetary Science, 16, p. 605-654.

KAUFFMAN, E. G., ELDER, W. P., and SAGEMAN, B. B. (1991): High resolution correlation: a new tool in chronostratigraphy. In: Einsele, G., Ricken, W., and Seilacher, A., eds., Cycles and Events in Stratigraphy. Springer Verlag. p. 795-819.

KAUFFMAN, E. G. and CALDWELL, W. G. E.(1993): The Western Interior Basin in space and time. In: Caldwell, W. G. E. and Kauffman, E. G., eds., Evolution of the Western Interior Basin. Geological Association of Canada, Special Paper 39, p. 1-30.

KLEMME, H. D. and ULMISHEK, G. F., (1991): Effective petroleum source rocks of the world: Stratigraphic distribution and controlling depositional factors. American Association of Petroleum Geologists Bulletin, 75, no. 12, p. 1809-1851.

KÖPPEN, W. and WEGENER, A. (1924): Die Klimata der Geologischen Vorzeit. Gebrüder Borntraeger, Berlin.

KUHNT, W. and WIEDMANN, J. (1995): Cenomanian-Turonian source rocks: Paleobiogeographic and paleoenvironmental aspects. In: Paleogeography, paleoclimatology and source rocks, Huc, A. Y, ed., American Association of Petroleum Geologists Studies in Geology 40, 213-231.

KUHNT, W., HERBIN, J. P., THUROW, J., and WIEDMANN, J. (1990): Distribution of Cenomanian-Turonian organic facies in the Western Mediterranean and along the adjacent Atlantic margin. In: Deposition of Organic Facies (Edited by A.Y. Huc American Association of Petroleum Geologists Studies in Geology 30, 133-160.

KUMP, L. R. and SLINGERLAND, R. L. (1999): Circulation and stratification of the early Turonian Western Interior Seaway: Sensitivity to a variety of forcings. In: Barrera, E. and Johnson, C. C., eds., Evolution of the Cretaceous Ocean-Climate System. Boulder, Colorado, Geological Society of America, Special Paper 332, p. 181-190.

KUYPERS, M. M. M., PANCOST, R., and SINNINGHE DAMSTÉ, J. S. (1999a): A large and abrupt fall in atmospheric CO2 concentrations during Cretaceous times. Nature, 399, p. 342-345.

LaFERRIERE, A. P., HATTIN, D., and ARCHER, A. W. (1987): Effects of climate, tectonics and sea-level changes on rhythmic bedding patterns in the Niobrara Formation (Upper Cretaceous), U. S., Western Interior. Geology, 15, p. 233-236.

LAGRANGE, J. L. (1772): Essai sur le problème des trois corps. Oeuvres, vol. 6, p. 272-292, Gauthier-Villars, Paris.

LANGBEIN, W. B. and ISERI, K. T. (1960): General introduction and hydrologic definitions; Manual of hydrology; Part 1, General surface-water techniques. Geological Survey Water-Supply Paper. p. 29.

LANGBEIN, W. B. and SCHUMM, S. A. (1958): Yield of sediment in relation to mean annual precipitation. EOS 39, p. 1076-1084.

LARSON, R. L. (1991): Geological consequences of superplumes. Geology 19, 963-966.

LASKAR, J., JOUTEL, F., and BOUDIN, F. (1993): Orbital, precessional, and insolation quantities for the Earth from –20 Myr to +10 Myr. Astronomy and Astrophysics, v. 270, p. 522-533.

LONGORIA, J. F. (1998a): The Mesozoic of the Mexican cordillera in Nuevo Leon, NE Mexico. International Symposium on Foraminifera, Special Publication, Sociedad Mexicana de Paleontologiá, A. C., p. 1-44.

(1998b): Geologic excursion to the Mesozoic of the Nuevoleones Cordillera. International Symposium on Foraminifera, Special Publication, Sociedad Mexicana de Paleontologiá, A. C., p. 45-64.

LOPEZ, D. A. (1995):Geology of the Sweetgrass hills, north-central Montana. Montana Bureau of Mines and Geology Memoir 68, 35 p..

LOTH, B., GRAF, H.-F., and OBERHUBER, J. M. (1993): Snow cover model for global climate simulation. Journal of Geophysical Research, v. 98, p. 10451-10464.

LUDVIGSON, G. A., WITZKE, B. J., GONZALES, L. A., HAMMOND, R. H., and PLOCHER, O. W., (1994): Sedimentology and carbonate geochemistry of concretions from the Greenhorn Marine Cycle (Cenomanian-Turonian), eastern margin of the Western Interior Seaway. In: Shurr, G. W., Ludvigson, G. A., and HAMMOND, R. H., eds., Perspectives on the Eastern Margin of the Cretaceous Western Interior Basin. Boulder, Geological Society of America Special Paper 287, p. 145-174.

LYELL; C. (1830-1832): Principles of Geology. 1st edition, Murray, London.

MACLEOD, K. G., HUBER, B. T., PLETSCH, T., and ROEHL, U. (2001): Maastrichtian foraminiferal and paleoceanographic changes on Milankovitch timescales. Paleoceanography, 16, p. 133-154.

McFARLANE, N. A. (1987): The effect of orographically excited gravity wave drag in general circulation of the lower stratosphere and troposphere. Journal of Atmospheric Science, v.44, p. 1775-1800.

MIDDELBURG, J. J., VLUG, T., and VANDER NAT, F. J. W. A. (1993): Organic matter mineralisation in marine systems. Global and Planetary Change, 8, p. 47-58.

MILANKOVITCH, M. M. (1920): Théorie Mathematique des Phénomènes Thermiques produits par la Radiation Solaire. Gauthier-Villars, Paris.

(1930): Mathematische Klimalehre und astronomische Theorie der Klimaschwankungen. In: Köppen, W., Geiger, R., eds., Handbuch der Klimatologie. I. Bornträger, Berlin.

(1941): Kanon der Erdbestrahlung. Beograd. Königlich Serbische Akademie, 484 pp.

MOESLE, B (1995): Faziesanalytische Untersuchungen am organischem Material in Sedimenten aus der Lower Colorado Group (Alb-Turon) im Westkanadischen Sedimentären Becken (Südalberta, Kanada). Mahaliac Scientific Studies. Edition Prairie. Belgium. 162 p..

MOLNAR, P. and ENGLAND, P. 1990: Late Cenozoic uplift of mountain ranges and global climate change: Chicken or egg ? Nature, 346, p. 29-34.

MONGER, J. W. H. (1993): Cretaceous tectonics of the North American Cordillera. In: Caldwell, W. G. E. and Kauffman, E. G., eds., Evolution of the Western Interior Basin. Geological Association of Canada Special Paper 39, p. 31-47.

MOORE, R. (1949): The meaning of facies. In: Sedimentary Facies in Geologic History. Geological Society of America Memoir, 39, p. 1-39.

MÜLLER, P. J. and SUESS, E., (1979): Productivity, sedimentation rate and sedimentary organic matter in the oceans. 1. Organic carbon preservation. Deep-Sea Research, 26A, p. 1347-1362.

OBRADOVICH, J. (1993): A Cretaceous time scale. In: Caldwell, W. G. E. and Kauffman, E. G., eds., Evolution of the Western Interior Basin. Geological Association of Canada Special Paper 39, p. 379-396.

PARK, J. and HERBERT, T. D. (1987): Hunting for paleoclimatic periodicities in a geologic time series with an uncertain time-scale. Journal of Geophysical Research, 92, p. 14027-14040.

PARK, J. and OGLESBY, R. J. (1990): A comparison of precession and obliquity effects in a Cretaceous paleoclimate simulation. Geophysical Research Letters, 17, p. 1929-1932.

PARK, J. and OGLESBY, R. J. (1991): Milankovitch rhythms in the Cretaceous: A GCM modeling study. Palaeogeography, Palaeoclimatology, Palaeoecology, 90, p. 329-355.

PEDERSEN, T. F. and CALVERT, S. E., (1990): Anoxia vs. productivity: what controls the formation of organic carbon-rich sediments and sedimentary rocks? Bulletin American Association of Petroleum Geologists, 74, 454-466.

PHILLIPS, T. (2001): http://science.nasa.gov/headlines/y2001/ast03jul_1.htm.

PINNEKER, E. V. (1980): General hydrology. Cambridge Earth Science Series, pp.141.

POLLARD, D. and THOMPSON, S. L. (1995): Use of a land-surface-transfer scheme (LSX) in a global climate model: the response to doubling stomatal resistance. Global and Planetary Change, 10, p. 129-161.

(1998): Driving a high-resolution dynamic ice-sheet model with GCM climate: ice-sheet initiation at 116,000 BP. Annals of Glaciology, 25, p. 296-304.

PRATT, L. M., (1981): A paleo-oceanographic interpretation of the sedimentary structures, clay minerals, and organic matter in a core of the Middle Cretaceous Greenhorn Formation near Pueblo, Colorado. Ph. D. thesis, Princeton University, Princeton, New Jersey, 176 p..

(1984): Influence of paleoenvironmental factors on the preservation of organic matter in middle Cretaceous Greenhorn Formation near Pueblo, Colorado. American Association of Petroleum Geologists Bulletin, 68, p. 1146-1159.

(1985): Isotopic studies of organic matter and carbonate in rocks of the Greenhorn marine cycles. In: Pratt, L. M. and Kauffman, E. G., and Zelt, F. B., eds., Fine-grained Deposits and Biofacies of the Cretaceous Western Interior Seaway: Evidence of Cyclic Sedimentary Processes, Field Trip Guidebook No. 4: Tulsa, Society of Economic Paleontologists and Mineralogists, p. 38-48.

PRATT, L. M. and THRELKHELD, C. N. (1993): Stratigraphic significance of $^{13}C/^{12}C$ ratios in Mid-Cretaceous rocks of the Western Interior, U. S. A.. In: Stott, D. F. and Glass, eds., The Mesozoic of middle North America. Canadian Society of Petroleum Geologists Memoir 9, p. 305-312.

PRATT, L. M. and KING, J. D. (1986): Variable marine productivity and high eolian input recorded by rhythmic black shales in mid-Cretaceous pelagic deposits from central Italy. Paleoceanography, 1, p. 507-522.

PRATT, L. M., ARTHUR, M. A., DEAN, W. E., and SCHOLLE, P. A (1993): Paleoceanographic cycles and events during the Late Cretaceous in the Western Interior Seaway of North America. In: Caldwell, W. G. E. & Kauffman, E. G., eds., Evolution of the Western Interior Basin. Geological Association of Canada, Special Paper 39, p. 333-354.

PRELL, W. and KUTZBACH, J. (1992): Sensitivity of the Indian monsoon to forcing parameters and implications for it’s evolution. Nature, 360, p. 647-652.

PRICE, R. A., MONGER, J. W. H., and MULLER, J. E. (1981): Cordilleran cross section , Calgary to Victoria. In: Thompson, R. I. and Cook, D. G., eds., Field Guides to Geological and

Mineralogical Deposits. Geological Association of Canada-Mineralogical Association of Canada, Annual Meeting, Calgary, p. 261-334.

PROKOPH, A., VILLENEUVE, M., AGTERBERG, F. P., and RACHOLD, V. (2001): Geochronology and calibration at the Cenomanian-Turonian boundary. Geology, 29, no. 6, p. 523-526.

RAUP, D. M. and SEPKOWSKI, J. J. (1982): Periodicity in extinctions in the geological past. Proceedings of the Natural Academy of Sciences, USA, 81, p. 801-805.

RAUSCH, P. J. and WILLIAMSON, D. L. (1990): Computational aspects of moisture transport in global models of the atmosphere. Quarterly Journal of the Royal Meteorological Society, 116, 1071-1090.

RICKEN, W. (1991): Variation of sedimentation rates in rhythmically bedded sediments – distinction between depositional types. In: Einsele, G., Ricken, W., and Seilacher, A., Cycles and events in stratigraphy. Springer-Verlag, Berlin, p. 167-187.

RICKEN, W. (1994): Complex rhythmic sedimentation related to third-order sea-level variations: upper Cretaceous, western Interior Basin , U. S. A.. In: deBoer, P. L. and Smith, D. G., eds., Orbital Forcing and Cyclic Sequences. International Association of Sedimentologists Special Publication 19, Oxford, Blackwell Scientific Publications, p. 167-193.

ROBINSON ROBERTS, L. N., and KIRSCHBAUM, M. A. (1995): Paleogeography of the Late Cretaceous of the Western Interior of Middle North America-Coal Distribution and Sediment Accumulation. Robinson Roberts, L. N. and Kirschbaum, M. A., eds., U. S. Geological Survey Professional Paper 1561, 115 p..

RYAN, W. B. F. and CITA, M. B. (1977): Ignorance concerning episodes of ocean-wide stagnation. Mar. Geol. 23, p. 197-215.

SAGEMAN, B. B. and ARTHUR, M. A. (1994): Early Turonian paleogeographic/paleobathymetric map, Western Interior, U. S.. In: Caputo, M. V., Peterson, J. A., and Franczyk, K. J., eds., Mesozoic Systems of the Rocky Mountain Region, USA. Tulsa, Society of Economic Paleontologists and Mineralogists, Rocky Mountain Section, p. 457-469.

SAGEMAN, B. B., RICH, J., ARTHUR, M. A., DEAN, W. E., SAVDRA, C. E., and BRALOWER, T. J. (1998): Multiple Milankovitch cycles in the Bridge Creek Limestone (Cenomanian-Turonian),

Western Interior Basin. In: Dean, W. E., Scott, R. W., and Franks, P. C., eds., Stratigraphy and paleoenvironments of the Cretaceous Western Interior Seaway, USA, SEPM Concepts in Sedimentology and Paleontology No. 6, p. 153-171.

SAGEMAN, B. B., RICH, J., ARTHUR, M. A., BIRCHFIELD, G. E., and DEAN, W. E. (1997): Evidence for Milankovitch periodicities in Cenomanian-Turonian lithologic and geochemical cycles, Western Interior U. S., Journal of Sedimentary Research, v. 67, p. 285-301.

SALTZMAN, B. (1984): Modeling the late-Quaternary glacial variations with multi-component climatic systems. In: Proceedings of the Symposium on ice and climate modeling. Shneider, S. H. and MacQueen, A. D., eds., Annals of Glaciology. 5; p. 225-227.

SALTZMAN, B. & MAASCH, K. A. (1988): Carbon cycle instability as a cause of the Late Pleistocene ice age oscillations: Modeling the asymetric response. Global Biogeochemical Cycles 2: p. 177-185.

SARNTHEIN, M. (1978): Sand deserts during glacial maximum and climatic optimum. Nature, 271, p. 43-46.

SAVRDA, C. E., BOTTJER, D. J., and SEILACHER, A. (1991): Redox-related benthic events. In: Einsele, G., Ricken, W., and Seilacher, A., Cycles and events in stratigraphy. Springer-Verlag, Berlin, p. 524-541.

SCHLANGER, S. O. and JENKYNS, H. C., (1976): Cretaceous oceanic anoxic events - Causes and consequences. Geologie en Mijnbouw, 55, p. 179-184.

SCHLANGER, S. O., JENKYNS, H. C., and PREMOLI SILVA, I. (1981): Volcanism and vertical tectonics in the Pacific Basin related to global Cretaceous transgressions. Earth Planetary Science Letters, 52, 435-449.

SCHLANGER, S. O., ARTHUR, M. A., JENKYNS, H. C., and SCHOLLE, P. A., (1987): The Cenomanian/Turonian oceanic anoxic event, 1. Stratigraphy and distribution of organic-carbon-rich beds and the marine $\delta^{13}C$ excursion. In: Brooks, J. and Fleet, A., eds., Marine Petroleum Source Rocks: London, Geological Society of London Special Publication 26, p. 371-399.

SCHOLLE, P. A. and ARTHUR, M. A. (1980): Carbon isotope fluctuations in Cretaceous pelagic limestones: potential stratigraphic and petroleum exploration tools. American Association of Petroleum Geologists Bulletin 64, 67-87.

SCHWARZACHER, W. and FISCHER, A. G. (1982): Limestone-shale bedding and pertubations of the Earth's orbit. In: Einsele, G., Ricken, W., and Seilacher, A., eds., Cyclic and event stratification . Berlin, Springer-Verlag, p. 72-95.

SCOTESE, C. R., BAMBACH, R. K., BARTON, C., VAN DER VOO, R., and ZIEGLER, A. M. (1979): Paleozoic base maps. Journal of Geology, 87, 3, p. 217-277.

SCOTESE, C. R., VAN DER VOO, R., and ROSS, W. C. (1981): Mesozoic and Cenozoic base maps. Am. Assoc. Petr. Geol. Bull., 65, 989 p..

SCOTT, W. R. (1977): Early Cretaceous environments and paleocommunities in the southern Western Interior. In: Kauffman, E. G., ed., Cretaceous facies, faunas, and paleoenvironments across the western Interior Basin. The Mountain Geologist, 14, p. 155-168.

SEIBOLD, E. and BERGER, W. H. (1982): The sea floor. An Introduction to Marine Geology. Springer, Berlin, Heidelberg, New York, 288 p..

SELLERS, P. J., MINTZ,, Y., SUD, Y. C., and DALCHER, A. (1986): A simple biosphere model (SiB) for use within general circulation models. Journal of Atmospheric Science, 43, p. 505-531.

SELLWOOD, B. W., PRICE, G. D., and VALDES, P. J. (1994): Cooler estimates of Cretaceous temperature. Nature, 370, p. 453-455.

SEMTNER, A. J. (1976): A model for the thermodynamic growth of sea-ice in numerical investigations of climate. Journal of Pysical Oceanography. 6, p. 379-389.

SEMTNER, A. J. and CHERVIN, R. M. (1992): Ocean general circulation from a global eddy-resolving simulation. Journal of Geophysical Research, 97, p. 5493-5550.

SEPKOWSKI, J. J. (1989): Periodicity in extinction and the problem of catatrophism in the history of life. Journal of the Geological Society, London, 146, p. 7-19

SHORT, D. A., CROWLEY, T. J., MENGEL, J. G., HYDE, W. T., NORTH, G. R. (1990): Modeling 100,000 year power in monsoon time series. EOS, Transactions, American Geophysical Union. 71; 43, 1367 p..

SINNINGHE DAMSTÉ, J. S. (2001): http://kellia.nioz.nl/projects/ctnet/research.html.

SIROCCO, F. (1989): Accumulation of eolian sediments in the northern Indian ocean; record of the climatic history of Arabia and India. Reports Geologisch-Paleontologisches Institut Universität Kiel, 27, 185 p..

SLINGO, A. and SLINGO; J. M. (1991): Response of the National Center for Atmospheric Research Community Climate Model to improvement in the representation of clouds. Journal of Geophysical Research, 96, p. 15341-15357.

SLOAN, L. C. and MORRILL, C. (1998): Orbital forcing and Eocene continental temperatures. Palaeogeography, Palaeoclimatology, Palaeoecology, 144, p. 21-35.

SLOAN, L. C., BLUTH, G. J. S., and FILIPELLI, G. (1997): A comparison of spatially-resolved and global mean reconstructions of continental denudation under ice-free and present conditions. Paleoceanography, 12, p. 147-160.

SPICER, R. A. and CORNFIELD, R. M. (1992): A review of marine and terrestrial climates of the Cretaceous with implications for “modeling” the greenhouse Earth. Geological Magazine, 129, p. 169-180.

STELCK, C. R. and WALL, J. H. (1954): Kaskapau foraminifera from Peace River area of western Canada. Research Council of Alberta, Report 68, 81 p.

STOTT, D. F. (1993):Evolution of the Cretaceous foredeeps. In: Caldwell, W. G. E. & Kauffman, E. G., eds., Evolution of the Western Interior Basin. Geological Association of Canada, Special Paper 39, p. 131-150.

SUMMERFIELD and HULTON (1994): Natural controls of fluvial denudation rates in major world drainage basins. Journal of Geophysical Research, 99, p. 13871-13883.

SUMMERHAYES, C. P. (1981): Organic facies of middle Cretaceous black shales in the deep North Atlantic. American Association of Petroleum Geologists Bull. 86, p. 335-345.

THOMPSON, S. L. and POLLARD, D. (1995a): A global climate model (GENESIS) with a land-surface-transfer scheme (LSX). Part I: Present climate simulations. Journal of climate, 8, p. 732-761.

(1997): Greenland and Antarctic mass balances for present and doubled atmospheric CO_2, from the GENESIS Version 2 Global Climate Model. Journal of Climate, 10, p. 871-900.

THOMPSON, S. L., RAMASWAMY, V. and COVEY, C. (1987): Atmospheric effects of nuclear war aerosols in general circulation model simulations: Influence of smoke optical properties. Journal of Geophysical Research, 92, p. 10942-10960.

TORNAGHI, M. E., PREMOLI SILVA, I., and RIPEPE, M. (1989): Lithostratigraphy and planktonic foraminiferal biostratigraphy of the Aptian-Albian “Scisti a Fucoidi” in the Piobbico area: background for cyclostratigraphy. Riv. Ital. Paleont. Stratigr., 95, p. 223-264.

TRICOT, C. and BERGER, A. (1986): Sensitivity of present-day climate to astronomical forcing. In: Wanner, H. and Siegenthaler U., eds., Long and short term variability of climate. Lecture Notes in Earth Sciences. 16; Springer-Verlag, p. 133-152.

UPCHURCH, G. R. and WOLFE, J. A., (1993): Cretaceous vegetation of the Western Interior and adjacent regions of North America. In: Caldwell, W. G. E. & Kauffman, E. G., eds., Evolution of the Western Interior Basin. Geological Association of Canada, Special Paper 39, p. 243-282.

VAIL, P. R., MITCHUM, R. M., Jr., and THOMPSON, S., III, (1977): Global cycles of relative changes of sea level. In: Payton, C. E., ed., Seismic Stratigraphic Applications to Hydrocarbon Exploration. Tulsa, American Association of Petroleum Geologists Memoir 26, p. 83-98.

VALDES, P. J., SELLWOOD, B. W., and PRICE, G. D. (1994): Modelling late Jurassic Milankovitch climate variations. In: Orbital Forcing Timescales and Cyclostratigraphy, House, M. R. and Gale, A. S., eds., Geol. Soc. Spec. Publ., 85, p. 115-132.

VLADIMIROV, V. L. (1999): http://www.grid.unep.ch/bsein/index.html.

WASHINGTON, W. M. and MEEHL, G. A. (1996): High-latitude climate change in a global coupled ocean-atmosphere-sea ice model with increased CO_2. Journal of Geophysical Research. V. 101, 12795-12801.

WASHINGTON, W. M. and PARKINSON, C. L. (1986): An introduction to three-dimensional climate modeling. Mill Valley, California, University Science Books and Cambridge University Press, 422 p..

WATKINS, D. K. (1989): Nannoplankton productivity fluctuations and rhythmically bedded pelagic carbonates of the Greehorn Limestone (Upper Cretaceous). Palaeogeography, Palaeoclimatology, and Palaeoecology, 74, p. 75-86.

WEST, O. L. O., LECKIE, R. M., and SCHMIDT, M. (1998): Foraminiferal paleoecology and paleoceanography of the Greenhorn cycle along the southwestern margin of the Western Interior Sea. In: Stratigraphy and paleoenvironments of the Cretaceous Western Interior Seaway, USA. SEPM Concepts in Sedimentology and Paleontology No. 6. p. 79-99.

WHITE, T. S., WITZKE, B. J., and LUDVIGSON, G. A. (2000): Evidence for an Albian Hudson arm connection between the Cretaceous Western Interior Seaway of North America and the Labrador Sea. Geological Society of America Bulletin, 112, p. 1342-1355.

WILLIAMS, G. P. (1988a): The dynamical range of global circulations - I. Climate Dynamics, 2, p. 205-260.

(1988b): The dynamical range of global circulations - II. Climate Dynamics, 3, p. 45-84.

WILLIAMS, G. D. and BURK, C. F. (1964): Upper Cretaceous. In: McCrossan, R. G. and Claister, R. P., eds., The Geological History of Western Canada. Alberta Society of Petroleum Geologists, p. 169-189.

WILLIAMS, G. D. and STELCK, C.R. (1975): Speculations on the Cretaceous Paleogeography of North America. In: Caldwell, W. G. E., ed., The Cretaceous system in the Western Interior of North America. Geological association of Canada Special Paper 13, p. 1-20.

WILLIAMSON, D. L. (1990): Semi-Lagrangian moisture transport in the NMC spectral model. Tellus, 42A, p. 413-428.

WILLIAMSON, D. L. and RAUSCH, P. J. (1989): Two-dimensional semi-Lagrangian transport with shape-preserving interpolation. Monthly Weather Review, 117, p. 102-129.

WILLIAMSON, D. L., KIEHL, J. T., RAMANATHAN, V., DICKINSON, R. E. and HACK, J. J. (1987): Description of NCAR Community Climate Model (CCM1). Boulder, Colorado, National Center for Atmospheric Research, NCAR Technical Note, v.NCAR/TN-285+STR, 112 p..

WILSON, K. M., POLLARD, D., HAY, W. W., THOMPSON, S. L., and WOLD, C. N. (1994): General circulation model simulations of Triassic climates: Preliminary results. In: Klein, G. D., ed., Pangaea: Paleoclimate, tectonics and sedimentation during accretion, zenith, and breakup of a supercontinent. Geological Society of America. Special Paper 288, p. 91-116.

WITZKE; B. J. and LUDVIGSON, G. A., (1994): The Dakota Formation in Iowa and the type area. In: Shurr, G. W., Ludvigson, G. A., and HAMMOND, R. H., eds., Perspectives on the Eastern Margin of the Cretaceous Western Interior Basin. Boulder, Geological Society of America Special Paper 287, p. 43-87.

WOLFE, J. A., FOREST, C. E., and MOLNAR, P. (1998): Paleobotanical evidence of Eocene and Oligocene paleoaltitudes in midlatitude western North America. Geological Society of America bulletin, v. 110, p. 664-678.

YOUNG, K. (1986): Cretaceous marine inundations of the San Marcos platform, Texas. Cretaceous Research, v.7, p. 117-140.

13. Appendix

13.1. Data sheets / Results of geochemical analyses

CAN-III-00	Thistle Creek					
		TC	TOC	Ccarb	CaCO3	d13C
-2.	Limonite					
-1.	Limestone	9,372	0,509	8,863	73,856	-26,30
16.	Marly shale	2,517	1,667	0,850	7,083	-25,40
15.	Marly shale	2,374	1,470	0,904	7,533	-25,80
14.	Marly shale	2,701	1,455	1,246	10,383	-25,80
13.	Marly shale	2,777	1,583	1,195	9,954	-25,90
12a.	Limestone	8,797	0,926	7,871	65,591	-26,10
12b.	Marly shale	3,013	0,931	2,082	17,347	-24,60
11.	Marly shale	2,516	1,798	0,718	5,983	-26,00
10.	Marly shale	2,464	1,851	0,614	5,112	-26,10
9.	Marly shale	2,578	1,789	0,789	6,571	-26,10
8.	Marly shale	7,380	1,005	6,375	53,122	-25,20
7.	Marly shale	2,220	1,318	0,903	7,521	-26,10
6.	Marly shale	2,803	1,862	0,942	7,846	-26,00
5.	Marly shale	2,648	1,892	0,756	6,300	-26,50
4.	Marly shale	2,913	1,902	1,011	8,425	-26,60
3.	Marly shale					
2.	Marly shale					
1.	Limestone	5,094	1,165	3,930	32,746	-26,45

CAN-II-00	Big Horn River					
		TC	TOC	Ccarb	CaCO3	d13C
1.	Concretio. Limestone	8,315	0,676	7,638	63,651	-24,30
2.	Marly shale	2,319	1,704	0,615	5,121	
3.	Marly shale	2,304	1,243	1,061	8,842	-25,00
4.	Marly shale	2,555	1,757	0,798	6,646	-24,65
5.	Marly shale	2,337	1,532	0,805	6,708	-25,92
6.	Marly shale	2,833	1,871	0,962	8,017	-25,10
7.	Marly shale	3,056	1,827	1,229	10,242	-25,80
8.	Marly shale	2,680	0,327	2,353	19,605	
9.	Marly shale	2,842	2,023	0,820	6,829	-25,15
10.	Marly shale	2,342	1,636	0,706	5,879	-25,60
11.	Marly shale	2,610	1,770	0,840	7,000	-26,05
12.	Marly shale	2,957	1,894	1,064	8,863	-25,40
13.	Marly shale	3,331	0,304	3,027	25,221	-24,80
14.	Marly shale	2,288	1,693	0,596	4,963	-23,45
15.	Marly shale	3,443	1,948	1,495	12,458	-25,70
16.	Marly shale	3,369	1,880	1,489	12,404	-25,70
II.-1.	Limestone	9,270	0,789	8,480	70,669	-26,14
II.-2.	Marly shale	4,828	1,314	3,515	29,288	-25,70
II.-3.	Limestone	8,351	0,724	7,627	63,561	
II.-4.	Marly shale					

II.-5.	Limestone	8,584	0,756	7,828	65,233	-25,80
II.-6.	Marly shale					
II.-7.	Limestone	8,771	0,766	8,004	66,701	-24,60
II.-8.	Marly shale	2,723	1,578	1,146	9,546	-25,50
II.-9.	Limestone	8,401	0,659	7,742	64,518	-25,90
II.-10.	Marly shale					
II.-11.	Limestone	8,807	0,879	7,928	66,064	-25,80
17.	Marly shale	5,435	1,421	4,014	33,450	
18.	Marly shale	4,798	0,332	4,466	37,216	
19.	Marly shale	2,907	1,849	1,058	8,813	-26,90
20.	Marly shale	3,230	1,618	1,612	13,433	-25,50
21.	Marly shale	2,998	1,859	1,140	9,496	-25,50
22.	Marly shale	2,517	1,406	1,111	9,258	-25,40
23.	Marly shale	2,944	0,758	2,186	18,216	-25,60

CAN-I-00	**Burnt Timber Creek**					
		TC	**TOC**	**Ccarb**	**CaCO3**	**d13C**
X-Bentonite	Bentonite					
	Marly shale					
	Limest. concretion					
	Marly shale					
X-1	Bentonite					
	Marly shale					
1.	Limonite					
2a.	Marly shale	2,028	0,132	1,896	15,801	-27,55
2b.		2,366	0,954	1,412	11,768	-26,60
2c.		2,190	0,813	1,377	11,471	-26,03
X-2	Bentonite					
3.	Marly shale					
4.	Marly shale	4,274	0,305	3,968	33,070	
5a.	Marly shale	2,830	0,299	2,531	21,095	-25,80
5b.		3,338	0,323	3,015	25,122	-26,00
5c.		5,773	0,468	5,305	44,212	-25,80
6.	Marly shale	2,549	0,175	2,374	19,783	
7.	Marly shale	2,751	0,300	2,451	20,425	-26,00
8.	Silty-marly shale	2,829	0,720	2,109	17,574	-24,60
9.	Marly shale	4,599	0,264	4,335	36,125	-26,30
10.	Marly shale	1,879	1,628	0,251	2,092	-25,90
11.	Marly shale	4,232	0,269	3,962	33,020	-26,05
12.	Marly shale	3,201	0,257	2,943	24,525	-24,90
13.	Limonite					
14.	Marly shale	2,259	0,439	1,819	15,160	-24,70
15.	Marly shale	2,806	0,889	1,917	15,972	
16.	Marly shale	4,036	0,264	3,772	31,435	-26,90
17.	Marly shale	2,738	0,237	2,501	20,840	-25,90
18.	Marly shale	3,195	0,256	2,938	24,487	-26,65
19.	Marly shale	2,963	0,208	2,754	22,953	-27,48

MT-I-00	**Cone**					
		TC	**TOC**	**Ccarb**	**CaCO3**	**d13C**
1.	Calcareous shale	6,400	4,201	2,200	18,329	-26,50

		6,389	4,329	2,060	17,167	
		7,344	4,942	2,402	20,017	-26,40
2.	Bentonite					
3.	Calcareous shale	5,296	3,470	1,827	15,221	-26,44
4.	Bentonite					
5.	Marly shale	5,214	3,473	1,741	14,508	-26,00
6.	Bentonite					
7.	Marly shale	8,487	5,656	2,831	23,592	-26,30
8.	Bentonite					
9a.	Calcareous shale	7,506	3,328	4,179	34,821	-24,80
9b.		7,846	4,488	3,358	27,983	-26,20
10a.	Calcareous shale	7,600	4,818	2,783	23,188	-26,37
10b.		8,728	5,783	2,945	24,542	
10c.		9,285	6,126	3,159	26,325	
11.	Bentonite					
12.	Calcareous shale	6,323	4,095	2,228	18,563	-26,40
13.	Bentonite/Limonite					
14a.	Calcareous shale	8,660	6,185	2,475	20,625	-25,30
14b.		6,972	4,264	2,709	22,571	-26,30
14c.		7,988	3,528	4,460	37,163	-26,60
15.	Bentonite					
16a.	Calcareous shale	8,437	3,584	4,853	40,438	-25,50
16b.		7,273	1,844	5,429	45,242	-24,50
17.	Bentonite					
18.	Sand. Calcareous shale					
19.	Limonite					
20.	Calcareous shale	9,692	0,517	9,175	76,461	-26,70
21.	Bentonite					
22.	Silt. calcareous shale					
23.	Bentonite					
24.	Sand. calcareous shale	10,635	0,468	10,167	84,723	-26,00
25.	Bentonite					
26.	Sand. calcareous shale	10,585	1,234	9,352	77,929	-26,80
27.	Limonite					
28.	Sand. calcareous shale					
29.	Bentonite					
30.	Sand. calcareous shale					
31.	Bentonite					
32.	Sand. calcareous shale					
33.	Bentonite					
34.	Sand. calcareous shale					
35.	Bentonite					
36.	Sand. calcareous shale					

MT-II-00	**Landfill**					
		TC	**TOC**	**Ccarb**	**CaCO3**	**d13C**
BL96-23,5	Silt. shale (no CaCO3)	1,063	0,904	0,159	1,324	-22,70
BL96-24,3	Silt. shale (no CaCO3)	1,430	0,818	0,612	5,103	-23,70
BL96-26,0	Marly shale	0,381	0,221	0,160	1,336	-26,20
BL96-26,5	Marly shale	0,988	0,707	0,281	2,343	-23,50
BL96-27,0	Marly shale	1,099	0,781	0,317	2,644	-23,60
BL96-27,5	Calcareous shale	1,447	1,028	0,420	3,496	-23,10

BL96-28,0	Calcareous shale	1,423	0,951	0,471	3,928	-23,10
BL96-28,5	Calcareous shale	1,259	0,844	0,415	3,456	-23,40
BL96-29,0	Calcareous shale	1,745	1,208	0,538	4,479	-23,10
BL96-29,5	Calcareous shale	1,926	1,254	0,672	5,596	-22,80
BL96-30,0	Calcareous shale	2,114	1,412	0,703	5,854	
BL96-30,5	Calcareous shale	1,954	1,121	0,833	6,942	-24,10
BL96-31,0	Calcareous shale	1,849	1,072	0,777	6,475	-23,50
BL96-31,5	Calcareous shale	2,051	1,208	0,843	7,021	-23,50
BL96-32,0	Calcareous shale	1,690	0,800	0,890	7,413	-23,80
BL96-32,5	Calcareous shale	2,527	1,260	1,267	10,558	-23,40
BL96-33,0	Calcareous shale	2,299	1,214	1,085	9,037	-22,10
BL96-33,5	Calcareous shale	2,318	1,242	1,076	8,967	-23,70
BL96-34,0	Calcareous shale	2,036	1,019	1,017	8,472	
BL96-34,5	Calcareous shale	2,148	1,188	0,960	7,996	-23,60

NM-I-00	**Emery Gap**					
		TC	**TOC**	**Ccarb**	**CaCO3**	**d13C**
PBC 3	Limestone	10,475	0,252	10,223	85,190	-26,24
		9,686	0,099	9,587	79,891	-24,09
1.	Marly shale					-27,20
PBC 4	Bentonite					
2.	Marlstone / Marly shale	10,305	0,924	9,381	78,178	-25,50
3.	Calcareous shale					
PBC 5	Bentonite					
4.	Calcareous shale					
PBC 6	Limestone	10,525	0,119	10,407	86,721	
5.	Calcareous shale	9,937	0,276	9,661	80,506	
PBC 7	Limestone	10,750	0,113	10,637	88,645	
6.	Calcareous shale					
PBC 8	Marlstone					
7.	Calcareous shale	9,575	0,407	9,167	76,394	-25,80
PBC 9	Limestone					
8.	Calcareous shale	9,288	0,355	8,932	74,435	
PBC 10	Limestone	10,645	0,068	10,577	88,144	
PBC 11	Bentonite					
9.	Calcareous shale	10,650	1,606	9,045	75,371	
PBC 12	Limestone	10,990	0,118	10,872	90,602	
10.	Calcareous shale	10,255	0,458	9,797	81,641	
PBC 13	Limestone	10,690	0,171	10,519	87,659	
11.	Calcareous shale					
PBC 14	Limestone	10,875	0,139	10,736	89,468	
12a.	Calcareous shale	9,094	0,154	8,940	74,499	-25,00
12b.		9,158	0,259	8,898	74,150	-25,00
12c.		9,244	0,541	8,703	72,522	-25,50
PBC 15	Limestone	10,235	0,119	10,116	84,299	-25,30
13.	Calcareous shale	9,575	0,088	9,487	79,055	
PBC 16	Limestone					
PBC 17	Bentonite					
PBC 18	Limestone	10,695	0,140	10,555	87,955	
PBC 19	Bentonite					
14 a.	Calcareous shale					
14 b.	Calcareous shale	8,971	0,154	8,817	73,473	-25,00

NM-II-00	Las Vegas					
		TC	TOC	Ccarb	CaCO3	d13C
PBC 1	Limestone	10,800	0,088	10,712	89,267	-23,50
PBC 2 a.	Marly shale					
PBC 2 b.	Mergelstein					
1.	Marly shale					
PBC 3	Limestone	9,306	0,288	9,019	75,154	-22,10
2 a.	Calcareous shale					
2 b.	Calcareous shale					
2 c.	Marly shale	6,280	0,393	5,887	49,060	-23,41
PBC 4	Bentonite					
3.	Marly shale					
PBC 5	Bentonite					
4 a.	Marly shale					
4 b.	Marly shale					
PBC 6	Limestone	9,060	0,247	8,813	73,438	-23,60
5.	Calcareous shale					
PBC 7	Limestone	9,929	0,219	9,709	80,909	-23,20
		10,140	0,135	10,005	83,373	
6. - 8.	Marly shale					
PBC 10	Limestone	8,873	0,271	8,601	71,676	-22,72
PBC 11	Bentonite					
PBC 14	Limestone	10,190	0,080	10,110	84,254	-23,50
12a.	Calcareous shale	7,316	0,493	6,822	56,852	-22,10
12b.		8,871	1,503	7,368	61,400	
PBC 15	Limestone	9,380	0,085	9,295	77,460	-22,77
13.	Marly shale	8,338	1,647	6,691	55,754	
PBC 16	Limestone	9,275	0,121	9,153	76,276	-22,57
PBC 16 b.	Calcareous shale	8,382	0,169	8,213	68,443	
PBC 17	Bentonite					
14 a.	Limestone	9,527	0,148	9,379	78,156	
14 b.	Calcareous shale	9,263	1,273	7,990	66,583	-22,80
14 b.	Calcareous shale	7,600	0,402	7,198	59,983	-22,90
14 b.	Calcareous shale	6,052	0,792	5,260	43,835	
PBC 18	Limestone	9,734	0,309	9,425	78,545	-23,40
PBC 19	Bentonite					
15.	Calcareous shale					
PBC 20	Limestone	9,512	0,299	9,212	76,769	-23,73

TX-I-00	Hot Springs					
		TC	TOC	Ccarb	CaCO3	d13C
1a. Unten	Limestone	8,951	0,053	8,898	74,148	-26,20
1b.		8,906	0,053	8,853	73,774	
2.	Bentonite					
3.	Calcareous shale/Limestone	8,487	0,073	8,414	70,118	
4.	Limestone					
5.	Calcareous shale/Limestone					
6.						
7.	Calcareous shale/Limestone					
8a.	Calcareous shale/Limestone	7,904	0,069	7,835	65,292	
8b.		6,909	0,069	6,839	56,995	-24,00

8c.		8,281	0,052	8,229	68,575	-28,10
9.	Calcareous shale/Limestone					
10a. Unten	Calcareous shale/Limestone	8,952	0,048	8,903	74,196	
10b.		8,009	0,080	7,929	66,072	
11.	Calcareous shale/Limestone					
12a.	Limestone	10,107	0,061	10,046	83,713	
12b. Oben		9,998	0,060	9,938	82,816	-27,30
13a.	Calcareous shale/Limestone	8,555	0,030	8,525	71,039	-28,20
13b.		5,215	0,040	5,174	43,117	
14.	Limestone	9,898	0,050	9,848	82,067	
15a. Unten	Calcareous shale/Limestone	8,444	0,071	8,373	69,777	-27,20
15b. Oben		7,948	0,057	7,891	65,762	-27,00
16.	Limestone	10,625	0,064	10,561	88,005	
17.	Calcareous shale/Limestone	9,053	0,055	8,997	74,978	-27,90
18.	Limestone	9,623	0,065	9,558	79,646	
		10,890	0,057	10,833	90,274	
19.	Calcareous shale/Limestone					
20a.	Limestone	9,352	0,050	9,302	77,520	
20b.	unverw.	9,658	0,104	8,553	79,611	-27,55
20c.		10,356	0,219	10,137	84,472	
21a.	Calcareous shale/Limestone	8,922	0,070	8,852	73,764	-27,40
21b.		7,167	0,296	6,871	57,257	-26,90
21c.		9,912	0,121	9,791	81,588	-26,40
22a.	Limestone	9,808	0,054	9,754	81,284	-27,20
22b.		8,473	0,107	8,365	69,710	-27,40
		9,285	0,451	8,833	73,610	
23.	Calcareous shale/Limestone	8,217	0,728	7,488	62,404	

MX-I-00	**La Boca Canyon**					
		TC	**TOC**	**Ccarb**	**CaCO3**	**d13C**
1.	Limestone	10,100	0,303	9,797	81,645	-25,30
2.	Calcareous shale					
3.	Limestone	9,082	0,072	9,009	75,076	-25,00
4a.	Calcareous shale	8,548	0,050	8,498	70,813	-24,70
4b.		7,902	0,069	7,832	65,270	-24,80
5.	Limestone	8,939	0,071	8,868	73,897	-25,10
6.	Calcareous shale					
7.	Bentonite					
8.	Calcareous shale					
9.	Limestone	9,010	0,183	8,827	73,555	
10.	Calcareous shale	8,589	0,093	8,496	70,796	-24,80
11.	Limestone	8,827	0,218	8,608	71,734	
12.	Calcareous shale					
13.	Bentonite					
14.	Calcareous shale					
15a.	Limestone	10,240	0,358	9,882	82,353	-25,50
15b.		10,008	0,627	9,381	78,173	-26,50
15c.		9,131	0,079	9,051	75,427	-24,90
16.	Calcareous shale	9,188	0,064	9,124	76,034	
17.	Bentonite / Limonite					
18.	Calcareous shale	8,313	0,051	8,262	68,854	-25,30
		9,107	0,099	9,008	75,063	-25,20

19.	Limestone	9,610	0,153	9,457	78,807	-25,30
		9,479	0,059	9,420	78,496	
20.	Calcareous shale					
21.	Limestone	9,112	0,252	8,860	73,831	-25,40
22.	Calcareous shale					
23a.	Limestone	8,400	0,234	8,166	68,049	-24,95
23b.		10,490	0,387	10,103	84,192	-26,93
24.	Calcareous shale					
25.	Limestone	10,057	0,201	9,856	82,131	
26.	Calcareous shale	8,538	0,048	8,490	70,748	
27.	Limestone	9,497	0,082	9,414	78,450	-25,00
28.	Calcareous shale	8,236	0,046	8,190	68,248	-25,50
A	Limestone	10,095	0,219	9,876	82,304	
B	Limestone	8,981	0,050	8,931	74,424	-26,10
C	Calcareous shale	9,703	0,431	9,272	77,265	-25,20
D	Limestone	9,116	0,113	9,002	75,017	

13.2. Photo plates

Outcrop photos

Photo 1: The complete outcrop at location CAN-III-00 (Thistle Creek). Numbered beds are explained in Figure 14.

Photo 2: The uppermost part at location CAN-III-00 (Thistle Creek). Numbered beds are explained in Figure 14.

Photo 3: The whole outcrop of location CAN-II-00 (Big Horn River), incl. Markerbeds II.-1. through II.-11. (Figure 15).

Photo 4: Markerbeds II.-1. through II.-11. at location CAN-II-00 (Big Horn River), (Figure 15).

Photo 5: The whole outcrop of location CAN-I-00 (Burnt Timber Creek); see Figure 16.

Photo 6: Fossil-rich bed (4.) of location CAN-I-00 (Burnt Timber Creek) (see Figure 16).

Photo 7: The whole outcrop of location MT-I-00 (Cone); see Figure 17.

Photo 8: Bed 24. at location MT-I-00. Uppermost part of the section. Numbered beds are explained in Figure 17.

Photo 9: The whole outcrop of location MT-II-00 (Landfill); Figure 18.

Photo 10: Beds 2. and 3. at location MT-II-00 (Landfill). Numbered beds are explained in Figure 18.

Photo 11: The central part at location NM-I-00 (Emery Gap) showing the interbedding between limestones and shales. Numbered beds are explained in Figure 19.

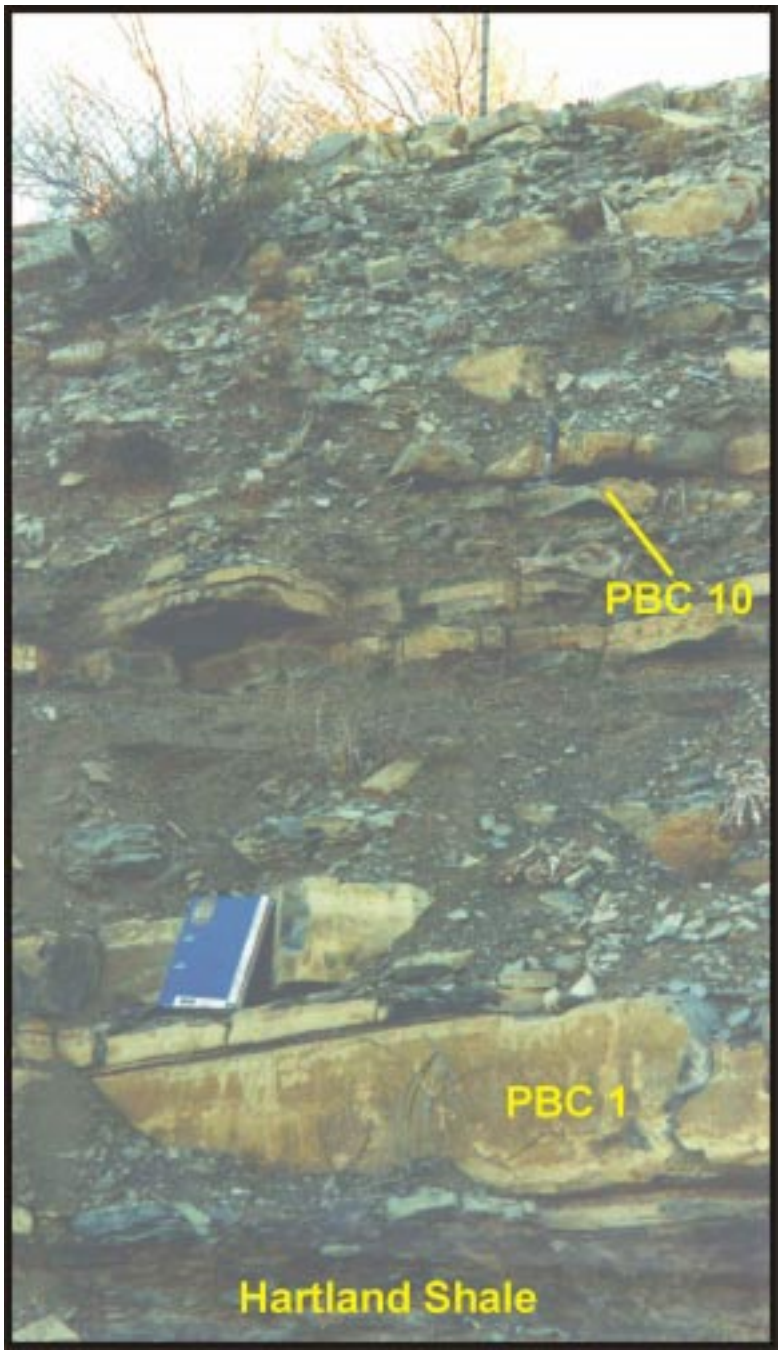

Photo 12: The complete section at Las Vegas, New Mexico (NM-II-00), including the underlaying Hartland Shale.

Numbered beds are explained in Figure 20.

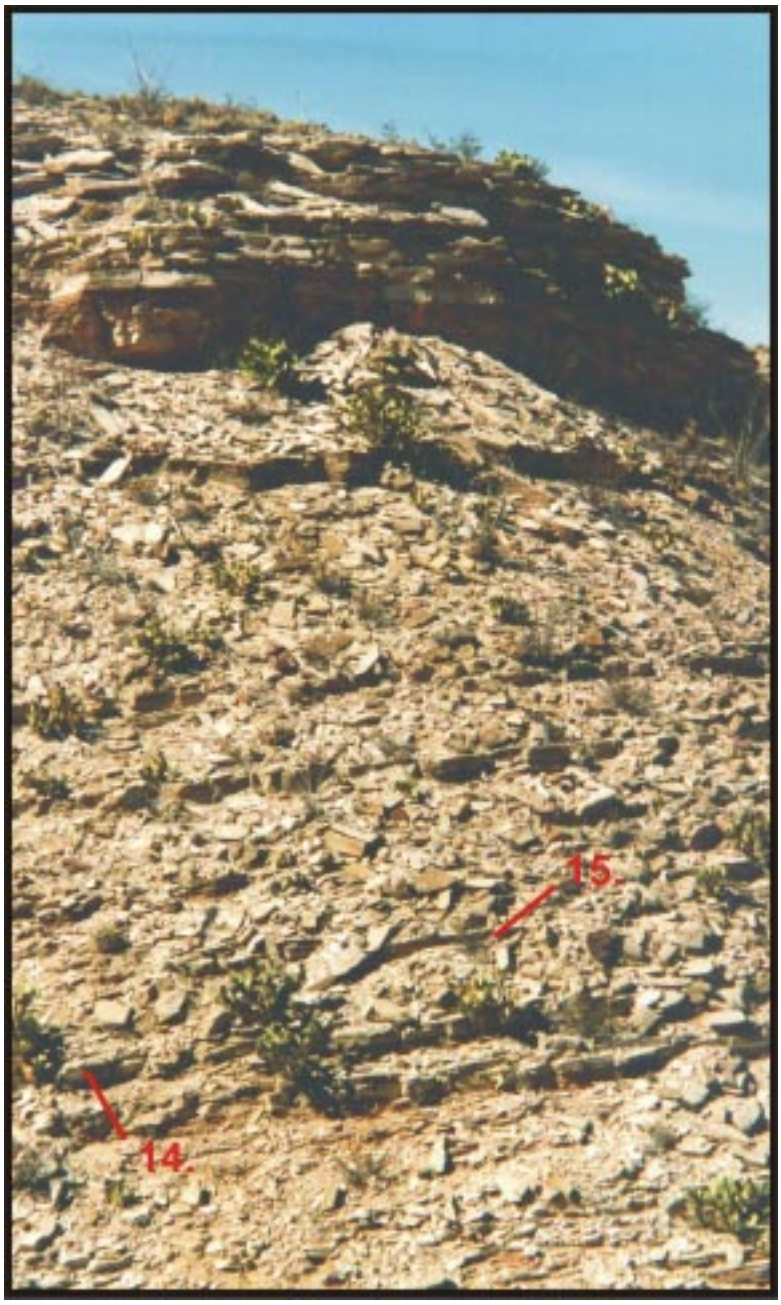

Photo 13: The complete section at Hot Springs locality in Big Bend national Park, Texas (TX-I-00). Numbered beds are explained in Figure 21.

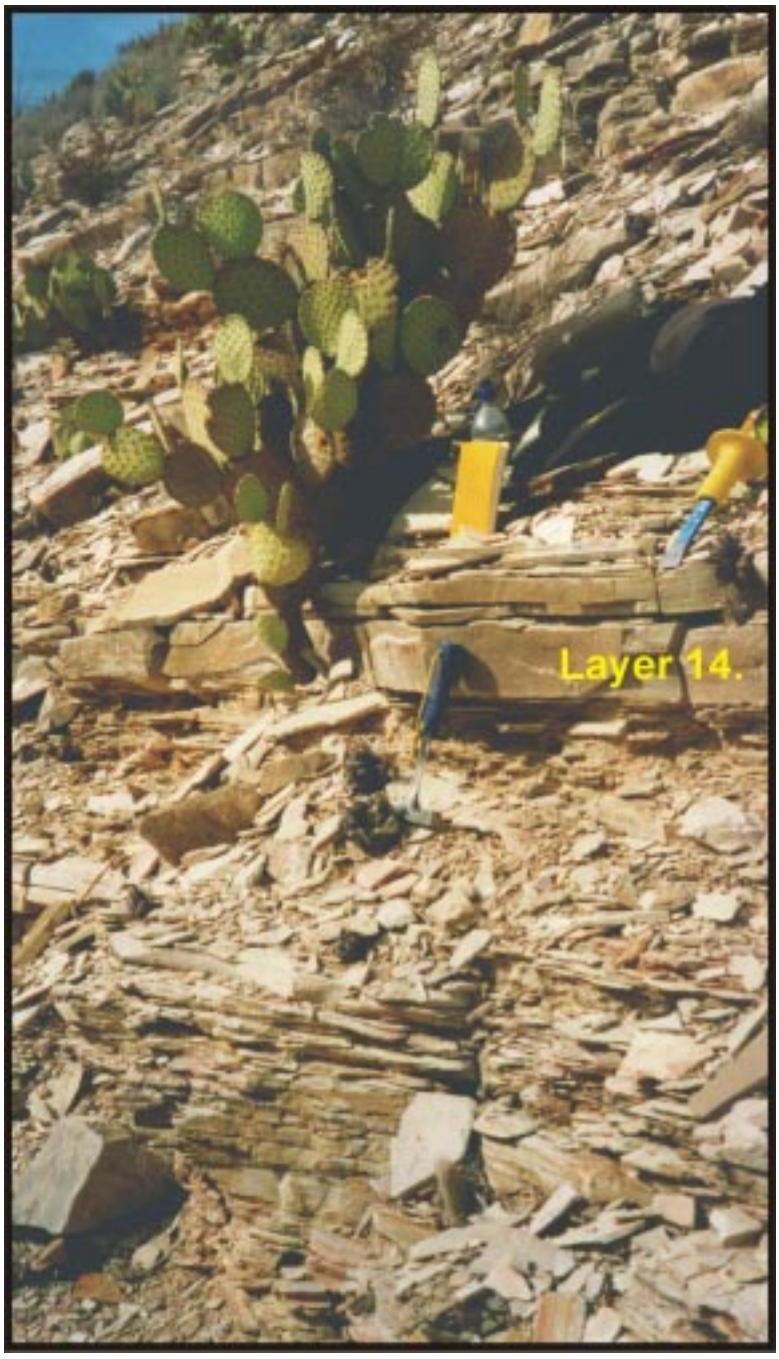

Photo 14: Detailed photo of the central part of the section at Hot Springs, Texas (TX-I-00). Bed 14. is one of the massive limestone beds at this locality. Numbered beds are explained in Figure 21.

Photo 15: The whole outcrop of location MX-I-00 (La Boca Canyon). Numbered beds are explained in Figure 22.

Photo 16: A typical bentonite of location MX-I-00 (La Boca Canyon). Numbered beds are explained in Figure 22.

13.3. Figure index